A spectroscopic and photometric study of stellar populations in a sample of clusters in the Magellanic Clouds

Dottorando:
Dott. Alessio Mucciarelli

Relatori:
Ch.mo Prof. Francesco R. Ferraro
Dott.ssa Livia Origlia
Dott. Eugenio Carretta

Coordinatore:
Ch.mo Prof. Lauro Moscardini

A tutte le mie Gala

" Con questi frammenti ho puntellato le mie rovine "
T. S. Eliot La terra desolata

" Gli astronomi sono meschini quanto i poeti:
a colazione arrivano a litigare per la marmellata "
I. Allende Il mio paese inventato

Contents

Chapter 1

Introduction

This Ph.D. Thesis has been carried out in the framework of a long-term and large project devoted to describe the main photometric, chemical, evolutionary and integrated properties of a representative sample of Large and Small Magellanic Cloud (LMC and SMC respectively) clusters. The globular clusters system of these two Irregular galaxies provides a rich resource for investigating stellar and chemical evolution and to obtain a detailed view of the star formation history and chemical enrichment of the Clouds. Therefore, the importance of this cluster system results twofold:

1. they represent ideal templates of stellar populations of known ages and metallicities in order to study the contribution of evolved sequences, Red Giant Branch (RGB) and Asymptotic Giant Branch (AGB) *in primis*, to the total light as a function of the age;

2. they represent good tracers of the chemical enrichment history of the Magellanic Clouds (MCs) and a detailed analysis of their abundance patterns distribution is a fundamental tool to investigate the role played by the main chemical contributors, as Supernovae Type II (SN II), Type Ia (SN Ia) and AGB stars.

The results discussed here are based on the analysis of high-resolution photometric and spectroscopic datasets obtained by using the last generation of imagers and spectrographs. The principal aims of this project are summarized as follows:

- The study of the AGB and RGB sequences in a sample of MC clusters, through the analysis of a wide near-infrared photometric database, including 33 Magellanic globulars obtained in three observing runs with the near-infrared camera SOFI@NTT (ESO, La Silla). The entire sample of selected clusters is reported in the map of Fig. 1.1, where the globulars are grouped according to their age and marked with different colors, blue for young (<500

5

Myr) clusters, green for intermediate-age (∼500 Myr- 8 Gyr) clusters and red for the old clusters.

- The study of the chemical properties of a sample of MCs clusters, by using optical and near-infrared high-resolution spectra. 3 observing runs have been secured to our group to observe 9 LMC clusters (with ages between ∼100 Myr and ∼13 Gyr) with the optical high-resolution spectrograph FLAMES@VLT (ESO, Paranal) and 4 very young (<30 Myr) clusters (3 in the LMC and 1 in the SMC) with the near-infrared high-resolution spectrograph CRIRES@VLT. These clusters are marked in Fig. 1.1 as filled points. All the target stars are selected by using the near-infrared photometric database described above.

- The study of the photometric properties of the main evolutive sequences in optical Color-Magnitude Diagrams (CMD) obtained by using HST archive data, with the final aim of dating several clusters *via* the comparison between the observed CMDs and theoretical isochrones. The determination of the age of a stellar population requires an accurate measure of the Main Sequence (MS) Turn-Off (TO) luminosity and the knowledge of the distance modulus, reddening and overall metallicity. For this purpose, we limited the study of the age just to the clusters already observed with high-resolution spectroscopy, in order to date only clusters with accurate estimates of the overall metallicity.

In Fig. 1.2 a scheme summarizes the global project, emphasizing the links between the 3 main tasks of this project and the aim to obtain a new Age-Metallicity Relation (AMR) for the MCs, a crucial information in the broad context of galaxy evolution.

1.1   Magellanic clusters in the framework of the stellar evolution

The Magellanic globular clusters provide an unique tool to investigate the integrated spectrophotometric behavior of stellar populations as a function of both age and chemical composition, given their wide range of ages and metallicities. The necessity to define reliable and homogeneous metallicity and age scales for this cluster system is a fundamental step in order to well calibrate the so-called *evolutive clock*, a theoretical tool able to describe the temporal evolution of the Spectral Energy Distribution (SED) of a stellar population. The spectral evolution of a Simple Stellar Population (SSP), an aggregate of coeval and chemical homogeneous stars, and its most relevant color glitches are ideal clocks for dating primeval galaxies and deriving a
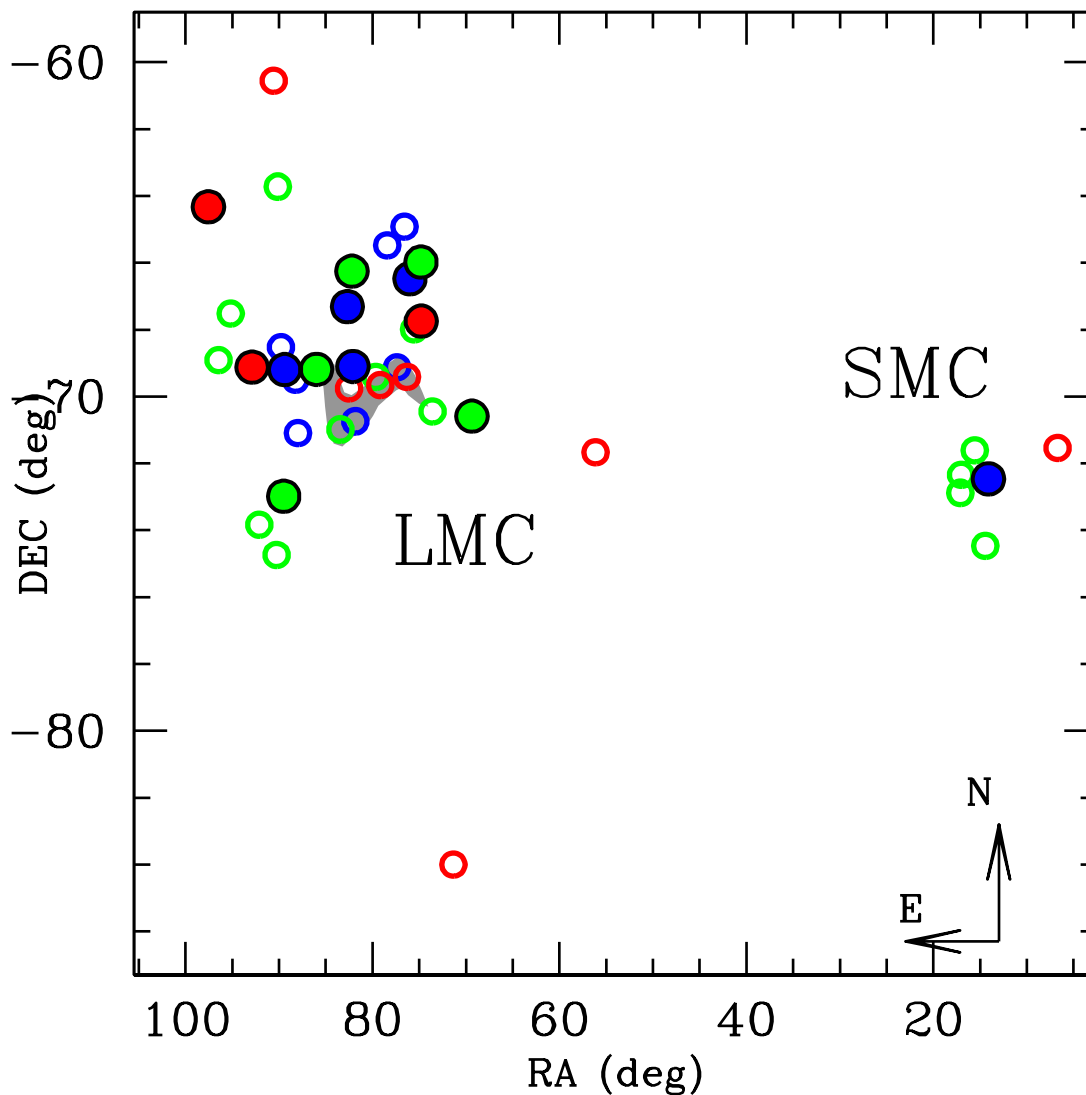
Figure 1.1: Spatial distribution of the LMC and SMC globular clusters observed with the near-infrared camera SOFI@NTT. Young clusters are marked as blue circles, intermediate-age clusters as green circles and old clusters as red circles. The filled circles indicate the clusters observed with high-resolution spectrographs (FLAMES@VLT and CRIRES@VLT).

suitable relation between look-back time and redshift. Stellar evolution theory predicts that red stars dominate the bolometric luminosity of a SSP after its first evolutionary stages. Two main events (the so-called Phase Transitions, Ph-Ts) should significantly mark the spectral evolution of a SSP during its lifetime. They are due to the sudden appearance of red and bright AGB after $\sim 10^8$ yrs (AGB Ph-T) and RGB after $\sim 10^9$ yrs (RGB Ph-T). From an observational point of

7
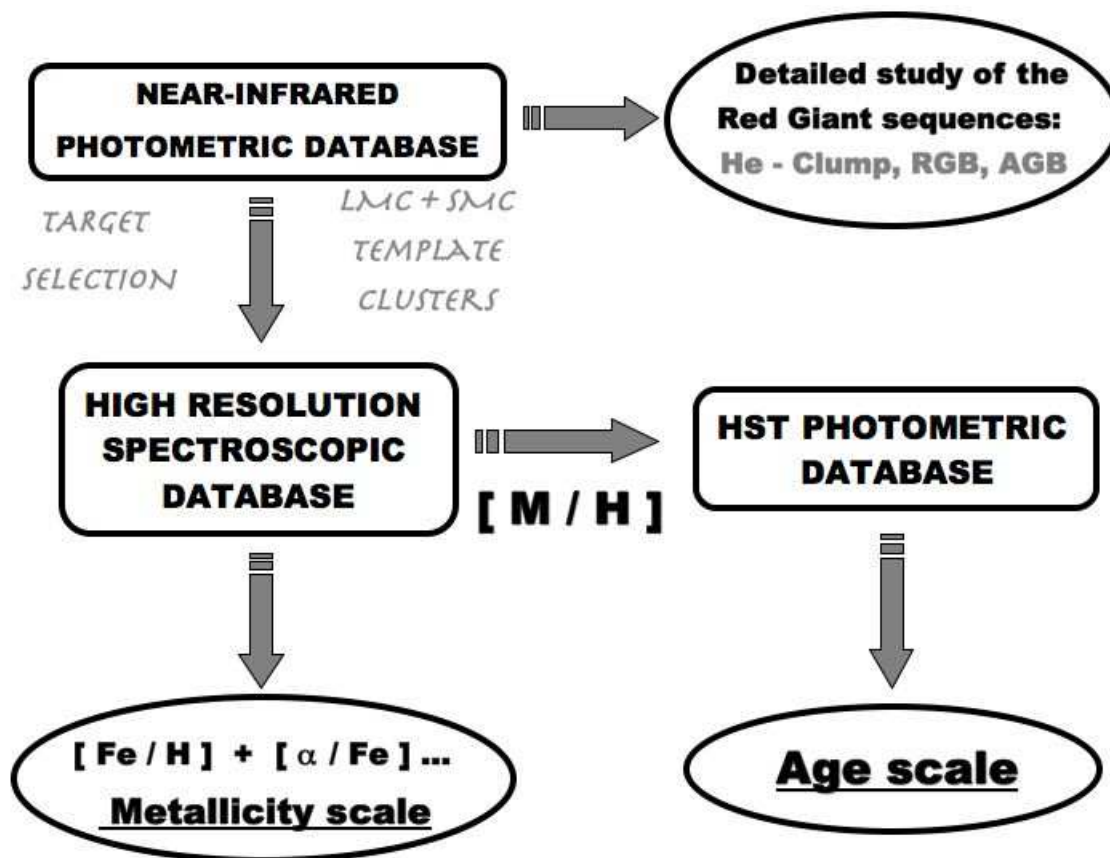
Figure 1.2: Diagram of the global project with the link between the different pieces that compose the work.

view, if these Ph-Ts are detected in SSPs of known age and metallicity, it becomes possible to yield the appropriate calibration of the clock. Once stellar aggregates formed, their SED evolve because of the continuos changes of their stellar content. The accurate calibration (in terms of age and metallicity) of the evolution of their emissivity represents the core of the *evolutive clock*. This tool results pivotal to trace the evolutive history of stellar populations and covers a key role in cosmological issues, because it can be used to date the primeval galaxies (as discussed in Renzini & Buzzoni, 1986; Buzzoni, 1989, 2002). The empirical calibration and following reading of the clock which drives the spectral evolution of SSPs and represents the basic tool for a quantitative description of galaxy evolution at high redshift, are the final goal of our global project.

1.2   Magellanic clusters in the framework of the chemical evolution

Modern cosmological theories based on the cold dark matter paradigm predict that all galaxies form from a local over-density in the primordial matter distribution, growing via the accretion of smaller *building blocks*. The most obvious candidates to be these fragments are the dwarf spheroidal (dSph) and the dwarf Irregular (dIrr) galaxies (Searle & Zinn, 1978; Zinn, 1980). A detailed screening of the chemical signatures of the stellar populations (both field and clusters) in these classes of galaxies, coupled with an accurate age determination, represents a fundamental step to understand in detail the evolutionary processes that shape galaxies. Moreover, the comparison of the Milky Way (MW) abundance patterns with its satellite ones provides stringent constraints to the origin of these galactic systems in the framework of the *merging* scenario described above. Clearly, if the Galactic Halo formed from dSphs or dIrrs (or objects like them), it should have kept some memory of their kinematical and chemical properties (see Geisler et al., 2007).

Direct measurements of chemical abundances of resolved stars in the Galactic satellites by using high resolution spectroscopy are actually a new and intriguing field of research. The recent advent of 8-10 m class telescopes provides first chemical information for several dSphs (Shetrone et al., 2003; Letarte et al., 2006), the Sagittarius (Sgr) dSph remnants (Bonifacio et al., 2000; Monaco et al., 2005, 2007; Sbordone et al., 2007) and the LMC and SMC (Hill, Andrievsky & Spite, 1995; Hill et al., 2000; Johnson, Ivans & Stetson, 2006). The observation of resolved stars in extragalactic systems with high-resolution spectrographs is limited by their intrinsic faintness: indeed the brightest targets stars are typically V$\sim$16-17 and they require several hours of integration time to achieve appropriate S/N. Fig. 1.3 summarizes the actual *state of the art* about our knowledge of the chemical signatures for three representative α-elements ([O/Fe], [Mg/Fe] and [Ca/Fe] ratios) from high resolution spectroscopic database for the Milky Way, dSph galaxies, Sgr, LMC field stars and clusters and SMC field stars. These results are based on very limited samples, typically 3-5 stars for each dSph, some tens for Sgr and less an hundred stars in the MCs. These samples provide only first guesses about the chemical properties of these stellar populations, emphasizing the necessity to expand these database.

1.3   Thesis organization

This Thesis is organized as follows:

Chapter 2 summarizes briefly the vast literature on the stellar populations in the MCs,
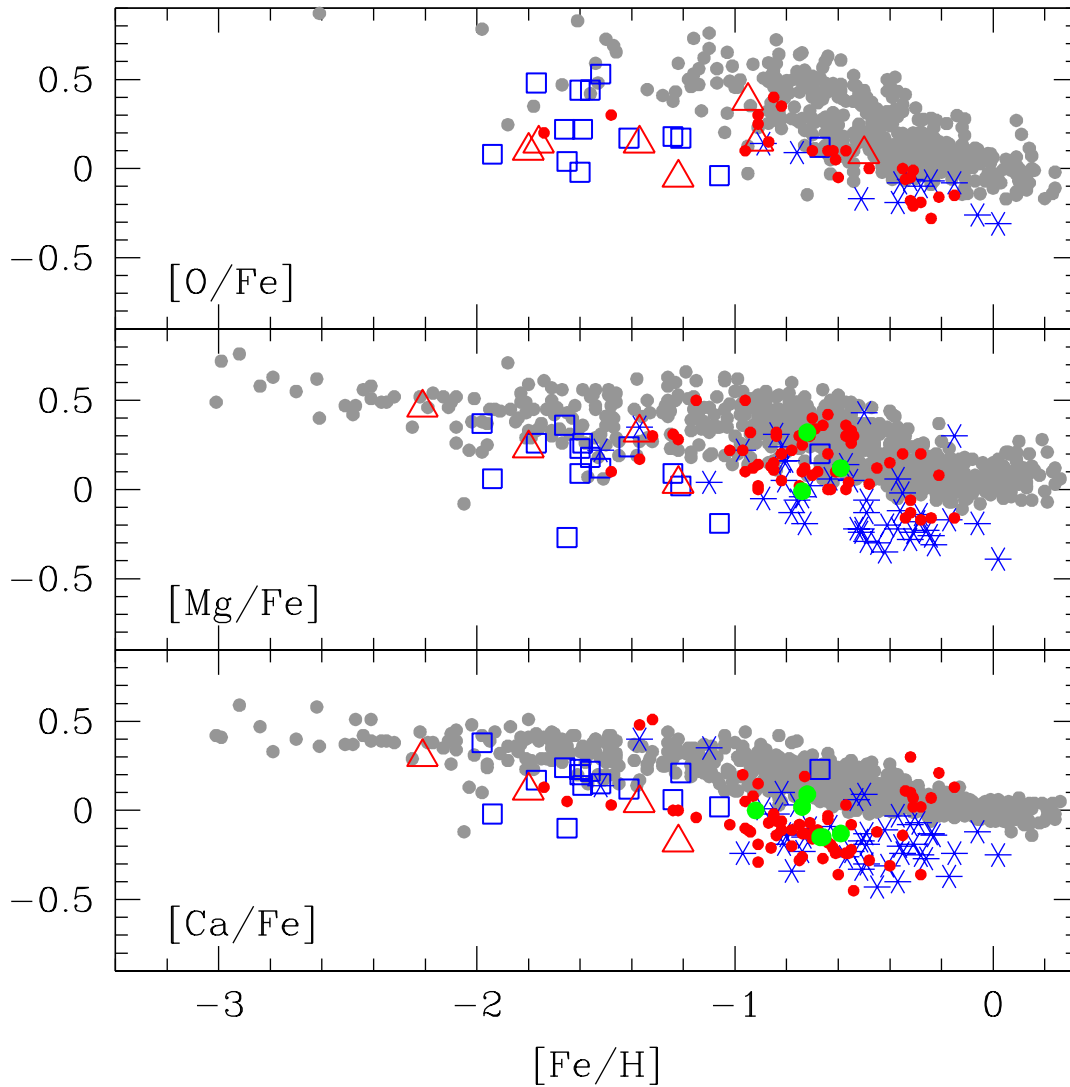
Figure 1.3: Summary of the actual knowledge of [O/Fe], [Mg/Fe] and [Ca/Fe] abundance ratios in the dSphs and dIrrs, in comparison to the Galactic abundance patterns. The MW stars are marked as grey points (data from Fulbright, 2000; Gratton et al., 2003; Reddy et al., 2003; Reddy, Lambert & Allende Prieto, 2006), LMC field stars as red points (Hill, Andrievsky & Spite, 1995; Pompeia et al., 2006), LMC clusters as red triangles (Hill et al., 2000; Johnson, Ivans & Stetson, 2006) SMC field stars as green points (Hill, 1997), dSph galaxies as blue empty squares (Shetrone et al., 2003) and Sgr dSph galaxy as blue asterisks (Bonifacio et al., 2000; Monaco et al., 2005, 2007; Sbordone et al., 2007)

concentrating mostly on our actual knowledge of the global properties of the Magellanic globular clusters, in terms of age and chemical composition.

Chapter 3 describes the near-infrared photometric analysis of LMC and SMC clusters, the

morphological properties of the observed sequences (AGB, RGB and He-Clump) and the definition of suitable population ratios in order to study the contribution of AGB and RGB sequences to the total cluster light as a function of its age.

Chapter 4 focuses on the results obtained from our observational campaign with the high-resolution spectrograph UVES@FLAMES. We describe the results about the first 4 intermediate-age LMC clusters analyzed so far. For each cluster we derived up to 20 abundance ratios sampling the main chemical elemental groups, namely light odd-Z, α, iron-peak and neutron-capture elements.

Chapter 5 presents the first results of our project devoted to obtain detailed ages of the *template* clusters for which we have already studied the chemical composition. The analysis of the 2 intermediate-age clusters NGC 1978 and NGC 1783 is discussed.

Finally, Chapter 6 summarizes schematically the overall results and briefly describes the ongoing projects and the future perspectives of this study.

Publications

(1) "Red giant stars in the Large Magellanic Cloud clusters"**A.Mucciarelli**, L.Origlia, F.R.Ferraro, C. Maraston, V. Testa, 2006, ApJ, 646, 939

(2) "On the iron content of NGC 1978 in the LMC: a metal rich homogeneous cluster" F.R.Ferraro,**A.Mucciarelli**, E.Carretta, L.Origlia, 2006, ApJL, 645, 33

(3) "Infrared photometry of Cepheids in the LMC clusters NGC 1866 and NGC 2131" V,Testa, M.Marconi, I.Musella, V.Ripepi, M.Dall'Ora, F.R.Ferraro, **A.Mucciarelli**, M.Mateo, P.Coté, 2007, A&A, 462, 599

(4) "The globular cluster NGC 1978 in the Large Magellanic Cloud" **A.Mucciarelli**, F.R.Ferraro, L.Origlia, F.Fusi Pecci,2007, AJ, 133, 2053

(5) "The intermediate-age globular cluster NGC 1783 in the Large Magellanic Cloud" **A.Mucciarelli**, L.Origlia, F.R.Ferraro, 2007, AJ, 134, 1813

(6) "Chemical composition of red giant stars in four intermediate-age globular clusters in the Large Magellanic Cloud" **A.Mucciarelli**, E. Carretta, L.Origlia, F.R.Ferraro, 2008, accepted for publication in AJ

(7) "The solar photospheric abundance of Europium. The impact of the 3-D hydrodinamical atmosphere CO^5BOLD models" **A.Mucciarelli**, E. Caffau, B. Freytag, H.-G. Ludwig, P. Bonifacio, 2008, accepted for publication in A&A

(8) "Near-Infrared Photometry of 4 stellar clusters in the Small Magellanic Cloud" **A.Mucciarelli**, L.Origlia, C. Maraston, F.R.Ferraro, 2008, submitted

Chapter 2

The Magellanic Clouds and their stellar cluster system

The MCs are the nearest galaxies with a present-day star-formation activity and represent a formidable laboratory for the study of stellar populations. They exhibit several epochs of star formation, likely linked to their mutual tidal interactions and with the MW (Bekki et al., 2004; Bekki & Chiba, 2005). Given their proximity, stellar populations in the MCs can be easily resolved, offering an excellent laboratory in a multitude of astrophysical issues.

The globular cluster system of the MCs plays a key role to gain a comprehensive picture of stellar cluster formation and their role in the evolutionary framework of their parent galaxies. In this Chapter we summarize the principal works in the vast literature about the stellar content in the MCs, focusing on the actual knowledge about ages and chemical compositions of the different stellar populations.

2.1 The Magellanic Clouds: morphology and structure

The Irregulars are gas-rich galaxies that evidence the lack of spiral density waves and bulge/nuclear regions and often exhibit a disk-like structure. The most massive Irregulars with a disky structure and residual spiral features are called *Magellanic spirals* (see Grebel, 2004). In particular, the LMC is a Barred Magellanic Spiral, because of the central, high surface brightness Bar; instead the SMC is the prototype of the so-called *Magellanic irregulars*, because it is less luminous and less massive than the other Magellanic spirals, and without spiral and barred structures. Fig. 2.1 reports a 3-D representation of the Local Group (Grebel, 1999) with the position of all the member galaxies (Spirals, Irregulars, dSphs and dwarf Ellipticals).

The MCs are the two most massive Irregulars in the Local Group and located in immediate

Figure 2.1: A scaled 3-D representation of the Local Group (Grebel, 1999). The open circles indicate the large spiral galaxies (M31, M32 and the MW), blue symbols the Irregular galaxies (including the LMC and the SMC), green symbols the dwarf Ellipticals and the orange symbols the dSphs. The dashed ellipsoid marks a radius of 1 Mpc around the Local Group barycenter (indicated as a red cross).

proximity of the MW, with a distance of 50 and 60 kpc for LMC and SMC respectively. These galaxies are one of the most important stepping stones on the path that leads to the extragalactic distance scale and several methodologies have been applied to infer the distance of the two Clouds, e.g. the Red Clump magnitude level (Alves et al., 2002), the variable stars, both Cepheids and RR Lyrae (Bono et al., 2002; Dall'Ora et al., 2004), the observations of the Supernova remnant 1987A (Panagia, 1999). All these analysis evidence an high level of consistency. In his monographic review about the MCs, Westerlund (1997) provides unweighted averages (obtained by using all distance determinations published prior to 1996) of $(m - M)_0$=18.48±0.04 and 18.94±0.05 for

the LMC and SMC, respectively. The following review presented by Alves (2004), including the distance determinations for the LMC obtained since 2002, provides an average distance modulus of $(m - M)_0$=18.50±0.02. This value yields an Hubble constant H_0=71±10 km/s/Mpc, in excellent agreement with that derived from the *Wilkinson Microwave Anisotropy Probe* of H_0=72±5 km/s/Mpc (Spergel et al., 2003). Several studies (at different wavelengths and based on different tracers) in the last decades derived a complex structure for the LMC. We report in Fig. 2.2 a sketch with the main features of this galaxy (from Staveley-Smith et al. , 2003). The main components are:

- the Disk — The generally accepted consensus about the LMC structure indicates an approximately planar galaxy with a circular geometry at large radii. When observed in the H I wavelengths, the LMC appears more symmetrical than in optical bands. Staveley-Smith et al. (2003) analyzed the large-scale H I structure of the LMC, evidencing a well-defined, nearly circular disk that forms the main body of the galaxy.

- the central Bar — This high surface brightness region results off-centered with respect to the center of the optical disk. Recently, Zaritsky (2004) proposed that the LMC Bar is a triaxal bulge. Assuming its luminosity of the order of $10^8 L_{B,\odot}$, the Faber-Jackson relationship provides a velocity dispersion of ∼70 Km/s. Recently, Cole et al. (2005) derive from a large Bar giant star sample a velocity dispersion of ∼30-40 Km/s, rejecting this hyphotesis.

- a (possible) kinematically hot halo — The presence of a *hot* spheroidal stellar halo has been investigated from several studies but without a definitive answer. The first evidence of a kinematically hot population was reported by Hughes, Wood & Reid (1991) analyzing a sample of long period variables. Recently, the sample of 43 Bar RR Lyrae stars studied by Minniti et al. (2003), and with a large velocity dispersion (σ_v=53±10 km/s) provides another hint to the existence of an halo component. On the other hand, other works have failed to detect this population (e.g. Schommer et al., 1992; Carrera et al., 2007).

- the Magellanic Stream, a trailing filament of neutral hydrogen that originates from the MCs and stretches for over ∼100 degrees in the Southern Sky. The widely accepted explanation for this feature links the Stream to the gravitational interactions between the Clouds and the MW.

- the Magellanic Bridge, a gaseous and stellar structure that connects the two Clouds. Differently to the Magellanic Stream, which appears to be a pure gas feature, the Bridge

includes a known stellar population

- 30 Doradus is an extended H II region in the north-east side of the LMC and represents the most active starbust region known in the Local Group.
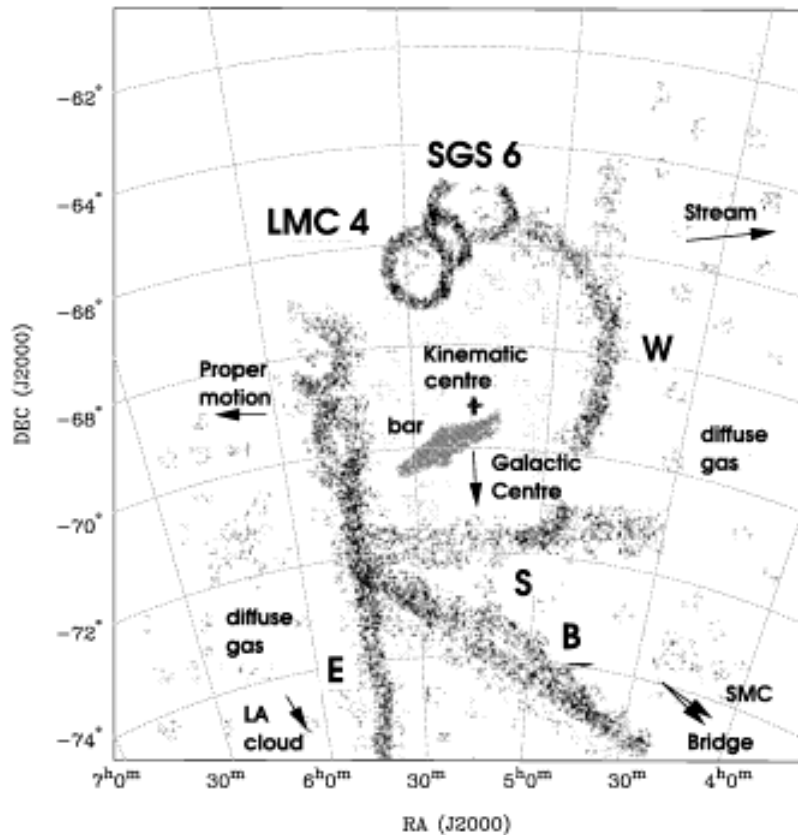
Figure 2.2: A schematic representation of the LMC structure derived by Staveley-Smith et al. (2003) from the H I maps. The kinematic center, the Bar, the main H I arms and the supergiant shells are plotted.

2.2 The Magellanic cluster system: so far, so near

The MC cluster system exhibits striking differences from that of our own Galaxy, where a clear-cut dichotomy is observed between young and intermediate-age sparse open clusters and old compact globular clusters. MCs include a large population of populous stellar clusters with

mass, morphology and dynamic comparable to the Galactic ones, but distributed in more wide and complex age and metallicity ranges.

Many general aspects of this GC system appear in contrast to the properties observed in the Galactic Globular clusters (GGCs) (see e.g. Westerlund, 1997; van den Bergh, 1998). These differences reflect differences in the dynamical and chemical history of the host galaxies. In summary, we can define some main differences:

- The very huge age distribution covered by these clusters ranges from ∼12-13 Gyr (corresponding to the primeval stellar populations born both in the LMC and SMC) to a few Myr, with the existence of very young massive cluster in *embryonic* stage (the most known case is the cluster R136 (Hunter, 1999) with an age of <5 Myr and located in the 30 Doradus). This distribution results to be not continuous in the LMC, with a lack of clusters in the range between ∼3 and ∼13 Gyr, the so-called *Age Gap* (Rich, Shara & Zurek, 2001; Bekki et al., 2004; Mackey, Payne & Gilmore, 2006). Natural consequence of this wide age distribution is the wide distribution of the integrated colors, already investigated by several authors (e.g. Searle, Wilkinson, & Bagnuolo, 1980; van den Bergh, 1981; Persson et al., 1983).

- A corresponding wide metallicity distribution (Olszewski et al., 1991; Grocholski et al., 2006), with the detection of metal-poor objects (with [Fe/H] between –2.5 and –1.5 dex) and a large fraction of metal-rich clusters ([Fe/H]≥–0.6 dex).

- The MC clusters are one order of magnitude less massive than the GGCs. Fig. 2.3 (upper panel) shows the mass distribution of a sample of LMC clusters by Mackey & Gilmore (2003), that results to be peaked at M∼ $4 \cdot 10^4 M_\odot$ (in comparison we report also the mean mass value for the GGCs, ∼ $2 \cdot 10^5 M_\odot$, see Harris, 1996).

- The MC clusters result more flattened with respect to the Galactic counterparts, with more stark departures from the spherical symmetry (Geisler & Hodge, 1980; van den Bergh & Morbey, 1984). White & Shawl (1987) show that more than 60% of the GGCs exhibits a mean ellipticity ϵ <0.10 (with a mean value of $\epsilon = 0.07$). Both Geisler & Hodge (1980) and Goodwin (1997) estimated mean ellipticity for the LMC GCs higher than the GGCs one, finding $\epsilon = 0.22$ and 0.14, respectively. Fig. 2.3 (lower panel) shows the ellipticity distribution of the LMC clusters sample by Geisler & Hodge (1980), with marked the average value for the GGCs.
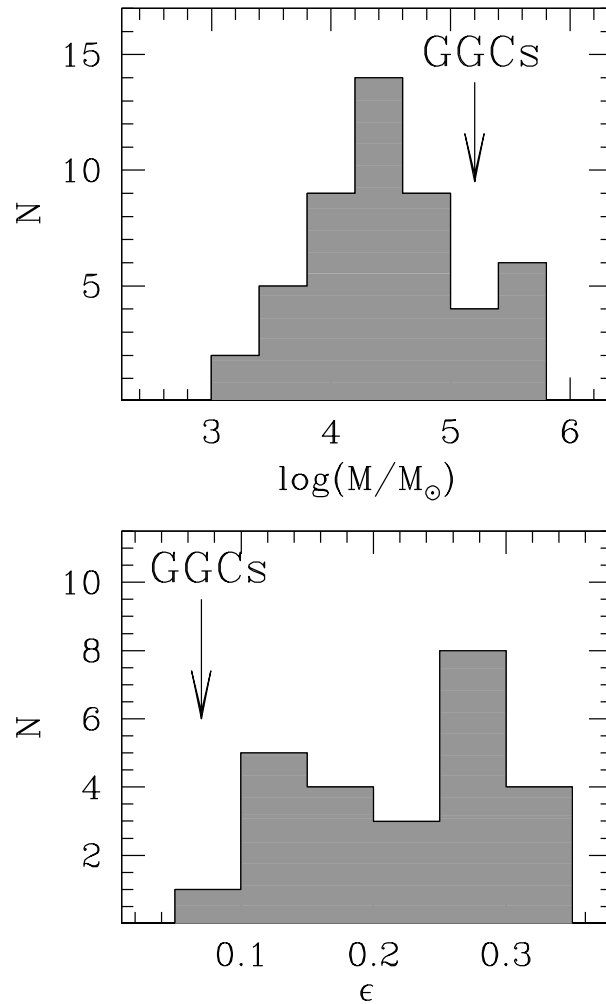
Figure 2.3: Upper panel: histogram of the mass distribution of the LMC clusters, data from Mackey & Gilmore (2003). The arrow indicates the average value from the GGCs. Lower panel: histogram of the ellipticity distribution of the LMC clusters, data from Geisler & Hodge (1980). The arrow indicates the average value from the GGCs.

- A large fraction of *apparently* binary (or multiple) clusters has been observed in the LMC (see e.g. Bhatia et al., 1991; Bhatia, 1992; Dieball, Muller,& Grebel, 2002; Portegies Zwart & Rusli, 2007). Pietrzynski & Udalski (2000) presented a wide atlas of the candidates binary clusters, including 745 star clusters and a total of 100 multiple cluster candidates with a maximum separation of 18 pc.

2.3 The age distribution of the MC stellar populations

The wideness of the age distribution covered by the stellar populations in the MCs (and in particular by their globular clusters) represents one of the most intriguing feature of these galaxies. The star formation history (SFH) of MC field stellar populations is not yet well known. Some studies, based on HST data in small fields, suggest that the LMC SFH (both in the disk and in the Bar) developed in a continuous way, with an increase of the star formation rate in the last few Gyrs. Smecker-Hane et al. (2002) obtained CMDs of a field centered in the LMC Bar and in another located in the Disk (see Fig. 2.4), deriving similar SFHs at older ages ($\sim$7-15 Gyr). The Bar SFH results dominated by two distinct enhancements in the Star Formation Rate from 4 to 6 and from 1 to 2 Gyr ago, while the Disk exhibits a nearly constant Star Formation Rate. A definitive consensus about the Star Formation Rate and the epochs of the main star formation episodes of the SMC is not yet reached: the main periods of star formation in the SMC disk are recognized by Harris & Zaritsky (2004) at 400 Myr, 3 Gyr and 9 Gyr, Dolphin et al. (2001) present a continuous star formation rate in the halo with a dominant episode between 5 and 8 Gyr and Rafelski & Zaritsky (2005) argue that the cluster age distribution shows few peaks, without significative *gaps*.

In order to describe the different stellar populations of the MCs (both field and cluster), we can distinguish three main age families:

- **Old population**: this stellar population is considered coeval to the Galactic Halo and includes the first stars born in the early ages of the MCs. Actually 15 *bona fide* old LMC and 3 SMC clusters are known and considered as *ideal* counterparts of the GGCs.

  Testa et al. (1995) and Brocato et al. (1996) provided the first ages for some old LMC clusters based on the direct measurement of the MS TO region. They found that the observed objects (namely NGC 1786, 1841, 2210 and 2257) have ages comparable with the metal-poor Galactic clusters, supporting a scenario in which the cluster formation in the two environments is coeval and similar. Olsen et al. (1998) analyzed WFPC2@HST CMDs for other 6 old LMC clusters (namely NGC 1754, 1835, 1898, 1916, 2005 and 2019), finding that all these globulars show very similar ages to GGCs and for three objects evidenced a discrepancy between the metallicity inferred from the RGB and the previous determination by Olszewski et al. (1991).

  Studies concerning the old SMC clusters point toward a slightly younger ages of these
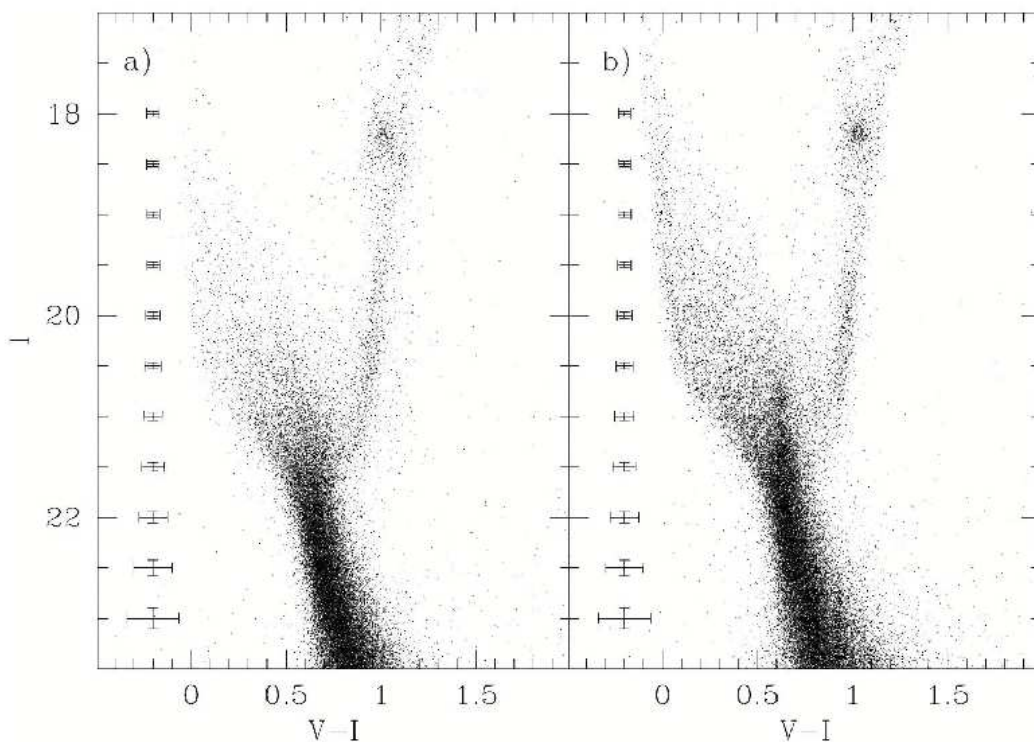
Figure 2.4: (V, V-I) CMDs obtained of 2 LMC stellar fields obtained by using WFPC2@HST. Left panel: field located at $1.7°$ from the center of the LMC. Right panel: field located in the LMC Bar. Figure from Smecker-Hane et al. (2002).

objects with respect to the old LMC clusters. Shara et al. (1998) derived for the old SMC cluster NGC 121 an age that is 2 Gyr younger than that of most Galactic and old LMC clusters (result confirmed by the recent findings by Glatt et al., 2008).

- **Intermediate population**: in this class we include stellar populations with ages between ~0.5 and ~10 Gyr. The intermediate-age clusters represent the majority of the entire LMC and SMC cluster population, as discussed by Olszewski et al. (1991). Despite the similar extension, the age distribution of the cluster and the field stars in the LMC appears to be distinctive for the presence of the so called *Age Gap*, corresponding to the lack of clusters in the wide range between ~3 and ~13 Gyr (Rich, Shara & Zurek, 2001). One only cluster, namely ESO121-SC03, has been detected in this age range (Mateo, Hodge & Schommer, 1986; Mackey, Payne & Gilmore, 2006), but it is likely that this cluster has been originated in the SMC (where the *Age Gap* is not observed and the cluster age distribution appears to

20

be continuos) and tidally captured from the LMC. Bekki & Chiba (2005) discussed three possible scenarios to solve this problem: (1) after the initial burst of clusters at the epoch of the galaxy formation (∼13 Gyr ago) the cluster formation has been interrupted until ∼3 Gyr ago; (2) the cluster formation has been not suspended after the initial burst. The cluster with ages between ∼13 and 3 Gyr have been tidally stripped, or (3) preferentially destroyed by the LMC tidal field. The most recent theoretical investigations (Bekki et al., 2004; Bekki & Chiba, 2005) have shown that the main episodes of star formation in the LMC can be related to the close encounters with the SMC. These latter events could be also responsible for the formation of the off-center Bar and the age distribution of the LMC GC system. Several studies investigated the properties of these clusters in different spectral ranges, near-infrared (Sarajedini et al., 2002; Ferraro et al., 1995; Grocholski et al., 2007), optical (Brocato, Di Carlo & Menna, 2001; Gallart et al., 2003; Kerber, Santiago & Brocato, 2007) and ultraviolet (Meurer, Cacciari & Freeman, 1990; Cole et al., 1997).

- **Young population**: as already discussed above, the MCs display a stark star-forming activity, confirmed from the presence of numerous globular clusters with ages less than 1 Gyr (Johnson et al., 2001; Kerber et al., 2002; Sirianni et al., 2002). One of the most largely studied LMC cluster, namely NGC 1866, belongs to this population (Testa et al., 1999; Barmina, Girardi & Chiosi, 2002).

The first method adopted almost three decades ago to date the MC clusters was described by Searle, Wilkinson, & Bagnuolo (1980) and based on the location of each cluster in the integrated color-color plane. They introduced a simple classification of these clusters into 7 classes (called SWB type). A more refined version of this method was proposed by Elson & Fall (1985). They divided the sequence described by the MC clusters in the $(U - B)_0$-$(B - V)_0$ diagram in 52 intervals of equal length (see Fig. 2.5) and assigned a value (the so called s–parameter) to each cluster by projecting it normally onto the curve. This parameter correlates linearly with the logarithm of the age and represents an easy tool to date these clusters. Different temporal calibrations of the s–parameter have been presented in the last two decades (Elson & Fall, 1985, 1988; Meurer, Cacciari & Freeman, 1990; Girardi et al., 1995)
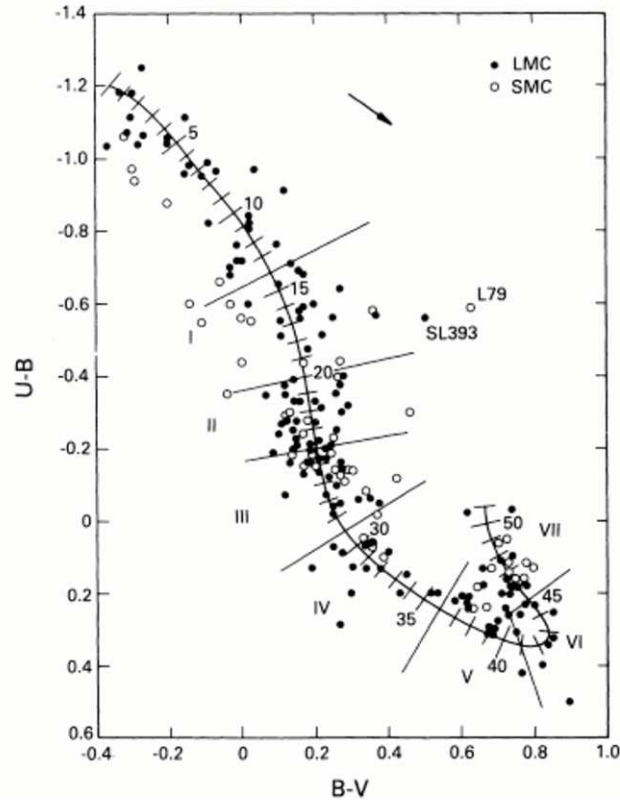
Figure 2.5: Color-color diagram for the LMC (filled circles) and SMC (open circles) globular clusters, obtained from the data of van den Bergh (1981). The solid curve is divided in 51 intervals, according to the s–parameter and the large bars indicate the approximate boundaries of SWB type I-VII. Figure from Elson & Fall (1985).

2.4 The chemical composition of the Magellanic Clouds

2.4.1 The field stars

The metallicity distribution of the LMC field stars has been investigated by using the Ca II triplet method in several works (e.g. Cole, Smecker-Hane & Gallagher, 2000; Cole et al., 2005; Carrera et al., 2007). Cole et al. (2005) analyzed 373 red giant stars located in the LMC Bar, deriving a metallicity distribution peaked at the median value of [Fe/H]=–0.40 dex. This distribution, reported in Fig. 2.6, can be described by the sum of two gaussian distributions, the first (that includes the majority of the stars) with a mean value of [Fe/H]=–0.37 dex (with a dispersion of $\sigma = 0.15$ dex) and the second with mean metallicity of [Fe/H]=–1.08 dex($\sigma = 0.46$ dex). Half of the

observed stars show metallicity between –0.51 and –0.28 dex, and only ∼10% are more metal-poor than [Fe/H]=–0.7 dex. By using the Padua isochrones (Girardi et al., 2000), they estimated the ages for the target stars, obtaining that ∼90% of the sample is younger than ∼6 Gyr.

Carrera et al. (2007) discussed the metallicity of several hundreds of LMC giant stars located in four fields at different distance from the Bar center (3°, 5°, 6° and 8°) and observed with HYDRA spectrograph at the CTIO 4m telescope. The metallicity distributions derived in each field are plotted in Fig. 2.7. The most inner fields exhibit mean metallicities very similar to that obtained by Cole et al. (2005) (with [Fe/H] between –0.45 and –0.50 dex); the outer field shows a decrease of the metallicity, with a mean metallicity of [Fe/H]=–0.79 dex.
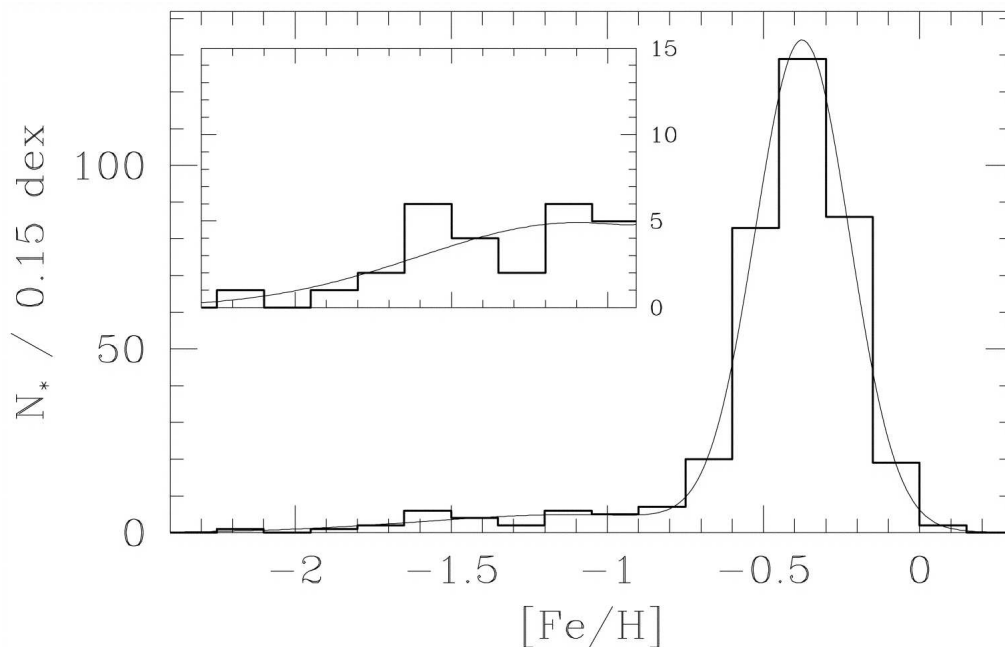
Figure 2.6: Metallicity distribution from the sample of Cole et al. (2005) including 373 giant stars of the LMC Bar. The inner panel shows the metal-poor tail of the distribution.

The optical high-resolution spectroscopic database actually available for the MC field stars include less than one hundred stars.

The first chemical abundances based on high resolution spectra have been presented by several groups to study small samples of F supergiants in the LMC (Russell & Bessell, 1989; McWilliam
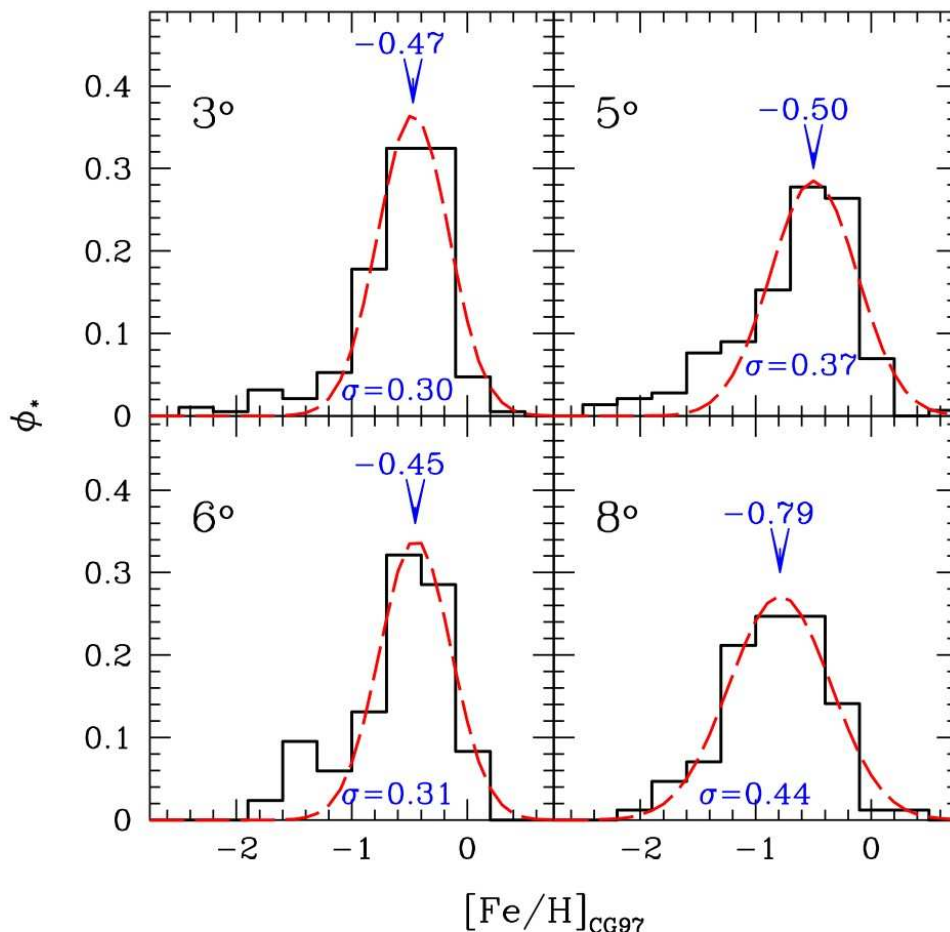
Figure 2.7: Metallicity distributions from the sample of Carrera et al. (2007) including 4 LMC Disk fields. In each panel the mean metallicity and the corresponding dispersion are reported.

& Williams, 1991; Hill, Andrievsky & Spite, 1995; Luck et al., 1998) and just 6 K supergiants in the SMC (Hill, 1997). Hill, Andrievsky & Spite (1995) analyzed 9 F supergiant stars (located in different regions of the LMC Disk) by using CASPEC and EMMI spectra (mounted at NTT@ESO, La Silla). These stars are metal-rich (from [Fe/H]=–0.34 dex and [Fe/H]=–0.15 dex) with a general depletion of the [O/Fe] and [Mg/Fe] ratios with respect to the solar value, but with enhanced ratios for [Ca/Fe] and [Ti/Fe]. Moreover, the neutron capture elements Ba and Eu result to be enhanced (>0.3 dex).

Smith et al. (2002) analyzed an handful of LMC field stars by using high-resolution infrared

spectra obtained with Phoenix spectrometer. These stars span a metallicity range from [Fe/H]=–1.1 dex and [Fe/H]=–0.3 dex, with [Na/Fe] and [Ti/Fe] ratios lower than their corresponding Galactic values at the same metallicity level by about ∼0.1-0.5 dex (similar to the findings in the dSph galaxies by Shetrone et al., 2003). Moreover, the [O/Fe] ratio results subsolar in all the target stars.

Recently, Pompeia et al. (2006) presented the first large sample (62 giant stars) of LMC disk stars observed with the high-resolution spectrograph GIRAFFE@FLAMES and spanning a range between [Fe/H]=–1.74 dex and –0.28 dex. Their findings confirm the previous ones by Hill, Andrievsky & Spite (1995), with an overall deficiency of the [α/Fe] ratios with respect to the Galactic patterns and an anomalous abundance pattern for the neutron-capture elements, that display a strong enhancement for [Ba/Fe] and [La/Fe] and a depletion for [Y/Fe] and [Zr/Fe]. Moreover, this sample exhibits stark depletions for [Na/Fe] and [Cu/Fe], that remark the substantial chemical difference between this environment and our Galaxy.

2.4.2 The globular clusters

Actually, the major quantity of information about the metallicity of these clusters derived mainly from two extensive surveys based on the Ca II triplet analysis. Olszewski et al. (1991) presented radial velocities for 81 LMC clusters and [Fe/H] ratios for 71 objects of this sample and these results have been adopted as the references for the metallicities of the LMC clusters. Fig. 2.8 (upper panels) shows the histograms for the [Fe/H] and radial velocity distributions obtained from the dataset by Olszewski et al. (1991). The metallicity distribution exhibits a large peak at ∼–0.50 dex with very few objects with [Fe/H] between –1.8 and –1 dex and a secondary peak with [Fe/H]<–1.8 dex and corresponding to the old population. The clusters appear to be distributed uniformly between V_{rad}=188 and 343 km/s, according to the HI velocity distribution by Staveley-Smith et al. (2003). No clear correlation between these two parameters has been found.

Recently, Grocholski et al. (2006) obtained new metallicity estimates for 28 populous LMC clusters by using near infrared FORS2@VLT spectra (metallicity and radial velocity distributions are plotted in Fig. 2.8, lower panels). The intermediate-age clusters in this sample evidence a very tight distribution, with a mean iron content of [Fe/H]=–0.48 dex (σ=0.09 dex), without clusters with solar metallicity (at odds with the findings of Olszewski et al., 1991). This metallicity for the LMC intermediate-age clusters results very similar to the previous study about the LMC Bar by Cole et al. (2005), indicating a similar chemical evolution for the Bar and the Disk. Moreover, they identify a possible intermediate, metal-poor cluster, namely NGC 1718, that they estimate to
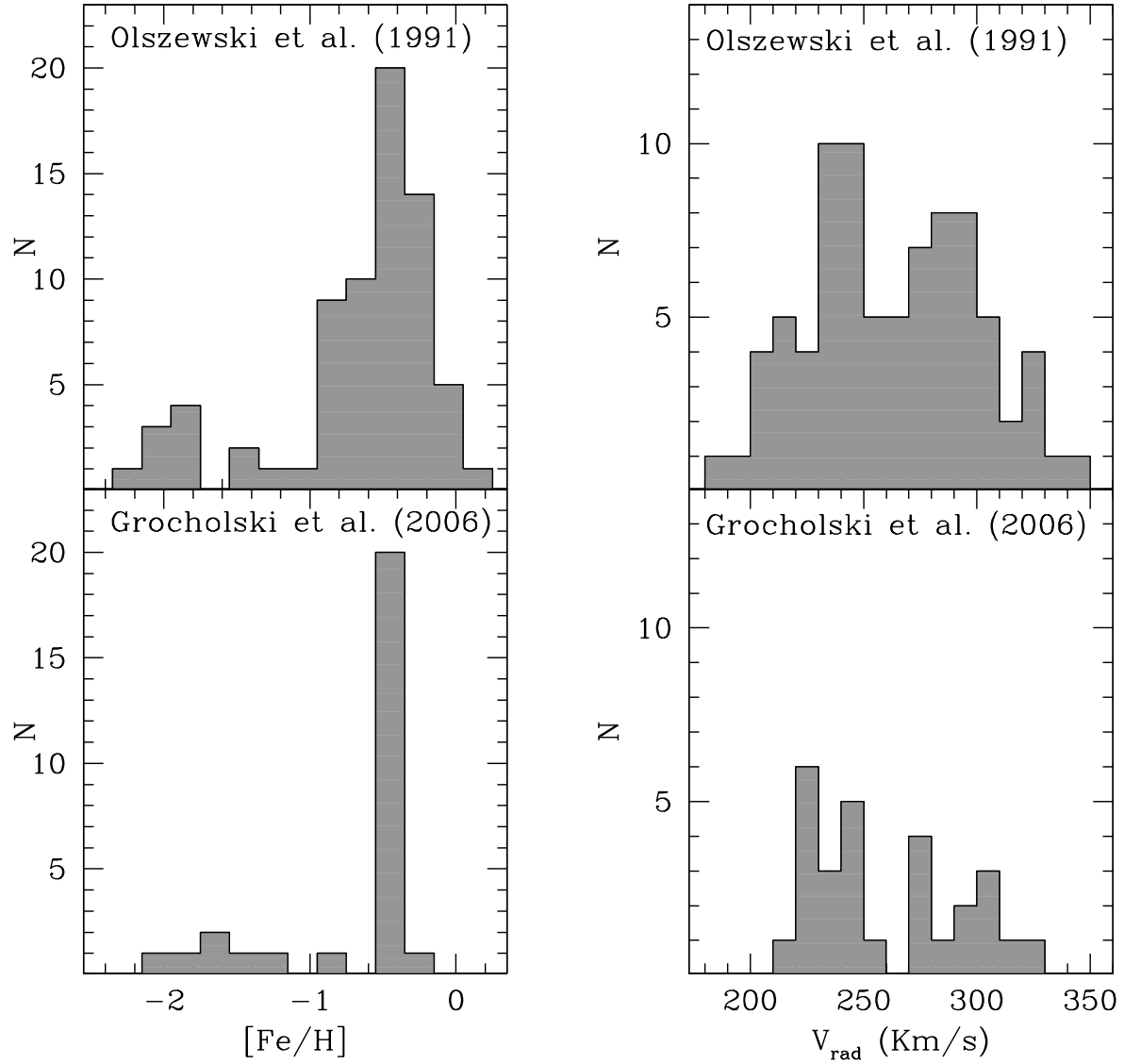
Figure 2.8: Left: metallicity distribution from the sample by Olszewski et al. (1991) (upper panel) and by Grocholski et al. (2006) (lower panel). Right: heliocentric radial velocity distribution from the sample by Olszewski et al. (1991) (upper panel) and by Grocholski et al. (2006).

have ∼2 Gyr and an iron content of [Fe/H]=–0.80 dex, lower than the other intermediate clusters of about 0.30 dex.

A detailed scenario of the chemical patterns for the different populations of LMC clusters by using high resolution spectroscopy is still lacking and only sparce and incomplete datasets are actually available.

Several studies have concerned 3 young, populous clusters, namely NGC 1818 (Richtler, Spite & Spite, 1989; Korn et al., 2000), NGC 2004 (Korn et al., 2000, 2002) and NGC 2203 (Smith et al., 2002), indicating an high metallicity ([Fe/H]>–0.6 dex) and a mild deficiency of α-elements. On the other hand, the chemical analysis by Oliva & Origlia (1998) based on near-infrared spectra for several young LMC and SMC clusters indicates an enhancement of the [Si/Fe] ratio (generally greater than 0.3 dex). Hill et al. (2000) presented chemical abundances of Fe, O and Al from high-resolution spectra of 10 red giant stars in 4 LMC globular clusters, namely NGC 1866, NGC 1978, ESO 121 and NGC 2210, spanning the entire age range of the LMC clusters system. They found [Fe/H]=–0.50, –0.96, –0.91 and –1.75 dex, respectively, finding in particular a strong discrepancy (∼–0.6 dex) for the iron content of NGC 1978 with respect to the previous one of Olszewski et al. (1991). All these clusters exhibit slightly enhanced [O/Fe] and slightly depleted [Al/Fe] with respect to the solar ratios. The older cluster in this sample (NGC 2210) displays a strong dispersion in the [Al/Fe] ratio of the three observed stars, according to the chemical dishomogeneity observed in the GGCs but without significant spread in the [O/Fe] ratio.

A detailed study of the chemical signatures of 4 old LMC clusters (namely NGC 1898, NGC 2005, NGC 2019 and Hodge 11) has been presented by Johnson, Ivans & Stetson (2006), confirming the low iron content (<–1.2 dex) of the old population. They generally found abundance ratios comparable to those of the Galactic GCs. Exceptions are the [Ca/Fe] and [Ti/Fe] ratios, similar to the solar values, and [V/Fe] and [Ni/Fe] which are significantly underabundant (by a factor of 2-3) with respect to the solar ratio.

For the SMC, the database available is limited to some very young clusters (see e.g. Oliva & Origlia, 1998; Hill, 1999), confirming the low iron content ([Fe/H]<–0.8 dex) of these objects but the level of the α-enhancement remains unclear and debated (e.g., for the cluster NGC 330 Oliva & Origlia (1998) estimated a [Si/Fe]=0.5 dex and Hill (1999) a mild depletion for the same ratio of about 0.2 dex with respect to the solar value).

2.5 Open issues

In the light of the literature review presented in this Chapter, we can summarize some open questions about the MC stellar populations:

- — Despite several works have been dedicated to dating individual Magellanic clusters, an homogeneous age scale based on the direct measurement of the MS-TO region has never been computed. The only homogeneous scale actually available is the one based on the s–parameter. This parameter needs to be accurately calibrated by using precise age measurements. A crude comparison between the ages inferred from the s–parameter and from MS-TO measurement, evidences as the s–parameter provides good ages for the young clusters but fails to date the oldest population (see e.g. the age determinations presented by Bomans et al., 1995; Brocato et al., 1996; Mighell, Sarajedini & French, 1998).

- — Currently, an homogeneous metallicity scale for the Magellanic clusters based on high-resolution spectra is still lacking. The only metallicity scale results to be the landmark study by Olszewski et al. (1991), based on the Ca II triplet method. Despite this work represents a gold-mine of information about the iron content for several clusters, some papers suggested for individual cluster discrepant metallicities. Olsen et al. (1998) noted as the metallicity by Olszewski et al. (1991) for 3 old LMC clusters are not able to well reproduce the observed RGB slope. Hill et al. (2000) found for 2 LMC clusters strong differences ($\sim$0.2 dex for NGC 2210 and $\sim$0.6 dex for NGC 1978) with respect to the previous ones. Also the comparison between the clusters analyzed both by Olszewski et al. (1991) and Grocholski et al. (2006) evidenced strong discrepancies.

- — A detailed screening of the chemical patterns of the different MC stellar populations is still lacking. The high-resolution spectroscopic samples actually available provide precious information about the α-elements and the possible depletion of these in the metal-rich regime with respect to the Galactic patterns. On the other hand, some works identify opposite trend, with the detection of metal-rich supergiant stars with enhanced [Ca/Fe] ratios (Hill, Andrievsky & Spite, 1995) or very-young, metal-poor stellar clusters with enhanced [Si/Fe] ratios (Oliva & Origlia, 1998).
  Several elements, as Cu, Y, Zr, Ba, exhibit peculiar patterns (Pompeia et al., 2006), pointing toward the differences of chemical evolutions between the MCs and the MW. On the other side, for several other interesting elements (e.g. Li, Al, Mn, Nd, Eu) the information actually

available are limited to few stars or inexistent.

- — The AMR for the MCs is yet not well known. Normally, the adopted AMR is defined by globular clusters. The combination of the Olszewski et al. (1991) metallicity scale with the sparce age estimates available in literature (as discussed in Rich, Shara & Zurek, 2001) provide a preliminary frame of AMR, affected by large scatter and the dishomogeneity of the age-axis. Other works, based on Washington (Bica et al., 1998) or Stromgrem (Dirsch et al., 2000) photometry, investigated the AMR by using the globular clusters or, alternatively, the $alpha$ content of planetary nebulae (Dopita et al., 1997). All these works provided similar results, with a metallicity jumps from [Fe/H]$\sim$–1.5 dex for the oldest objects to [Fe/H]$\sim$– 0.5 for the youngest ones. The surveys devoted to study the metallicity distribution of the field stars by using Ca II triplet (Cole et al., 2005; Carrera et al., 2007) provide metallicities for large sample of stars but the determination of the age for field stars is not a trivial matter and the resulting ages are largely uncertain, especially for the oldest populations. Generally, a possible evidence emerges from these surveys: the AMR in the LMC Bar has remained approximately constant in the last 5 Gyr (Cole et al., 2005), while in the Disk has increased in the time (Carrera et al., 2007). This finding seems to confirm the theoretical scenario drawn by Bekki et al. (2004) in order to explain the formation and the chemical evolution of the LMC, suggesting that the Bar would have formed from disk material as a consequence of tidal interactions between the Clouds and the MW about 5 Gyr ago.

Chapter 3

The Near-Infrared photometric survey of the Magellanic clusters

Based on the results published in :

— Mucciarelli, Origlia, Ferraro, Maraston & Testa, 2006, ApJ, 646, 939

— Mucciarelli, Origlia, Maraston & Ferraro 2008, submitted

In this Chapter we describe the near-infrared (J, H and K bands) photometric database of MC clusters, collected by our team in these last years by using the near-infrared camera SOFI@NTT. A detailed investigation of the main near-infrared properties of these clusters, both young-intermediate and old, is a crucial task to well-study the red giant sequences (He-Clump, RGB and AGB stars) and their contribution to the total cluster light. For this purpose, we obtained quantitative estimates of star population ratios (by number and luminosity) in the sampled evolutionary sequences and compared with theoretical models in the framework of probing the so-called Phase Transitions. An empirical calibration for these events, both in terms of age and metallicity, is a necessary step to use the SSPs as suitable templates in order to predict the age of unresolved SSPs and of more complex stellar systems as the galaxies (see e.g. Renzini & Buzzoni, 1986).

3.1 Theoretical background

A SSP is defined as an aggregate of coeval, initially chemically homogeneous, single stars and described by 4 main parameters, its age, its chemical composition (He and metal fractions Y and Z) and the initial mass function (IMF). The stellar clusters represent the best example of SSPs provided by the nature; on the other side, the galaxies are complex stellar population (CSP)

including different stellar generations, with various ages and metallicities. However, a CSP can be expanded in a series of SSPs and these latter cover the role of stellar units in order to model more complex populations. The continuos evolution of a SSP, due to the evolution of its stellar content (the so called passive evolution), modifies its SED.

The total bolometric luminosity of a SSP of age *t* can be expressed as the sum of two terms, related to the MS stars and post-MS (PMS) stars:

$$L_{TOT}^{bol}(t) = L_{MS}^{bol}(t) + L_{PMS}^{bol}(t).$$

The first term depends on the adopted mass-luminosity relation L(M,t) and IMF $\Phi(M)$:

$$L_{MS}^{bol}(t) = \int_{M_{inf}}^{M_{TO}} L(M,t)\Phi(M)dM.$$

The second term, that takes into account the PMS stars contribution, is directly proportional to the amount of fuel burned during any evolutionary phase and can be expressed in the following analytic form:

$$L_j^{bol}(t) = 9.75 \cdot 10^{10} \cdot b(t) \cdot F_j(M_{TO}) \ (L_\odot)$$

where b(t) is the *evolutionary flux* and $F_j(M_{TO})$ is the nuclear fuel burned by stars with $M = M_{TO}$ in their PMS evolutionary phase *j*. The function b(t) is given by

$$b(t) = \Phi(M_{TO})|\dot{M}_{TO}| \ (\text{stars yr}^{-1}),$$

and includes the IMF Φ computed for $M = M_{TO}$ and the time derivative $\dot{M}_{TO}$ of the analytic relation that correlates M_{TO} and t. The *evolutionary flux* indicates the number of stars evolving off the MS per year and represents the *death rate* of the population. The fuel is defined as

$$F_j = m_j^H + 0.1m_j^{He} \ (M_\odot)$$

where m^H and m^{He} indicate the mass of hydrogen and helium burned during the evolutionary phase j.

By using this approach (the so-called *Fuel Consumption Theorem*, see Renzini & Buzzoni, 1986) it is possible to compute the time evolution of the relative contribution of any evolutionary phase *j* (both MS and PMS) to the total light of the population. Fig. 3.1 reports the time evolution of the ratio L_j^{bol}/L_{TOT}^{bol} for the different evolutionary stages computed by Maraston (1998) for a SSP with solar Z and adopting a Salpeter IMF. Briefly, three age regimes can be identified in this diagram: (1) Age younger than ∼300 Myr: the integrated light of the SSP is completely dominated from the

MS stars that in the first 100 Myr contribute more than 60%, while the central He-burning phase contribute for an almost constant 25%.

(2) Age between ∼300 and ∼2 Gyr: the major contributor derives from the AGB stars that reach a maximum value (∼ 40%) at ∼500-600 Myr.

(3) Age older than ∼2 Gyr: the energetic of the SSP is dominated by the RGB stars; for ages older than ∼15 Gyr the relative contributor of the MS stars again dominates the energetic of old SSPs, because the MS integrated luminosity decreases more slowly than b(t) (see also Maraston, 1998).
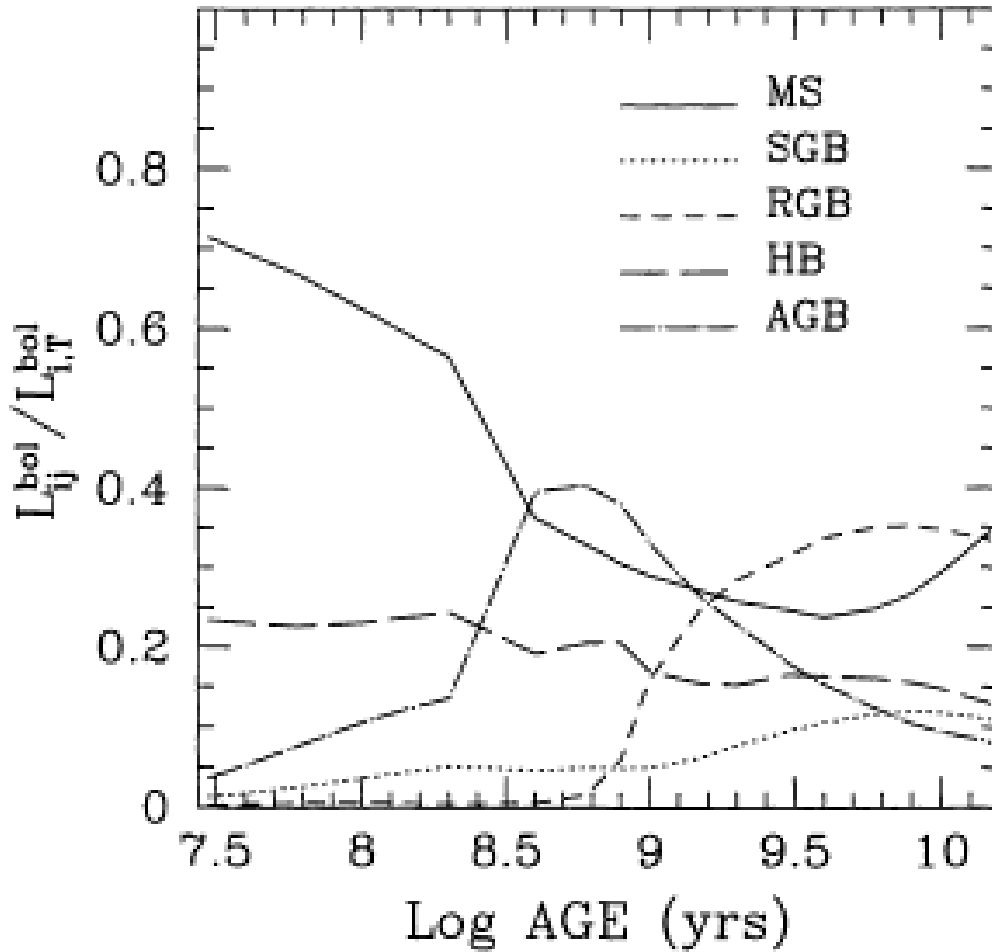
Figure 3.1: The time evolution of the relative contributions L_j^{bol}/L_{TOT}^{bol} of stars in the various evolutionary stages to the integrated bolometric luminosity of a stellar population.

These three phases are marked from the fast increase of the contributor of AGB and RGB respectively and corresponding to the first appearance in the SSP of AGB stars with C-O degenerate cores and RGB stars with He degenerate cores (Sweigart, Greggio & Renzini, 1989, 1990). These events are called AGB and RGB Phase Transition (Renzini & Buzzoni, 1986) and represent the main events in the temporal evolution of the spectro-photometric properties of a SSP. From a *integrated* point of view, they mark the epochs of the reddening of the SED. From a *resolved* point of view, these events correspond to changes of the morphology for AGB and RGB sequences, with the full development of these branches in the CMD .

3.2   Description of the photometric sample and observations

A total of 33 Magellanic *template* clusters, both in the LMC and in the SMC, have been selected accordingly to the *s*-parameter (already discussed in Chapter 2), in order to well sample the different age families of this cluster system. J, H, Ks images of these clusters have been obtained with the near IR imager/spectrometer SOFI (Moorwood, Cuby & Lidman, 1998) mounted at the ESO 3.5m NTT (La Silla, Chile) in three different observing runs: (1) 12-14 January 2000 (Program 64.N-0038(A) PI: Ferraro); (2) 27-30 December 2001 (Program ID 68-D-0287(A) PI: Ferraro); (3) 1-3 January 2006 (Program ID 076.D-0381(B) PI: Ferraro).

SOFI is equipped with a 1024×1024 Rockwell IR-array detector. All the observations presented here have been performed with a scale of $0.292''/pixel$, providing a $\approx 5' \times 5'$ field of view, each frame. The observations were obtained in good seeing conditions ($0.7'' - 0.8''$ on average). Total integration times of 2 min in J, 4 min in H and 8 min in Ks for the LMC clusters and of 4 min in J, 8 min in H and 16 min in Ks for the SMC clusters (split into sets of shorter exposures) have been secured, allowing to obtain accurate (S/N$\geq$30) photometry down to J$\approx$ 19 and H, Ks$\approx$ 18.5.

For each target cluster, a control field (a few arcminutes away from each cluster center) has been observed adopting the same instrumental configuration; these field images have been used to construct median-average sky frames. A large sample of high S/N flat fields in each bands has been acquired by using an halogen lamp swichted on and off alternatively. The final cluster and field frames have been sky-subtracted and flat-field corrected.

The complete list of all the observed clusters is reported in Tab. 3.1, with the coordinate α and δ (see Sect. 3.6.2), the s–parameter by Elson & Fall (1988) and Girardi & Marigo (2007), the corresponding population and the host galaxy. Moreover, Tab. 3.2 lists the main information

about metallicity, age (inferred by adopting the temporal calibration by Girardi et al., 1995) and reddening available for these clusters.

Cluster	α (J2000)	δ (J2000)	s	Population	Galaxy
NGC 2164	05:58:55.65	-68:31:00.75	23	YOUNG	LMC
NGC 2157	05:57:36.74	-69:11:53.58	25	YOUNG	LMC
NGC 2136	05:52:58.54	-69:29:32.32	26	YOUNG	LMC
NGC 2031	05:33:39.00	-70:59:14.54	27	YOUNG	LMC
NGC 1866	05:13:38.88	-65:27:53.30	27	YOUNG	LMC
NGC 2134	05:51:57.54	-71:05:51.63	28	YOUNG	LMC
NGC 1831	05:06:16.47	-64:55:12.76	31	YOUNG	LMC
NGC 2249	06:25:49.50	-68:55:14.25	34	INT.	LMC
NGC 1987	05:27:17.29	-70:43:56.78	35	INT.	LMC
NGC 2209	06:08:34.87	-73:50:06.46	35	INT.	LMC
NGC 2108	05:43:57.30	-69:10:55.93	36	INT.	LMC
NGC 2190	06:01:00.67	-74:43:29.10	36	INT.	LMC
NGC 2231	06:20:43.67	-67:31:13.05	37	INT.	LMC
NGC 1783	04:59:08.42	-65:59:12.75	37	INT.	LMC
NGC 1651	04:37:33.86	-70:35:09.24	39	INT.	LMC
NGC 2162	06:00:30.20	-63:43:15.27	39	INT.	LMC
NGC 1806	05:02:11.87	-67:59:10.11	40	INT.	LMC
NGC 2173	05:57:59.28	-72:58:42.83	42	INT.	LMC
NGC 1978	05:28:45.34	-66:14:09.12	45	INT.	LMC
NGC 1841	04:45:23.301	-83:59:55.30	42	OLD	LMC
NGC 2005	05:30:13.098	-69:45:35.54	46	OLD	LMC
NGC 1835	05:05:05.560	-69:24:08.06	47	OLD	LMC
NGC 1466	03:44:33.339	-71:40:18.87	48	OLD	LMC
NGC 1786	04:59:07.486	-67:44:47.44	48	OLD	LMC
NGC 2210	06:11:32.155	-69:07:18.11	48	OLD	LMC
NGC 1898	05:16:38.938	-69:39:47.69	50	OLD	LMC
NGC 2257	06:30:12.798	-64:19:35.81	51	OLD	LMC
NGC 330	00:56:17.96	-72:27:45.05	19	YOUNG	SMC
NGC 416	01:07:58.82	-72:21:18.96	35	INT.	SMC
NGC 419	01:08:17.35	-72:53:04.30	39	INT.	SMC
NGC 339	00:57:46.19	-74:28:17.58	47	INT.	SMC
NGC 361	01:02:10.09	-71:36:18.73	49	INT.	SMC
NGC 121	00:26:48.29	-71:32:10.03	52	OLD	SMC

Table 3.1: Near-Infrared photometric dataset for the observed MC clusters: coordinates, s–parameter (from Elson & Fall, 1988; Girardi & Marigo, 2007, for LMC and SMC clusters respectively), corresponding population and host galaxy.

Cluster	[Fe/H] (dex)	Age (Myr)	$E(B-V)$
NGC 2164	-0.60^a	81	0.10
NGC 2157	-0.60^a	114	0.10
NGC 2136	-0.55^b	135	0.10
NGC 2031	-0.52^b	160	0.18
NGC 1866	-0.50^d	160	0.10
NGC 2134	-1.00^a	190	0.10
NGC 1831	$+0.01^c$	315	0.10
NGC 2249	-0.12^a	524	0.10
NGC 1987	-1.00^a	620	0.12
NGC 2209	-1.20^a	620	0.07
NGC 2108	-1.20^a	734	0.18
NGC 2190	-0.12^c	734	0.10
NGC 2231	-0.67^c	869	0.08
NGC 1783	-0.45^a	869	0.10
NGC 1651	-0.37^c	1218	0.10
NGC 2162	-0.23^c	1218	0.07
NGC 1806	-0.23^c	1442	0.12
NGC 2173	-0.24^c	2021	0.07
NGC 1978	-0.96^d	3353	0.10
NGC 1841	-2.20^a	2021	0.07
NGC 2005	-1.80^e	3970	0.10^1
NGC 1835	-1.79^c	4700	0.12
NGC 1466	-2.17^c	5564	0.07
NGC 1786	-1.87^c	5564	0.12
NGC 2210	-1.76^d	5564	0.10
NGC 1898	-1.22^e	7789	0.09
NGC 2257	-2.00^a	9232	0.07
NGC 330	-1.33^f	42	0.06^2
NGC 416	-0.80^g	620	0.08^3
NGC 419	-0.60^g	1218	0.08^4
NGC 339	-0.70^g	4700	0.03^3
NGC 361	-1.45^h	6587	0.07^3
NGC 121	-1.71^h	10700	0.05^3

Table 3.2: Near-Infrared photometric dataset for the observed MC clusters: metallicity, age from the s–parameter (see Tab. 3.2), E(B-V). References for the metallicity: (a) Sagar & Pandey (1989); (b) Dirsch et al. (2000); (c) Olszewski et al. (1991); (d) Hill et al. (2000); (e) Johnson, Ivans & Stetson (2006); (f) Oliva & Origlia (1998); (g) de Freitas Pacheco, Barbuy & Idiart (1998); (h) Mighell, Sarajedini & French (1998). References for the reddening: for the LMC clusters values Persson et al. (1983); for the SMC clusters values from (1) Olsen et al. (1998), (2) Gonzalez & Wallerstein (1999), (3) Mighell, Sarajedini & French (1998), (4) Hunter et al. (2003).

3.3 The data reduction, astrometry and center of gravity

The photometric analysis was performed by using *DAOPHOT-II* (Stetson, 1987). For each observed field all the images in the J,H,Ks filters were carefully aligned and trimmed in order to have three output images, one per filter, slightly smaller than the original ones but perfectly registered. Then, a *DAOPHOT-II* Point Spread Function (PSF) fitting run was applied to each image. The output catalog with the instrumental magnitudes has been checked for any spurious detection or missing object (typically 3–4 stars at most) which have been included in the catalog by hand.

The instrumental magnitudes have been transformed into the Two-Micron All-Sky Survey (2MASS) photometric system, by using the large number of stars (typically a few hundred) in common. The overall dispersion of these transformations is $\sigma \leq 0.01$ mag in all the three filters.

The calibrated photometric catalogs in each filter were finally matched and merged together in a global catalog, using the CataXcorr and Catacomb softwares developed at the Bologna Observatory for an optimized cross-correlation.

3.4 The CMDs

In Fig. 3.2– 3.8 we reported the CMDs for the LMC clusters and surrounding fields grouped accordingly with the ages inferred by the s–parameter, while Fig. 3.9 and 3.10 plot the CMDs for the SMC clusters and corresponding fields, respectively. The photometric sample presented here has been selected in order to span the wide age range that characterize the Magellanic cluster system, with the presence both of very young and old objects. In this way, the corresponding CMDs exhibit different morphologies and in order to well describe the main observed morphological features, we have divided the clusters in groups, according to their s–parameter and different CMD morphology.

3.4.1 Young clusters

The observed CMDs for the young group of cluster (Fig. 3.2 and 3.3 for the LMC clusters and Fig. 3.9 and 3.10 for the SMC cluster NGC 330) appear quite complex, hence particular care has been devoted to separate the cluster population from the LMC field. In order to help the reader identify the two populations we have plotted in the last panel of Fig. 3.2 a sketch showing the mean location of cluster (grey regions) and field (dashed region) population in the CMD. The main properties of these CMDs can be summarized as follows:

(i) Magnitudes as faint as K≈ 18.5 have been measured.

(ii) The brightest objects at K < 13 are likely AGB stars.

(iii) A blue sequence is clearly visible at -0.3< $(J - K)$ < 0.3 and K>15.5, corresponding to the brightest end of the cluster MS.

(iv) Helium clump cluster stars define a sequence at $K = 13 - 14$ and $(J - K) \sim 0.2$ in the youngest objects (namely NGC 2164, NGC 2157, NGC 2136). In older clusters (namely NGC 2031, NGC 1866, NGC 2134, NGC 1831), they define a clump at progressively lower magnitudes ($K = 14 - 15$) and redder colors ($0.4 < (J - K) < 0.6$).

(v) The direct comparison of each panel in Figs. 3.2 and 3.3 clearly shows the significant contribution of the LMC field stars. As schematically shown in the last panel of Fig. 3.2, most of the stars in the region $0.4 < (J - K) < 1$ and $K > 12$ are indeed LMC field stars, with a well defined RGB at $12 < K < 16$ and the He-clump at K≈17.

3.4.2 Intermediate-age clusters

The observed CMDs for the second group of cluster (Fig. 3.4, 3.5, 3.6, 3.7, 3.9 and 3.10) show the following characteristics:

(i) Magnitude limits down to K≈ 18.5, i.e. about 1.5 mag below the He-clump, which is clearly visible as a clump of stars at K ≈ 17 for the LMC clusters and K ≈ 17.5 for the SMC clusters (see Fig. 3.9).

(ii) A well-populated and extended RGB.

(iii) The brightest objects at K < 12 and at K < 12.5 in the LMC and SMC clusters respectively are likely AGB stars.

(iv) Unlike the first group of clusters, in these objects cluster and field populations do overlap.

3.4.3 Old clusters

We grouped here the 8 LMC clusters plotted in Fig. 3.8 and the SMC cluster NGC 121 (see Fig. 3.9 and 3.10). All these clusters evidence the well populated RGB; the He-Clump is not detected, due to the old age of these objects (Testa et al., 1995; Brocato et al., 1996; Olsen et al., 1998, showed as all these clusters exhibit Blue Horizontal Branch).

LMC
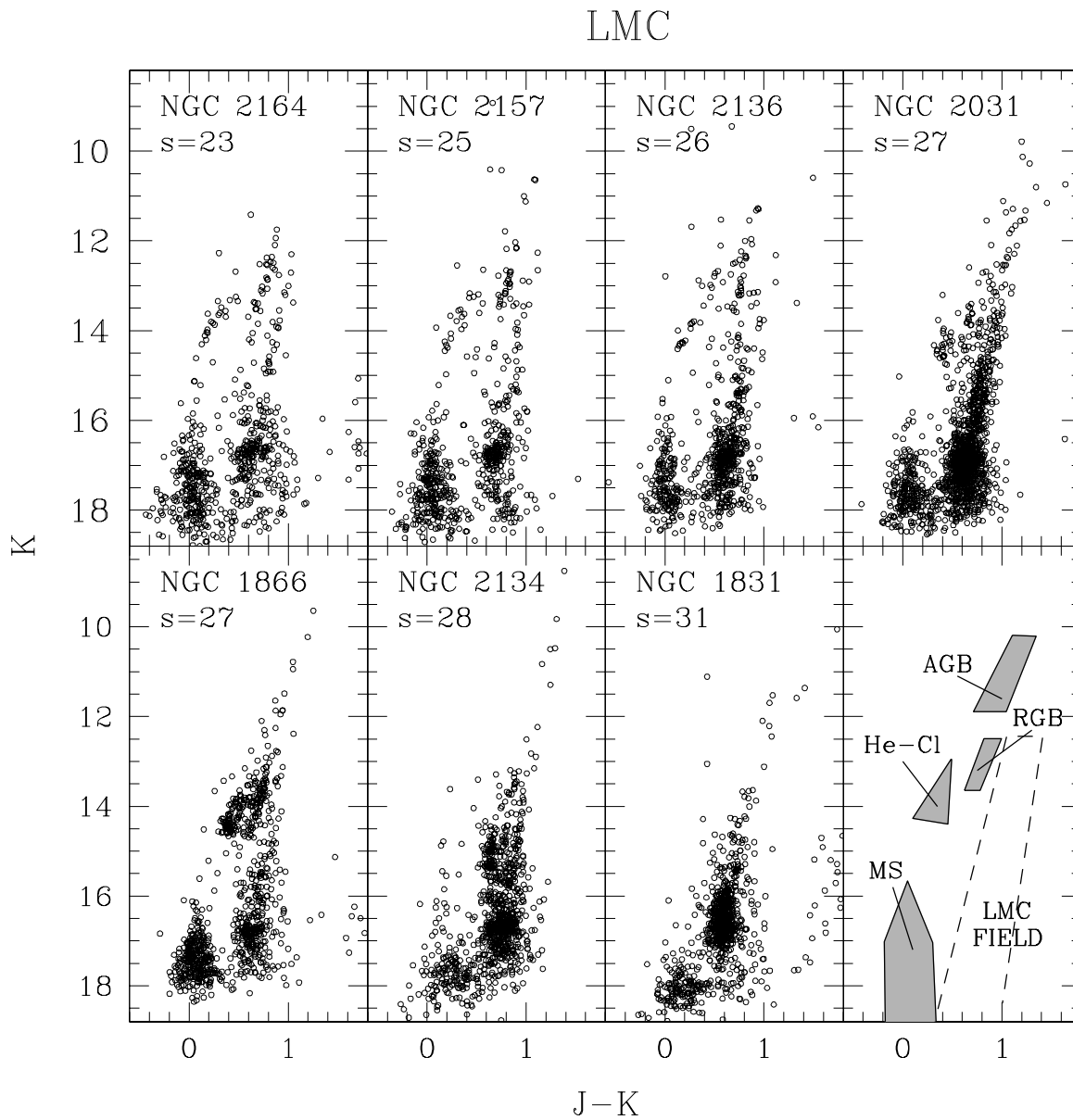
Figure 3.2: (K, J–K) CMDs of the 7 observed LMC clusters with $s = 23 - 31$. In the last panel a sketch of the CMD loci dominated by the cluster (grey regions) and the LMC field (dashed box) populations are also shown for sake of clarity.

LMC
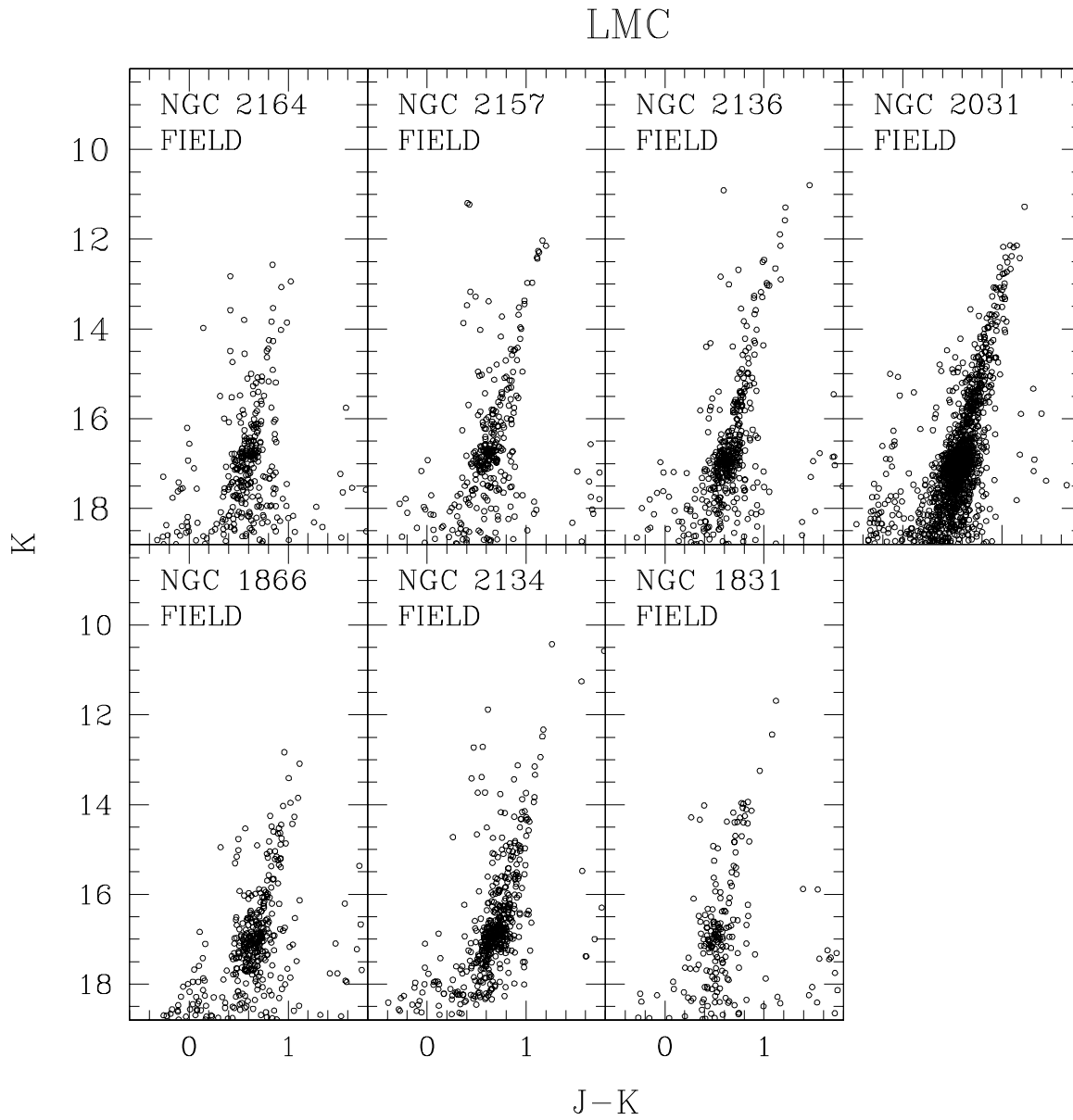
Figure 3.3: (K, J–K) CMDs of the fields adjacent to the 7 observed LMC clusters with $s = 23 - 31$.
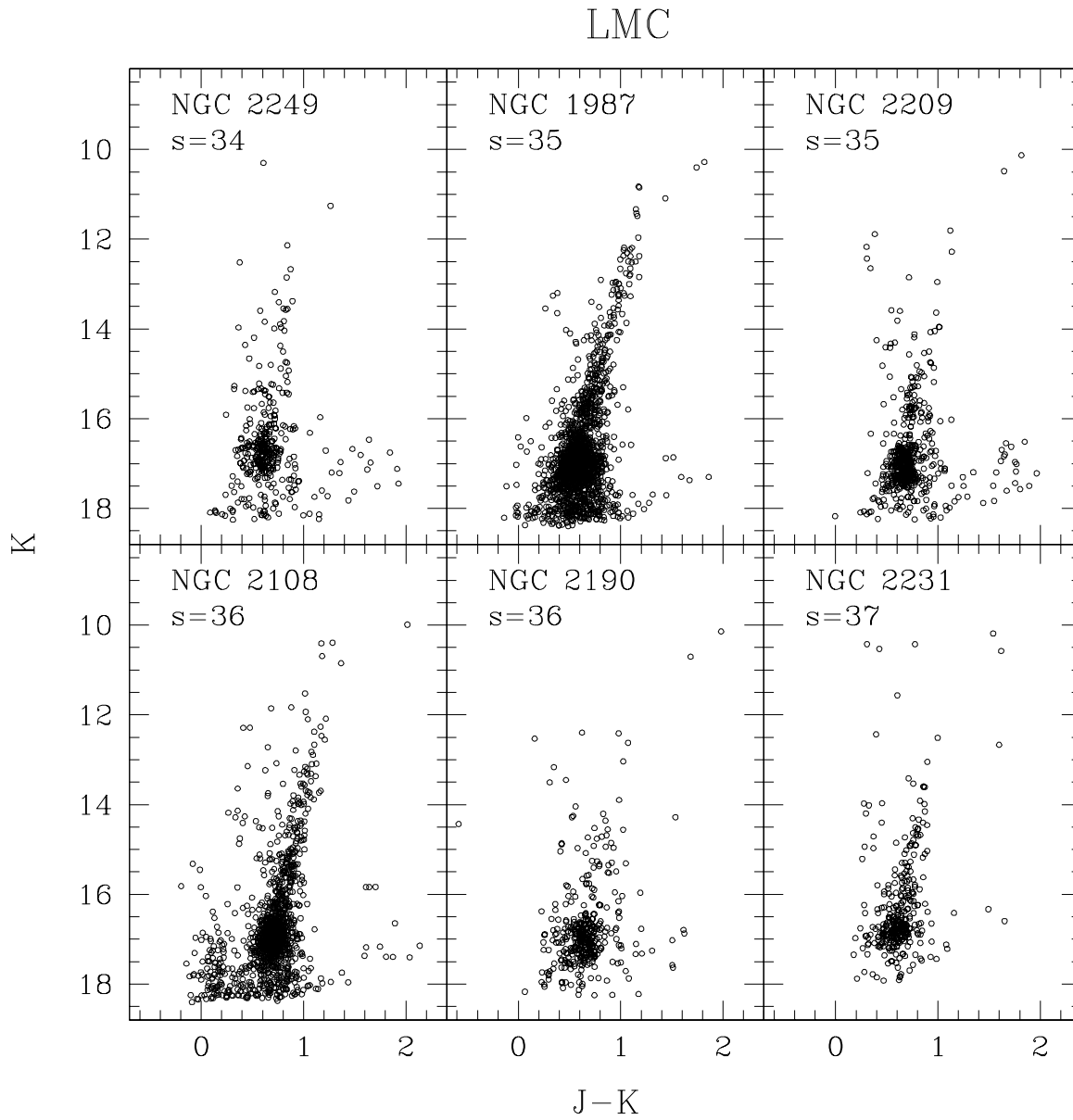
Figure 3.4: (K, J–K) CMDs of 6 observed LMC clusters with $s = 34 - 37$
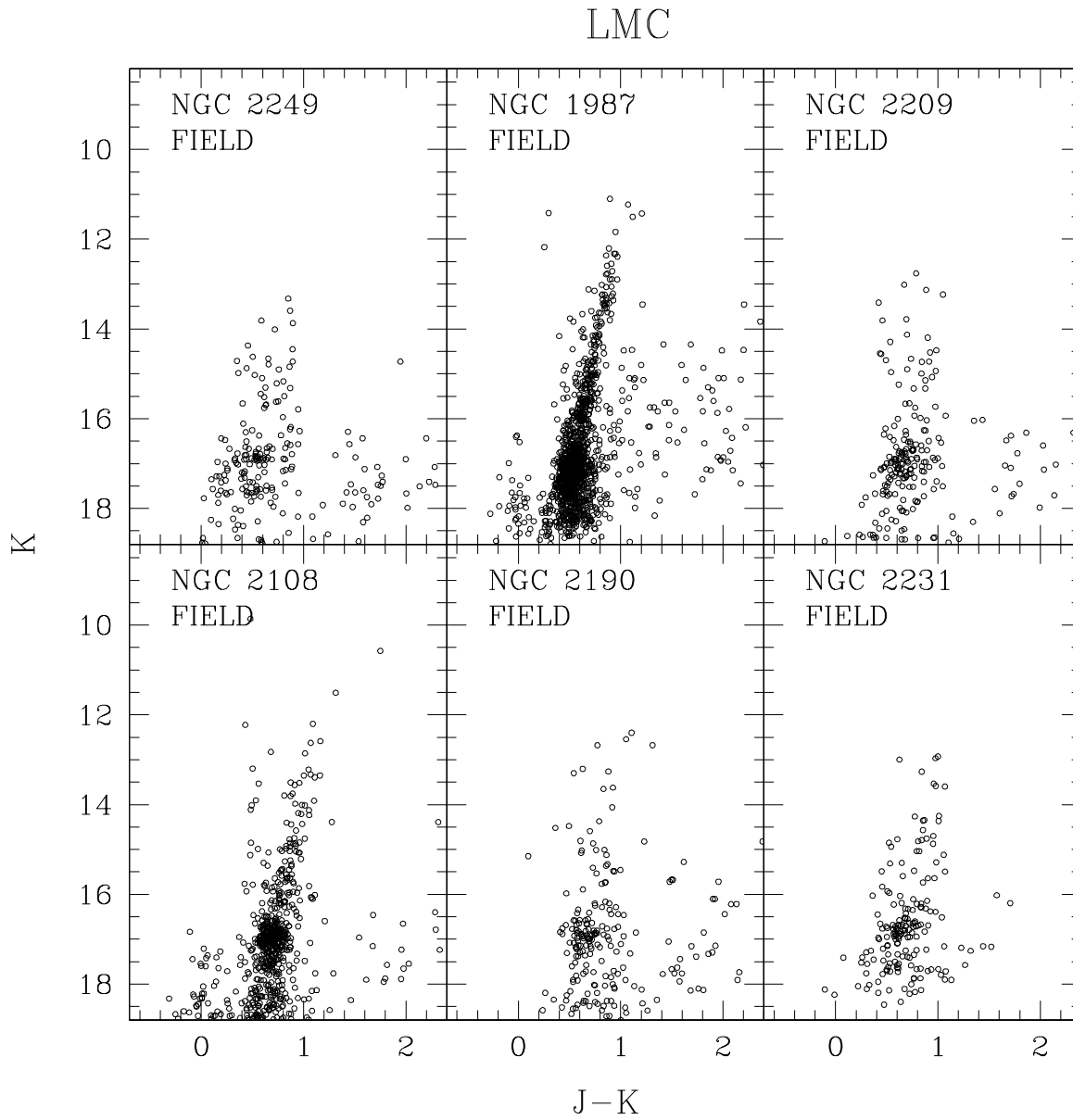
Figure 3.5: (K, J–K) CMDs of the fields adjacent to 6 observed LMC clusters with $s = 34 - 37$.

LMC
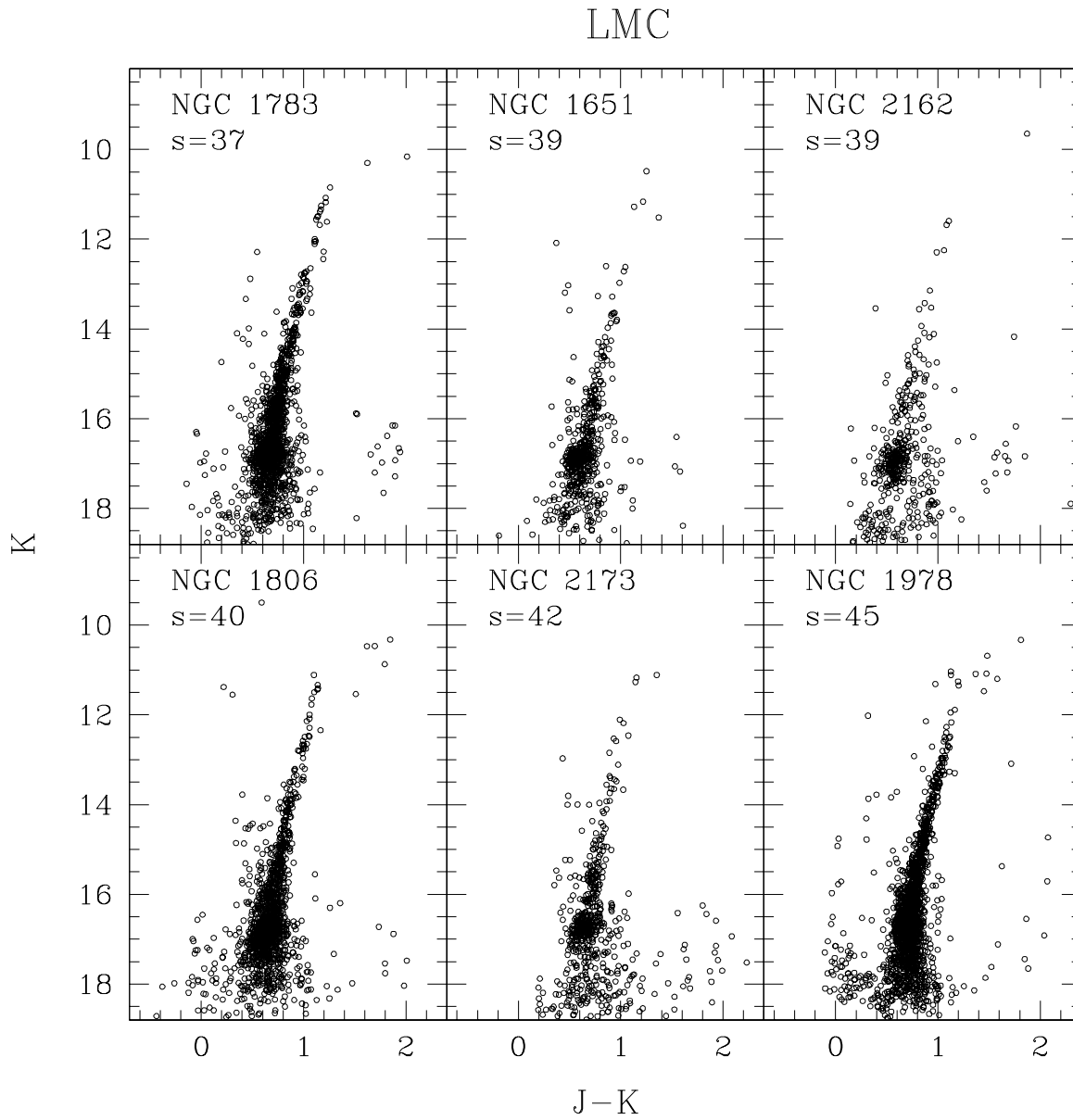
Figure 3.6: (K, J–K) CMDs of 6 observed LMC clusters with $s = 37 - 45$.
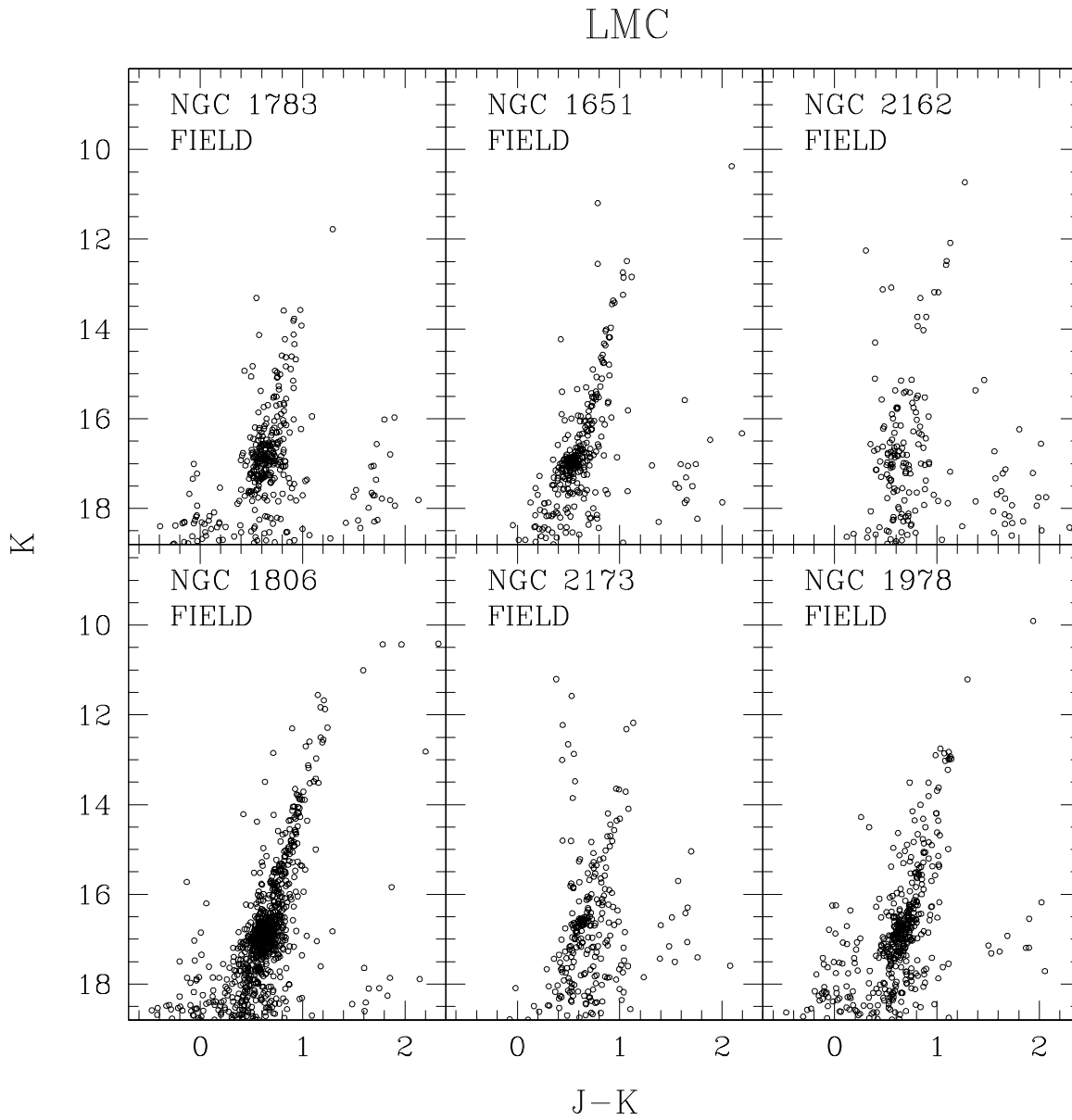
Figure 3.7: (K, J–K) CMDs of the fields adjacent to 6 observed LMC clusters with $s = 37 - 45$.
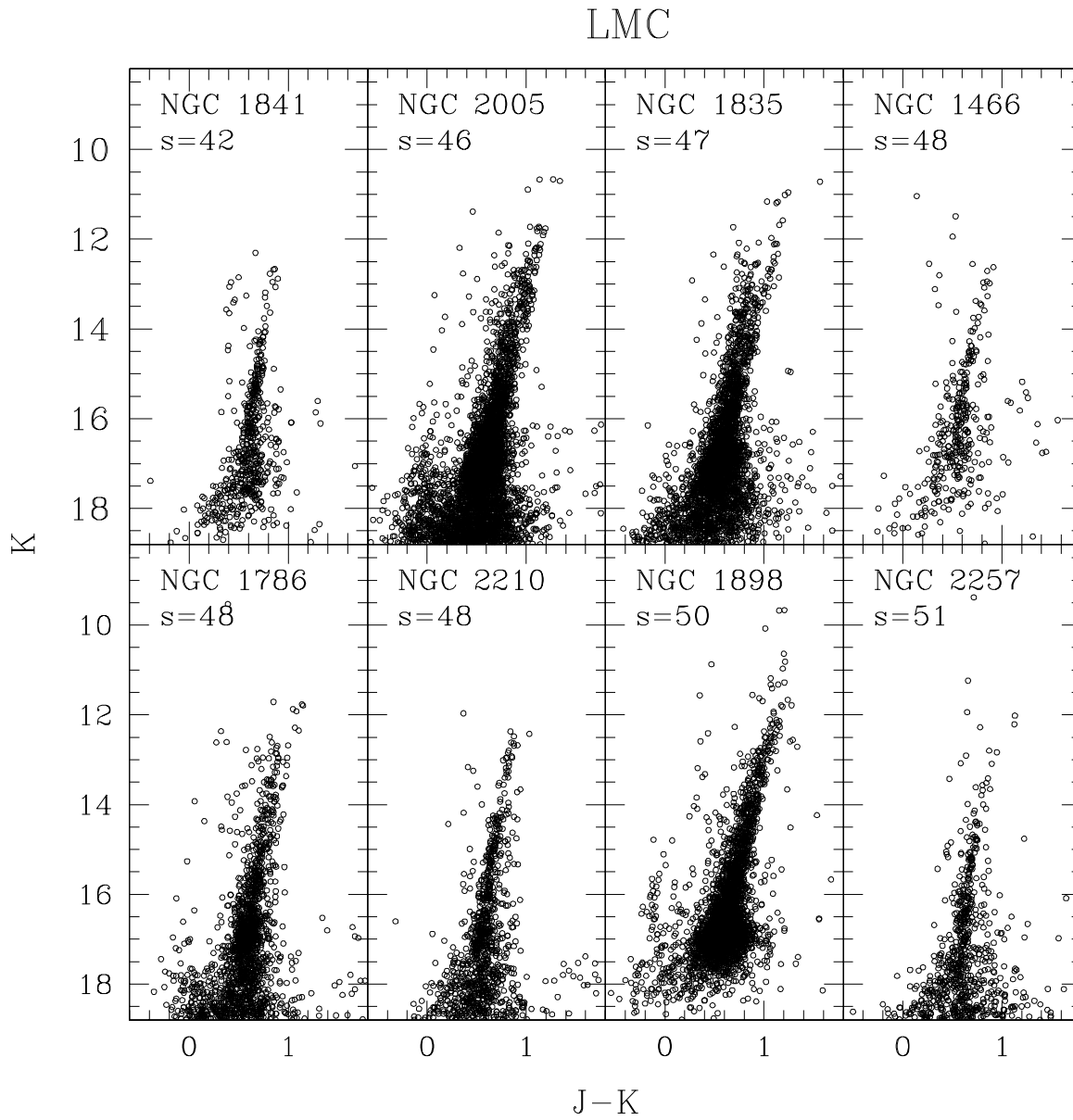
Figure 3.8: (K, J–K) CMDs of the 8 observed old LMC clusters.

SMC
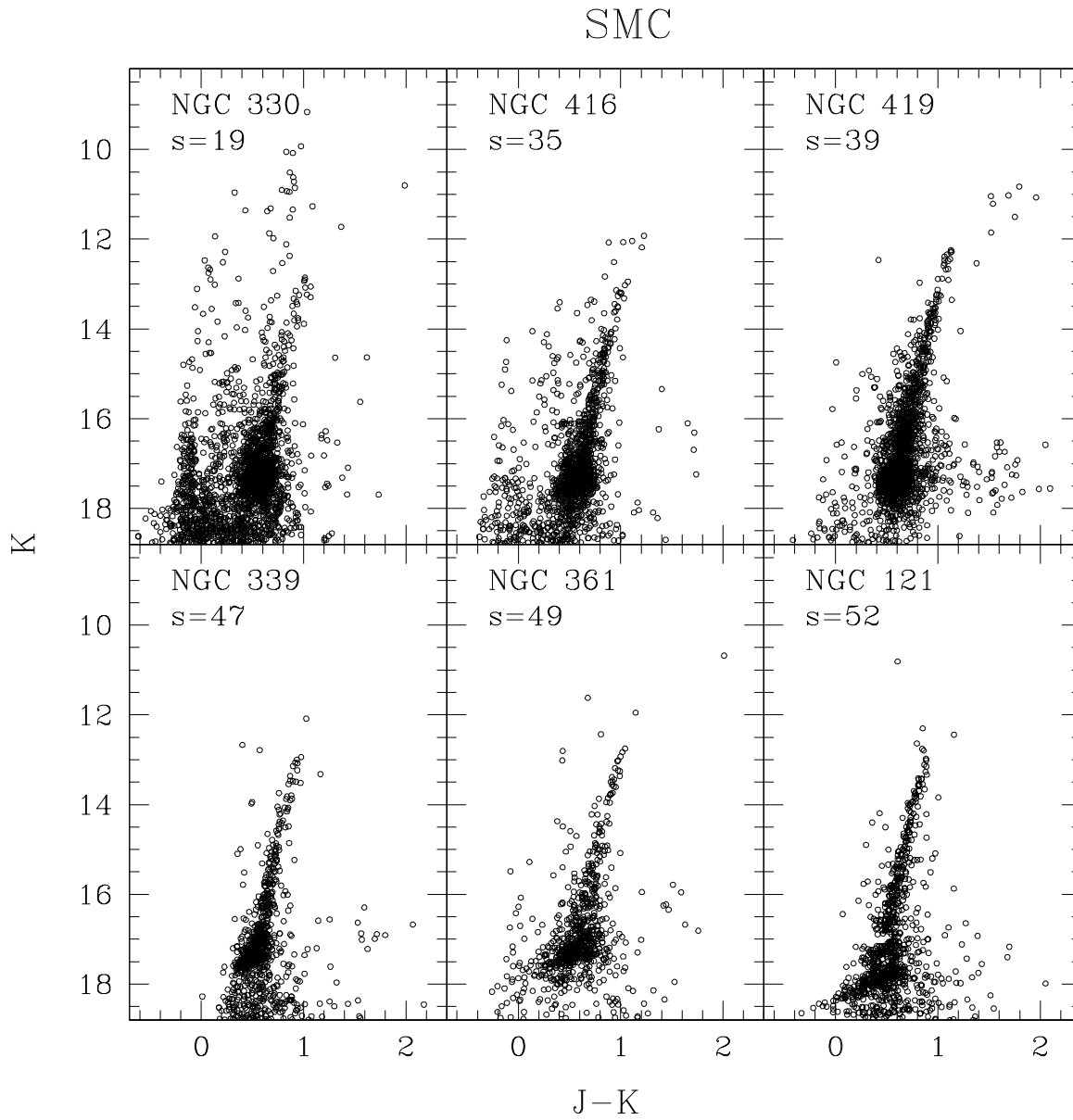
Figure 3.9: (K, J-K) CMDs of the 6 observed SMC clusters.
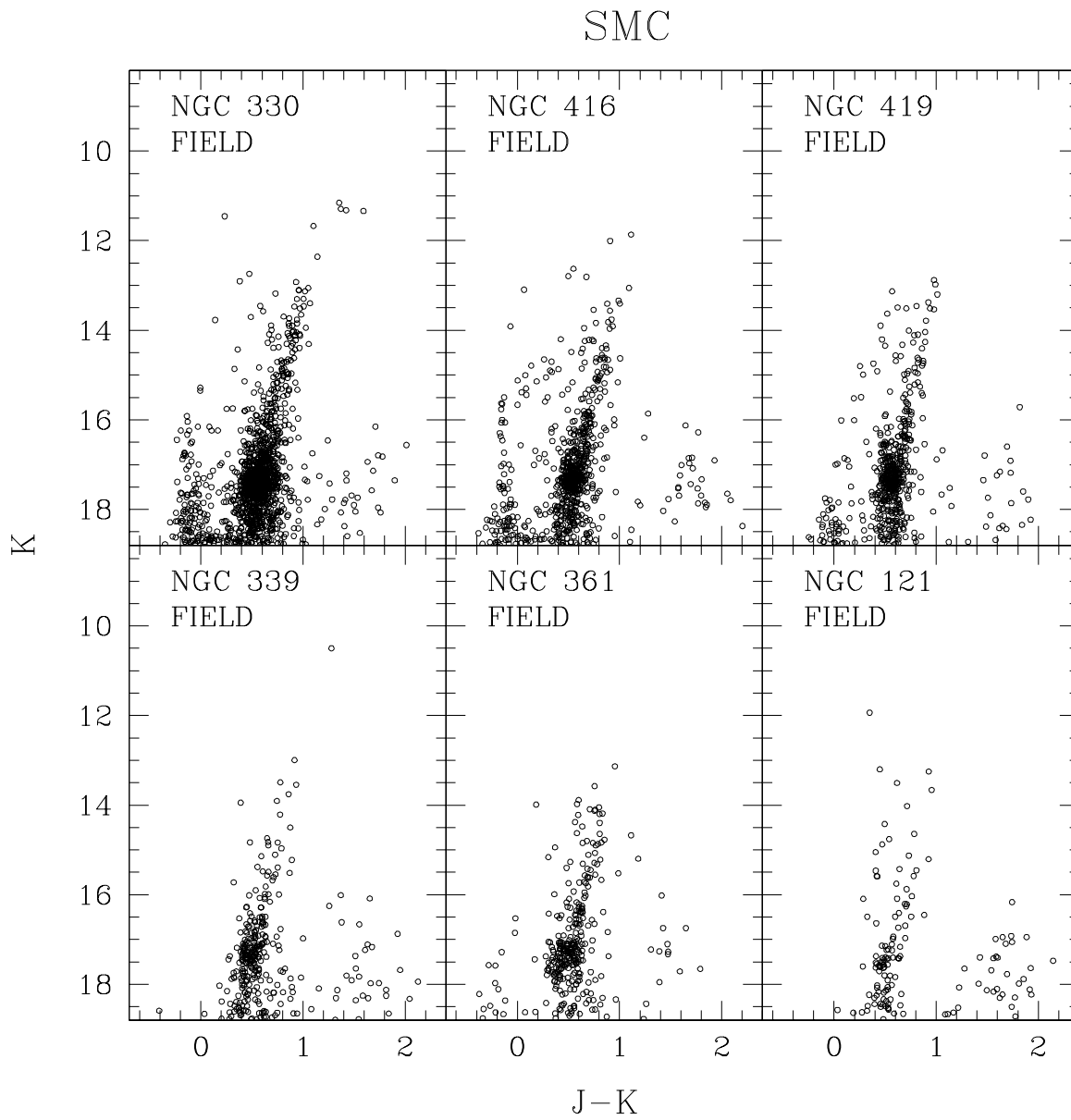
Figure 3.10: (K, J-K) CMDs of the fields adjacent to the 6 observed SMC clusters.

3.5 Basic assumptions

3.5.1 Reddening

Correction for extinction is computed accordingly to the $E(B - V)$ values reported in Table 3.2 and the Rieke & Lebofsky (1985) interstellar extinction law:

$$J_0 = J - 0.874 \cdot E(B - V)$$

$$H_0 = H - 0.542 \cdot E(B - V)$$

$$K_0 = K - 0.347 \cdot E(B - V).$$

The infrared dust maps by Schlegel, Finkbeiner, & Davis (1998) in the direction of the observed clusters provide very similar (on average within ± 0.03 mag) $E(B - V)$ corrections, with the exception of NGC 2031, for which the discrepancy is about 0.1 mag. However, the overall impact of such a discrepancy on the infrared magnitudes is always small (well within 0.1 mag), hence reddening correction is not a critical issue in this context.

Absolute and bolometric magnitudes have been obtained by adopting a distance modulus $(m - M)_0 = 18.5$ (van den Bergh, 1998; Alves, 2004) and suitable bolometric corrections by using the $(J - K)_0$ color and the empirical calibrations by Montegriffo et al. (1998). In computing luminosities, we adopted $M_\odot^{Bol} = 4.74$ and $M_\odot^K = 3.41$ for the Sun. In the following all the derived luminosities are expressed in unit of $10^4 L_\odot$.

3.5.2 Age scale

A suitable calibration of the LMC cluster age is still a major concern since homogeneous determinations based on the MS TO, for a significant number of clusters, are not available yet. Here we use the $s-$parameter. Being a pure empirical quantity, it needs to be calibrated with age. The most used calibrations by Elson & Fall (1988) based on canonical models

$$\log t = 6.05 + 0.079 \cdot s$$

and by Girardi et al. (1995) based on overshooting models

$$\log t = 6.227 + 0.0733 \cdot s$$

provide somewhat surprisingly, very similar ages (within 10-15 %). Although a new calibration of the *s*-parameter as a function of age is urged, in the following we adopted the most recent one

by Girardi et al. (1995) and based on the models with overshooting by Bertelli et al. (1994). We assume a conservative error of $\delta s = \pm 1$, which translates into a $\approx 20\%$ age uncertainty. Only for the SMC cluster NGC 416 we adopted the age derived by Mighell, Sarajedini & French (1998) by MS TO measurement. Indeed, Mighell, Sarajedini & French (1998) presented WFPC2@HST photometry for the clusters NGC 339, 361 and 416, finding very similar ages, attributing to these an age of $\tau \approx$ 5-7 Gyr. We note that these age estimates are in good agreement with the ages inferred from the s–parameter for the clusters NGC 339 and 361, but not for NGC 416, that exhibits a strong discrepancy between these two age determinations ($\Delta \tau \approx$ 5 Gyr).

3.6 Star counts and integrated luminosities

A quantitative analysis of the AGB and RGB populations (by number and luminosity) is crucial to empirically calibrate the relative lifetimes and to quantitatively evaluate the impact of each evolutionary stage on the total luminosity of a SSP. In order to obtain reliable stellar counts and luminosities in each branch, we proceeded as follows: *(1)* stars in each evolutionary stage have been identified on the basis of suitable selection boxes as defined in the CMDs (as shown in Fig. 3.12, 3.13 and Fig. 3.18); *(2)* each sample of stars has been corrected for incompleteness, following the standard *artificial star* technique (see below); *(3)* the contamination from foreground/background stars in each population has been evaluated and statistically subtracted to the observed samples. While the definition of the selection boxes (*step (1)*) for the AGB and RGB populations are described in Sects. 3.8 and 3.9, respectively, in the following we briefly discuss the procedure adopted to perform *step (2)* and *step (3)*.

3.6.1 Completeness and field decontamination

The degree of completeness can be quantified by using the widely-used artificial star technique. For each cluster we have derived the RGB fiducial line and then a population of artificial stars, having magnitudes, colors, and luminosity functions resembling the observed distributions was generated and added to the original images. Since crowding effects are more severe in the central regions, the frame area sampling the cluster has been divided in three concentric regions (*Region A, B and C*, see left panel of Fig. 3.11) and the completeness has been estimated independently in each of them. The maximum spatial extension of each cluster has been estimated from the cluster radial density profile. A total of $\approx$200,000 artificial stars have been simulated in each cluster in about 1000 simulation runs. Indeed, in order to not alter the crowding conditions, only 100–200

stars have been simulated in each run. The fraction of recovered objects in each magnitude interval was estimated as $\Lambda = \frac{N_{rec}}{N_{sim}}$, and a suitable completeness curve was obtained in each of the A,B,C regions (see right panels of Fig. 3.11).
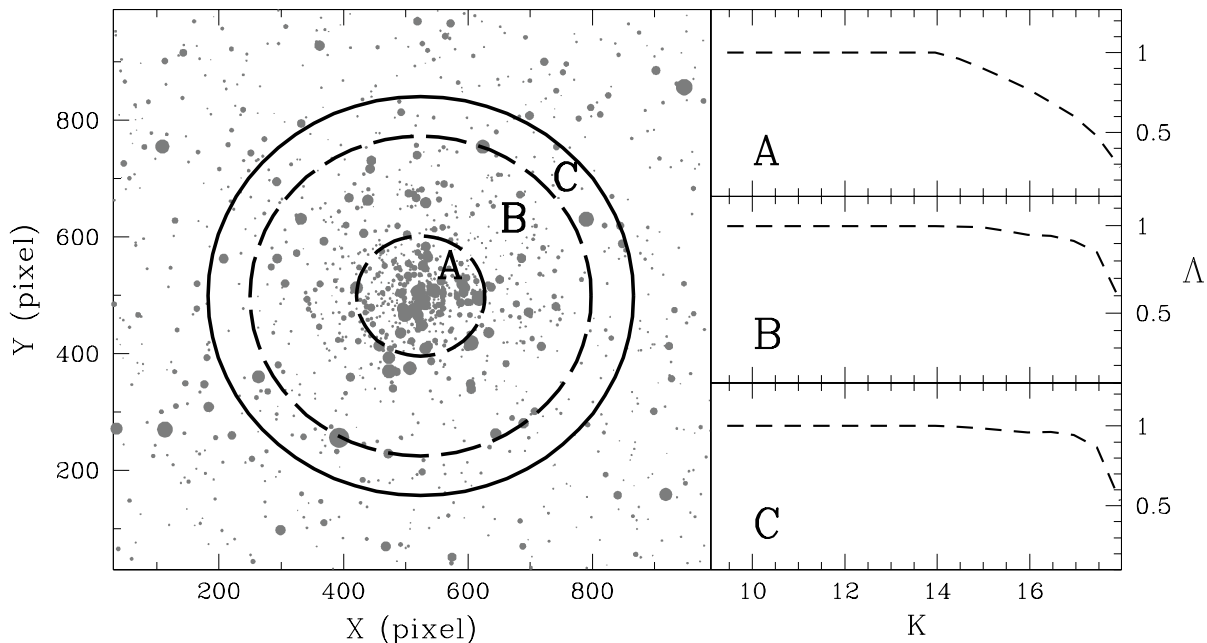
Figure 3.11: An example of cluster radial mapping. *Left panel*: the cluster frame is divided into 3 concentric annuli, to account for different crowding conditions. *Right panel*: completeness curve for each radial sub-region, as labeled in the left panel.

Star counts in each radial region have been finally corrected for incompleteness, by dividing each observed distribution by the corresponding Λ factors. We note that the number of stars lost for incompleteness (n_{comp}) in each bin of magnitude is

$$n_{comp} = n_{obs}(1/\Lambda - 1)$$

where n_{obs} is the number of stars observed in that bin. The total number of stars has been finally obtained by summing the completeness-corrected number of stars of the A,B,C regions.

The artificial star technique provides only a first-order correction. In fact, the observed distribution is, in principle, distorted because of two main phenomena: the loss of faint stars due to incompleteness and an excess of bright stars due to possible blending effects of two or more faint stars into a brighter one. Only the first effect is taken into account by the artificial star

simulation. Blending from faint MS stars is a more complicated effect to simulate, however in the near IR it is negligible (Testa et al., 1999) .

Another important effect which needs to be investigated, is the degree of contamination of the selected samples by the foreground/background stars. In this study we have applied a statistical decontamination technique, using a control field adjacent to the clusters. The total number of stars observed in each evolutionary sequence (AGB, RGB and He-clump) has been counted accordingly to the *selection boxes* both in the cluster (see Figs. 3.2, 3.4, 3.6 and 3.9) and field (see Figs. 3.3, 3.5, 3.7 and 3.10) CMDs, and corrected for incompleteness (see above). The star counts in the field population have been scaled to take into account the different surveyed area, and their contribution have been subtracted from the cluster population.

In summary, for each radial region, each selection box corresponding to each evolutionary stage has been divided in bins of magnitude (typically 0.2 mag wide). Then, the "corrected" number of stars in each bin has been computed as follows:

$$n_{corr} = n_{obs} + n_{comp} - n_f$$

where n_{obs} is the number of stars observed in that bin, n_{comp} is the number of stars lost for incompleteness, n_f is the expected number of field stars.

Analogously, the total luminosity of each evolutionary stage can be computed accordingly to the following relation:

$$L_{corr} = (\sum_{i=1}^{n} L_i^{obs}) + (n_{comp} \times L_{eq}) - (n_f \times L_{eq})$$

where the term $\sum_{i=1}^{n} L_i^{obs}$ is the total luminosity of the stars observed in a given bin, n_{comp} is the number of stars lost for incompleteness, n_f is the expected number of field stars, and L_{eq} is the equivalent luminosity of that bin, that is the luminosity of a star with magnitude equal to the mean value of the bin.

Finally, star counts and total luminosity of each evolutionary stage have been obtained by summing the contribution of all the bins in each selection box.

3.6.2 Integrated magnitudes

In order to properly perform cluster to cluster comparisons, one needs to take into account the size of the total cluster population. Hence both star counts and luminosities needs to be normalized to a reference population or to the cluster integrated luminosity.

The large FoV of SOFI offers the opportunity to independently determine the near-infrared integrated magnitudes for the program clusters. In doing this, we adopted a simple approach, by performing aperture photometry over the entire cluster extension (typically $90''$). In order to correct for the field contamination, an equivalent aperture photometry has been also performed on each control field and the resulting luminosity has been subtracted from the cluster value.

The cluster center has been computed by applying a standard technique (Calzetti et al., 1993) which uses the knowledge of the position of individual stars in the innermost region of the cluster, allowing an high precision determination of the center of gravity. Hence, by applying the procedure described in Montegriffo et al. (1995) we computed C_{grav} by simply averaging the α and δ coordinates of stars lying within a fixed radius from a first-guess center estimated by eye. The barycenter of the stars is then derived iteratively (see also Ferraro et al., 2003b). The center of gravity (C_{grav}) of the programme clusters are listed in Tab. 3.1. Our new estimates turn out to be reasonably consistent (within ~ 10") with available determinations (as those in the SIMBAD astronomical database by the CDS, Strasbourg). The typical 1σ uncertainty of our estimates is ~ 5 pixels corresponding to 1.5" in both α_{J2000} and δ_{J2000}. The position of the center of 2 clusters, namely NGC 2136 and NGC 2173, appears to be significantly (up to 2 arcmin) different from the SIMBAD coordinates.

The case of NGC 2136 deserves an additional comment. Indeed, a small *twin* cluster, namely NGC 2137, is present at an angular distance of $1.34'$ (Hilker, Richtler & Stein, 1995). Since its integrated luminosity, although significantly fainter, is contaminating the aperture photometry of NGC 2136, it has been properly subtracted.

Integrated K magnitudes, colors and derived bolometric luminosities in the K band and in bolometric for the entire sample of 33 clusters are listed in Table 3.6.2.

3.6.3 Error budget

Formal errors are directly estimated from the photometric samples, by assuming that star counts follow the Poisson statistics. The errorbars for the various population ratios (by number and/or by luminosity) have been computed accordingly to the following formula

$$\sigma_R = \frac{\sqrt{R^2 \cdot \sigma_D^2 + \sigma_N^2}}{D}$$

with $R = N/D$, N being the numerator and D the denominator of the ratio.

In the computation of the population ratios different error sources are at work, depending on the observable.

Cluster	K	J–K	H–K	L_{TOT}^{K}	L_{TOT}^{Bol}
NGC 2164	8.57	0.61	0.12	19.76	12.82
NGC 2157	8.29	0.66	0.19	25.79	15.18
NGC 2136	7.97	0.67	0.12	34.57	19.78
NGC 2031	8.22	0.94	0.32	28.14	11.36
NGC 1866	7.28	0.74	0.15	65.02	33.13
NGC 2134	9.16	0.74	0.19	11.52	5.88
NGC 1831	8.31	0.80	0.23	25.16	11.67
NGC 2249	9.98	0.93	0.34	5.40	2.06
NGC 1987	8.81	0.99	0.32	16.00	5.75
NGC 2209	8.95	1.22	0.34	13.79	3.54
NGC 2108	8.81	1.15	0.40	16.38	4.96
NGC 2190	9.27	1.19	0.32	10.43	2.83
NGC 2231	9.33	1.10	0.33	9.81	2.97
NGC 1783	7.09	1.03	0.28	77.53	25.77
NGC 1651	8.89	0.97	0.30	14.72	5.32
NGC 2162	9.07	1.25	0.37	12.40	3.07
NGC 1806	7.08	1.05	0.27	79.11	25.97
NGC 2173	9.05	1.03	0.30	12.33	4.02
NGC 1978	7.18	0.89	0.29	71.10	28.69
NGC 1841	9.22	0.68	0.11	10.57	54.05
NGC 2005	7.87	0.59	—-	48.47	22.20
NGC 1835	7.87	0.79	—-	58.58	15.92
NGC 1466	9.58	0.45	0.05	9.96	60.37
NGC 1786	8.17	0.43	0.11	36.49	23.02
NGC 2210	8.87	0.49	0.10	19.15	10.49
NGC 1898	7.71	0.61	0.13	55.79	24.57
NGC 2257	10.07	0.54	0.12	10.44	51.98
NGC 330	7.54	0.17	0.78	87.90	36.51
NGC 416	8.68	0.13	0.68	30.76	14.01
NGC 419	7.49	0.31	1.09	92.05	23.22
NGC 339	9.38	0.10	0.72	16.14	6.84
NGC 361	8.94	0.11	0.78	24.21	9.73
NGC 121	8.81	0.11	0.71	27.29	12.53

Table 3.3: Integrated K magnitude, colors and luminosities of the target clusters

- total cluster luminosity: the main source of uncertainty in this case is the positioning of the cluster center. We estimate that an off-centering of 5 pixels corresponds to a 5% variation in luminosity. An additional uncertainty of $\approx 10\%$ has been considered in the computation of bolometric luminosities, in order to take into account the uncertainty in the bolometric corrections.

- AGB luminosity: a conservative uncertainty of 0.2 mag in setting the faint end of the AGB luminosity distribution, implies a $\approx$5% variation in the total AGB luminosity. However, for this observable the major source of uncertainty is the random error associated to the number of detected AGB stars (in the Poisson regime $\sigma \propto \sqrt{N}_{AGB}$), which can suffer large fluctuations due to the small number statistics. On average, the overall σ_R associated to the $\frac{L^K_{AGB}}{L^K_{TOT}}$ ratio turns out to be 30%.

- number and luminosity of C-stars: as in the case of AGB stars, these observables and their associated errors suffer large fluctuations due to the small number statistics. On average, the overall σ_R associated to the $\frac{L^K_{C-star}}{L^K_{TOT}}$ ratio turns out to be $\approx$50%.

- RGB luminosity: in the clusters showed in Fig. 3.4, 3.6 and 3.9 the RGB is well populated, hence the estimated luminosity is much less affected by statistical fluctuations or by the selection box definition. On average, we estimate a $\sigma_R \approx$20% for the RGB population ratios.

3.7 Theoretical models

The population ratios defined following the procedure described above have been compared with theoretical predictions computed by using SSP models by Maraston (1998) and Maraston et al. (2001), for which the synthetic colors have been calibrated on the observed integrated colors of MC clusters. The adopted evolutionary code estimates the energetics of any post-MS phase by using the fuel consumption theorem (discussed in Sect. 3.1) and allows us to model the two key AGB and RGB Ph-Ts.

The main synthetic ingredients that mostly influence the theoretical predictions are as follows:

(1) The adopted stellar evolutionary tracks. The stellar tracks used here are taken from Cassisi & Salaris (1997) and Bono et al. (1997). There are *canonical* tracks, without *overshooting*, in which the most recent input physics (opacities, equation of state, etc.) are adopted. The mixing-length parameter has been calibrated on the Sun and scaled to other metallicities by using empirical

relations (Salaris & Cassisi, 1996).

(2) The integration method. The method adopted to determine the number of stars (and luminosity) in any post-MS phase in the fuel consumption approach is different with respect to that used in the isochrone technique (Charlot & Bruzual, 1991), which is based on the mass dispersion along the post-MS phases. Conversely here, the post-MS stellar track of a mass equal to the TO mass at a given stellar population age is divided into a suitable number of subphases. Then, the evolutionary timescale is combined with the fuel consumption in order to evaluate the number of stars and their luminosity in each subphase.

(3) The temperature-color transformations. Transformations are taken from the Basel table (Lejeune, Cuisinier & Buser, 1997), in which the classical Kurucz library down to 3500 K is linked to models for cooler temperatures (Bessell et al., 1989), and recalibrated on the observed colors of individual stars.

In order to make a preliminary check of the impact of the different treatment of mixing on the observables described in the previous sections, we have computed SSP models with the procedure outlined in this section, but adopting the stellar tracks with overshooting from Girardi et al. (2000).

3.8 The contribution of the AGB and C-stars

Theoretical models (Renzini & Buzzoni, 1986; Maraston, 1998, 2005) predict that the most important contributors to the integrated cluster light between 10^8 and 10^9 yrs are AGB stars. The AGB population includes both O-rich (M-type) and C-rich stars. During the thermal pulsing phase (hereafter TP-AGB) an AGB star becomes C-rich if it undergoes the third dredge-up mixing process (see e.g. Iben & Renzini, 1983). The presence of C-stars in stellar clusters depends on their age and metallicity (Renzini & Voli, 1981).

In intermediate age clusters the bulk of the AGB population is more luminous than the RGB Tip, and a minor overlap does exist between the faintest end of the AGB and the brightest portion of the RGB. Here we use our data set in order to investigate the contribution to the cluster luminosity of the brightest portion of the AGB populations as a function of the cluster age. In order to consider the young-intermediate age clusters that spans a large range of ages (from 80 Myr to 7 Gyr, see Tab. 3.1), in the following we consider only AGB stars brighter than K$\approx$ 12.3 and K$\approx$ 12.62, corresponding to the RGB Tip level for the LMC and SMC clusters in our sample (see Cioni et al., 2000).

The left panel of Fig. 3.12 shows the brightest portion of the K_0, $(J-K)_0$ cumulative CMD, where

all the stars detected in the 19 surveyed LMC clusters are plotted. The selection box adopted to sample the bright AGB population is over-plotted to the diagram. The right panel of Fig. 3.12 shows the cumulative $(J - H)_0, (H - K)_0$ color-color diagram for the selected AGB stars. This diagram is especially suitable to isolate C-stars, since they are significantly redder than O-rich stars (see also Cioni et al., 2005). As shown in Fig. 3.12 a population of 26 candidate C-stars (plotted as *filled circles*) has been identified on the basis of their extremely red colors in the 19 surveyed clusters. Fig. 3.13 shows the same diagrams computed for the 4 SMC intermediate-age clusters, where 10 candidate C-stars have been identified.
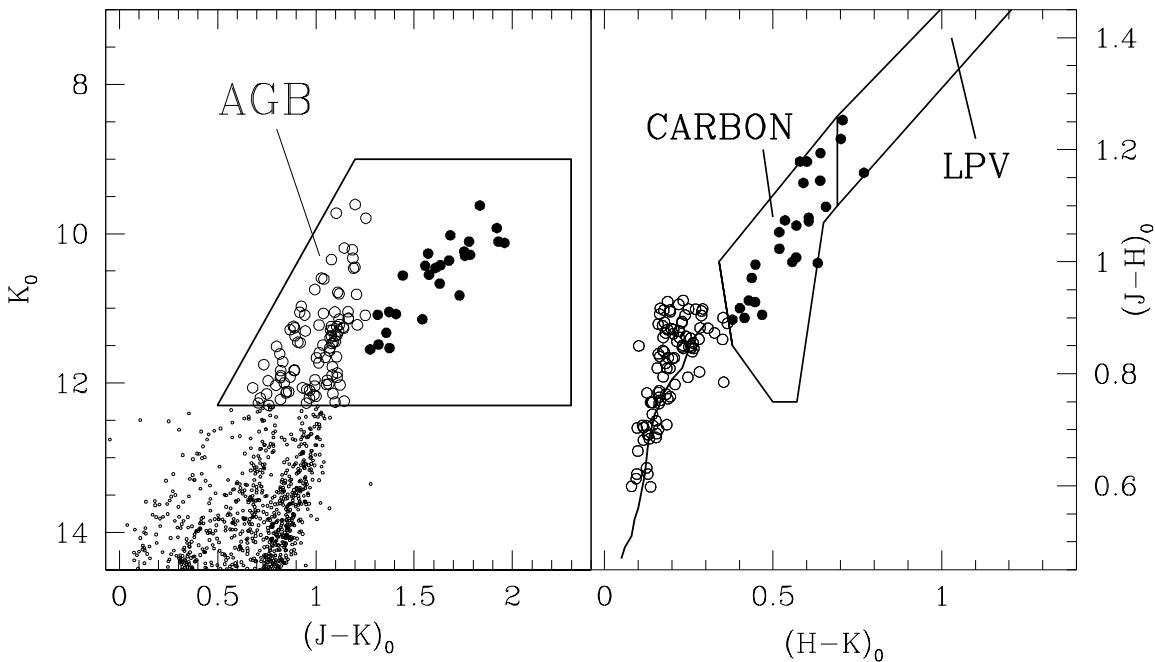
Figure 3.12: *Left panel*: cumulative, de-reddened $K_0, (J - K)_0$ CMD for the young-intermediate LMC cluster sample. The selection box adopted to isolate the AGB population (*large circles*) is shown. *Right panel*: de-reddened color-color $(J - H)_0, (H - K)_0$ diagram of the AGB stars. In both panels *open circles* are O-rich AGB, *filled circles* are C-stars. *Solid line* boxes to distinguish C-stars and Long Period Variables (LPV) are from Bessell & Brett (1988), (see also Ferraro et al., 1995). The mean locus for K giant stars (*solid line*) is from Frogel et al. (1978).
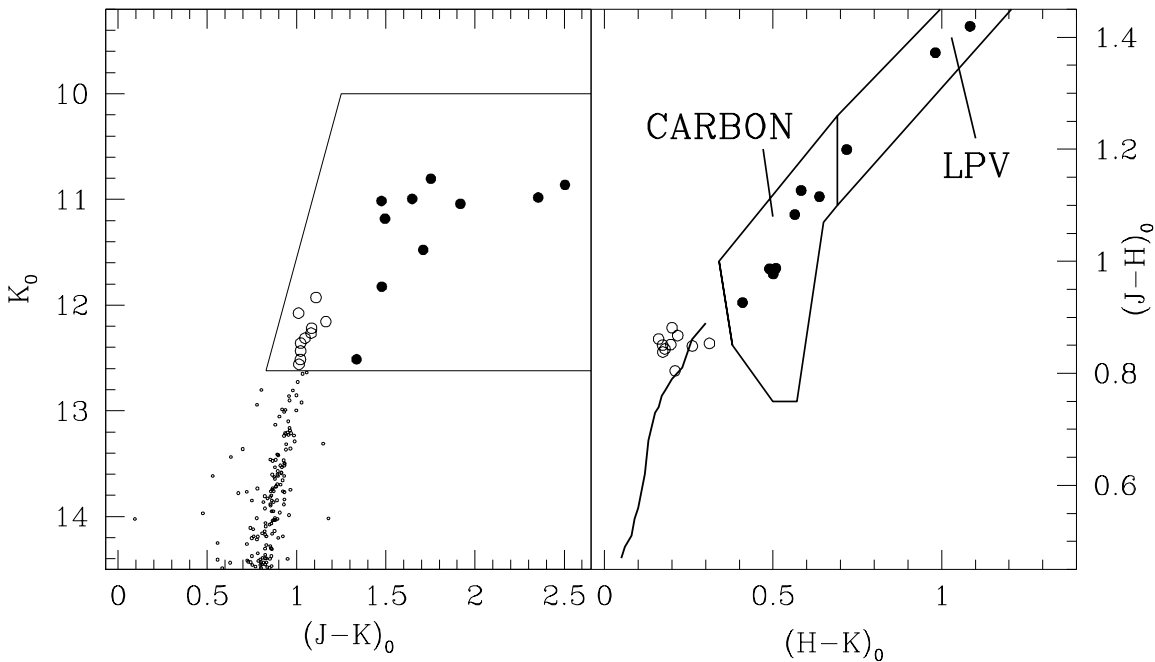
Figure 3.13: *Left panel*: cumulative, de-reddened $K_0, (J - K)_0$ CMD for the intermediate SMC clusters. The selection box adopted to isolate the AGB population (*large circles*) is shown. *Right panel*: de-reddened color-color $(J - H)_0, (H - K)_0$ diagram of the AGB stars. Same symbols and references of Fig. 3.12.

Note also that the artificial star experiments demonstrated that stars lying in the brightest portion of the RGB can be safely recovered (with an overall photometric uncertainty of ~ 0.03 mag) even in the innermost region of the clusters, excluding the possibility that blending of RGB stars could produce spurious bright objects lying within the AGB selection box.

We used both the cumulative color-magnitude and color-color diagrams in Fig. 3.12 and 3.13 to make a census (both by number and luminosity) of the AGB stars brighter than the RGB Tip as well as of C-stars in each cluster. Although the number and the luminosity of AGB stars are affected by large fluctuations due to the small-number statistics, we still performed a statistical decontamination, following the procedure described in Sect. 3.6.1.

The number of AGB stars counted in each clusters and the number adopted after the field decontamination are listed in Table 3.4. Once the accurate census of the AGB population (by number and luminosity) is available for all the sampled clusters, a number of suitable diagnostics tools can be used in order to study the AGB properties as a function of the age.

Cluster	N_{AGB}^{Obs}	N_{AGB}^{Field}	N_{AGB}^{Dec}	$\frac{L_{AGB}^{K}}{L_{TOT}^{K}}$	N_{C-star}	$\frac{N_{C-star}}{L_{TOT}^{Bol}}$	$\frac{N_{C-star}}{L_{TOT}^{K}}$	$\frac{L_{C-star}^{K}}{L_{TOT}^{K}}$
NGC 2164	2	0	2	0.10	0	0	0	0
NGC 2157	9	1	8	0.52	0	0	0	0
NGC 2136	9	1	8	0.31	1	0.05	0.03	0.09
NGC 2031	7	1	6	0.64	0	0	0	0
NGC 1866	12	0	12	0.36	0	0	0	0
NGC 2134	2	1	1	0.71	0	0	0	0
NGC 1831	7	1	6	0.45	3	0.26	0.12	0.31
NGC 2249	1	0	1	0.32	0	0	0	0
NGC 1987	9	4	5	0.90	3	0.52	0.19	0.61
NGC 2209	4	0	4	0.72	2	0.56	0.14	0.58
NGC 2108	5	1	4	0.87	1	0.20	0.06	0.34
NGC 2190	2	0	2	0.74	2	0.71	0.19	0.72
NGC 2231	1	0	1	0.32	1	0.34	0.10	0.32
NGC 1783	16	1	15	0.36	2	0.08	0.03	0.11
NGC 1651	4	0	4	0.51	1	0.19	0.07	0.09
NGC 2162	4	1	3	0.73	1	0.32	0.08	0.59
NGC 1806	13	4	9	0.22	4	0.15	0.05	0.17
NGC 2173	5	1	4	0.53	1	0.25	0.08	0.15
NGC 1978	13	1	12	0.25	4	0.14	0.06	0.13
NGC 416	1	0	1	0.04	0	0	0	0
NGC 419	17	0	17	0.41	10	0.43	0.11	0.33
NGC 339	1	0	1	0.08	0	0	0	0
NGC 361	1	0	1	0.06	0	0	0	0

Table 3.4: Star counts and luminosities for AGB and C-stars. Star counts are corrected for incompleteness. K-band and bolometric luminosities are in units of $10^4 L_\odot$.

The upper panel of Fig. 3.14 shows the ratio between the AGB and the cluster integrated K-band luminosity, as a function of the cluster age. It is remarkable the rapid increase (up to a factor 2) of the AGB luminosity at $\approx 200\ Myr$ which reaches its maximum contribution in the 300-700 Myr range followed by a rapid decrease. Note that in 2 clusters (namely NGC 2108 and NGC 1987 at $s = 35 - 36$ corresponding to $t \sim 600 - 700 Myr$) the brightest portion of the AGB population account for $\approx 90\%$ of the total cluster luminosity. These results are in good agreement with Ferraro et al. (1995), who found that the maximum contribution of the AGB to the cluster light occurs at $s = 35$, corresponding to an age of $\approx 600\ Myr$.

The lower panel of Fig. 3.14 shows the same ratio as in the upper panel but with the clusters grouped in five age bins accordingly to their s–parameter, namely s=23-26, 27-31, 35-36, 37-39 and 40-45, respectively. For each bin we computed the weighted mean and the corresponding standard deviation. Theoretical predictions from Maraston (1998, 2005) for [Z/H]=–0.33 are also
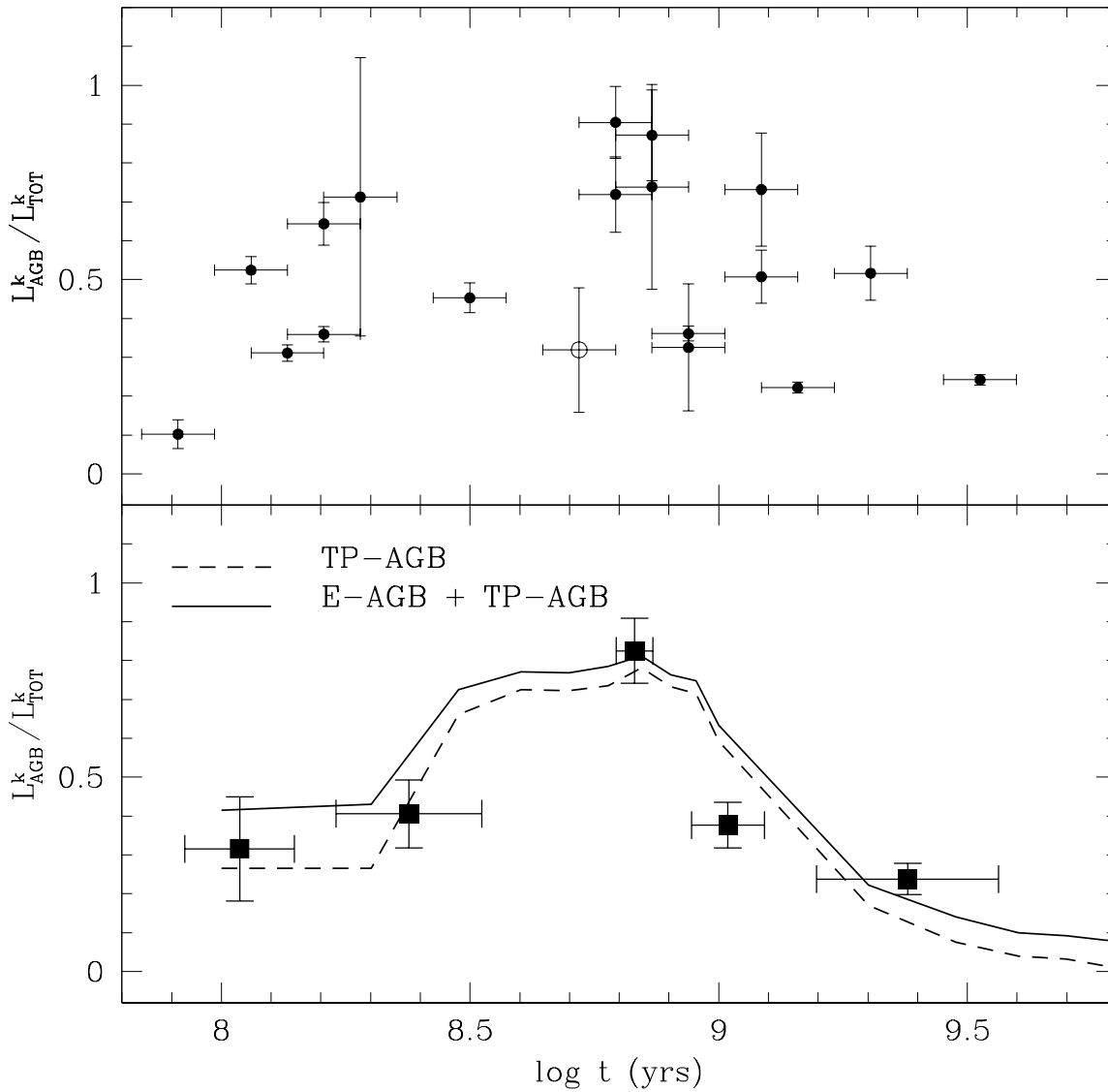
Figure 3.14: Upper panel: observed AGB contribution to the total cluster K-band luminosity as a function of age for the LMC clusters. The open circle marks the intrinsically poor populated cluster NGC 2249. Lower panel: weighted mean and standard deviation of the same ratio with the LMC clusters grouped in five age bins, accordingly with their s–parameter, namely s=23-26, 27-31, 35-36, 37-39 and 40-45, respectively (the cluster NGC 2249 has been excluded). Theoretical predictions for the temporal evolution of the entire AGB (E-AGB and TP-AGB, *solid line*) and for the dominant TP-AGB (*dashed line*) are overplotted. Both models are computed at [Z/H]= −0.33.
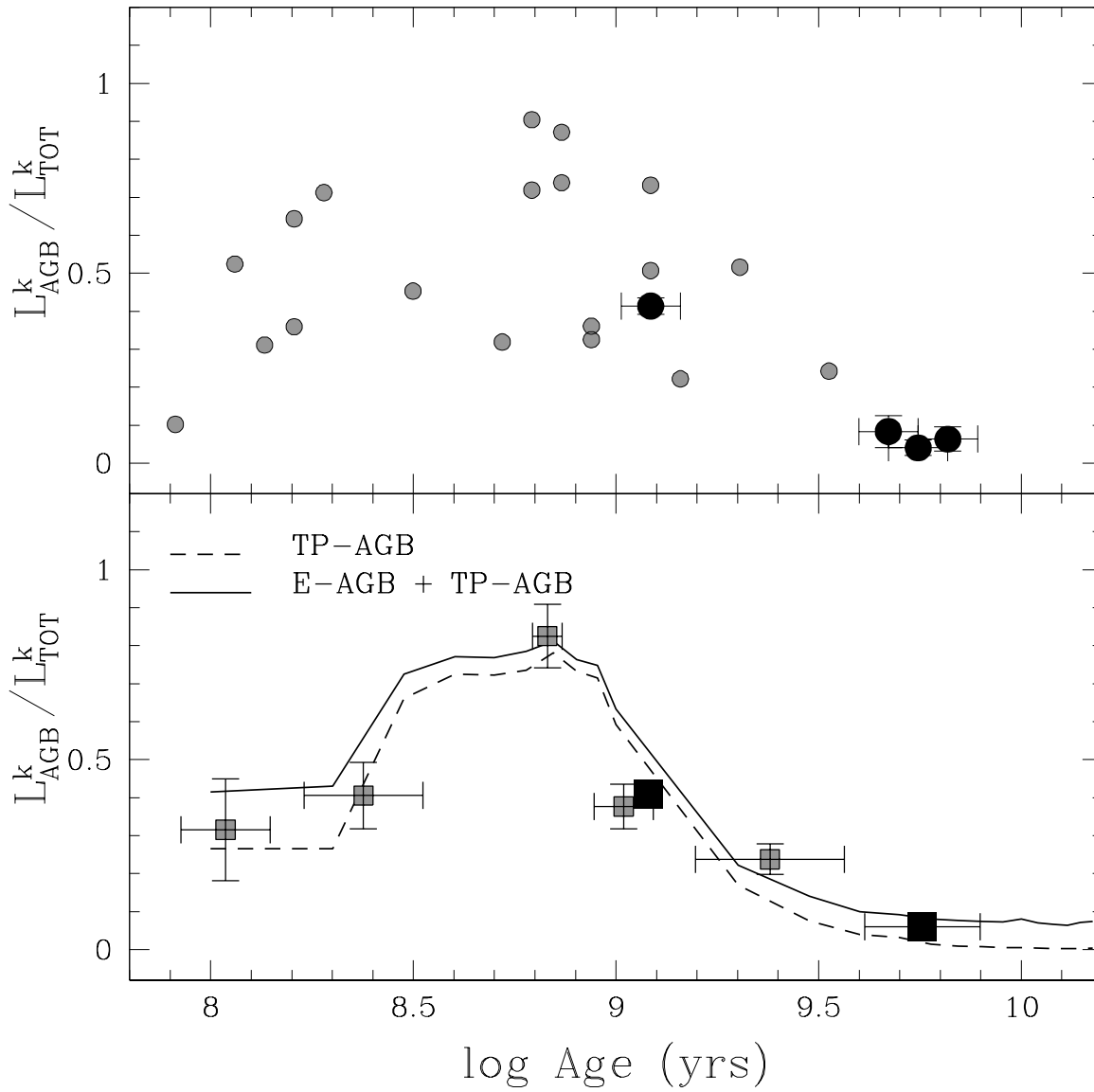
Figure 3.15: Upper panel: observed AGB contribution to the total cluster K-band luminosity as a function of age for the SMC clusters (black points). Grey circles indicate the values for the LMC clusters (see Fig. 3.14). Lower panel: weighted mean and standard deviation of the same ratio with the SMC clusters grouped in 2 age bins, accordingly with their s–parameter (black squares). Grey squares indicate the age bins obtained from the LMC clusters (see Fig. 3.14). Theoretical predictions for the temporal evolution of the entire AGB (E-AGB and TP-AGB, *solid line*) and for the dominant TP-AGB (*dashed line*) are overplotted. Both models are computed at [Z/H]= −0.33.

plotted. In these models the TP-AGB energetics was calibrated with previous (Frogel, Mould & Blanco, 1990; Ferraro et al., 1995) intermediate age MC cluster data (see Maraston (1998) for full details). Our new observations nicely confirm the modeling and those early results. Old canonical models of stellar evolution (Renzini & Buzzoni, 1986) were dating the occurrence of the AGB Ph-T at significantly earlier epochs ($\approx 10^7 \ yrs$) of the stellar lifetime with respect to the new models. This discrepancy is due to a different treatment for the TP-AGB stars that experiencing the envelope burning process (Renzini & Voli, 1981; Bloecker & Schoenberner , 1991), as widely discussed in Maraston (1998). Moreover, Fig. 3.15 reports the results obtained for the 19 LMC clusters (plotted as grey symbols) in comparison with the same population ratios for the 4 SMC clusters (black symbols). The cluster NGC 419 (with an age of $\sim$1.2 Gyr) results in good agreement with the behaviour showed from the other LMC clusters with comparable ages. The 3 SMC clusters with ages of $\sim$5-7 Gyr (an age range not sampled in the LMC, because corresponding to the *Age Gap*) evidence a marginal contribution ($\sim 5\%$) from the AGB stars, confirmed from the total lack of C-stars in these clusters (see Tab. 3.4).

As a further evidence, Fig. 3.16 shows the ratio between the number of C-stars and total bolometric luminosity and the ratio between the K luminosity of C-stars and the total K-band cluster luminosity, as a function of the cluster age. The number of C-stars in each cluster is listed in Table 3.4. We assumed all these stars being cluster members. Indeed, we estimate that the probability to find a field C-star within the sampled cluster area is $<$30%. The contribution of C-stars to the total cluster luminosity as a function of the cluster age, closely follows the one shown by the entire AGB population (see Fig. 3.14 and 3.15) and it turns out to be larger than 50% in the $700-1000 \ Myr$ age range. In NGC 2190 (with $s = 36$, hence $t = 730 \ Myr$) the C-stars accounts for 70% of its total luminosity. Previous works by Frogel, Mould & Blanco (1990) also found that the fraction of luminosity from bright AGB and C-stars is maximum for SWB V clusters (i.e. s between 35 and 40). Moreover, the C-stars accounts for less than 20% of the total luminosity for ages larger than $\sim$2 Gyr, with a zero contribution in the range $\sim$5-7 Gyr, due to the total lack of observed C-stars in the 3 older SMC clusters, as showed in Fig. 3.17. This latter result is in well agreement with the theoretical predictions that show that there is a minimum envelope mass needed for the occurrence of the third dredge-up. Stars with initial mass of the order of $\sim$1-1.2 $M_{\odot}$ present a residual envelope mass which is too small and they cannot experience the third dredge-up.

It is worth noticing the case of NGC 2249, whose age ($log \ t = 8.72$) corresponds to the

61

epoch when the AGB contribution is expected to reach its maximum. Conversely, both Figs. 3.14 and 3.16 shows that NGG 2249 (marked with an open circle) has a very low AGB luminosity for its age. Indeed no C-stars and only 1 AGB have been detected in this cluster. On the other hand, NGC 2249 is the least luminous cluster in our sample ($L_K \approx 5 \times 10^4 L_\odot$), hence the fastest evolutionary stages (as the AGB) are expected to be intrinsically poorly populated in its CMD.

Figure 3.16: *Upper panel*: the number of C-stars normalized to the K-band luminosity of the cluster as a function of age. *Lower panel*: the K-band luminosity of the C-stars normalized to the total cluster luminosity as a function of age. The *open circle* marks the intrinsically poor populated cluster NGC 2249.
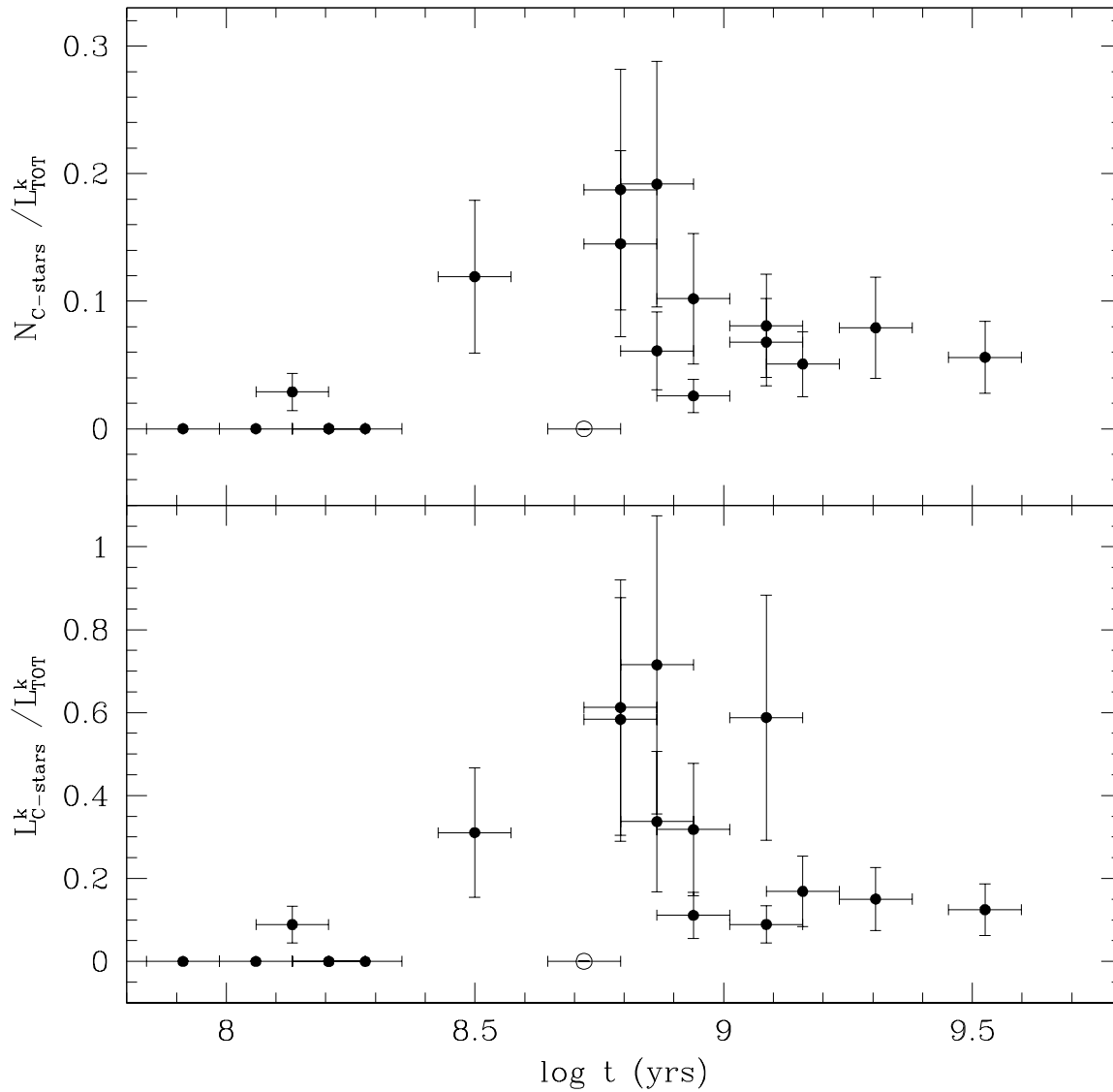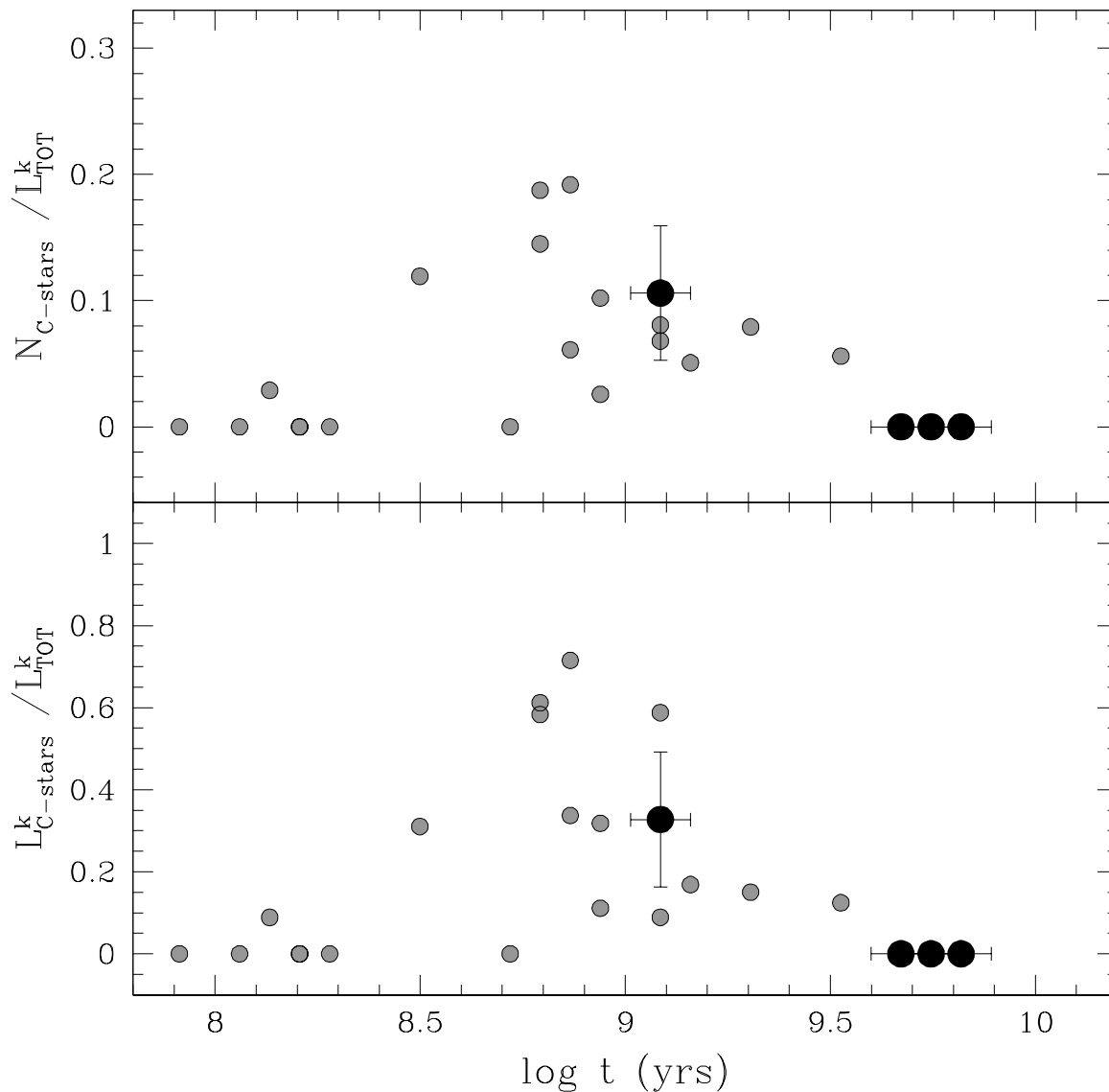
Figure 3.17: *Upper panel*: the number of C-stars normalized to the K-band luminosity of the cluster as a function of age for the SMC clusters (black points) *Lower panel*: the K-band luminosity of the C-stars normalized to the total cluster luminosity as a function of age foe the SMC clusters. Grey points indicate the LMC clusters showed in Fig. 3.16.

3.9 The contribution of the RGB stars: probing the RGB Phase Transition

For the analysis of the RGB Ph-T we have considered the intermediate-age clusters in our database with $s > 34$. Obviously the 7 youngest LMC clusters in our sample (Fig. 3.2) are not considered in the following discussion because they have not developed a populous RGB yet. The considered sample covers a wide range of ages (from $500\ Myr$ up to $7\ Gyr$) and it allows to probe the entire development of the RGB.

Using the cumulative K_0, $(J - K)_0$ CMDs for the 12 LMC and the 4 SMC clusters we identified the mean loci of the upper RGB and the He-Clump and defined the corresponding selection boxes sampling these populations. As discussed in Sect. 3.8 the RGB Tip is expected to be at $K_0 \approx 12.3$ for the LMC and at $K_0 \approx 12.62$ for the SMC . As an example, Fig. 3.18 shows the de-reddened CMD of NGC 1651 where the two selection boxes for the RGB and He-clump population, respectively, have been plotted.

Since the photometric errors can significantly broaden the faint sequences, the size of the boxes including the base of the RGB and the He-clump has been conservatively assumed to be ≈ 5 times the photometric error at that level of magnitude[1].

Population counts and luminosities for stars in the RGB and He-clump evolutionary stage have been obtained and corrected for incompleteness and field contamination accordingly with the procedure discussed in Sect. 3.6.1. The results are listed in Table 3.5 and plotted in Figs. 3.19 and 3.19. Fig. 3.19 shows the behavior of the number of RGB stars normalized to the number of He-Clump stars as a function of the cluster age. Fig. 3.19 shows the bolometric luminosities of RGB stars normalized to the bolometric luminosities of He-Clump stars as a function of the cluster age (upper panel) and the bolometric luminosities of RGB stars normalized to the bolometric luminosities of entire cluster as a function of age (lower panel).

Note that, in a few high density clusters (see Table 3.5) with severe crowding, completeness drops down to 60% at the He-clump magnitude level in the innermost A region (see Fig. 3.11). Hence, in these clusters star counts and luminosities have been computed only in the outer B and C regions.

At an age of $\approx 500\ Myr$ the rapid increase of the RGB population ratios (by a factor of ≈ 3 in number and ≈ 4 in luminosity) in a timescale as short as $\approx 400\ Myr$ flags the occurrence of

---

[1]Note that, since the boxes sample the bulk of the population along each evolutionary stage, a slightly different assumption in the selection box size has a negligible impact on the overall results.
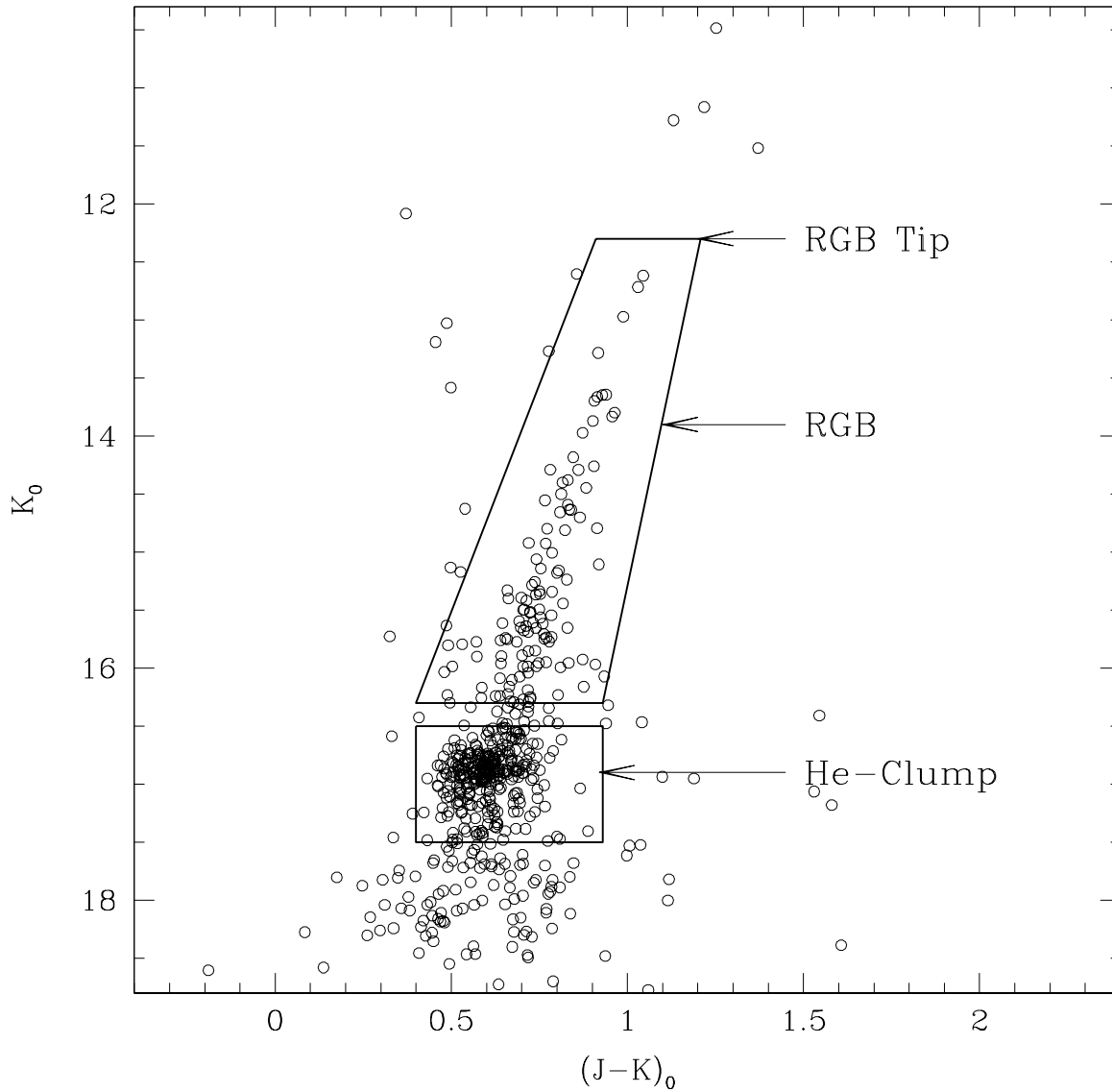
Figure 3.18: An example of a K_0, $(J - K)_0$ de-reddened CMD with the selection boxes adopted to distinguish the RGB and the He-Clump populations for clusters with $s > 34$ (see Fig. 3.4 and 3.6). The position of the RGB Tip is also indicated.

Cluster	N_{RGB} [a]	N_{He-C} [a]	L_{RGB}^{bol} [b]	L_{He-C}^{bol} [b]
NGC 2249	9	98	0.16	0.51
NGC 1987	42	322	0.92	2.05
NGC 2209	24	160	0.61	0.81
NGC 2108	40	231	1.11	1.38
NGC 2190	28	174	0.94	0.89
NGC 2231	36	114	0.71	0.59
NGC 1783[c]	150	352	4.58	1.98
NGC 1651	43	177	1.16	1.09
NGC 2162	40	143	0.99	0.78
NGC 1806[c]	75	218	2.25	1.30
NGC 2173	36	84	1.11	0.48
NGC 1978[c]	182	402	5.03	2.23
NGC 416	190	299	5.47	1.66
NGC 419[c]	263	608	8.69	3.85
NGC 339	107	188	3.09	1.20
NGC 361	109	180	4.25	1.23

Table 3.5: Star counts and bolometric luminosities for RGB and He-Clump stars. (a) Star counts are corrected for incompleteness and field contamination. (b) Bolometric luminosities are in units of 10^4 $L_\odot$. (c) Due to severe crowding conditions, star counts and luminosities have been computed only in the outer B and C regions, see Fig. 3.11.

the RGB Ph-T. At the age of ≈ 900 Myr a progressive flattening of the ratios suggests that the full development of an extended and well populated RGB has occurred. The overall increase of the population ratios between ≈ 500 Myr and ≈ 3.5 Gyr is a factor ≈ 5 by number and ≈ 7 by luminosity. These two figures support the hypothesis that the cluster set presented here properly samples the epoch of the full development (in both luminosity and star number) of the RGB. This result fully confirms the finding by Ferraro et al. (1995), who identified NGC 1987 and NGC 2108 as the two intermediate-age clusters on the verge of the RGB Ph-T.

Empirical data have been compared to theoretical predictions. In Fig. 3.19 and Fig. 3.19, we over-plotted the predictions of canonical models (Maraston, 1998, 2005) with $[Z/H] = -0.33$. The models nicely agree with the observations over the entire range of considered ages, well describing the epoch, the duration and the increasing contribution of the RGB phase. In Fig. 3.19 we report also the prediction of overshooting models (Girardi et al., 2000) with [Z/H]=–0.4. The major difference between the two scenarios is the delay time (≈ 500 Myr) at which the RGB Ph-T occurs when overshooting is taken into account, somewhat in contrast to the observations. The two models well agree each other and with observations after the completion of the RGB Ph-T. The mismatch shown in Fig. 3.19 suggests some problems with the evolutionary timescales of the

overshooting models by Girardi et al. (2000) and/or with the Girardi et al. (1995) calibration of the s–parameter. However, a similar discrepancy was already noted by Ferraro et al. (1995) in the previous generation of overshooting models. A new calibration of the s–parameter in terms of age by using high-quality CMDs and updated models is urgently needed to clarify this issue.

It is worth noticing the population ratio excess (both by number and by luminosity, see Figs. 3.19 and 3.19) of NGC 1783, when compared with other clusters with similar values of the $s-$parameter (i.e., NGC 2231). It is likely that this cluster is older than suggested by the $s-$parameter, since its CMD (see Fig. 3.6) shows a fully populated RGB, typical of clusters with s–parameter$\geq$40. Indeed, its RGB morphology is more similar to that one of clusters such as NGC 1806, NGC 2173 and NGC 1978 rather than that one of NGC 2231 (see Fig. 3.4 and 3.6). This evidence further supports the urgency of a new homogeneous calibration of the age scale of LMC cluster

Furthermore, we have computed the same population ratios for the 4 intermediate-age SMC clusters. The adopted procedure is the same used for the LMC clusters, by using suitable boxes defined on the cumulative CMD of these clusters and adopting as RGB-Tip magnitude level K_0=12.62 and distance modulus of $(m - M)_0$=18.99 (Cioni et al., 2000). These clusters allows to study the evolution of the RGB in an age range not covered by the LMC clusters and for a more metal-poor metallicity. The results are listed in Tab. 3.5 and plotted in Fig. 3.21 and 3.21 (as black points), in comparison with the LMC clusters (as grey points). We plotted both the predictions of the canonical models for [Z/H]=-0.33 (solid line) and for [Z/H]=-1.35. The cluster NGC 416 displays population ratios slightly higher with respect to the theoretical predictions (in a similar way to the one noted for the LMC cluster NGC 1783) but consistent with the development of the RGB Ph-T. The other 3 clusters show an increase in the population ratios between RGB and He-Clump stars, both in counts and luminosities. All these observed ratios well follow the behaviour described by the theoretical models computed with [Z/H]=-1.35.
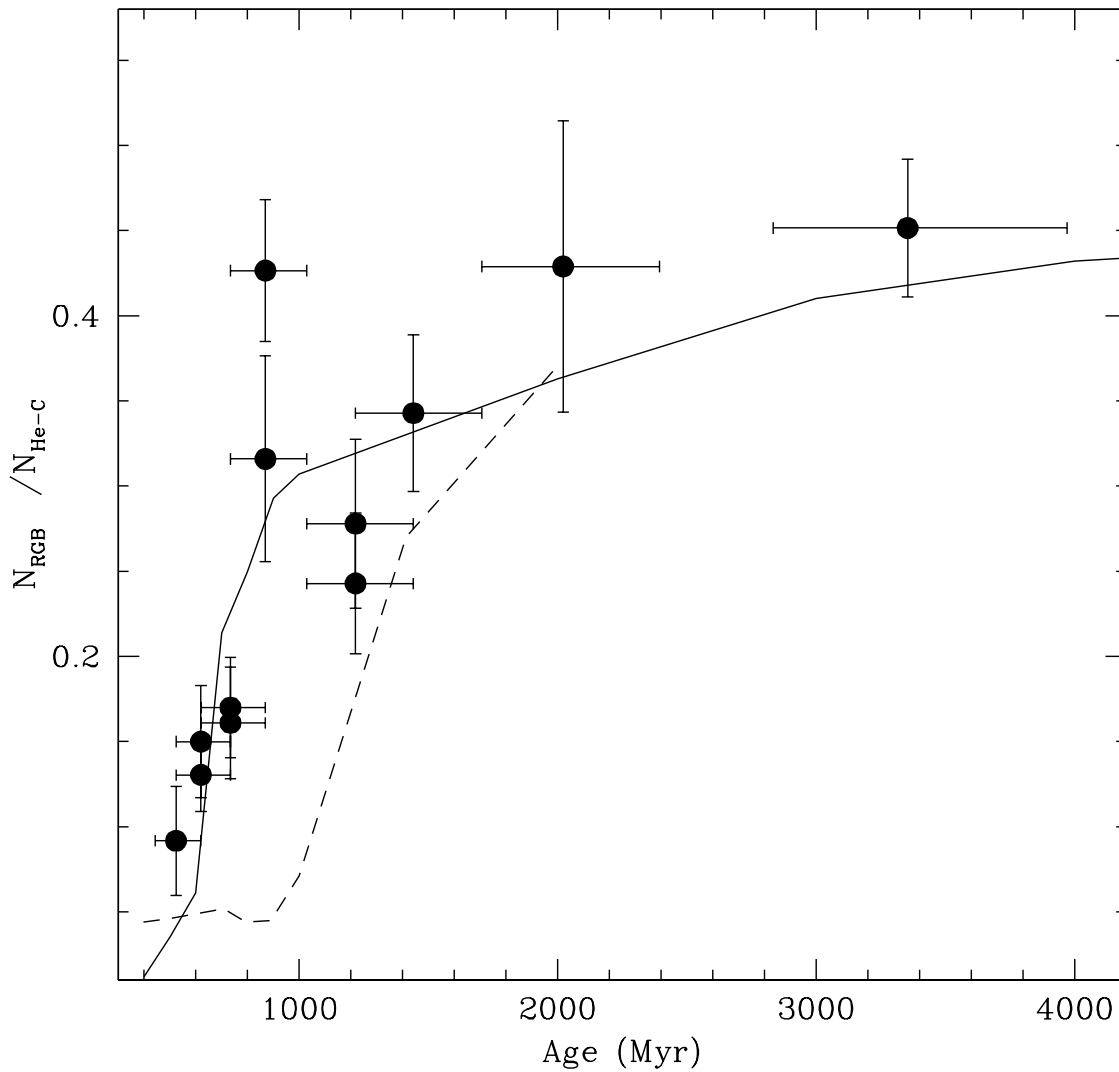
Figure 3.19: Ratio between the number of the bright RGB and He-Clump stars as a function of age for the 12 LMC clusters with $s > 33$. Stars belonging to the two populations are selected accordingly to the selection boxes shown in Fig. 3.18. The solid line represents the prediction of the canonical theoretical model with [Z/H]$= -0.33$ (Maraston, 1998) and the dashed line the prediction of the overshooting models with [Z/H]=-0.4 (Girardi et al., 2000).
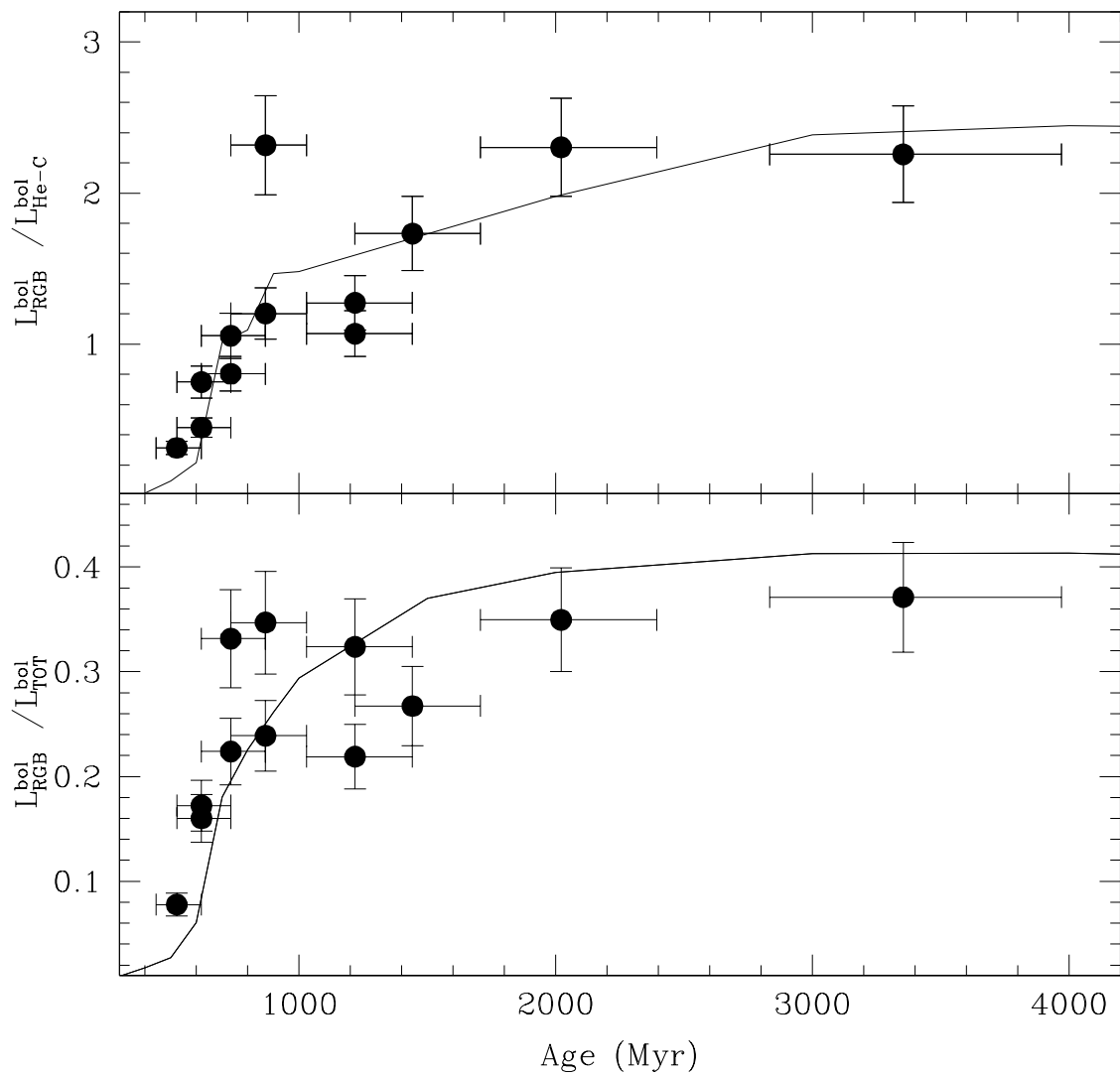
Figure 3.20: Upper panel: the bolometric luminosity of the RGB normalized to the He-Clump as a function of age for the 12 LMC clusters with $s > 33$. The line represents the prediction of the canonical theoretical model with $[Z/H] = -0.33$ (Maraston, 1998). Lower panel: the bolometric luminosity of the RGB normalized to the total bolometric luminosity for the 12 LMC clusters. The line represents the prediction of the canonical theoretical model with $[Z/H] = -0.33$ (Maraston, 2005).
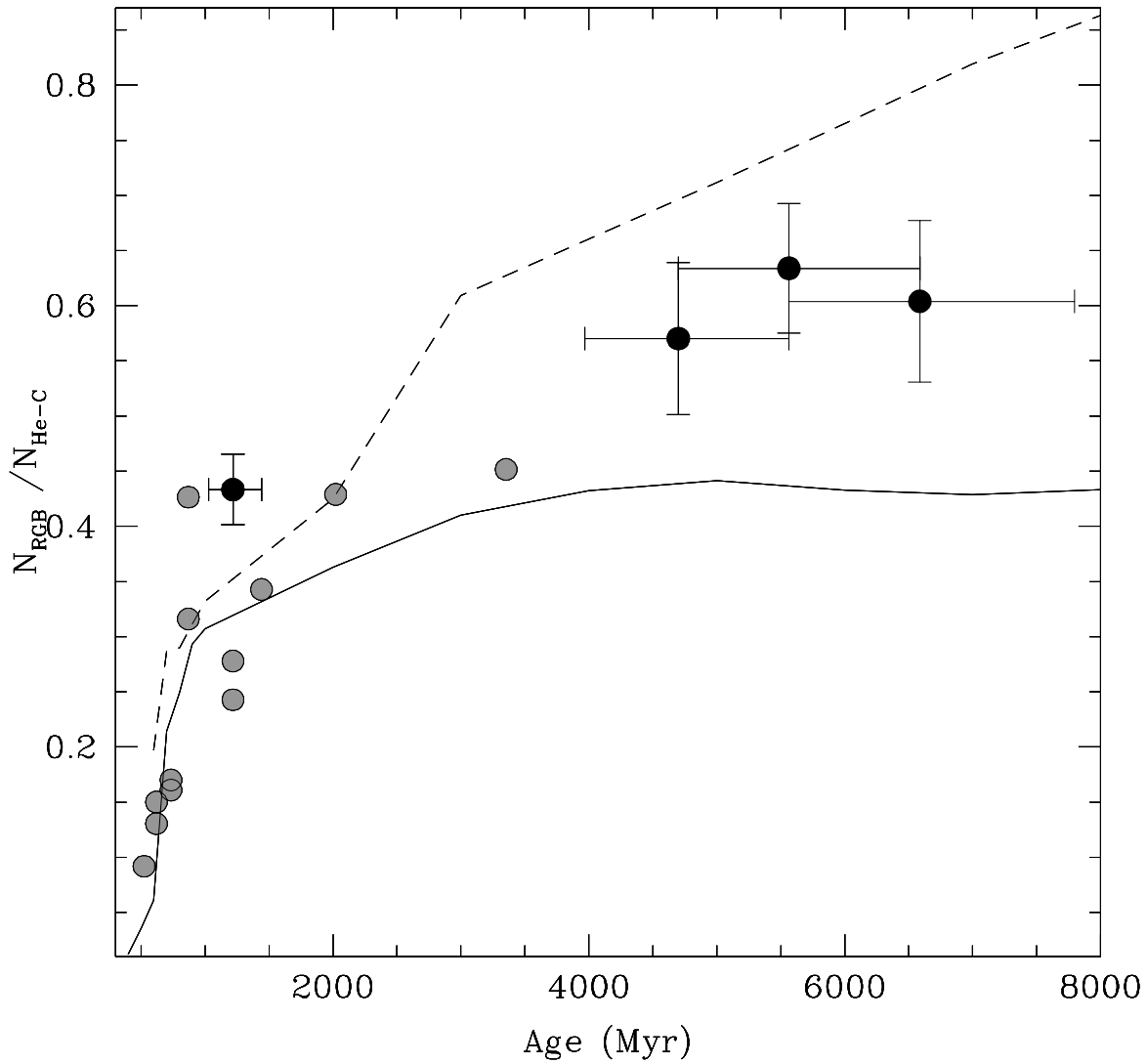
Figure 3.21: Ratio between the number of the bright RGB and He-Clump stars as a function of age for the 4 intermediate-age SMC clusters *grey circles*, in comparison with the 12 LMC clusters showed in Fig. 3.19 (open circles). The lines represent the prediction of the canonical theoretical model with [Z/H]= -0.33 (solid line) and [Z/H]= -1.35(dashed line) (Maraston, 1998).
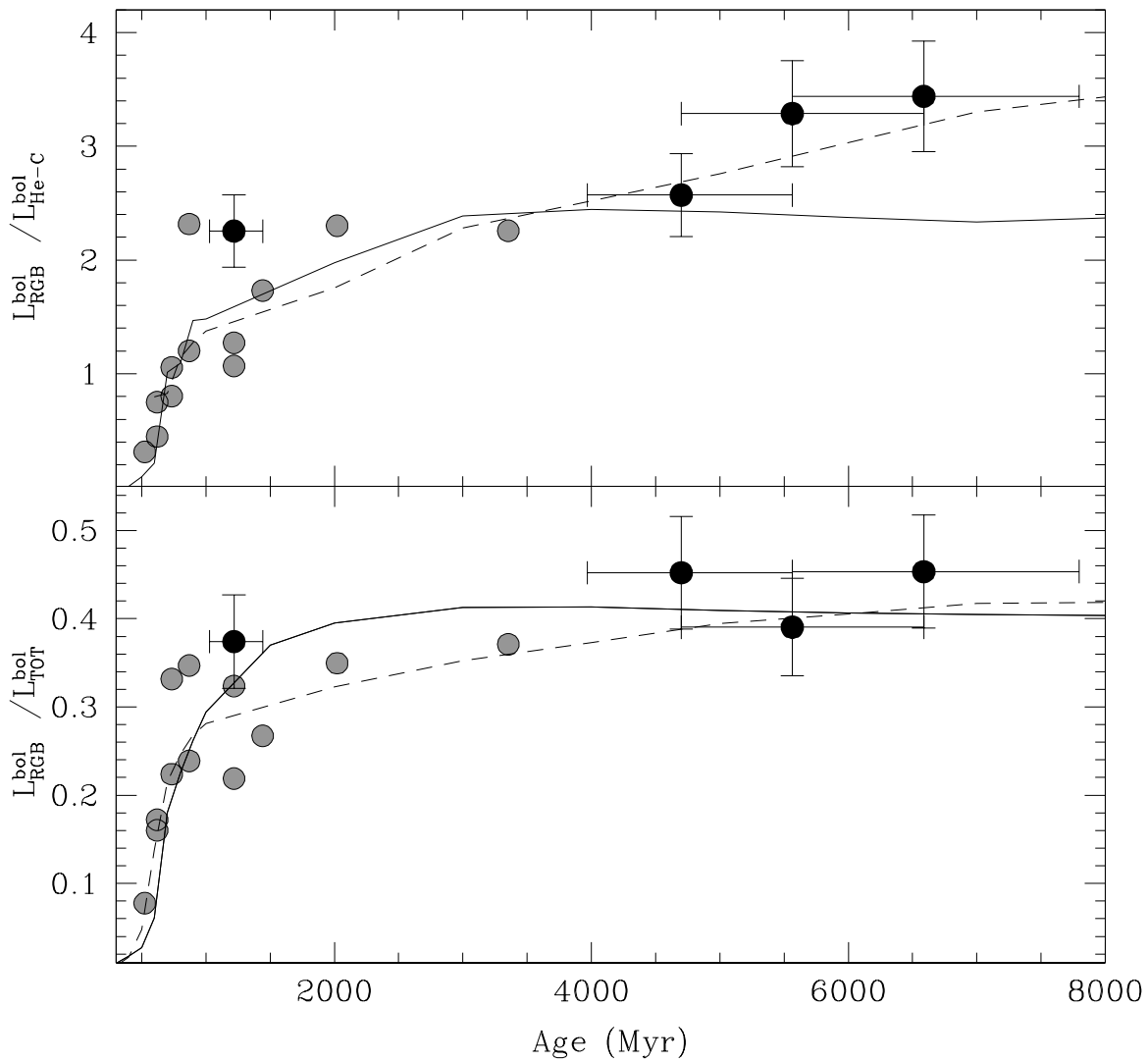
Figure 3.22: Upper panel: the bolometric luminosity of the RGB normalized to the He-Clump as a function of age for the 4 intermediate-age SMC clusters. Symbols and lines are as in Fig. 3.21. Lower panel: the bolometric luminosity of the RGB normalized to the total bolometric luminosity for the 4 intermediate-age SMC clusters.

Chapter 4

The chemical composition of the LMC clusters

Based on the results published in :

— Ferraro, Mucciarelli, Carretta & Origlia, 2006, ApJL, 645, 939

— Mucciarelli, Carretta, Origlia & Ferraro, 2008, accepted for publication in AJ

Despite the new generation of 8-meter class telescopes, detailed chemical information about the LMC clusters from high-resolution spectra is limited to a few stars in a few clusters and they are insufficient to draw a global picture of the chemical properties of these objects and to constrain the timescales of the chemical enrichment. In this Chapter, we present the first results about the project of a large high-resolution spectroscopic survey devoted to the screening of the main chemical properties of some *template* LMC clusters. We have observed a total of 9 LMC clusters with the optical high-resolution spectrograph UVES@FLAMES (VLT, ESO), 2 with ages less than ∼1 Gyr (namely NGC 2157 and 2108), 4 of intermediate age (NGC 1651, 1783, 1978 and 2173) and 3 old (NGC 1786, 2210 and 2257). The 4 intermediate-age clusters have been already analyzed and discussed in this Chapter; the analysis of the other observed clusters is currently in progress.

The overall goal of this project is twofold:

(1) the definition of a new and homogeneous metallicity scale for the LMC GC system based on high resolution spectra of giant stars, members of a representative number of *pillar* clusters, sampling different ages. This scale, combined with high-quality optical photometric datasets, will be crucial to obtain precise ages for these clusters (as discussed in Chapter 5);

(2) a detailed comparison of the cluster populations and their chemical abundance patterns with those in the LMC fields and in other galactic environments. This is crucial to constrain the

AMR and the overall star formation and chemical enrichment of the LMC. Moreover, a detailed knowledge of the whole chemistry of the GC system (both young and old clusters) is fundamental to understand the formation of the dwarf Irregulars (like LMC and SMC) in the framework of the hierarchical models (see the accurate review by Geisler et al., 2007).

4.1   The derivation of the chemical abundances: basic equations

The major portion of the stellar spectrum originates in the stellar atmospherical region called *photosphere* and its thickness depends mainly from the stellar gravity and the opacity of the photospherical gas. The most efficient way to transfer the energy through the stellar photosphere is the radiation. The basic equation to describe the radiative transfer is the following:

$$\frac{dI_\nu}{d\tau_\nu} = -I_\nu + S_\nu$$

where I_ν is the intensity of the energy flow, τ_ν is the optical depth (defined as $\tau_\nu = \int \kappa_\nu \rho dx$, where κ_ν is the absorption coefficient and dx represents the thickness of a gas element) and S_ν is the source function, defined as the ratio between the emission and absorption coefficient.

The concept of thermodynamical equilibrium cannot be applied to a stellar photosphere as whole but it is applied only to small volumes of the photosphere. In the one dimensional model atmospheres (e.g. the Kurucz models adopted in this work) the photosphere is described as the overposition of several layers and all the thermodynamical quantities depend only on height (in the case of plane-parallel geometry) or radius (in the case of spherical models). This approximation is called Local Thermodynamic Equilibrium (LTE) and allows to describe the excitation, the ionization, the source function and the thermal velocity distribution by using one only temperature in each layer. In this approximation the source function is described by using the Planck function

$$S_\nu = B_\nu = \frac{2h\nu^3}{c^2} \cdot \frac{1}{e^{(h\nu/kT)} - 1}$$

where *h* is the Planck constant, *c* the light speed and *k* the Boltzmann constant. Two fundamental equations that rule the population of the levels involved in a transition are the Boltzmann and the Saha equations.

The Boltzmann equation provides the ratio of populations in two different levels *m* and *n*:

$$\frac{N_n}{N_m} = \frac{g_n}{g_m} \cdot e^{-(\chi_n - \chi_m)/k \cdot T}$$

74

where g_j is the statistical weight of the level j, with $g_j=2J+1$, with J the inner quantum number. The Boltzmann equation provides also the ratio between the population of the level n and the total number of atoms of a specie:

$$\frac{N_n}{N} = \frac{g_n}{u(T)} \cdot 10^{-\theta \chi_n}$$

where u(T) is the partition function defined as

$$u(T) = \sum_i g_i \cdot e^{-\chi_i / k \cdot T}$$

Moreover, the Saha equation allows to compute the number of atoms in the ionization level *j+1* with respect to the atoms in the ionization level *j*:

$$\frac{N_{j+1}}{N_j} = \frac{\Phi(T)}{P_e}$$

where

$$\Phi(T) = 0.6665 \cdot \frac{u_{j+1}}{u_j} \cdot T^{-2.5} \cdot 10^{-\theta \chi_{Ion}}$$

The combination of these two equations provides the number of atoms in a given ionization level with respect to the total number of atoms of the element.

Generally, for a weak line dominated by Doppler broadening the equivalent width (EW) (normalized to the corresponding wavelength) can be expressed according to the follow formula (see Gray, 1992):

$$\lg\left(\frac{EW}{\lambda}\right) = \lg\left(\frac{\pi e^2 (N_j/N)N_H}{m_e c^2 u(T)}\right) + \lg\left(\frac{N_{El}}{N_H}\right) + \lg\left(gf\lambda\right) - \theta\chi - \lg \kappa_\nu$$

where e is the electron charge, m_e the electron mass, (N_j/N) is the number of atoms of a generic element in the ionization state *j* with respect to the total number of atoms of that element, N_H is the total number of hydrogen atoms per unit volume.

The procedure to derive chemical abundances from stellar absorption lines is an elaborate numerical process involving different steps, summarized as follows:

- Define a model atmosphere, normally based on the radiative and hydrostatic equilibrium. Theoretical model atmospheres serve as the fundamental tool for the analysis of observed stellar spectra. The basic parameters that described a stellar atmosphere(effective temperatures, surface gravities, chemical composition, opacity and additional velocity fields) are described as a function of the optical depth τ;

- compute atomic level populations at each depth point (generally, assuming LTE);

- compute the absorption coefficients as functions of the depth and distance from the line centre;

- solve the equation of radiative transfer (see e.g. Gray, 1992, for a detailed discussion about the integration methods) in order to produce a synthetic spectrum as a function of the assumed abundances of each element of interest;

- convolve the synthetic spectrum with the surface velocity field (e.g., effects of rotation and granulation) and with the instrumental profile;

- compare the obtained synthetic spectrum with the observed spectrum or EWs of the absorption lines of interest.

4.2   Description of the sample, target selection and observations

The observations were performed by using the multi-object spectrograph FLAMES (Pasquini et al., 2002), mounted at the Kueyen 8 m-telescope (UT2) of the ESO Very Large Telescope on Cerro Paranal (Chile). We used FLAMES in the UVES+GIRAFFE/MEDUSA combined mode for a total of 8 UVES and 132 MEDUSA fibres. Here we present the results of the UVES Red Arm observations which provide high resolution (R~ 47000) spectra in the 4800-6800 $\mathring{A}$ wavelength range for 6-7 stars in one shot. The spectra were acquired during 3 nights allocated to the ESO Program 072.D-0342(A). Additional observations were performed as back-up programmes in two Visitors Mode runs (ESO Program 072.D-0337(A) and ESO Program 074.D-0369(A)). The selection of the target stars is based on our high quality near-infrared (J, H and K filters) photometric catalogs of a large sample of LMC clusters, as secured by our group (see Chapter 3). These catalogs have been astrometrized onto the 2MASS system. The selected stars for the spectroscopic survey belong to the bright portion of the RGB (K<14), whose tip is located at $K_0 \approx 12.1$ (Cioni et al., 2000), in order to minimize the possible contamination by AGB stars, and without bright companions. Fig. 4.1 shows the (K, J-K) CMDs of the 4 clusters with marked the spectroscopic targets. The spectra have been acquired in series of 4-6 exposures of $\approx$45min each: the pre-reduction procedure has been performed by using the UVES ESO-MIDAS pipeline (Mulas et al., 2002), which includes bias subtraction, flat-field correction and wavelength calibration with a reference Th-Ar calibration lamp. All the exposures relative to a given star have been sky-
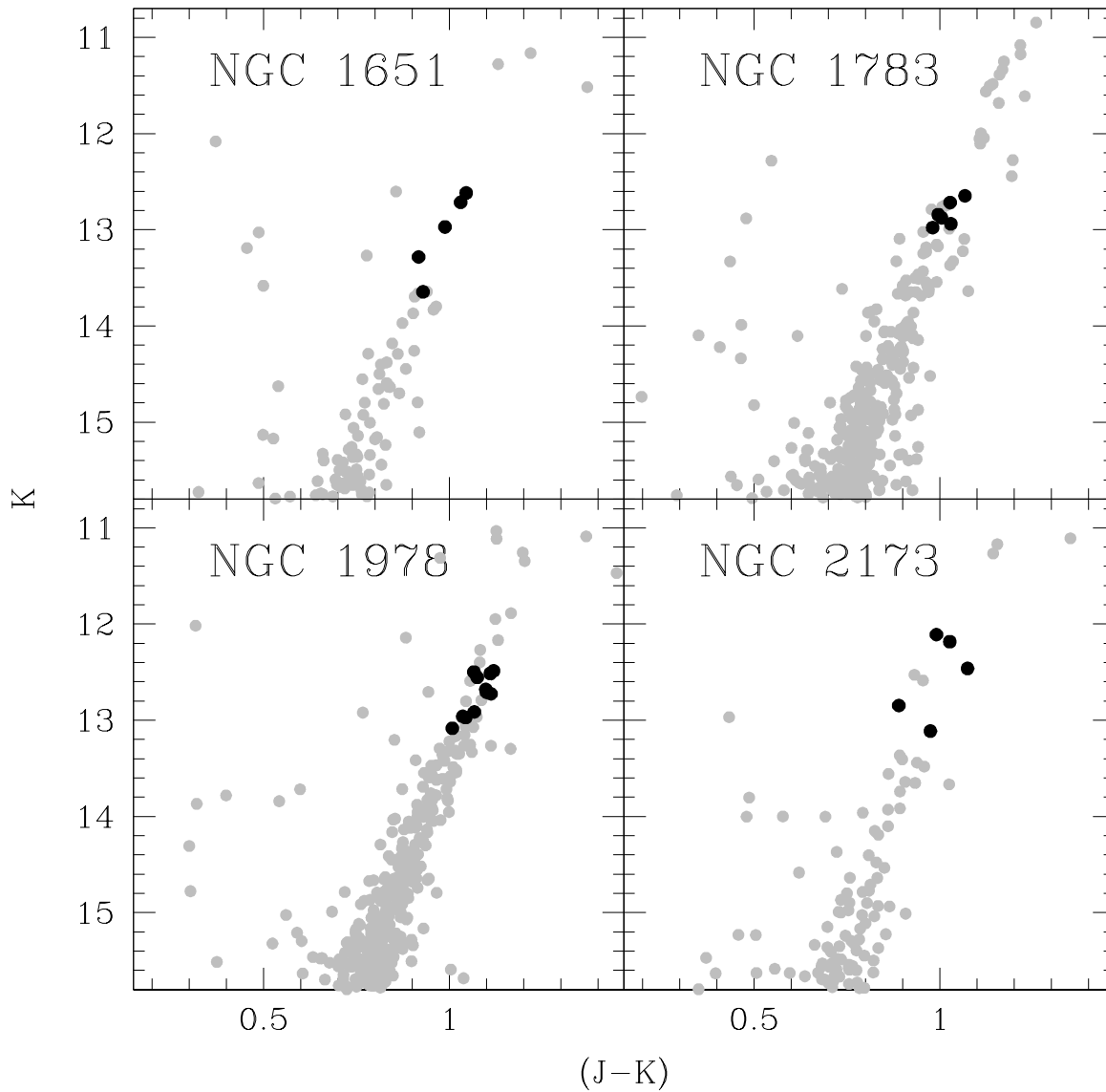
Figure 4.1: K, J-K color-magnitude diagrams for the upper RGB of the 4 observed LMC clusters (Mucciarelli et al., 2006): the black points indicate the target stars of the present work.

subtracted, corrected for radial velocity (by using several tens of metallic lines) and average-combined together, providing a final, equivalent spectrum of total exposure time of 3-5 hrs, with a typical S/N≈30-40 (at about 6000 $\mathring{A}$). Fig. 4.2 shows some portions of the final, combined spectrum of the star NGC 2173-5 with marked several spectral features of interest.

The radial velocities included heliocentric corrections, calculated by using the IRAF task RVCORRECT. We find v_r =233.1±1.8 km/s (rms=3.6 km/s), v_r =277.6±1.0 km/s (rms=2.3 km/s), v_r =236.8±0.4 km/s (rms=1.2 km/s), v_r =293.1±1.5 km/s (rms=3.1 km/s) for NGC 1651, NGC 1783, NGC 1978 and NGC 2173, respectively. These values are in excellent agreement with previous determinations by Olszewski et al. (1991) and Grocholski et al. (2006). Tab. 4.1 lists the main data for each observed star: S/N, heliocentric radial velocity, near-infrared magnitude J_0 and color $(J - K)_0$, right ascension and declination (see Chapter 3).

4.3 Equivalent widths

The analysis of the observed spectra and the computation of the chemical abundances (for Fe and other elements) was performed by using the ROSA package (Gratton, 1988). The line EWs from the observed spectra have been measured by Gaussian fitting of the line profiles, adopting a relationship between EW and FWHM (see e.g. Bragaglia et al., 2001). The local continuum has been derived by applying an iterative clipping average over the points with highest counts around each line.

An empirical estimate of the internal error in the measurement of EWs can be obtained by comparing a large sample of line EWs in pairs of stars with similar physical parameters. We derived an average rms of 13.3, 8.5, 10.3 and 10.5 m$\mathring{A}$ for NGC 1651, NGC 1783, NGC 1978 and NGC 2173, respectively. Such rms estimates should be divided by $\sqrt{2}$, since they are distributed in equal proportion to the two stars in each pair, thus giving final values of 9.4, 6.0, 7.3 and 7.4 m$\mathring{A}$ for the 4 clusters, respectively. These errors are larger than those obtained from the Cayrel (1988) formula (which yields a typical uncertainty of ≈4.2 m$\mathring{A}$), since the latter neglects the uncertainty in the continuum location, which is the dominant source of error in metal-rich, crowded spectra of rather cool giants.

4.4 Oscillator strengths

The choice of the oscillator strengths is a crucial step in the chemical abundances determination, because the abundance depends linearly on the gf values (as described in the Sect. 4.1). In this
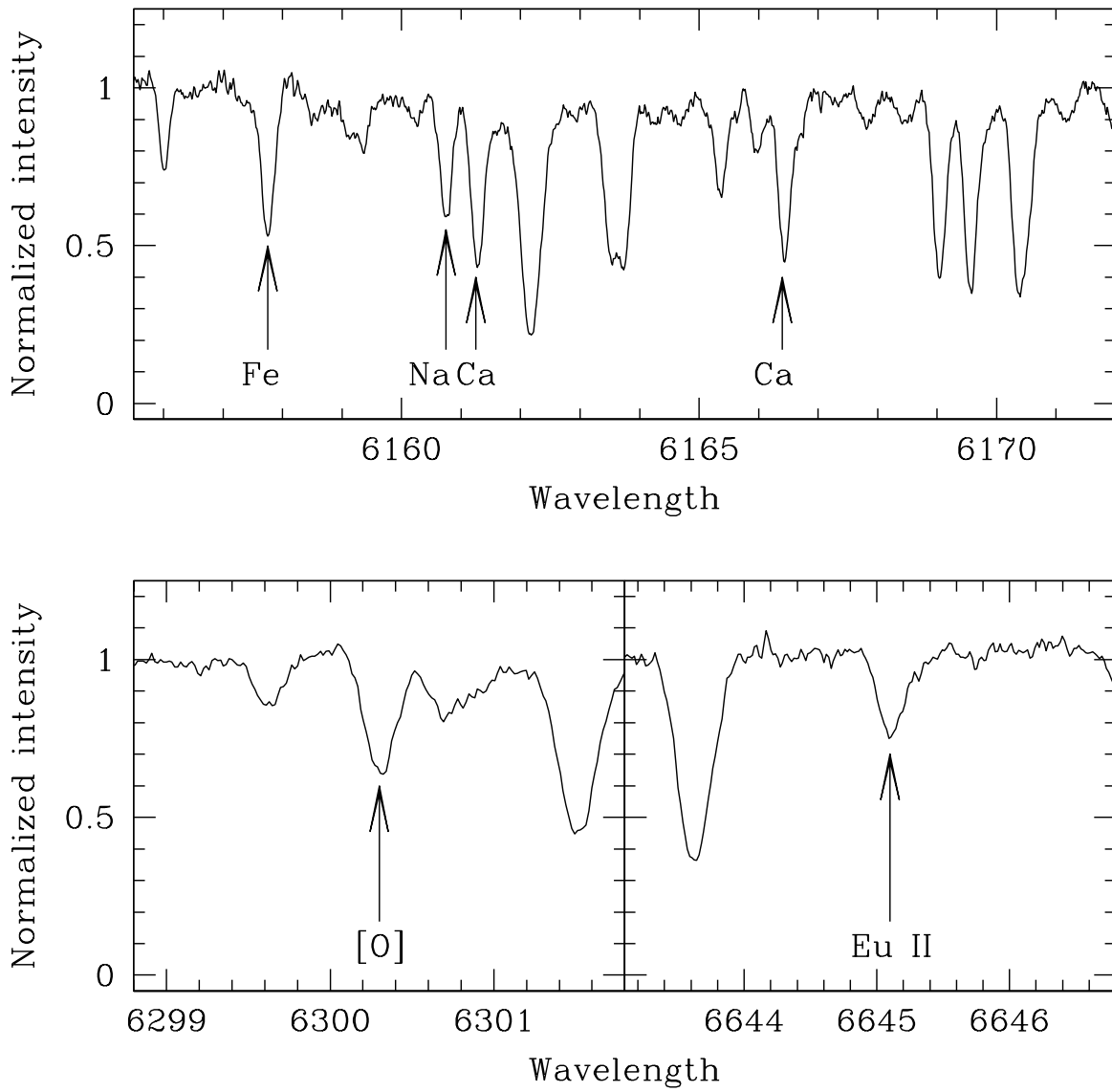
Figure 4.2: Portions of the spectrum of the target star NGC 2173-5. Some spectral features of interest are indicated.

Star ID	S/N	V_{helio} (km/s)	J_0	$(J - K)_0$	RA(J2000)	Dec(J2000)
1651-6	35	234.3	13.58	0.99	69.3880040	-70.6012635
1651-8	30	227.3	13.66	0.98	69.3799588	-70.5734344
1651-10	30	232.1	13.87	0.94	69.3844841	-70.5838366
1651-12	30	235.7	14.11	0.86	69.3573261	-70.5738910
1651-16	25	236.2	14.49	0.88	69.3824681	-70.5959887
1783-22	35	277.4	13.63	1.02	74.7264895	-65.9723560
1783-23	30	275.1	13.66	0.98	74.7793127	-65.9862323
1783-29	30	275.2	13.75	0.94	74.7830715	-65.9957701
1783-30	30	281.2	13.79	0.95	74.8010628	-65.9629302
1783-32	30	277.9	13.87	0.93	74.7707871	-65.9799639
1783-33	35	278.8	13.88	0.98	74.8011665	-65.9906700
1978-21	35	295.5	13.52	1.07	82.1515305	-66.2322134
1978-22	40	290.6	13.48	1.01	82.2014424	-66.2339097
1978-23	35	288.7	13.54	1.06	82.2092677	-66.2568186
1978-24	30	291.5	13.54	1.02	82.1915173	-66.2387280
1978-26	30	296.3	13.69	1.05	82.1751055	-66.2325960
1978-28	35	292.3	13.72	1.05	82.1774043	-66.2079169
1978-29	35	298.4	13.75	1.06	82.1906198	-66.2420488
1978-32	30	290.5	13.89	1.01	82.1764751	-66.2351731
1978-34	20	292.1	13.91	0.98	82.2041703	-66.2277628
1978-38	30	297.1	13.93	0.99	82.2221112	-66.2352105
1978-42	35	291.5	14.00	0.96	82.1706985	-66.2461504
2173-4	50	237.6	12.95	0.86	89.4861621	-72.9749781
2173-5	50	234.8	13.15	0.99	89.4910121	-72.9652585
2173-6	40	237.3	13.47	1.04	89.5475844	-72.9757905
2173-8	55	237.9	13.68	0.85	89.4955156	-72.9785015
2173-10	40	236.3	14.03	0.94	89.4816674	-72.9815157

Table 4.1: Main information about the target stars: S/N computed at 6000 $\mathring{A}$, heliocentric radial velocity, near-infrared magnitudes and colors, and coordinates.

work we employed the linelist described by Gratton et al. (2003), by using, whenever possible, laboratory and theoretical oscillator strengths with low uncertainties, typically below 0.05 dex (similar errors translate into abundance errors below 0.05 dex). For some transitions, for which accurate gf are not available, the oscillator strength values have been derived from an inverse solar analysis. All the references for the oscillator strengths are available in Gratton et al. (2003) and Carretta et al. (2004).

For the collisional damping, we adopted the recent theoretical models presented by Barklem, Piskunov & O'Mara (2000).

Finally, as reference solar abundances, we adopted the abundances obtained by Gratton et al. (2003), adopting the same linelist and procedure described in this Chapter and the solar model atmosphere by Kurucz (1994).

4.5 Stellar parameters

Stellar T_{eff} were obtained from the near-infrared color (J-K), corrected for reddening by using the E(B-V) values from Persson et al. (1983), and the extinction law defined by Rieke & Lebofsky (1985). We adopted two different color-T_{eff} transformations, namely by Montegriffo et al. (1998) and Alonso, Arribas & Martinez-Roger (1999, 2001). Since the derived temperatures are well in agreement within $\leq$ 50 K, we used the average of the two values.

Gravities were estimated by using the relation between T_{eff}, stellar mass and luminosity:

$$log(\frac{g}{g_\odot}) = 4 \, log(\frac{T_{eff}}{T_{eff,\odot}}) + 0.4 \, (M_{bol} - M_{bol,\odot}) + log(\frac{M}{M_\odot}),$$

by adopting the solar references log $g_\odot$=4.437, $T_{eff,\odot}$= 5770 K and $M_{bol,\odot}$= 4.75, according to the IAU recommendations (Andersen, 1999). For each target star M_{bol} has been estimated from the K magnitude, and using $(m-M)_0$= 18.5 (van den Bergh, 1998; Alves, 2004) and bolometric corrections by Montegriffo et al. (1998). Stellar masses have been estimated by using suitable isochrones (Castellani et al., 2003; Cariulo, Degl'Innocenti & Castellani, 2004), adopting ages derived from the s–parameter calibration (Elson & Fall, 1988; Girardi et al., 1995), and an average metallicity of Z=0.008 (Cole et al., 2005), typical of the LMC. We derived masses of 1.81, 1.98, 1.37 and 1.55 $M_\odot$ for NGC 1651, 1783, 1978 and 2173, respectively. All the program stars have similar T_{eff} ($\sim$3600-4000 K), and gravities log g ($\sim$0.5-1.2 dex).

Microturbulent velocities were estimated by eliminating the trend of abundances with the

expected line strengths, according to the prescription of Magain (1984) and by using a large number (80-90) of Fe I lines for each star.

The model overall metallicity [A/H] was chosen as that of the model atmosphere extracted from the grid of ATLAS models by Kurucz (1993), with the overshooting option switched on, whose abundance matches the one derived from Fe I lines when adopting the appropriate atmospheric parameters for each star.

Fig. 4.3 shows, as an example of consistency check, the iron abundance log n(Fe) from the Fe I lines as a function of the excitation potential χ, expected line strength and wavelength for one of the star in our sample, together with the linear fit to each distribution (dashed lines). The log n(Fe)-χ relationship for each target star shows only a marginal slope ($\sim$ –0.02 dex/eV and reported in Fig. 4.4 as a function of the T_{eff}), confirming that the adopted photometric T_{eff} well reproduce the excitation equilibrium. The lack of significant trends in the relationship between iron abundance and the expected line strength (Fig. 4.3, middle panel) supports the validity of the adopted v_t values. The derived iron abundances show no trend with the wavelength (Fig. 4.3, lower panel); this represents a good sanity check regarding the continuum placement.

4.6 Error budget

We computed the total uncertainty in the derived abundances, according to the treatment discussed by McWilliam et al. (1995). The variance of a generic abundance ratio [X] is estimated by using the following formula:

$$\sigma_{[X]}^2 = \sigma_{EW}^2 + \sigma_{T_{eff}}^2 \cdot (\frac{\partial [X]}{\partial T_{eff}})^2 + \sigma_{\log g}^2 \cdot (\frac{\partial [X]}{\partial \log g})^2 + \sigma_{[A/H]}^2 \cdot (\frac{\partial [X]}{\partial [A/H]})^2 + \sigma_{v_t}^2 \cdot (\frac{\partial [X]}{\partial v_t})^2,$$

where σ_{EW} is the abundance uncertainty due to the error in the EW measurement, σ_i is the internal error related to the atmospheric parameter i and $\frac{\partial [X]}{\partial i}$ indicates the differential variation of the derived abundance [X] with respect to the atmospheric parameter i. These latter terms have been computed for all the elements analyzed in this work by re-iterating the analysis varying each time only one parameter, by assuming variations of ΔT_{eff}=100K, $\Delta \log g$=0.2 dex, $\Delta [A/H]$=0.1 dex and Δv_t=0.2 km/s. Tab. 4.2 reports the results of such an analysis for the star NGC 1783-29. The terms of covariance that measure the correlation between the atmospheric parameters are not included in the above formula.

The main error sources in the determination of T_{eff} are the photometric error related to (J-
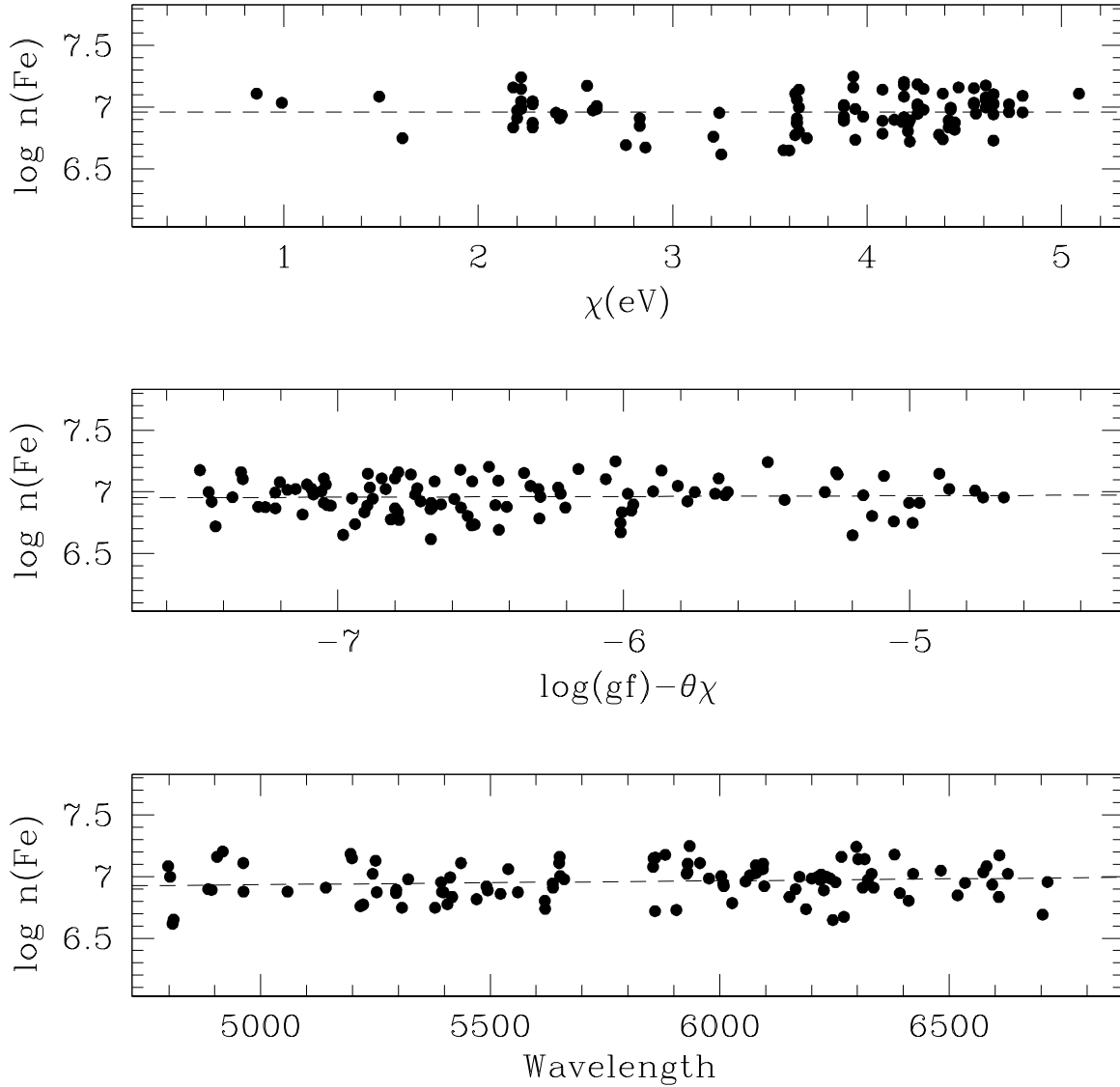
Figure 4.3: The trend of the derived abundances from Fe I lines for the star NGC 2173-8 as a function of the excitation potential χ (upper panel), the expected line strength (middle panel) and the wavelength (lower panel). The dashed lines represent the linear fit to each distribution.
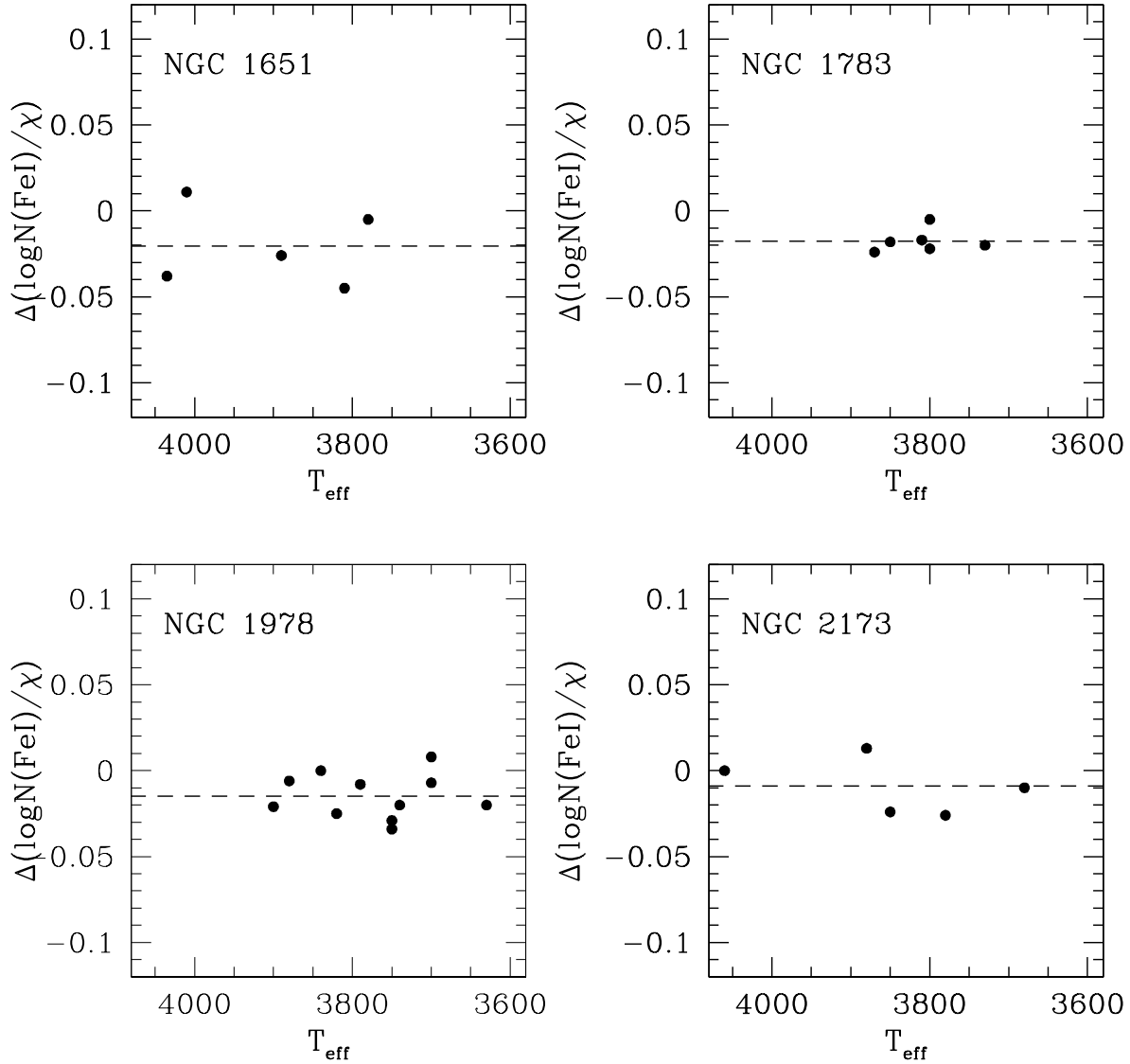
Figure 4.4: The slopes of the relationship between the neutral iron abundances and the excitation potential χ for individual stars in each cluster as a function of T_{eff}. Dashed lines represent the average slope for each cluster.

Ratio	T_{eff} +100 K	logg +0.2 dex	[A/H] +0.1 dex	v_t +0.2 km/s	$< N >$	σ_{EW}
$[O/Fe]$	0.028	0.042	0.040	-0.016	2	0.127
$[Na/Fe]$	0.085	-0.010	0.006	-0.075	4	0.090
$[Mg/Fe]$	0.004	0.001	0.027	-0.059	4	0.090
$[Al/Fe]$	0.069	0.003	0.005	-0.047	2	0.127
$[Si/Fe]$	-0.113	0.027	0.025	-0.047	4	0.090
$[Ca/Fe]$	0.063	-0.060	-0.032	-0.185	13	0.050
$[Sc/Fe]$II	0.018	0.101	0.093	-0.091	5	0.080
$[Ti/Fe]$	0.168	0.016	0.031	-0.167	13	0.050
$[V/Fe]$	0.156	0.004	0.024	-0.195	7	0.068
$[Cr/Fe]$	0.138	0.047	0.058	-0.073	14	0.048
$[Fe/H]$I	-0.016	0.019	0.028	-0.114	86	0.019
$[Fe/H]$II	-0.210	0.068	0.043	-0.063	2	0.127
$[Co/Fe]$	-0.033	0.024	0.026	-0.117	3	0.104
$[Ni/Fe]$	-0.040	0.028	0.028	-0.099	25	0.036
$[Y/Fe]$II	-0.016	0.081	0.034	-0.160	3	0.104
$[Zr/Fe]$	0.160	0.038	0.021	-0.154	3	0.104
$[Ba/Fe]$II	0.019	0.056	0.050	-0.090	3	0.104
$[La/H]$II	0.018	0.087	0.037	-0.113	1	0.180
$[Ce/H]$II	0.013	0.082	0.038	-0.062	1	0.180
$[Nd/Fe]$II	0.019	0.079	0.038	-0.166	2	0.127
$[Eu/Fe]$II	-0.014	0.083	0.036	-0.053	1	0.180

Table 4.2: Sensitivities of the abundance ratios to the variation of the atmospheric parameters (T_{eff}, log g, [A/H], v_t), with the corresponding average number of used lines ($< N >$) and the error of the abundance associated to the typical error in EW (σ_{EW}), as computed for star NGC 1783-29.

K) color and reddening E(B-V). All the program stars are brighter than K$\sim$14 and the typical photometric error for the (J-K) color is ~ 0.03 mag; for the reddening we assumed a conservative uncertainty of $\sim 20\%$. These terms translate into a ±60 K temperature uncertainty. In computing the uncertainty due to the stellar gravity, we took into account four main error sources: the error in T_{eff}, in mass ($\pm10\%$), in distance modulus (±0.1 mag) and in bolometric correction (±0.05 mag). From the quadratic sum of these uncertainties, a total error in $\log g$ of ±0.08 dex has been obtained. To estimate the error in the microturbolent velocity we repeated the analysis by changing the v_t value until the $1\sigma_{slope}$ value for the slope of the abundance - expected line strength relation has been reached. The internal error associated to v_t is typically 0.10-0.17 km/s.

An estimate of the error in the derived abundances due to the uncertainty in the measurement of EWs has been estimated by weighting the average Fe I line-to-line scatter (0.18 dex) with the square root of the mean number of measured lines N_i for each *i* element:

$$\sigma_{EW} = \frac{0.18}{\sqrt{N_i}}.$$

Finally, we assumed an additional ±0.1 dex uncertainty due to the choice of the best-fit model atmosphere.

4.7 Measured chemical abundances

Tab. 4.3–4.8 report the abundances of all analyzed elements (with the adopted reference solar values, the number of measured spectral lines and the corresponding line-to-line scatter) for the target stars and Tab. 4.9 and 4.10 summarize the average abundance ratios for the 4 LMC clusters with the number of used stars, the observed star-to-star scatter (σ_{obs}) and the expected error (σ_{exp}) computed according to the procedure described in Sect. 4.6. For each cluster, Fig. 4.5-4.9 plot the average values of the derived abundance ratios (big grey points).

For comparison, the corresponding abundance ratios of other intermediate-age stellar populations are reported, namely LMC disk giant stars by Pompeia et al. (2006) (empty triangles), intermediate-age LMC cluster giants by Hill et al. (2000) (empty squares), Galactic thin disk dwarfs by Reddy et al. (2003) (small grey points) and Sgr giant stars by Bonifacio et al. (2000); Monaco et al. (2005, 2007); Sbordone et al. (2007) (small black points).

4.7.1 Iron and Iron-peak elements

The mean iron abundance of the cluster NGC 1651 results [Fe/H]=–0.30$\pm$0.03 dex with rms=0.07 dex, whereas Olszewski et al. (1991) derived [Fe/H]=–0.37$\pm$0.20 dex. Photometric determinations

have been presented by Dirsch et al. (2000, from Stromgreen photometry) and Sarajedini et al. (2002, from isochrones fitting), suggesting [Fe/H]=–0.65 dex and [Fe/H]=–0.07±0.10 dex, respectively. Recently, Grocholski et al. (2006) estimated [Fe/H]=–0.53±0.03 dex, by using the Ca II triplet of 9 giant stars.

NGC 1783 shows a mean iron abundance of [Fe/H]=–0.35±0.02 dex with rms=0.06 dex. For this cluster only photometric determinations are available : Sagar & Pandey (1989) found [Fe/H]=–0.45 dex and de Freitas Pacheco, Barbuy & Idiart (1998) found [Fe/H]=–0.75 dex.

The results about the iron abundance of NGC 1978 ([Fe/H]=–0.38±0.02 dex with rms=0.07 dex) have been discussed in detail in Sect. 4.8.

The iron content of NGC 2173 turns out to be [Fe/H]=–0.51±0.03 with rms=0.07 dex. Olszewski et al. (1991) give [Fe/H]=–0.24±0.20 dex, de Freitas Pacheco, Barbuy & Idiart (1998) found [Fe/H]=–0.50 dex and Grocholski et al. (2006) found [Fe/H]=–0.42±0.03 dex, by using the Lick index and the Ca II triplet, respectively.

We also measured lines of several elements of the Fe-group, namely Sc, V, Cr, Co and Ni. Corrections for the hyperfine structure (HFS) due to non-zero nuclear magnetic moment, were applied to the ScII, V and Co lines, as in Gratton et al. (2003, and references therein). The abundance ratios between these elements and Fe is roughly solar in all the 4 clusters. In order to cross-check the abundances derived from the EW measurements, we performed a synthetic spectrum fitting for some lines of these elements, finding a negligible difference between these two determinations.

4.7.2 Light odd-Z elements

Na abundances were derived from the $\lambda\lambda$5682-88 $\mathring{A}$ and $\lambda\lambda$6154-60 $\mathring{A}$ doublets and they include non-LTE corrections computed according to Gratton et al. (1999). The differences between LTE and non-LTE derived abundances are generally as large as ∼0.2 dex, with a maximum discrepancy of ∼0.35 dex in the coolest star of the sample. Three clusters (NGC 1651, NGC 1783 and NGC 1978) exhibit mild depletion of [Na/Fe]≤–0.1 dex while this ratio is solar in NGC 2173, without appreciable intrinsic star-to-star scatter.

Al abundances were derived from the $\lambda\lambda$6696-98 $\mathring{A}$ doublet. These lines do not include non-LTE corrections, following the extensive discussion by Baumueller & Gehren (1996). All the target clusters are characterized by a significant depletion of [Al/Fe], typically $\leq$ –0.3 dex. Also for this ratio, the intrinsic star-to-star scatter is negligible. NGC 1978 was previously observed by Hill et al. (2000) who found [Al/Fe]=0.10 dex from the analysis of 2 giants, only. This value turns out

to be ∼0.6 dex higher that that found here ([Al/Fe]=–0.52 dex), the discrepancy is likely due to the strong difference (∼0.6 dex) in the iron content derived from the two analysis (see Sect. 4.8). Indeed, their [Al/H] abundance is consistent with our estimate within the errors.

4.7.3 α-elements

A number of lines for those elements formed through α-capture, namely O, Mg, Si, Ca and Ti, were measured. For all these elements we note an high level of homogeneity, with the star-to-star scatter consistent with the measured errors and without significant trends with T_{eff}.

The O analysis is based on the forbidden lines at $\lambda6300.31$ Å and $\lambda6363.79$ Å. These lines are not blended with telluric features, with the only exception of the line at $\lambda6300.31$ Å in the NGC 1978 spectra, which is blended with a telluric absorption line. For these stars this spurious contribution was removed by using the IRAF task TELLURIC and adopting as template spectrum an early type star. At the UVES resolution, the $\lambda6300.31$ Å feature is well separated from the ScII line at $\lambda6300.69$ Å but contaminated by the very close Ni transition at $\lambda6300.34$ Å. In order to measure the correct oxygen abundance we used spectrum synthesis convolved with a Gaussian instrumental profile.

To model the Ni line we used the measured abundance (see Sect. 4.7.1), while to model the various CN lines we needed to assume C and N abundances ([C/Fe]=–0.5 dex and [N/Fe]=+0.5 dex) since not directly measurable. However, it must be noted that the assumed C and N abundances in the typical range shown by RGB stars (e.g. –1<[C/Fe]<0.0 and 0.0<[N/Fe]<+1) have only a marginal impact on the derived O abundance. For the other α-elements we cross-checked the results derived by the EW measurements, by performing a synthetic spectrum fitting for some *test* lines. This sanity check confirms the reliability of the derived abundances for these elements. Furthermore, the spectral region between $\lambda6155$ and $\lambda6167$ Å (used to test the Ca abundances) includes the Ca line at $\lambda6162.17$ Å with strong damping wings, that are very sensitive to the electronic pressure and to the gravity but not sensitive to T_{eff}, v_t and non-LTE effects (see discussion in Mishenina et al., 2006). We are able to well-reproduce the wings shape of this line, confirming the reliability of the adopted gravities.

All 4 clusters show mildly subsolar [O/Fe] ratios (–0.04 — –0.11 dex), with star-to-star scatter less than 0.10 dex. For NGC 1978 Hill et al. (2000) measured [O/Fe]= 0.37 dex with a star-to-star scatter of 0.10 dex, clearly in disagreement with our determination ([O/Fe]=–0.11 dex), but this discrepancy can be again manly ascribed to the different iron content.

For the other elements, the [α/Fe] turns out to be roughly solar, with a mild enhancement of

[Mg/Fe] (~0.10-0.19 dex) and [Ti/Fe] in NGC 2173 (0.15 dex).

4.7.4   s and r-process elements

Several s-process elements, namely the light Y and Zr and the heavy Ba, La, Ce and Nd have been measured, together with Eu, a r-process element.

The Ba abundance was derived by measuring the EWs of three lines. The inclusion of the HFS has a negligible ($\leq$0.5%) effect on the derived Ba abundance, in agreement with Norris, Ryan & Beers (1997) findings for the λ6496.91 $\overset{\circ}{A}$ line. This was also verified by mean of spectrum synthesis simulations of the three lines, using both the single component line and the separated HFS components taken from the linelist by Prochaska (2000). Ce has an even atomic number *Z=58* and all of the isotopes have even neutron number *N*, hence there is no HFS. However, an isotopic splitting is possible but we did not consider it since the calculations of Aoki et al. (2001) show that it has a negligible impact on the derived abundance. The Nd line HFS can be neglected, because the only isotopes (the odd ^{143}Nd and ^{145}Nd) that show it account for ~20% (Den Hartog et al., 2003) of the total abundance, only. Finally, both the La II line at λ 6390.46 $\overset{\circ}{A}$ and the Eu II line at λ6645.1 $\overset{\circ}{A}$ have EWs small enough ($\leq$70 m$\overset{\circ}{A}$) to ignore the HFS. In order to check the possible impact of the HFS effects on the Eu abundances, we tested our abundances with the spectrum synthesis (by using the HFS parameters for this line by Lawler et al., 2001). We find a negligible difference between the two determinations, in agreement with the results by Gratton et al. (2006) and Carretta et al. (2007) for the Galactic GCs NGC 6441 and NGC 6338, respectively (whose metallicity is very similar to the mean metal abundance of the present sample).

In all the target clusters [Y/Fe] and [Zr/Fe] ratios result significantly depleted ($\leq$–0.30 dex) with respect to the solar value. Heavy-s elements show enhanced (~0.20-0.45 dex) [Ba/Fe], [La/Fe] and [Nd/Fe] ratios but [Ce/Fe] which turns out to be solar. Finally, all the clusters display an enhanced (>0.30 dex) [Eu/Fe] abundance ratio.

4.8   About the iron content of NGC 1978

This intermediate-age cluster is very massive ($\sim 2 \cdot 10^5 M_\odot$, Westerlund, 1997) and located in an high density stellar region, about 3.5° north of the bar field. It also shows a peculiar, very high ellipticity ($\epsilon = 0.3$, Geisler & Hodge, 1980; Fischer, Welch & Mateo, 1992). The multicolor BVRI photometry by Alcaino et al. (1999) has shown a broad RGB, consistent with a metallicity spread of [Fe/H]~0.2 dex. On the basis of this evidence, the authors suggested the possible existence of
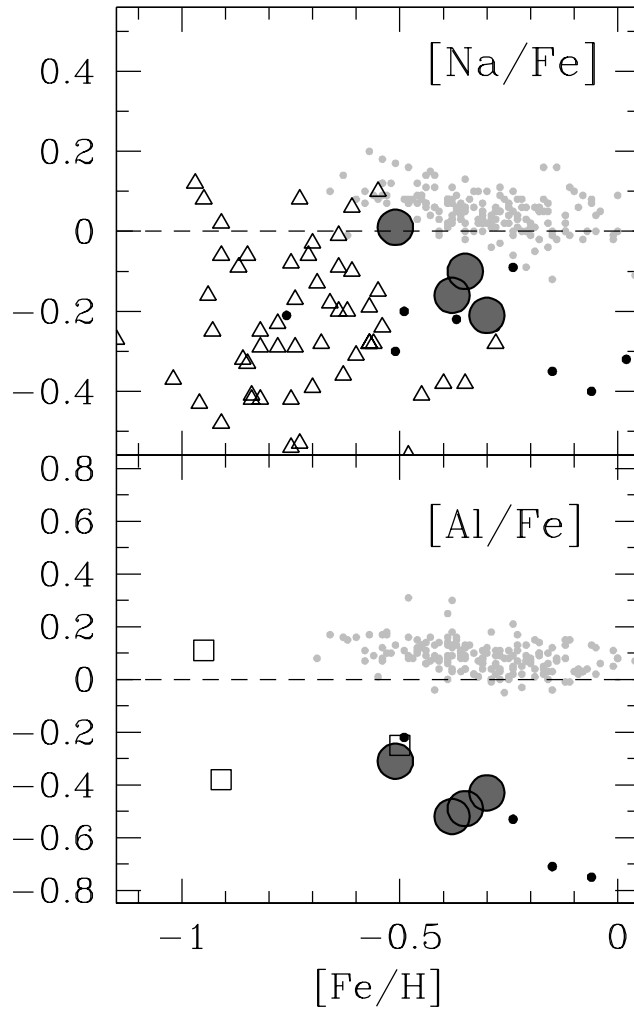
Figure 4.5: The trend of [Na/Fe] and [Al/Fe] as a function of [Fe/H] (upper and lower panel respectively) for the 4 analyzed LMC clusters (big grey points). For comparison, previous determinations of these abundance ratios in the LMC field (empty triangles from Pompeia et al. (2006)), other LMC clusters (empty squares from Hill et al. (2000)), the Galactic thin disk (little grey points from Reddy et al. (2003)) and Sgr (little black points from Bonifacio et al. (2000), Monaco et al. (2005), Monaco et al. (2007) and Sbordone et al. (2007)) are also plotted.
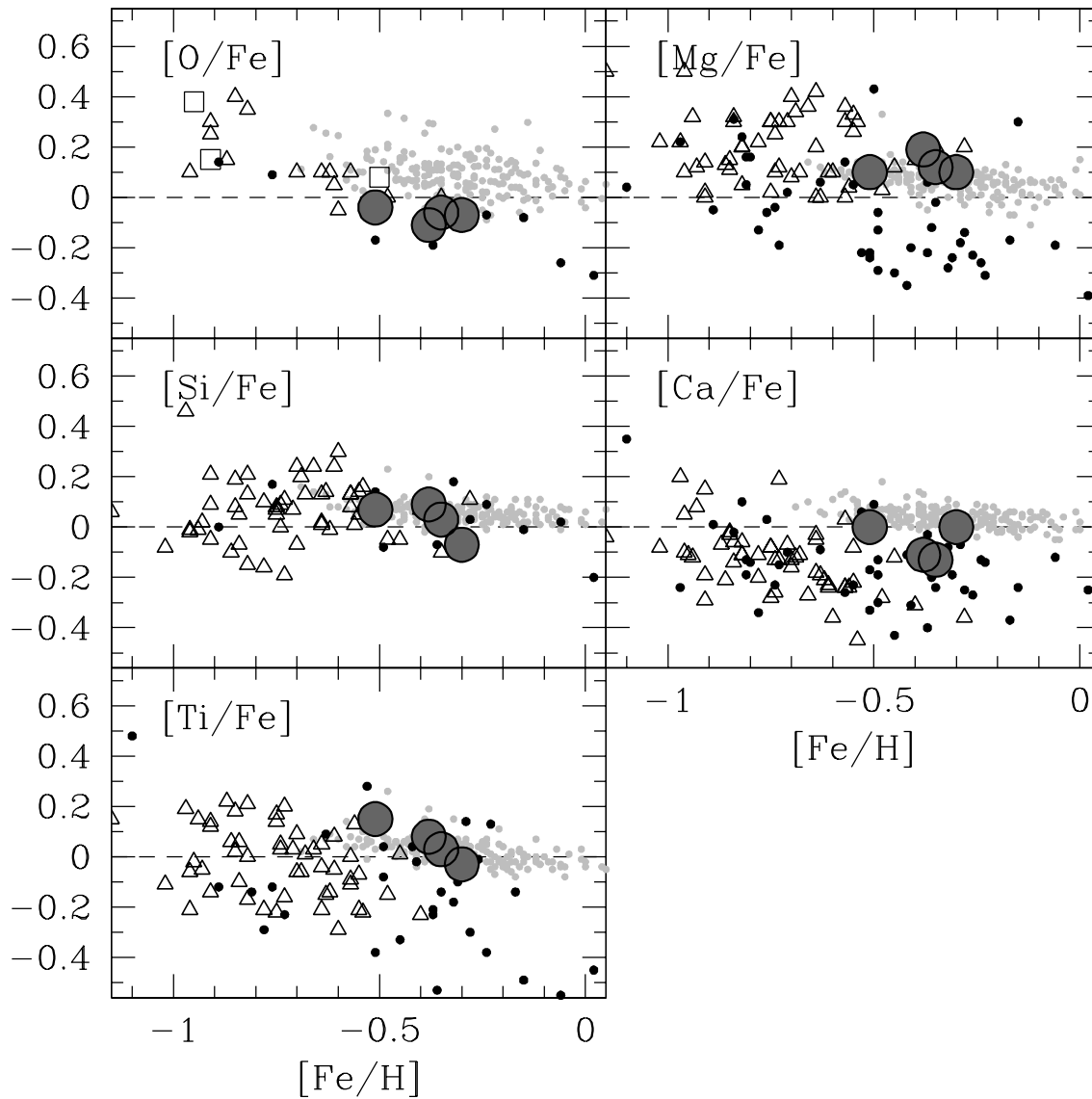
Figure 4.6: The trend of α-elements ([O, Mg, Si, Ca, Ti/Fe]) as a function of [Fe/H] for the 4 analyzed LMC clusters (same symbols and references of Fig. 4).
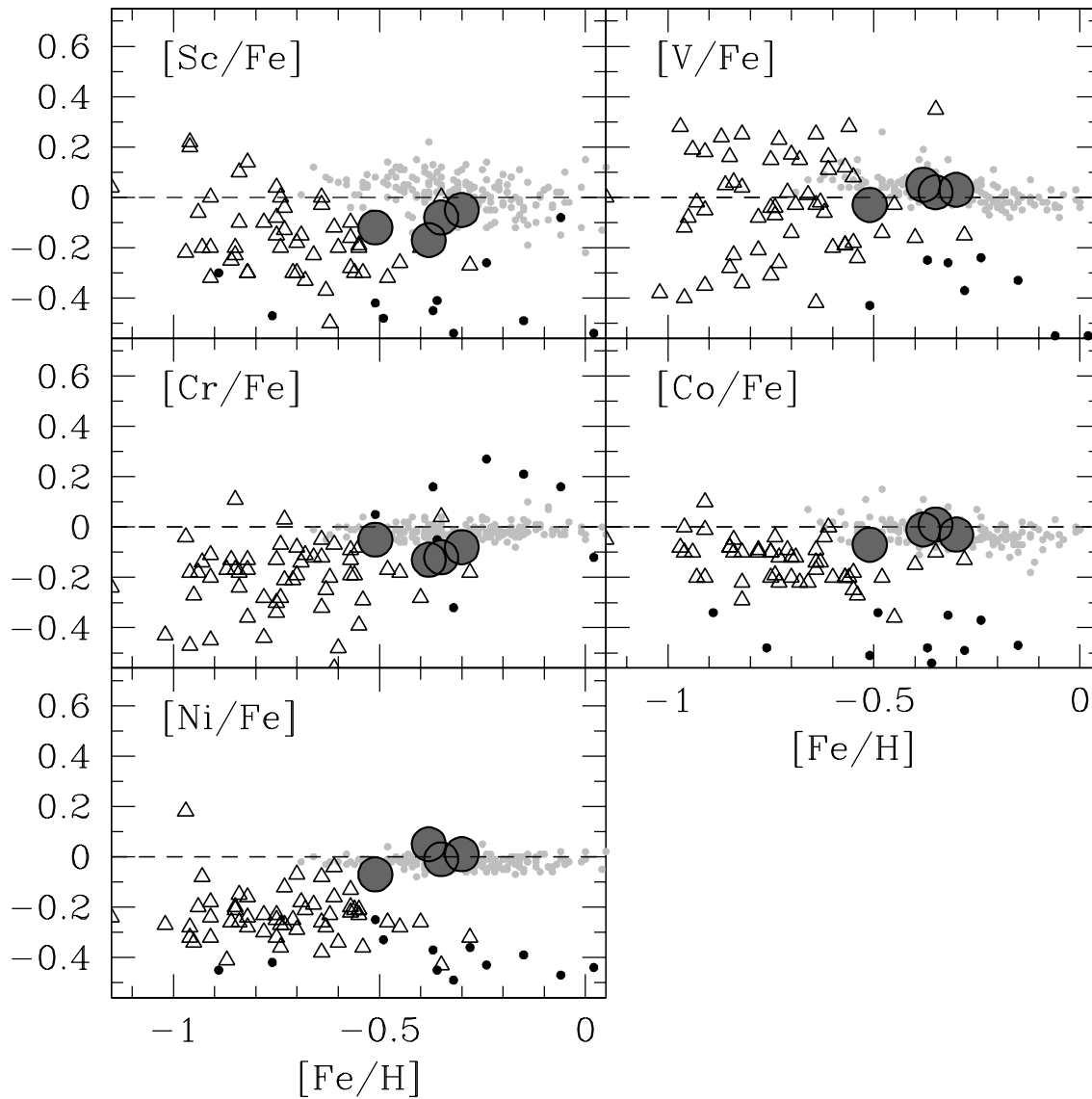
Figure 4.7: The trend of iron-peak elements ([Sc, V, Cr, Co, Ni/Fe]) as a function of [Fe/H] (same symbols and references of Fig. 4.5).
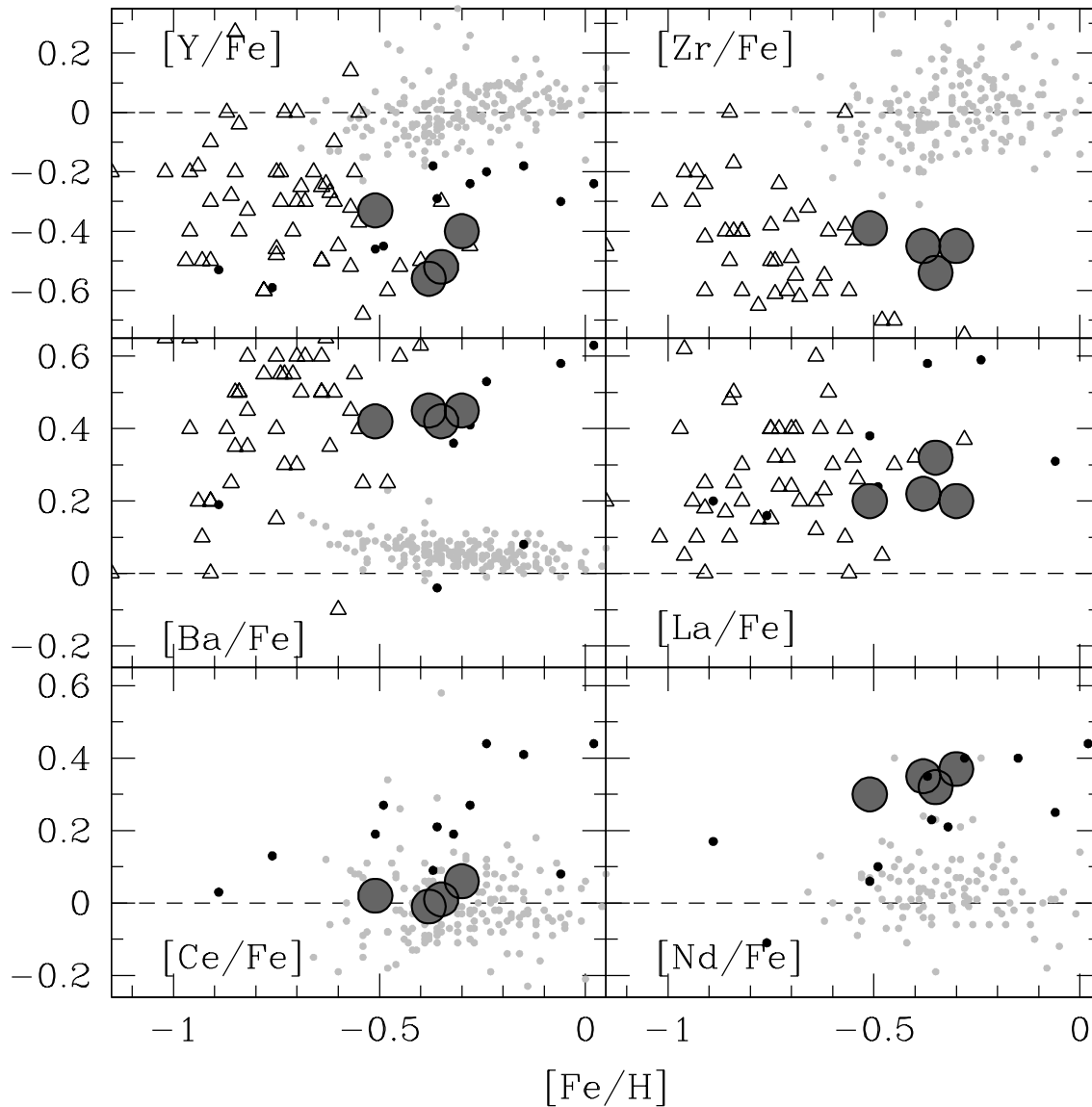
Figure 4.8: The trend of light ([Y,Zr/Fe]) and heavy ([Ba, La, Ce, Nd/Fe]) s-process elements as a function of [Fe/H] (same symbols and references of Fig. 4.5).
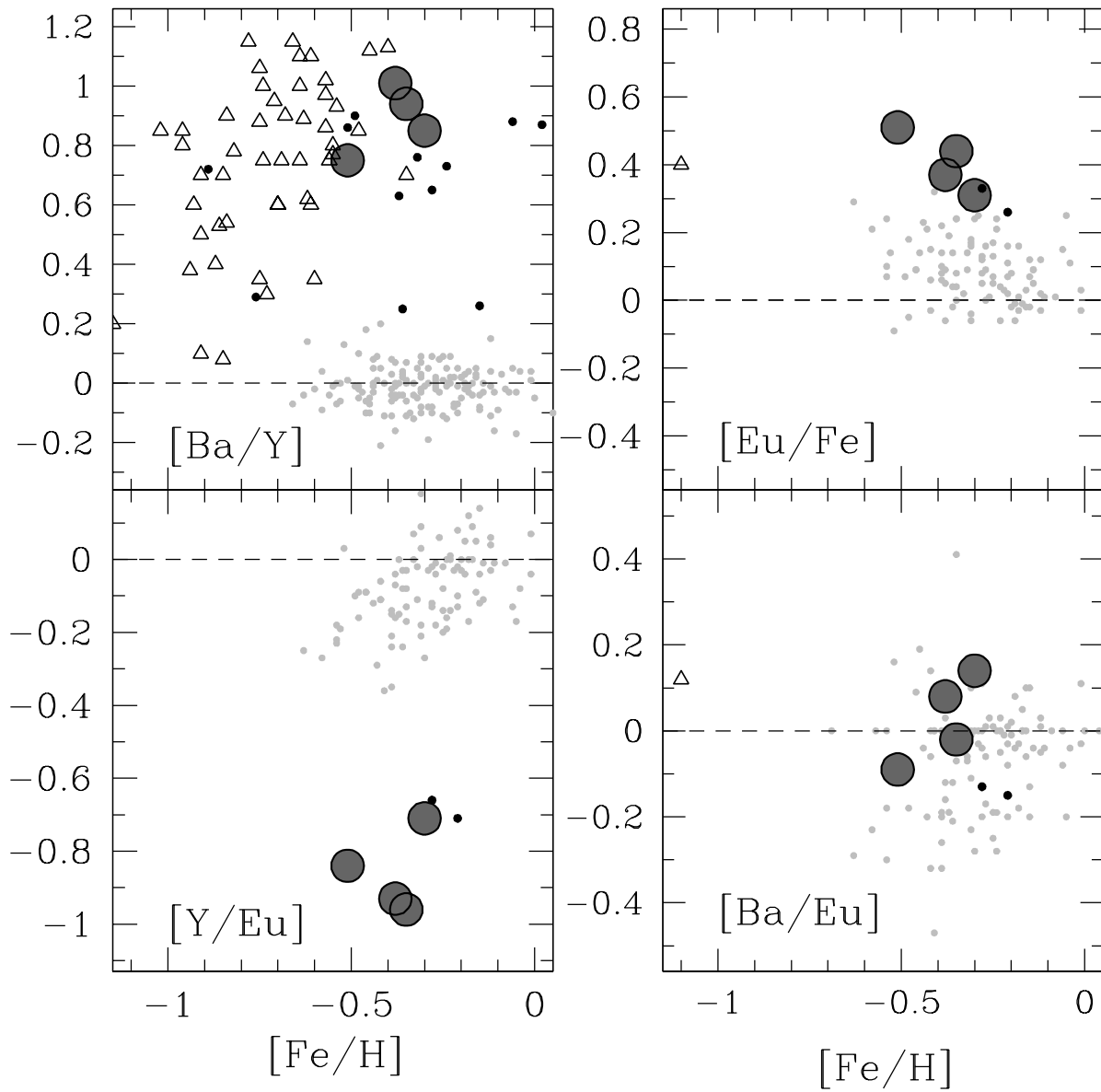
Figure 4.9: The trend of [Ba/Y], [Eu/Fe], [Y/Eu] and [Ba/Eu] as a function of [Fe/H] (same symbols and references of Fig. 4.5).

Star ID	T_{eff}	logg	[A/H]	v_t	n	[Fe/H]I	rms	n	[Fe/H]II	rms
	(K)	(dex)	(dex)	(km/s)		(dex)	(dex)		(dex)	(dex)
1651-6	3780	0.76	-0.25	1.48	79	-0.27	0.19	—	—	—
1651-8	3810	0.81	-0.40	1.52	81	-0.41	0.20	2	-0.18	0.01
1651-10	3890	0.92	-0.32	1.55	69	-0.32	0.19	2	-0.22	0.16
1651-12	4035	1.07	-0.31	1.70	89	-0.31	0.19	2	-0.20	0.10
1651-16	4010	1.20	-0.20	1.49	74	-0.21	0.15	2	-0.15	0.15
1783-22	3730	0.80	-0.27	1.35	79	-0.26	0.19	3	-0.35	0.05
1783-23	3810	0.85	-0.35	1.38	86	-0.34	0.17	—	—	—
1783-29	3870	0.91	-0.37	1.32	101	-0.38	0.20	2	-0.25	0.13
1783-30	3850	0.92	-0.36	1.37	79	-0.36	0.20	1	-0.27	—
1783-32	3800	0.92	-0.30	1.22	95	-0.31	0.19	3	-0.33	0.11
1783-33	3800	0.93	-0.41	1.32	75	-0.44	0.13	1	-0.40	—
1978-21	3790	0.64	-0.43	1.54	74	-0.43	0.16	—	—	—
1978-22	3700	0.55	-0.37	1.50	78	-0.39	0.17	7	-0.27	0.19
1978-23	3630	0.57	-0.24	1.35	70	-0.25	0.21	—	—	—
1978-24	3750	0.62	-0.30	1.40	59	-0.30	0.17	1	-0.17	—
1978-26	3820	0.71	-0.43	1.53	83	-0.42	0.17	1	-0.28	—
1978-28	3740	0.69	-0.33	1.28	85	-0.33	0.18	2	-0.17	0.01
1978-29	3750	0.71	-0.44	1.58	89	-0.44	0.21	4	-0.30	0.06
1978-32	3700	0.73	-0.40	1.39	84	-0.41	0.19	2	-0.30	0.18
1978-34	3900	0.83	-0.32	1.49	84	-0.32	0.20	—	—	—
1978-38	3840	0.81	-0.43	1.59	72	-0.44	0.14	2	-0.37	0.11
1978-42	3880	0.86	-0.43	1.55	92	-0.43	0.18	2	-0.26	0.17
2173-4	3850	0.51	-0.49	1.75	97	-0.50	0.18	9	-0.49	0.11
2173-5	3780	0.52	-0.47	1.73	101	-0.47	0.22	3	-0.37	0.13
2173-6	3680	0.62	-0.57	1.65	77	-0.57	0.21	—	—	—
2173-8	4060	0.83	-0.57	1.72	106	-0.58	0.14	17	-0.44	0.16
2173-10	3880	0.91	-0.42	1.65	97	-0.41	0.18	2	-0.35	0.12

Table 4.3: Adopted atmospheric parameters and inferred neutral and ionized iron abundances. Adopted reference solar abundances are log n(Fe I)=7.54 and log n(Fe II)=7.49.

Star ID	n	[O/Fe] (dex)	rms (dex)	n	[Na/Fe] (dex)	rms (dex)	n	[Mg/Fe] (dex)	rms (dex)	n	[Al/Fe] (dex)	rms (dex)
$\log N_\odot$		8.79			6.21			7.43			6.23	
1651-6	2	-0.12	0.05	4	-0.14	0.12	3	+0.16	0.13	2	-0.42	0.08
1651-8	2	-0.07	0.08	4	-0.41	0.07	2	+0.18	0.11	2	-0.69	0.13
1651-10	2	-0.05	0.06	4	-0.16	0.05	2	+0.16	0.07	2	-0.18	0.07
1651-12	2	-0.05	0.06	4	-0.03	0.10	3	+0.12	0.14	2	-0.28	0.06
1651-16	2	-0.10	0.08	4	-0.31	0.12	3	+0.10	0.16	2	-0.59	0.02
1783-22	2	-0.04	0.06	4	-0.13	0.13	3	+0.09	0.05	2	-0.45	0.12
1783-23	2	-0.12	0.11	4	-0.12	0.09	3	+0.12	0.05	2	-0.43	0.07
1783-29	2	0.00	0.04	4	-0.21	0.13	4	+0.09	0.09	2	-0.45	0.06
1783-30	2	-0.12	0.07	4	-0.20	0.13	4	+0.19	0.15	2	-0.36	0.08
1783-32	2	-0.04	0.10	4	+0.03	0.08	3	+0.09	0.08	2	-0.73	0.07
1783-33	2	+0.01	0.09	4	+0.00	0.11	4	+0.17	0.14	2	-0.55	0.09
1978-21	2	-0.03	0.06	4	-0.35	0.07	4	+0.17	0.16	2	-0.53	0.08
1978-22	2	-0.20	0.08	4	-0.05	0.13	4	+0.12	0.12	2	-0.50	0.01
1978-23	2	-0.15	0.07	4	+0.10	0.11	4	+0.21	0.09	2	-0.55	0.18
1978-24	2	-0.14	0.11	4	-0.24	0.14	4	+0.19	0.15	2	-0.41	0.11
1978-26	2	+0.02	0.08	4	-0.25	0.11	4	+0.23	0.07	2	-0.61	0.02
1978-28	2	-0.05	0.05	4	-0.06	0.15	4	+0.22	0.12	2	-0.55	0.02
1978-29	2	-0.06	0.08	4	-0.09	0.09	4	+0.22	0.10	2	-0.57	0.05
1978-32	2	-0.08	0.07	4	-0.19	0.09	4	+0.19	0.07	2	-0.39	0.08
1978-34	1	0.02	—	3	-0.36	0.09	3	+0.19	0.11	2	-0.56	0.05
1978-38	2	-0.02	0.08	4	-0.24	0.13	4	+0.20	0.10	2	-0.54	0.08
1978-42	2	-0.10	0.10	4	-0.21	0.11	4	+0.11	0.15	2	-0.55	0.02
2173-4	2	-0.04	0.12	4	+0.27	0.11	4	+0.15	0.08	2	-0.32	0.03
2173-5	2	-0.11	0.10	4	+0.04	0.09	4	+0.07	0.13	2	-0.35	0.07
2173-6	2	-0.07	0.07	4	-0.29	0.09	3	+0.09	0.05	2	-0.40	0.01
2173-8	2	-0.08	0.07	4	+0.18	0.12	4	+0.15	0.08	2	-0.14	0.09
2173-10	2	-0.05	0.08	4	-0.23	0.11	4	+0.04	0.16	2	-0.36	0.07

Table 4.4: Chemical abundances, number of measured lines and line-to-line scatter for O, Na, Mg and Al. Oxygen abundances are derived from spectral synthesis. Sodium abundances are corrected for departures from LTE.

Star ID	n	[Si/Fe] (dex)	rms (dex)	n	[Ca/Fe] (dex)	rms (dex)	n	[Sc/Fe]II (dex)	rms (dex)	n	[Ti/Fe] (dex)	rms (dex)
log $N_\odot$		7.53			6.27			3.13			5.00	
1651-6	4	-0.12	0.10	12	+0.04	0.16	5	-0.06	0.12	15	+0.11	0.14
1651-8	3	+0.00	0.04	12	+0.00	0.17	5	-0.11	0.10	13	+0.11	0.13
1651-10	3	-0.01	0.10	12	-0.02	0.14	5	+0.03	0.15	11	+0.09	0.13
1651-12	4	-0.12	0.10	11	+0.03	0.16	4	-0.09	0.09	9	+0.04	0.06
1651-16	3	-0.12	0.07	11	-0.07	0.13	4	+0.00	0.15	18	+0.15	0.15
1783-22	2	+0.04	0.04	13	-0.09	0.13	5	-0.06	0.16	14	+0.06	0.16
1783-23	4	+0.10	0.07	13	-0.13	0.12	5	-0.16	0.14	12	-0.06	0.07
1783-29	3	-0.06	0.04	12	-0.07	0.13	5	-0.04	0.16	13	+0.13	0.09
1783-30	3	-0.04	0.06	12	-0.17	0.14	3	-0.16	0.06	13	+0.03	0.15
1783-32	3	+0.05	0.08	13	-0.17	0.09	5	-0.01	0.10	16	+0.00	0.14
1783-33	4	+0.07	0.12	12	-0.15	0.09	4	-0.10	0.08	12	+0.01	0.14
1978-21	3	+0.06	0.11	13	-0.14	0.13	5	-0.18	0.11	15	+0.18	0.13
1978-22	3	+0.10	0.02	14	-0.12	0.18	4	-0.15	0.06	13	-0.02	0.09
1978-23	4	+0.14	0.07	14	-0.10	0.15	4	-0.26	0.06	14	+0.11	0.17
1978-24	4	+0.10	0.02	12	-0.13	0.17	4	-0.06	0.13	12	+0.08	0.15
1978-26	4	+0.05	0.12	9	-0.17	0.07	5	-0.18	0.15	15	+0.16	0.15
1978-28	3	+0.11	0.09	12	-0.11	0.15	5	-0.14	0.15	13	+0.07	0.12
1978-29	4	+0.14	0.08	11	-0.10	0.17	5	+0.01	0.12	15	+0.04	0.17
1978-32	3	+0.17	0.06	13	-0.11	0.14	3	-0.23	0.08	13	-0.09	0.15
1978-34	3	+0.05	0.03	12	-0.08	0.17	4	-0.15	0.08	13	+0.08	0.12
1978-38	3	+0.08	0.09	14	-0.08	0.16	5	-0.09	0.14	16	+0.00	0.19
1978-42	4	+0.04	0.07	8	-0.18	0.08	5	-0.31	0.11	17	+0.06	0.18
2173-4	4	+0.07	0.10	11	+0.00	0.16	4	-0.11	0.10	10	+0.18	0.15
2173-5	4	+0.04	0.04	12	-0.01	0.14	5	-0.19	0.13	14	+0.19	0.16
2173-6	3	+0.13	0.11	11	+0.02	0.14	4	-0.14	0.09	17	+0.15	0.15
2173-8	4	+0.05	0.07	13	+0.00	0.16	5	-0.15	0.09	19	+0.12	0.09
2173-10	4	+0.07	0.10	12	-0.09	0.16	4	+0.00	0.08	13	+0.09	0.06

Table 4.5: Chemical abundances, number of measured lines and line-to-line scatter for Si, Ca, Sc and Ti. Scandium abundances include HFS corrections.

Star ID	n	[V/Fe] (dex)	rms (dex)	n	[Cr/Fe] (dex)	rms (dex)	n	[Co/Fe] (dex)	rms (dex)	n	[Ni/Fe] (dex)	rms (dex)
$\log N_\odot$		3.97			5.67			4.92			6.28	
1651-6	8	+0.09	0.08	10	-0.14	0.15	2	-0.02	0.06	23	+0.00	0.16
1651-8	8	+0.08	0.13	13	0.00	0.14	2	-0.02	0.05	24	-0.04	0.13
1651-10	6	+0.05	0.06	12	-0.16	0.10	3	-0.01	0.11	23	+0.07	0.16
1651-12	8	-0.05	0.08	12	-0.04	0.16	3	-0.06	0.02	27	-0.02	0.16
1651-16	9	-0.03	0.12	15	-0.08	0.15	2	-0.03	0.14	30	+0.06	0.13
1783-22	7	+0.14	0.11	13	-0.16	0.15	2	+0.07	0.04	24	+0.00	0.15
1783-23	7	-0.13	0.15	14	-0.21	0.15	3	-0.05	0.05	26	-0.01	0.16
1783-29	7	+0.13	0.14	13	-0.05	0.16	3	+0.05	0.09	25	+0.00	0.12
1783-30	5	-0.04	0.12	16	-0.19	0.15	3	+0.00	0.06	25	-0.05	0.16
1783-32	7	+0.05	0.15	14	-0.07	0.15	3	-0.09	0.08	25	-0.01	0.15
1783-33	7	-0.01	0.15	14	-0.05	0.16	3	+0.05	0.10	28	+0.02	0.16
1978-21	9	+0.03	0.16	15	-0.12	0.16	3	-0.12	0.15	23	+0.02	0.14
1978-22	6	-0.09	0.13	14	-0.17	0.15	3	-0.10	0.15	26	+0.08	0.15
1978-23	5	+0.16	0.07	13	-0.03	0.17	3	-0.13	0.12	26	+0.11	0.15
1978-24	6	+0.18	0.13	14	-0.13	0.16	2	+0.09	0.05	25	+0.13	0.15
1978-26	6	+0.22	0.16	14	-0.12	0.16	3	-0.11	0.11	25	+0.10	0.16
1978-28	5	+0.15	0.08	9	-0.01	0.15	3	+0.04	0.13	27	+0.01	0.16
1978-29	6	+0.05	0.10	14	-0.10	0.15	3	+0.00	0.06	23	+0.04	0.10
1978-32	5	+0.13	0.12	13	-0.14	0.16	3	+0.09	0.13	24	+0.02	0.14
1978-34	6	+0.00	0.17	12	-0.20	0.15	2	+0.00	0.05	20	+0.11	0.16
1978-38	7	-0.14	0.05	13	-0.16	0.12	3	+0.11	0.15	31	-0.05	0.15
1978-42	7	-0.02	0.17	11	-0.17	0.16	3	+0.03	0.15	31	-0.02	0.12
2173-4	7	+0.04	0.09	18	-0.08	0.16	3	-0.11	0.13	30	-0.15	0.16
2173-5	7	+0.09	0.10	12	+0.03	0.12	3	+0.03	0.10	27	-0.05	0.1
2173-6	8	-0.03	0.13	11	-0.05	0.17	3	+0.01	0.13	16	-0.07	0.13
2173-8	11	-0.11	0.16	17	-0.11	0.14	3	-0.10	0.14	35	-0.04	0.13
2173-10	8	-0.13	0.07	12	-0.06	0.14	4	-0.20	0.15	32	-0.05	0.15

Table 4.6: Chemical abundances, number of measured lines and line-to-line scatter for V, Cr, Co and Ni. Vanadium and Cobalt abundances include HFS corrections.

Star ID	n	[Y/Fe]II (dex)	rms (dex)	n	[Zr/Fe] (dex)	rms (dex)	n	[Ba/Fe]II (dex)	rms (dex)	n	[La/Fe] II (dex)	rms (dex)
$\log N_\odot$		2.22			2.60			2.22			1.22	
1651-6	3	-0.39	0.02	3	-0.53	0.08	3	+0.44	0.11	1	+0.19	—
1651-8	2	-0.27	0.16	3	-0.41	0.13	3	+0.49	0.08	1	+0.34	—
1651-10	3	-0.51	0.11	2	-0.49	0.01	3	+0.49	0.09	1	+0.26	—
1651-12	2	-0.32	0.08	2	-0.41	0.07	3	+0.38	0.01	1	+0.12	—
1651-16	2	-0.50	0.12	1	-0.39	—	3	+0.44	0.04	1	+0.11	—
1783-22	2	-0.64	0.03	3	-0.38	0.11	3	+0.43	0.09	1	+0.34	—
1783-23	2	-0.40	0.09	3	-0.57	0.07	3	+0.44	0.10	1	+0.28	—
1783-29	2	-0.48	0.01	3	-0.57	0.07	3	+0.44	0.09	1	+0.35	—
1783-30	3	-0.58	0.14	2	-0.39	0.02	2	+0.40	0.12	1	+0.25	—
1783-32	2	-0.59	0.02	3	-0.67	0.06	2	+0.44	0.13	1	+0.37	—
1783-33	3	-0.43	0.13	2	-0.64	0.04	3	+0.37	0.08	1	+0.31	—
1978-21	2	-0.42	0.06	3	-0.29	0.10	3	+0.48	0.11	1	+0.31	—
1978-22	3	-0.42	0.08	3	-0.44	0.07	3	+0.37	0.11	1	+0.10	—
1978-23	1	-0.54	—	2	-0.26	0.07	3	+0.49	0.09	1	+0.20	—
1978-24	2	-0.41	0.05	2	-0.52	0.06	3	+0.47	0.10	1	+0.09	—
1978-26	2	-0.70	0.11	3	-0.52	0.12	2	+0.37	0.04	1	+0.30	—
1978-28	2	-0.57	0.04	3	-0.32	0.13	3	+0.52	0.10	1	+0.28	—
1978-29	2	-0.68	0.06	3	-0.56	0.13	3	+0.34	0.13	1	+0.19	—
1978-32	2	-0.50	0.02	2	-0.65	0.01	3	+0.38	0.03	1	+0.22	—
1978-34	2	-0.65	0.11	3	-0.38	0.14	3	+0.50	0.13	1	+0.21	—
1978-38	3	-0.46	0.12	3	-0.48	0.05	3	+0.57	0.09	—	—	—
1978-42	1	-0.55	—	3	-0.55	0.08	3	+0.41	0.11	1	+0.26	—
2173-4	2	-0.34	0.16	3	-0.37	0.04	3	+0.44	0.08	1	+0.17	—
2173-5	2	-0.35	0.05	4	-0.30	0.05	3	+0.36	0.11	1	+0.16	—
2173-6	2	-0.35	0.13	3	-0.35	0.07	3	+0.40	0.08	1	+0.29	—
2173-8	3	-0.36	0.18	3	-0.49	0.11	3	+0.47	0.09	1	+0.19	—
2173-10	3	-0.21	0.14	2	-0.44	0.04	3	+0.42	0.03	1	+0.18	—

Table 4.7: Chemical abundances, number of measured lines and line-to-line scatter for Y, Zr, Ba and La.

Star ID	n	[Ce/Fe]II (dex)	rms (dex)	n	[Nd/Fe]II (dex)	rms (dex)	n	[Eu/Fe]II (dex)	rms (dex)
$\log N_\odot$		1.55			1.50			0.51	
1651-6	1	-0.03	—	2	+0.41	0.15	1	+0.32	—
1651-8	1	+0.03	—	2	+0.52	0.08	1	+0.18	—
1651-10	1	+0.16	—	2	+0.30	0.06	1	+0.32	—
1651-12	1	+0.08	—	3	+0.40	0.03	1	+0.42	—
1651-16	—	—	—	2	+0.22	0.07	—	—	—
1783-22	1	+0.08	—	2	+0.29	0.01	1	+0.44	—
1783-23	1	+0.00	—	3	+0.22	0.07	1	+0.75	—
1783-29	—	—	—	3	+0.30	0.13	1	+0.52	—
1783-30	1	+0.10	—	2	+0.40	0.12	1	+0.26	—
1783-32	1	-0.13	—	1	+0.21	—	—	—	—
1783-33	1	-0.08	—	2	+0.49	0.05	1	+0.23	—
1978-21	1	-0.08	—	3	+0.56	0.08	1	+0.26	—
1978-22	1	+0.05	—	3	+0.44	0.13	1	+0.70	—
1978-23	1	-0.02	—	3	+0.39	0.15	1	+0.48	—
1978-24	—	—	—	4	+0.41	0.07	—	—	—
1978-26	1	-0.06	—	3	+0.36	0.07	1	+0.26	—
1978-28	1	+0.10	—	2	+0.31	0.10	1	+0.23	—
1978-29	1	-0.13	—	3	+0.32	0.14	1	+0.49	—
1978-32	1	+0.03	—	3	+0.33	0.12	1	+0.43	—
1978-34	—	—	—	1	+0.22	—	—	—	—
1978-38	1	+0.03	—	2	+0.16	0.02	1	+0.12	—
1978-42	1	-0.02	—	2	+0.35	0.08	—	—	—
2173-4	1	-0.02	—	2	+0.31	0.06	1	+0.37	—
2173-5	1	+0.07	—	3	+0.42	0.09	1	+0.37	—
2173-6	1	+0.00	—	2	+0.21	0.07	1	+0.94	—
2173-8	1	-0.01	—	2	+0.36	0.02	1	+0.64	—
2173-10	1	+0.05	—	2	+0.20	0.05	1	+0.26	—

Table 4.8: Chemical abundances, number of measured lines and line-to-line scatter for Ce, Nd and Eu.

Ratio	N_{star}	NGC 1651 Mean	σ_{obs}	σ_{exp}	N_{star}	NGC 1783 Mean	σ_{obs}	σ_{exp}
$[O/Fe]$	5	-0.07	0.04	0.14	6	-0.06	0.08	0.14
$[Na/Fe]$	5	-0.21	0.15	0.11	6	-0.10	0.10	0.11
$[Mg/Fe]$	5	+0.10	0.04	0.11	6	+0.12	0.04	0.10
$[Al/Fe]$	5	-0.43	0.21	0.14	6	-0.49	0.13	0.14
$[Si/Fe]$	5	-0.07	0.06	0.13	6	+0.03	0.06	0.12
$[Ca/Fe]$	5	+0.00	0.04	0.13	6	-0.13	0.04	0.12
$[Sc/Fe]$II	5	-0.05	0.06	0.15	6	-0.08	0.06	0.14
$[Ti/Fe]$	5	-0.03	0.02	0.16	6	+0.03	0.06	0.14
$[V/Fe]$	5	+0.03	0.06	0.18	6	+0.02	0.10	0.15
$[Cr/Fe]$	5	-0.08	0.07	0.12	6	-0.12	0.07	0.12
$[Fe/H]$	5	-0.30	0.07	0.10	6	-0.35	0.06	0.07
$[Fe/H]$II	5	-0.19	0.03	0.21	6	-0.29	0.06	0.19
$[Co/Fe]$	5	-0.03	0.02	0.17	6	+0.01	0.06	0.12
$[Ni/Fe]$	5	+0.01	0.05	0.09	6	-0.01	0.02	0.07
$[Y/Fe]$II	5	-0.40	0.11	0.16	6	-0.52	0.10	0.14
$[Zr/Fe]$	5	-0.45	0.06	0.22	6	-0.54	0.13	0.16
$[Ba/Fe]$II	5	+0.45	0.04	0.13	6	+0.42	0.03	0.10
$[La/Fe]$II	5	+0.20	0.10	0.21	6	+0.32	0.04	0.20
$[Ce/Fe]$II	4	+0.06	0.08	0.21	4	+0.01	0.10	0.19
$[Nd/Fe]$II	5	+0.37	0.11	0.14	6	+0.32	0.11	0.16
$[Eu/Fe]$II	4	+0.31	0.10	0.21	5	+0.44	0.21	0.20

Table 4.9: Mean abundance ratios for NGC 1651 and NGC 1783.

		NGC 1978			NGC 2173			
Ratio	N_{star}	Mean	σ_{obs}	σ_{exp}	N_{star}	Mean	σ_{obs}	σ_{exp}
$[O/Fe]$	11	-0.11	0.08	0.14	5	-0.04	0.03	0.14
$[Na/Fe]$	11	-0.16	0.13	0.13	5	+0.01	0.25	0.11
$[Mg/Fe]$	11	+0.19	0.04	0.14	5	+0.10	0.05	0.10
$[Al/Fe]$	11	-0.52	0.07	0.14	5	-0.31	0.10	0.14
$[Si/Fe]$	11	+0.09	0.04	0.12	5	+0.07	0.03	0.12
$[Ca/Fe]$	11	-0.11	0.05	0.15	5	+0.00	0.06	0.13
$[Sc/Fe]$II	11	-0.17	0.09	0.15	5	-0.12	0.07	0.14
$[Ti/Fe]$	11	+0.08	0.07	0.16	5	+0.15	0.04	0.16
$[V/Fe]$	11	+0.05	0.13	0.18	5	-0.03	0.09	0.18
$[Cr/Fe]$	11	-0.13	0.04	0.11	5	-0.05	0.05	0.11
$[Fe/H]$	11	-0.38	0.07	0.10	5	-0.51	0.07	0.09
$[Fe/H]$II	11	-0.26	0.06	0.18	5	-0.37	0.06	0.15
$[Co/Fe]$	11	-0.01	0.09	0.14	5	-0.07	0.09	0.13
$[Ni/Fe]$	11	+0.05	0.06	0.09	5	-0.07	0.04	0.08
$[Y/Fe]$II	11	-0.54	0.11	0.14	5	-0.32	0.06	0.15
$[Zr/Fe]$	11	-0.45	0.12	0.18	5	-0.39	0.07	0.18
$[Ba/Fe]$II	11	+0.45	0.07	0.11	5	+0.42	0.04	0.11
$[La/Fe]$II	10	+0.22	0.08	0.20	5	+0.20	0.05	0.20
$[Ce/Fe]$II	9	-0.01	0.07	0.20	5	+0.02	0.04	0.21
$[Nd/Fe]$II	11	+0.35	0.11	0.18	5	+0.30	0.09	0.16
$[Eu/Fe]$II	8	+0.37	0.19	0.20	5	+0.51	0.27	0.21

Table 4.10: Mean abundance ratios for NGC 1978 and NGC 2173.

two different sub-populations as the result of a merging. This scenario was furtherly supported by Hill et al. (2000) who analyzed the high resolution spectra of two giant stars located in the south-east region of the cluster. They found [Fe/H]=–1.1 and –0.82 dex, with a significant star-to-star difference (Δ[Fe/H]$\approx$0.3 dex). However, the same stars were previously observed by Olszewski et al. (1991), who found [Fe/H]=–0.46 and –0.38, i.e. a much higher (by a factor of $\approx$3) metallicity and a much smaller (Δ[Fe/H]$\approx$0.08 dex) star-to-star difference.

Our average metallicity is in good agreement with the previous estimate by Olszewski et al. (1991), who obtained [Fe/H]=–0.42$\pm$0.04 dex, while both these estimates disagree with the significant lower abundance ([Fe/H]=–0.96$\pm$0.15 dex) found by Hill et al. (2000). Unfortunately we did not re-observed the two stars measured by Hill et al. (2000), hence no direct comparison can be done. However, the relatively large number of giants measured in this work and the accurate tests we perform on the abundance analysis suggested that our result is quite solid. It is also worth noticing that high metallicity estimate for this intermediate-age cluster is in agreement with the recent finding (see e.g. Cole, Smecker-Hane & Gallagher, 2000; Smith et al., 2002; Cole et al., 2005) that the metallicity distribution of intermediate-age LMC field stars shows a remarkable peak in the abundance distribution at [Fe/H]$\approx -0.4 \pm 0.2$ dex.

It is interesting to note that NGC 1978 is in the age range where different star formation (SF) models provide significantly different predictions in the AMR. For example, the predictions of the two models discussed by Pagel & Tautvaisiene (1998) (see their Fig. 4), show significant differences for clusters in the 2-10 Gyr age range. The two models are also discussed by Hill et al. (2000) and compared with some observations (see their Fig. 4a). Here we just note that the current age estimate for NGC 1978 ($\approx$3.5 Gyr, Girardi et al., 1995), and our metallicity determination, place the cluster in a position within the age-metallicity diagram more consistent with a smooth SF rather than with a bursting model. Of course no firm conclusion can be reached on the basis of only one cluster, however we strongly emphasize how only the combination of accurate metallicities and age determinations could significantly improve our knowledge in the star formation history of the LMC.

NGC 1978 is one of the most massive stellar cluster in the LMC and it has been suspected to harbor a chemically inhomogeneous stellar population. Note that both the most massive stellar systems in the halos of our Galaxy (ω Cen, $M \sim 3 \cdot 10^6 M_\odot$, Merritt, Meylan & Mayor , 1997) and M31 (G1, $M \sim 7 \cdot 10^6 M_\odot$, Meylan et al., 2001) show evidence of a metallicity spread and a complex star formation history (Ferraro et al., 2004b; Sollima al., 2005). Curiously, both
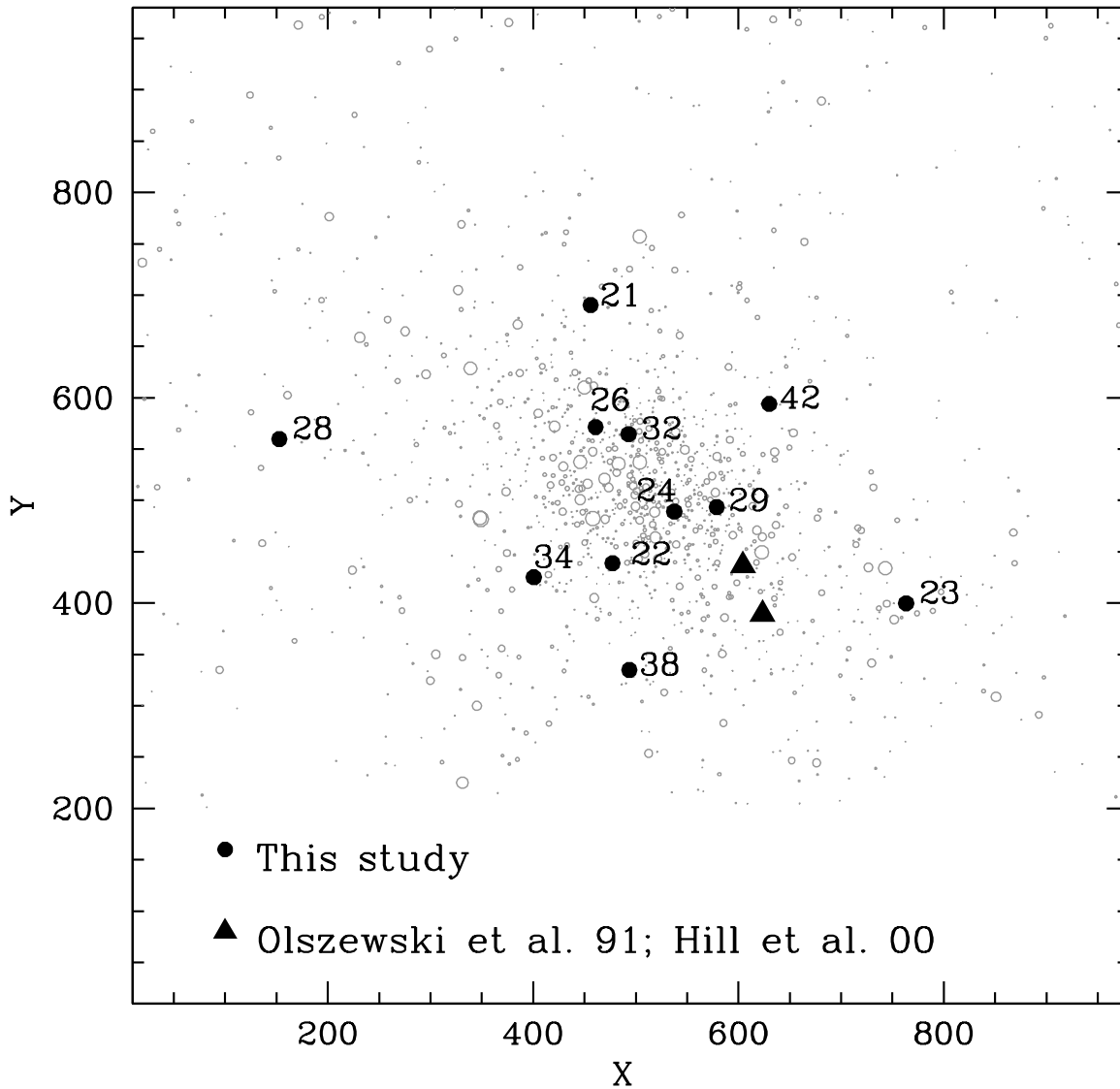
Figure 4.10: Location of the 11 program stars (black points) within the cluster area. X,Y coordinates are in pixels. The two filled triangles mark the position of the two stars measured by Olszewski et al. (1991); Hill et al. (2000).

these massive stellar systems show a relatively large ellipticity ($\epsilon \approx 0.2$), similar to NGC 1978. These properties have been interpreted as possible signatures of a merging event (note that several clusters in the MC appear to be binary (or show cluster-to-cluster interaction). Hence our findings deserve a few additional comments in the context of the cluster formation. The fact that our targets are well distributed within the entire cluster area (see Fig. 4.10) and that they show an high level of homogeneity in their iron abundance allows us to safely conclude that NGC 1978 does not show

any signature of metallicity spread. Also, the IR CMDs already discussed in Chapter 3 (see Fig. 3.6) do not confirm the presence of a significant spread along the RGB (contrary to the claim of Alcaino et al., 1999). Of course, our finding makes the merging hypothesis poorly convincing since it would require either that the two sub-units had similar metallicity or that the two gas clouds with different metallicities efficiently mixed at better than $\delta[Fe/H] = 0.07$ dex before star formation started. Both these occurrences are quite unlikely, hence we can safely conclude that there is not signature pointing at a merging event in the formation history of this cluster. Moreover, previous dynamical studies of this cluster (Fischer, Welch & Mateo, 1992) already found no evidence for merging. Finally, it is also worth noticing that ellipticity is a common feature of many LMC and Galactic clusters (see e.g. Goodwin, 1997) with no evidence of a metallicity spread. A few explanations for a large ellipticity, other than merging, can be advocated, the two most likely being either cluster rapid rotation and/or strong tidal interactions with the parent galaxy.

4.9   The global interpretation

All the 4 LMC globulars analyzed here, belonging to the same age population but located in different regions of the LMC disk, result to be *metal-rich*, with a mean metallicity of [Fe/H]=–0.38 dex (rms=0.09 dex). This finding confirms the previous low-resolution analysis based on the Ca II triplet by Olszewski et al. (1991) and Grocholski et al. (2006), that showed as the young and intermediate-age LMC clusters exhibit a very narrow metallicity distribution (Grocholski et al., 2006, estimated a mean metallicity of -0.48 dex with a rms=0.09 dex from 23 intermediate-age clusters). Our metallicities are also consistent with the mean metallicity of the LMC Bar ([Fe/H]=–0.37 dex) by Cole et al. (2005) and of the LMC disk ([Fe/H]∼-0.5 dex) by Carrera et al. (2007). The theoretical scenario for the formation of the LMC and its GCs drawn by Bekki et al. (2004) indicates as the efficient GC formation does not occur until the LMC and the SMC start to interact violently and closely (∼3 Gyr ago). Moreover, also the formation of the Bar is predicted to occur in the last ∼5 Gyr. The similar iron content between the LMC GC system and the LMC Bar seems to confirm this hypothesis.

Our chemical analysis also evidences an high degree of homogeneity for all the elements. Even the abundances of Na and Al show a low dispersion, at variance with Galactic GCs which show strong O-Na and Mg-Al anticorrelations (see e.g. Gratton, Sneden & Carretta, 2004, for an extensive review).

The depletion (by a factor of 2-3) of [Na/Fe] and [Al/Fe] abundance ratios with respect to

the solar and Galactic thin disk values, is consistent with the one observed in the LMC and Sgr fields. These two elements are likely connected to the SN II, because their main production sites are C and Ne burning (see Pagel, 1997; Matteucci, 2003), respectively. Another possible channel to produce Na and Al are the p-captures in the intermediate-mass AGB stars (NeNa and MgAl cycles). However, the high degree of homogeneity of their abundance in the LMC clusters and the lack of clear Na-O and Mg-Al anti-correlations seem to favor the SN II channel for their production. Also, since the Na and Al yields depend on the neutron excess and increase with metallicity (Pagel, 1997), under-abundant [Al/Fe] and [Na/Fe] ratios suggest that the gas from which the LMC clusters formed, should have been enriched by relatively low-metallicity SN II.

Also the α-elements are produced mainly by high-mass stars which end their short life exploding as SN II, but at variance with Na and Al, their production factors are poorly sensitive to metallicity. The [α/Fe] ratio represents a powerful diagnostics to clarify the relative role played by SN II (producers of α-elements) and SN Ia (main producers of Fe) in the chemical enrichment process. Indeed, there is time delay (Tinsley, 1979) between the explosion of SN II, occurring since the onset of the star formation event, and SN Ia, which happen later on (Greggio, 2005a). The roughly solar [α/Fe] abundance ratios measured in the LMC GCs well match those found in the LMC field and MW thin disk intermediate-age populations and are consistent with a standard scenario, where SN Ia had enough time to significantly enrich the gas with iron. Some depletion of [Mg/Fe], [Ca/Fe] and [Ti/Fe] is observed in the Sgr stars.

The bulk of the iron-peak elements are produced by the SN Ia, from stars with intermediate-mass progenitors and located in single-degenerate binary systems (Iwamoto et al., 1999), or from double-degenerate binary systems (Iben & Tutukov, 1984). Our derived abundances for these elements well trace iron, as do the LMC field and MW thin disk stars. We only note a mild discrepancy between our [Ni/Fe] solar ratio and the slightly underabundant ([Ni/Fe]$\sim$–0.2 dex) values by Pompeia et al. (2006), also observed in the Sgr stars that show a significant depletion (by a factor of 2-3) of iron-peak elements. It is interesting to note that the old LMC clusters analyzed by Johnson, Ivans & Stetson (2006) show a general depletion of the [iron-peak/Fe] ratios (in particular [V/Fe] and [Ni/Fe]): actually, an explanation for such a depletion for the iron-peak elements is still lacking.

The elements heavier than the iron-peak group are not built up from thermonuclear burning but via a sequences of neutron captures on seed Fe or Ni nuclei. If the time-scale of the neutron capture sequence is longer than the typical time-scale of the β-decay, the resulting elements are

106

called *slow* or s-process elements, while in case of fast neutron capture, the elements are called *rapid* or r-process elements. The s-process elements are mainly produced by low-mass ($\sim$1-4 $M_\odot$) AGB stars during the thermal instabilities developing above the quiescent He-burning shell (the so-called *main*-component), with a minor contribution by the high mass stars (the so-called *weak*-component) (see Busso, Gallino & Wasserburg, 1999; Travaglio et al., 2004). The bulk of these neutron captures are connected to the $^{13}C(\alpha,n)^{16}O$ and $^{22}Ne(\alpha,n)^{25}Mg$ reactions, which are major sources of neutrons.

The behaviour of the s-process elements in the LMC clusters appears to be *dichotomic*, with a deficiency of light s-elements (Y and Zr) and an enhancement of heavy ones (Ba, La and Nd), with the only exception of Ce, that shows a solar [Ce/Fe] abundance ratio. The [Ba/Y] abundance ratio represents a powerful diagnostic of the relative contribution of the heavy to the light s-process elements (see Venn et al., 2004). In our LMC clusters [Ba/Y] is enhanced by $\sim$0.9-1 dex (see Fig. 4.9): similar values have been observed also in the LMC field (Hill, Andrievsky & Spite, 1995; Pompeia et al., 2006) and in Sgr (Sbordone et al., 2007), but not in the MW, where the [Ba/Y] ratio is solar at most. The interpretation of these abundance patterns is complicated by the complexity (and uncertainty) of the involved nucleosynthesis. Theoretical models (Busso, Gallino & Wasserburg, 1999; Travaglio et al., 2004) indicate that the AGB yields could be metallicity-dependent. In particular, the heavy-s elements have their maximum production factor at lower metallicities than the light-s ones. Hence, an high [Ba/Y] ratio could suggest a major pollution of the gas by low-metallicity AGB stars. Moreover, abundance patterns for [Y/Fe] and [Ba/Fe] consistent with the Galactic values have been observed in the old LMC cluster by Johnson, Ivans & Stetson (2006). Being these objects the first ones formed in the LMC, these clusters have been not contaminated by the AGB stars, because the low-mass AGB stars had no time to evolve and incorporate completely their yields in the interstellar medium (differently to the intermediate-age clusters).

The [Eu/Fe] abundance ratio (see Fig. 4.9) measured in the LMC clusters and Sgr stars is enhanced by a factor of two with respect to the Galactic thin disk value. This is somewhat puzzling and inconsistent with the solar $< [\alpha/Fe] >$ measured in all the three environments. Indeed, Eu is a typical r-process element (Arlandini et al., 1999; Burris et al., 2000), whose most promising site of nucleosynthesis are SN II (SN II with low (M<11 $M_\odot$, Cowan & Sneden, 2004) mass progenitors are interesting candidates), although other alternative sites are possible (see e.g. Cowan & Sneden, 2004). Such an anomalous high [Eu/Fe] abundance ratio seems to suggest that

in the LMC clusters and Sgr the Eu is not or not only synthesized in a similar fashion as the α-elements.

Finally, the ratio between the s-process elements (which are predominantly formed through slow neutron captures, with a minor contribution from rapid neutron captures) and Eu (a pure r-process element) represents a powerful diagnostics to estimate the relative contribution of the different neutron-capture processes. The theoretical solar [Ba/Eu] in case of pure rapid neutron captures turns out to be –0.70 dex (Arlandini et al., 1999). The [Ba/Eu]≈0.0 dex abundance ratios measured in the LMC clusters as well as in the Galactic thin disk and Sgr stars, suggest that s-process elements should be mainly produced by AGB stars through slow neutron captures, with a minor (if any) contribution from massive SN II through rapid neutron captures.

At variance, the strong [Y/Eu] (≤–0.7 dex) depletion measured in the LMC clusters and Sgr stars is very different from the higher values ([Y/Eu]∼–0.20 dex at [Fe/H]=–0.40 dex, see Fig. 4.9) observed in the thin disk stars. This may suggest that rapid neutron captures can also have a different role in the production of light and heavy s-process elements, (as suggested by Venn et al. (2004) in order to explain similar patterns in the dSphs) but this seems to be environment-dependent. Alternatively, galactic winds could have been more effective in removing these elements from the LMC and Sgr (see e.g. Matteucci & Chiosi, 1983).

Chapter 5

The age of the LMC clusters: first results

Based on the results published in :

— Mucciarelli, Ferraro, Origlia & Fusi Pecci, 2007, AJ, 133, 2053

— Mucciarelli, Origlia & Ferraro, 2007, AJ, 134, 1813

Accurate ages for the LMC clusters based on the measurement of the luminosity of the MS-TO region are still sparse and very model (i.e. isochrones) dependent. The only homogeneous age-scale available still relies on the so called s–parameter (Elson & Fall, 1985, 1988), an empirical quantity related to the position of the cluster in the dereddened (U-B) vs (B-V) color-color diagram. The definition of a new homogeneous age scale for the LMC cluster system represents one of the most important and necessary step toward to a global understanding of the stellar populations in the LMC. With the ultimate goal of constructing an homogeneous age-metallicity scale for the LMC clusters, we started a program which makes use of the last generation of instruments (imager and multi-object spectrograph) in order to perform an appropriate study of stellar population, age, metal content and structural parameters for a number of pillar clusters. In this section we discuss the first results related to the accurate determination of the age of a number of *template* LMC clusters by using high-resolution photometry obtained with the Advances Camera for Survey (ACS) on board of Hubble Space Telescope (HST). We present the high resolution photometry for two intermediate-age clusters, namely NGC 1978 and NGC 1783, already studied by our group for their near-infrared photometric properties (see Chapter 3) and for their chemical signatures (see Chapter 4).

Stars with initial masses larger than $\sim$1-1.2 $M_\odot$ (the exact value depends on the initial chemical composition) during the central hydrogen burning phase develop a convective core. This derives

from the dependence of the CNO cycle efficiency on temperature. The extension of the convective core is classically defined by adopting the Schwarzschild criterion. It might be possible that a moving fluid element exhibits a nonzero velocity beyond the Schwarzschild boundary along a certain length. This mechanism, referred as *overshooting*, induces an increase of the central hydrogen burning phase lifetime (in order of the more hydrogen available) and of the luminosity of the star, due to the increase of the mean molecular weight.

Young stellar populations (with ages $\leq$300 Myr) are characterized by large convective cores. Theoretical studies (see e.g. the numerical simulations computed by Freytag, Ludwig & Steffen, 1996) suggest that the penetration of convective elements into a stable region (*via the Schwarzschild criterion*) can produce non-negligible evolutionary effects. These predictions seem to be confirmed by several works (Becker & Mathews, 1983; Barmina, Girardi & Chiosi, 2002; Chiosi & Vallenari, 2007) which require some amount of *overshooting* in the MS star convective core, in order to reproduce the observed morphologies and stellar counts of young clusters, although this issue is still matter of debate and the *theory-observation* comparison provides yet contradictory results (Testa et al., 1999; Barmina, Girardi & Chiosi, 2002; Brocato et al., 2003). At variance, in older ($\geq$5-6 Gyr) stellar populations the growth of large radiative cores tends to erase the possible evolutionary effects of *overshooting*. Intermediate-age stellar populations like those in NGC 1978 and NGC 1783 LMC stellar clusters represent the transition stage between these two regimes, where the amount of *overshooting* scales with the initial stellar mass, and thus represent ideal test-bench to study the *overshooting* effects.

5.1 Observations and data analysis

The photometric dataset discussed here consists of high-resolution images obtained with ACS@HST through the F555W and F814W filters, with exposure times of 300 and 200 sec for NGC 1978 and 250 sec and 170 sec for NGC 1783, for the filters F555W and F814W, respectively. These images have been retrieved from ESO/ST-ECF Science Archive (Proposal ID 9891, Cycle 12). The observations have been obtained with the Wide Field Channel (WFC) that provides a field of view of $\approx$200" $\times$200" with a plate scale of 0.05 arcsec/pixel. The WFC is a mosaic of two CCDs, both with 4096$\times$2048 pixels separated by a gap of $\sim$50 pixels. The first chip has been centered on the cluster center, while the second chip sampled a contiguous field. All images were reduced with the ACS/WFC pipeline, in order to perform bias and dark subtractions and flatfield correction. The photometric reduction was performed by using the *DAOPHOT-II* (Stetson, 1987)

PSF fitting method. The output catalog for NGC 1978 includes about 47,000 objects and the one obtained for NGC 1783 about 44,000. Both these catalogs have been calibrated in the *ACS/WFC Vega-mag* system, following the prescriptions of Bedin et al. (2005). Finally, both catalogs have been astrometrized in the 2MASS astrometric system by matching the IR catalogs (discussed in Chapter 3) and using the cross-correlation software CataXcorr. Both the final catalogs reach a magnitude limit of F555W∼ 26, deeper than the others CMDs previously published in literature for LMC clusters.

5.2   NGC 1978

5.2.1   The Color-Magnitude Diagram

Fig. 5.1 shows the calibrated CMD of NGC 1978 for the chip centered on the cluster. Stars in the brightest portion of the Giant Branches could be saturated and/or in the regime of non linearity of the CCD. Hence for stars brighter than F555W=17.6 (this magnitude level is marked with an horizontal dashed line in Fig. 5.1), magnitudes, colors and level of incompleteness are not safely measured. This CMD shows the typical evolutionary features of an intermediate-age stellar population, namely:

(1) the brightest portion of the MS at F555W<21 shows an hook-like shape, typical of the evolution of intermediate-mass stars ($M > 1.2 M_\odot$) which develop a convective core [1]. In particular, the so-called *overall contraction* phase (Salaris & Cassisi, 2006) is clearly visible between the brightest portion of the MS and the beginning of the Sub-Giant Branch (SGB) at F555W∼20.9.

(2) the SGB is a narrow, well-defined sequence at F555W∼20.7, with a large extension in color (δ(F555W-F814W) $\sim$ 0.6 mag). The blue edge of the SGB is broad and probably affected by blending, especially in the most internal region of the cluster.

(3) the RGB is fully populated; this is not surprising since this cluster has already experienced the RGB Phase Transition (see the discussion in Chapter 3).

(4) the He-Clump is located at F555W∼19.1 and (F555W-F814W)∼1.15.

Fig. 5.2 shows the CMD of the external part of the ACS@HST field of view (corresponding to r>140" from the cluster center). This CMD can be assumed as representative of the field population surrounding the cluster. In particular, the CMD shows two main components:

---

[1]Note that the width of the distribution in color of the bright portion of the MS ($\sigma_{(V-I)}$ ∼0.05 mag) turns out to be fully consistent with the observational errors estimated from the completeness experiments ($\sigma_V \sim \sigma_I$ ∼0.03 mag, corresponding to $\sigma_{(V-I)}$ ∼0.04 mag).
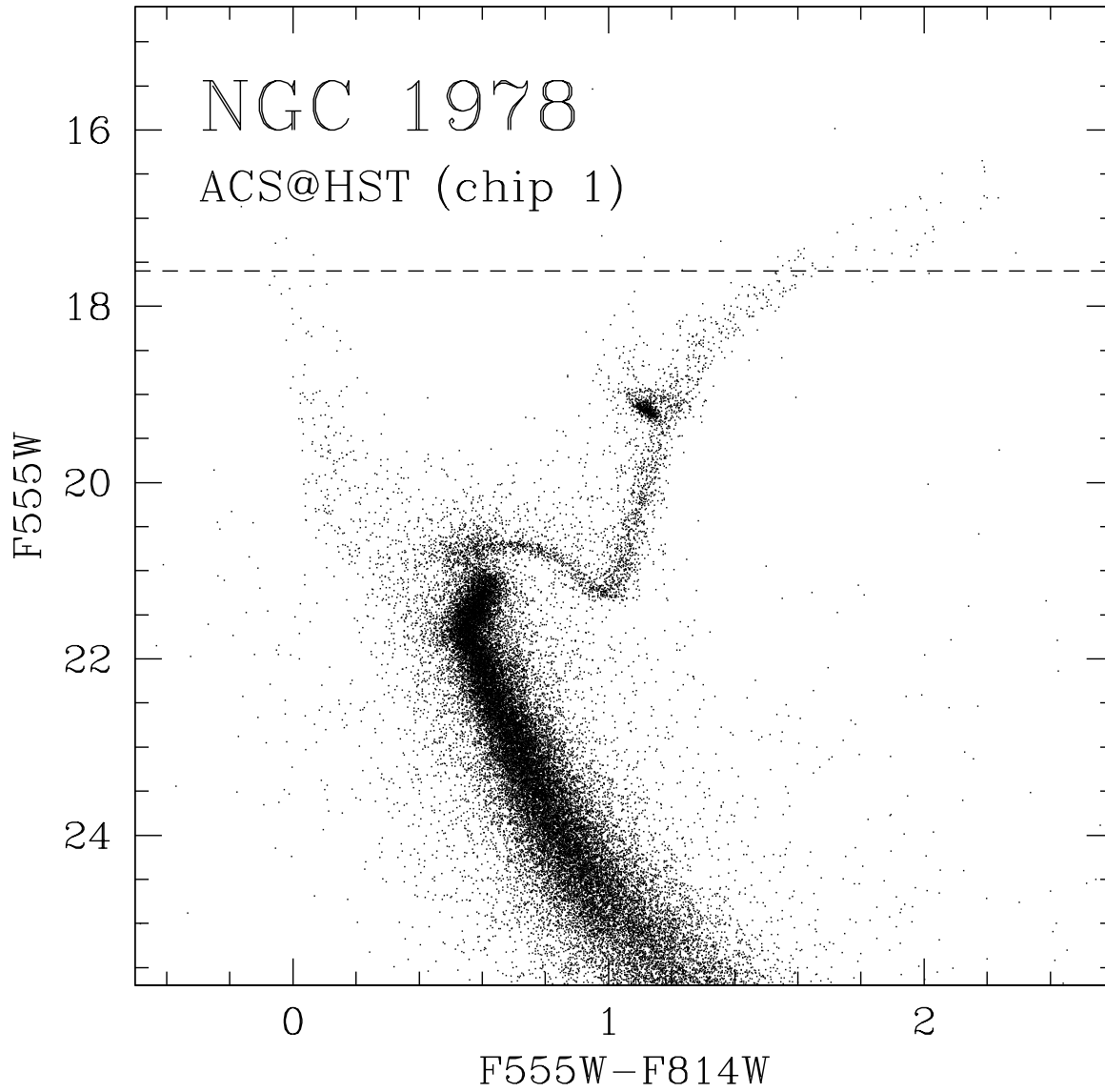
Figure 5.1: (F555W, F555W-F814W) CMD of the LMC cluster NGC 1978, obtained with ACS@HST (only first chip). The dashed line indicates the saturation level.

(1) a blue sequence extended up to F555W∼17.

(2) a SGB which merges into the MS at F555W∼22.2, corresponding to a population of ≈5 Gyr. We interpret this feature as a signature of the major star-formation episode occurred 5-6 Gyr ago, when LMC and SMC were gravitationally bound (Bekki et al., 2004).
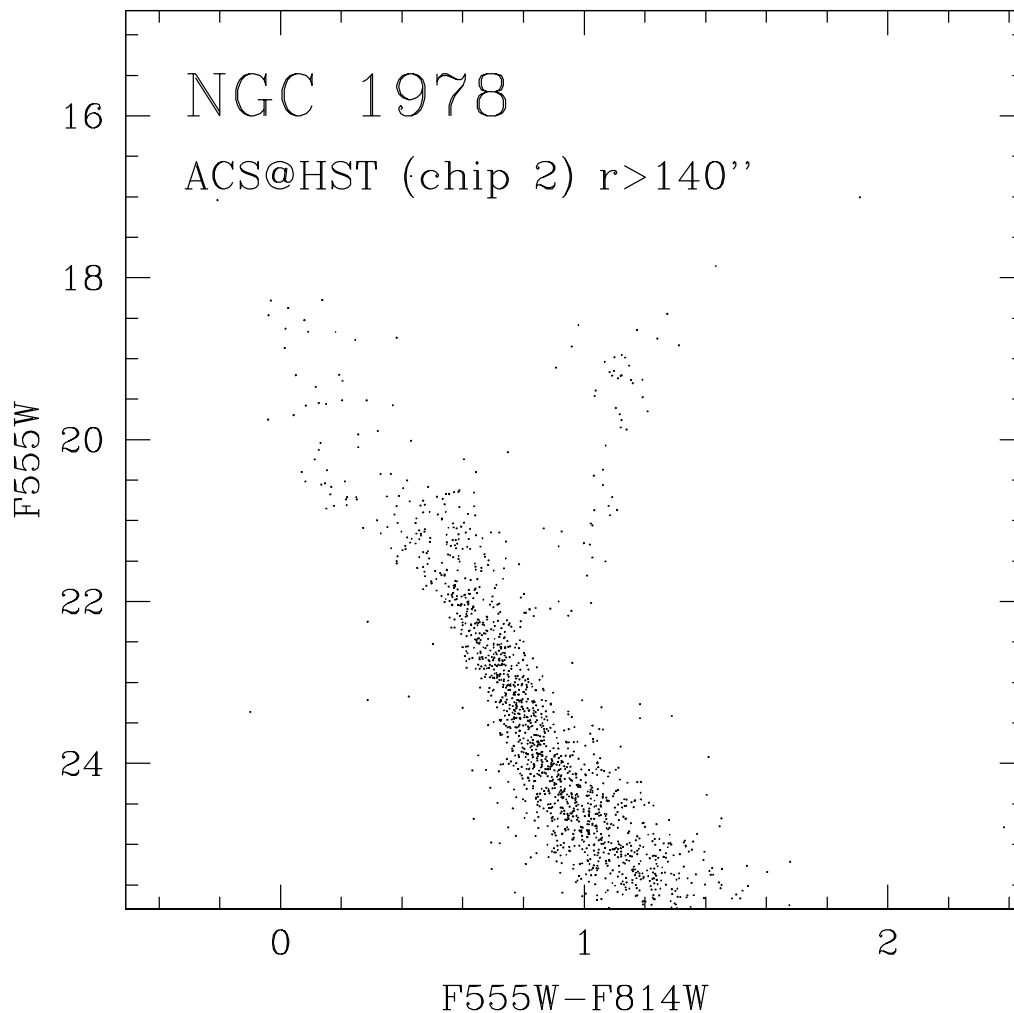

Figure 5.2: (F555W, F555W-F814W) CMD of the outer region (r>140" from the cluster center) of NGC 1978, as obtained with ACS@HST (only second chip).

5.2.2 Completeness

In order to quantify the degree of completeness of the final photometric catalog, we used the well-know artificial star technique (Mateo, 1988), and simulated a population of stars in the

same magnitude range covered by the observed CMD (excluding stars brighter than F555W=17.6, corresponding to the saturation level) and with (F555W-F814W)$\sim$ 0.8 mean color. The artificial stars have been added to the original images and the entire data reduction procedure has been repeated using the *enriched* images. The number of artificial stars simulated in each run ($\sim$ 2,000) are a small percentage ($\sim$5%) of the detected stars, hence they cannot alter the original crowding conditions. A total of $\sim$250 runs were performed and more than 500,000 stars have been simulated. In order to minimize the effect of incompleteness correction, we have excluded the very inner region of the cluster (r<20", where the crowding conditions are most severe) from our analysis. In Fig. 5.3 the completeness factor $\phi = \frac{N_{rec}}{N_{sim}}$ (defined as the fraction of recovered stars over the total simulated ones) is plotted as a function of the F555W magnitude in two different radial regions, namely between 20" and 60" and at r>60" from the cluster center, respectively. In the inner region the sample is >85% complete down to F555W$\approx$22, remaining $\sim$60% complete until to F555W$\sim$25, while in the outer region is >90% complete down to F555W$\approx$24.
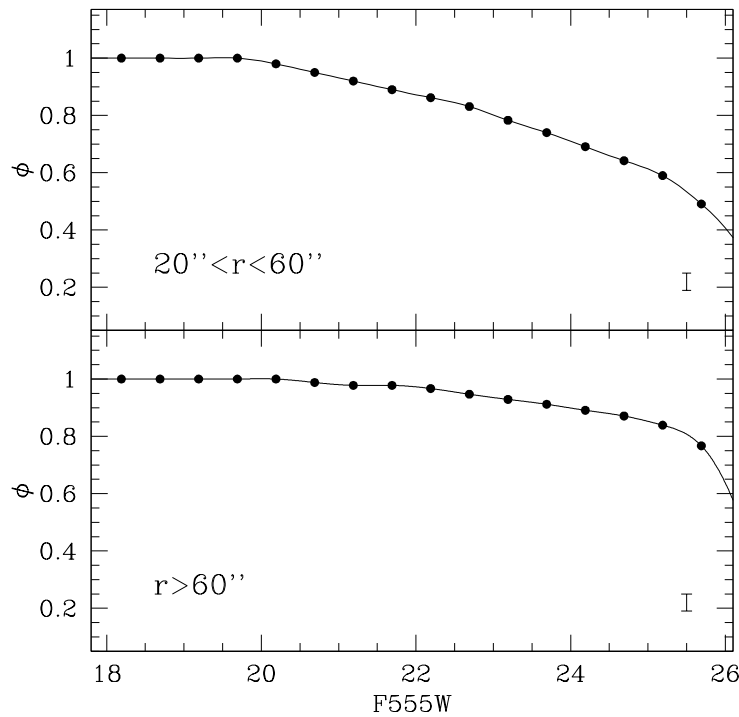
Figure 5.3: Completeness curves computed in two radial sub-regions of NGC 1978. The black points indicate the value of the $\phi = \frac{N_{rec}}{N_{sim}}$ parameter calculated for each magnitude bin. The completeness curves have been computed for F555W<17.6, corresponding to the saturation level. Tipycal errorbars are also indicated.

5.2.3 The RGB-Bump

The extended and populated RGB in NGC 1978 gives the possibility to search for the so-called RGB-Bump. This is the major evolutionary feature along the RGB. It flags the point when the H-burning shell reaches the discontinuity in the H-abundance profile left by the inner penetration of the convection. This feature has been predicted since the early theoretical models (Iben, 1968) but observed for the first time in a globular cluster almost two decades later (King, Da Costa & Demarque, 1984). Since that first detection the RGB-Bump was identified in several GGCs (Fusi Pecci et al., 1990; Ferraro et al., 1999; Zoccali et al., 1999) and in a few galaxies in the Local Group, e.g. Sextant (Bellazzini et al., 2001), Ursa Minor (Bellazzini et al., 2002), Sagittarius (Monaco et al., 2002). According to the prescriptions of Fusi Pecci et al. (1990), we have used the differential and integrated luminosity function (LF) to identify the magnitude level of the RGB-Bump in NGC 1978. In doing this, we have *(1)* selected stars belonging to the brightest (F555W<20.6) portion of the RGB; *(2)* carefully excluded the bulk of the He-Clump and AGB stars by eye; *(3)* defined the fiducial ridge line for the RGB, rejecting those stars lying at more than 2σ from the ridge line. Fig. 5.4 shows the final RGB sample (more than 600 stars) and both the differential and integrated LFs. The RGB-Bump appears in the differential LF as a well defined peak at $F555W^{bump} = 19.10$ and it is confirmed in the integrated LF as a evident change in the slope.

For both LFs the assumed bin-size is 0.1 mag; in order to check the uncertainty in the Bump magnitude level, we have tested the position of this feature by using LFs computed with different binning. The impact of the selected bin-size is not crucial: a difference of 0.2 mag corresponds to a variation <0.05 mag in the detection of RGB Bump. By considering the intrinsic width of the peak in differential LF, we estimate a conservative error <0.10 mag.

Finally, we note that the RGB Bump is brighter and reddest than of the bulk of the He-Clump and the latter merges into the RGB at faintest magnitude (F555W~19.3, see Fig. 5.4); hence the possibility of contamination is negligible.

5.2.4 The cluster ellipticity

Most globular clusters in the Galaxy show a nearly spherical shape, with a mean ellipticity [2] ϵ=0.07 (White & Shawl, 1987) and more than 60% with ϵ <0.10. One of the most remarkable exception is represented by ω Centauri that is clearly more elliptical than the other GGCs: its ellipticity is

---

[2]Note that ellipticity is defined here as ϵ=1-(b/a), where a and b represent major and minor axis of the ellipse, respectively.
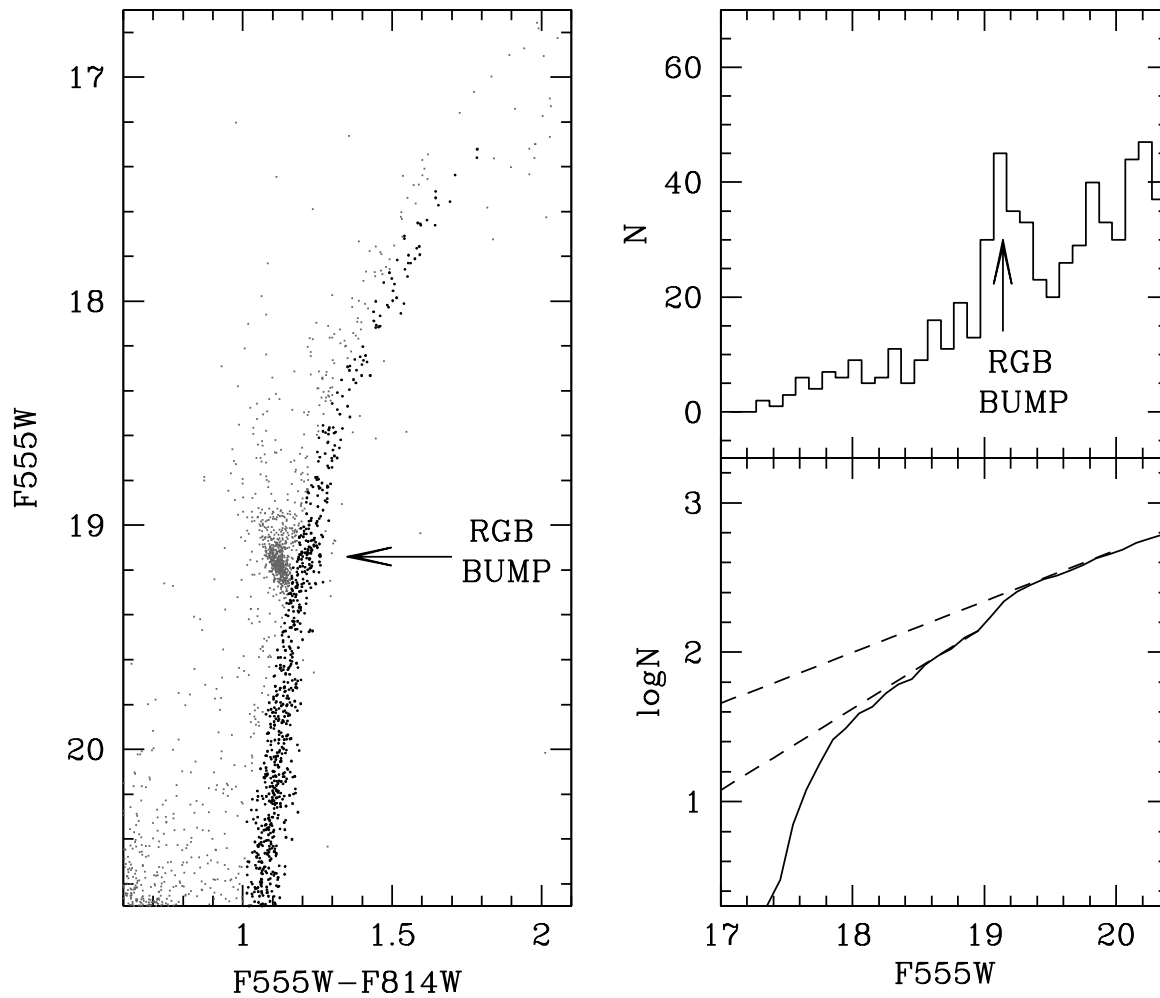
Figure 5.4: Left: the bright portion of the CMD of NGC 1978 (grey points) with the selected RGB stars (black points). The arrow indicates the magnitude of the RGB Bump. Right: differential (upper panel) and integrated (lower panel) LFs, computed for the RGB stars, excluding the He-Clump and AGB populations. The arrow in the upper panel indicates the position of the RGB Bump. The dashed lines in the lower panel are the linear fit to the regions above and below the RGB Bump.

ϵ=0.15 in the external regions with a evident decrease in the inner regions, with ϵ=0.08 (Pancino et al., 2003). Conversely, the LMC clusters (as well as those in the SMC) show on average a stronger departure from the spherical symmetry. Geisler & Hodge (1980) estimated the ellipticities of 25 populous LMC clusters, finding a mean value of ϵ=0.22; Goodwin (1997) obtained a lower average value for the LMC clusters (ϵ=0.14), but still higher than the mean ellipticity of the GGCs. Moreover, in the LMC the presence of many double or triple globular clusters has been interpreted as a clue of the possibility of merger episodes between subclusters with the result to create stellar clusters with high ellipticities (Bhatia et al., 1991). Previous determinations (Geisler & Hodge, 1980; Fischer, Welch & Mateo, 1992) suggested large values of ellipticity for NGC 1978.

We have used the ACS catalog to derive a new measurement of the ellipticity of the cluster, in doing this we computed isodensity curves and adopting an adaptive kernel technique, accordingly to the prescription of Fukunaga (1972). In doing this we have adopted the center of gravity of the cluster computed using the near-infrared photometry obtained with SOFI (see Chapter 3). The isodensity curves have been computed using all the stars in the first chip with F555W<22 (approximately two magnitudes below the TO region) in order to minimize the incompleteness effects [3]. Finally, we have fitted the isodensity curves with ellipses. Fig. 5.5 shows the cluster map with the isodensity contours (upper panel), the corresponding best fit ellipses (central panel) and their ellipticity as a function of the semi-major axis in arcsecond (lower panel). No evidence of subclustering or double nucleus is found. The average value of the ellipticity results ϵ= 0.30 (with a root mean square of 0.02), without any radial trend. This value is in good agreement with the previous estimates (Geisler & Hodge, 1980; Fischer, Welch & Mateo, 1992) and confirms the surprisingly high ellipticity of NGC 1978.

5.2.5 The cluster age

The determination of the age of a stellar population requires an accurate measure of the MS-TO magnitude and the knowledge of the distance modulus, reddening and overall metallicity. For NGC 1978 we used our determination of [Fe/H]=–0.38±0.02 dex and $< [\alpha/Fe] >$ almost solar (see Chapter 4), based on high-resolution spectra, to derive the overall metallicity [M/H]. In doing this, we adopted the relation presented by Salaris, Chieffi & Straniero (1993):

$$[M/H] \sim [Fe/H] + \log\left(0.694 \cdot 10^{<[\alpha/Fe]>} + 0.306\right),$$

---

[3]Note that a different assumption on the magnitude threshold does not affect the result.
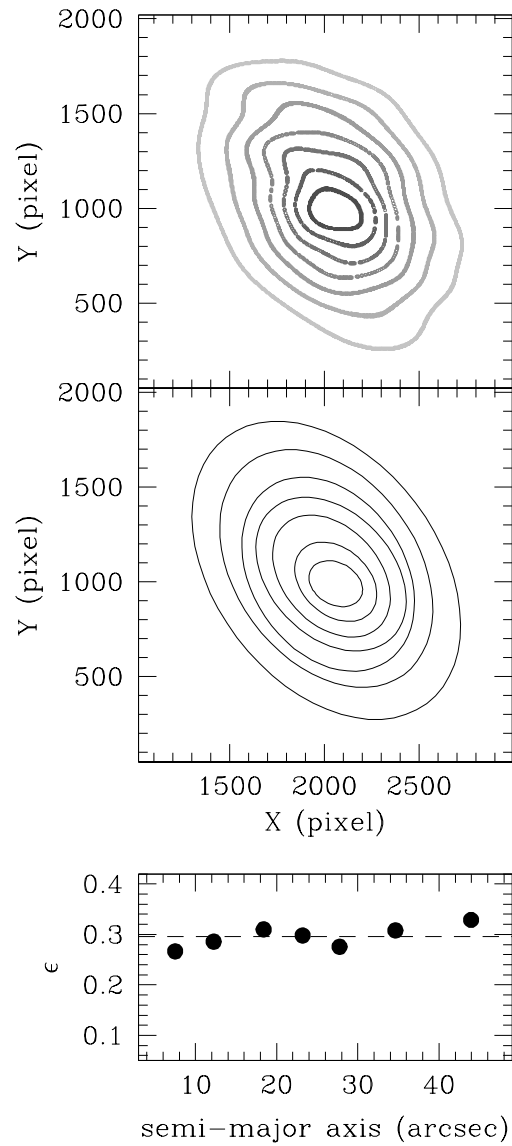
Figure 5.5: Upper panel: the map of NGC 1978 with the isodensity contours; central panel: the best fit ellipses of the isodensity contours; lower panel: ellipticity of the best fit ellipses as a function of the semi-major axis in arcsecond. The horizontal dashed line indicate the mean value.

118

obtaining [M/H]$\sim$–0.37 dex.

In the case of intermediate age stellar systems, the measurements of the age is complicated by the presence of a convective core, whose size needs to be parametrized. The overshooting efficiency is parametrized using the mixing length theory (Bohm-Vitense, 1958) with $\Lambda_{os}=l/H_p$ (where *l* is the mean free path of the convective element and H_p is pressure scale height) that quantifies the overshoot distance *above* the Schwarzschild border in units of the pressure scale height. Some models as the "Padua ones" define this parameter as the overshoot distance *across* the Schwarzschild border, hence the Λ_{os} values from different models are not always directly comparable.

We then use different sets of theoretical isochrones with different input physics, in order to study the impact of the convective overshooting in reproducing the morphology of the main evolutionary sequences in the CMD.

- **BaSTI models**: BaSTI (*A Bag of Stellar Tracks and Isochrones*) [4] evolutionary code described in Pietrinferni et al. (2004) computes isochrones with and without the inclusion of overshooting. The overshoot efficiency depends on the stellar mass: (1) $\Lambda_{os}= 0.2$ for masses larger than 1.7 $M_{\odot}$; (2) $\Lambda_{os} = 0.25 \cdot (M/M_{\odot} - 0.9)$ for stars in the 1.1-1.7 $M_{\odot}$ range; (3) $\Lambda_{os}= 0$ for stars less massive than 1.1 $M_{\odot}$.

- **Pisa models** : PEL (*Pisa Evolutionary Library*[5], Castellani et al., 2003) provides an homogeneous set of isochrones computed without overshooting and with two different values of Λ_{os}, namely 0.1 and 0.25.

- **Padua models** : in these isochrones (Girardi et al., 2000) [6] $\Lambda_{os}^{Padua}= 0$ for stars less massive than 1 $M_{\odot}$, where the core is fully radiative. The overshooting efficiency has been assumed to increase with stellar mass, according to the relation $\Lambda_{os}^{Padua} = M/M_{\odot} - 1$ in the 1-1.5 $M_{\odot}$ range; above 1.5 $M_{\odot}$ a constant value of $\Lambda_{os}^{Padua}= 0.5$ is assumed. Note that this value corresponds to $\Lambda_{os} \sim 0.25$ in the other models, where the extension of the convective region (beyond the classical boundary of the Schwarzschild criterion) is measured with respect to the convective core border.

---

[4]The BaSTI isochrones are available at the URL http://193.204.1.62/index.html.

[5]The PEL isochrones are available at the URL http://astro.df.unipi.it/SAA/PEL/Z0.html.

[6]The Padua isochrones are available at the URL http://pleiadi.pd.astro.it/

From each set of theoretical models, we selected isochrones with Z=0.008 (corresponding to [M/H]=– 0.40 dex), consistent with the overall metallicity of the cluster and we assumed a distance modulus $(m - M)_0 \sim 18.5$ (van den Bergh, 1998; Clementini et al., 2003; Alves, 2004) and E(B-V)= 0.10 (Persson et al., 1983). However, in order to obtain the best fit to the observed sequences with each isochrone set, we left distance modulus and reddening free to vary by $< |10|$% and $< |30|$% , respectively. Fig. 5.6 shows the best fit results for each isochrone set, while Tab. 5.1 lists the corresponding best fit values of age, reddening, distance modulus and the predicted magnitude level for the RGB-Bump.

Parameter	BaSTI Λ_{os}=0	BaSTI Λ_{os}=0.2	PEL Λ_{os}=0	PEL Λ_{os}=0.1	PEL Λ_{os}=0.25	PADUA Λ_{os}=0.25
Age (Gyr)	1.9	3.2	1.7	1.9	2.5	2.2
$(m - M)_0$	18.47	18.43	18.50	18.50	18.50	18.38
E(B-V)	0.09	0.09	0.09	0.09	0.09	0.07
M_{TO} ($M_\odot$)	1.47	1.45	1.49	1.49	1.44	1.45
V_{555}^{Bump}	19.10	19.22	18.73	18.88	19.39	19.44

Table 5.1: Age, distance modulus, reddening, TO mass and magnitude level of the RGB Bump from best-fit BaSTI, PEL and Padua isochrones.

The best fit solution from each model set has been identified as the one matching the following features: (*i*) the He-Clump magnitude level, (*ii*) the magnitude difference between the He-Clump and the SGB and (*iii*) the color extension of the SGB. The theoretical isochrones have been reported into the observational plane by means of suitable transformations computed by using the code described in Origlia & Leitherer (2000) and convolving the model atmospheres by Bessell, Castelli & Plez (1998) with the ACS filter responses. In the following, we briefly discuss the comparison between the observed evolutionary features and theoretical predictions.

- **BaSTI models**: By selecting canonical models from the BaSTI dataset, the best fit solution gives an age of 1.9 Gyr, with E(B-V)= 0.09 and a distance modulus of 18.47. Despite of the good matching of the He-Clump and SGB magnitude level, and the RGB slope, this isochrone does not properly reproduce the shape of the TO region and the *overall contraction phase* (*panel (a)* of Fig. 5.6). The best-fit solution from overshooting models gives an age of 3.2 Gyr, $(m - M)_0$= 18.43 and E(B-V)= 0.09, and matches the main loci of
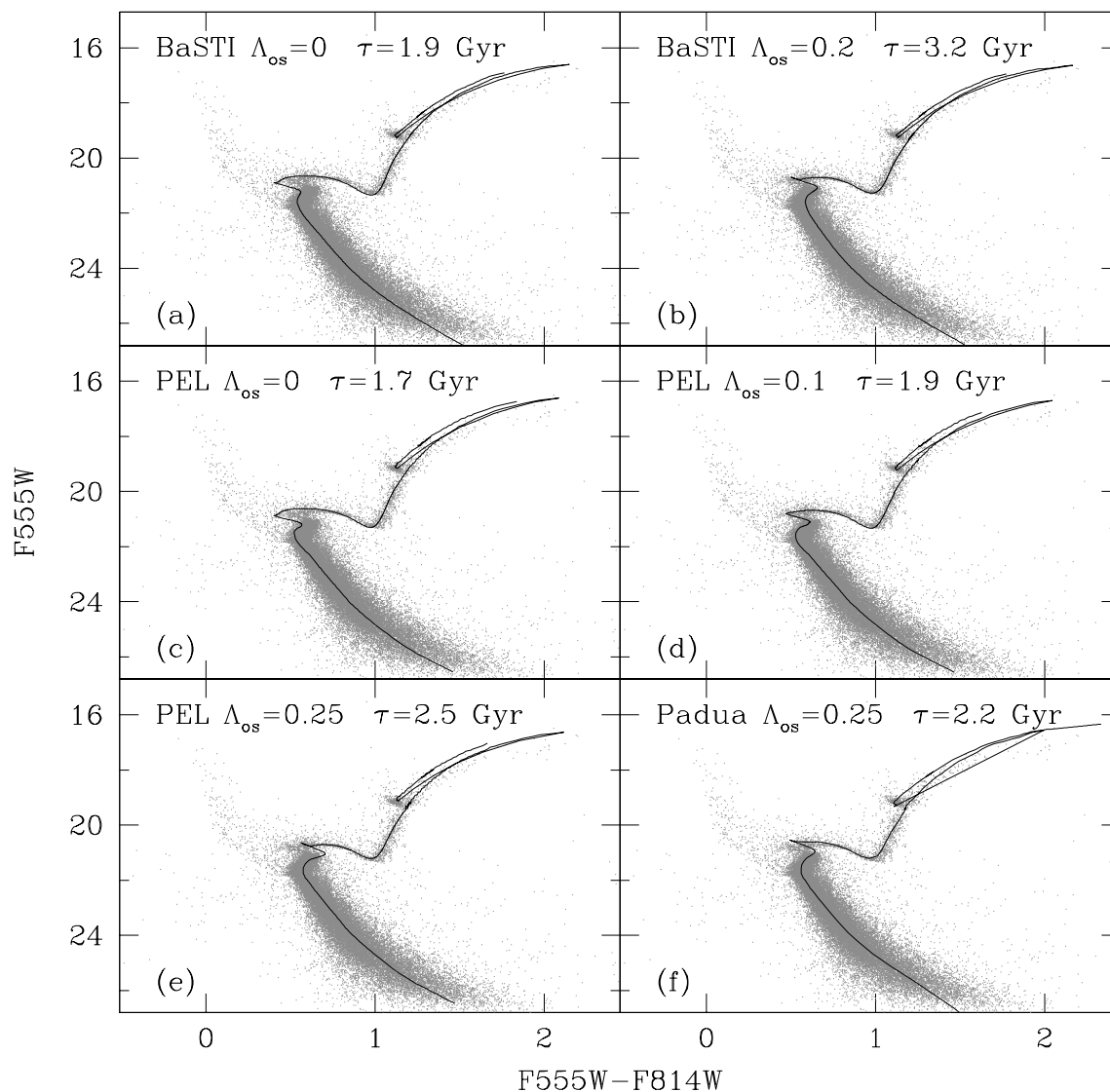
Figure 5.6: Best-fit theoretical isochrones overplotted to the observed CMD of NGC 1978 (only stars at r>20" from the cluster center are plotted) obtained with theoretical isochrones: each panel shows a different model and the corresponding Λ_{os} value and age. Reddening and distance moduli for each model are reported in Tab. 5.1.

the evolutionary sequences in the CMD. In particular, this isochrone provides a better match to the hook-like region (between the MS and the SGB, see *panel (b)* of Fig.6).

- **PEL models**: *Panels (c), (d)* and *(e)* of Fig. 5.6 show the best fit solutions obtained by selecting 3 different Λ_{os}. In all cases $(m - M)_0$= 18.5 and E(B-V)= 0.09 are used. As can be seen values of Λ_{os}= 0 and Λ_{os}= 0.25 isochrones fail to fit the SGB extension and the hook-like feature, conversely a very good fit is obtained with a mild-overshooting (Λ_{os}= 0.1) and an age of τ= 1.9 Gyr.

- **Padua models**: The best-fit solution gives τ= 2.2 Gyr, $(m - M)_0$= 18.38 and E(B-V)= 0.07 (*Panels (f)* of Fig. 5.6). This isochrone well-reproduces the complex structure of the TO and the core contraction stage, as well as the SGB structure and the RGB slope. However, it requires distance modulus and reddening significantly lower than those generally adopted for the LMC.

From this comparison, it turns out that only models with overshooting are able to best fit the morphology of the main evolutionary sequences in the observed CMD. In particular, the best fit solutions have been obtained with the BaSTI overshooting model with τ= 3.2 Gyr, the PEL mild-overshooting model (Λ_{os}= 0.1) and τ= 1.9 Gyr and the Padua model with Λ_{os}^{Padua}= 0.25 (corresponding to Λ_{os}= 0.25) and τ= 2.2 Gyr.

However, it must be noted that none of these models can fit satisfactorily the observed Bump level, the BaSTI and Padua models being $\approx$0.1 and 0.3 mag fainter, respectively, and the PEL model $\approx$0.2 mag brighter, perhaps suggesting that evolutionary tracks for stars with M>$1M_\odot$ still need some fine tuning to properly reproduce the luminosity of this feature. Since the comparison between the observed CMD and theoretical isochrones is somewhat qualitative, we also performed a quantitative comparison between theoretical and empirical population ratios: this yields a direct check of the evolutionary timescales. To do this, we define four boxes selecting the stellar population along the main evolutionary features in our CMD, namely the He-Clump, the SGB, the RGB (from the base up to F555W$\sim$ 19.4) and finally the brightest ($\sim$ 1 mag) portion of the MS; these boxes are shown in Fig. 5.7, overplotted to the cluster CMD. Star counts in each box have been corrected for incompleteness, by dividing the observed counts by the ϕ factor obtained from the procedure described in Sect. 5.2.2 (see also Fig. 5.3) for each bin of magnitude.
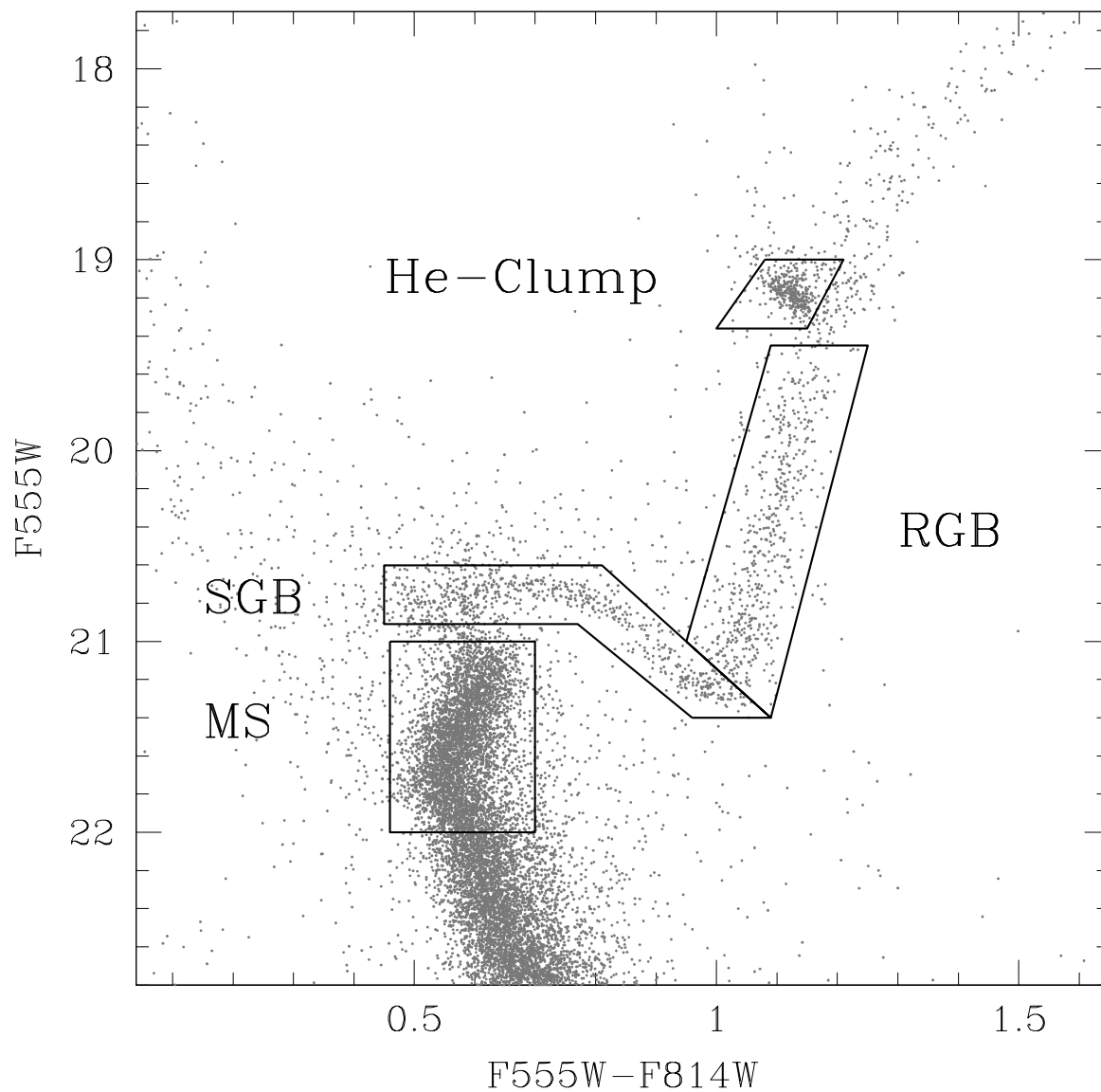
Figure 5.7: The bright portion of the NGC 1978 CMD (only stars at r>20" from the cluster center are plotted) with the selection boxes adopted to sample the MS, SGB, RGB and He-Clump populations.

Star counts have been also corrected for field contamination. To estimate the degree of contamination by foreground and background stars we have applied a statistical technique. We have used the CMD shown in Fig. 5.2 as representative of the field population. The number of stars counted in each box in the control field has been normalized to the cluster sampled area and finally subtracted from the cluster star counts. The *final* star counts per magnitude bin in each box have been estimated according to the following formula:

$$N_{corr} = \frac{N_{obs}}{\phi} - N_{field},$$

where N_{obs} are the observed counts and N_{field} the expected field star counts. We find $N_{MS}= 4331$, $N_{SGB}= 632$, $N_{RGB}= 450$ and $N_{He_{Cl}}= 311$, where N_{MS}, N_{RGB}, N_{SGB} and N_{He-Cl} are the number of stars in the box as sampling the MS, the RGB, the SGB and the He-Clump population, respectively.

Uncertainties in the computed population ratios have been estimated using the following formula

$$\sigma_R = \frac{\sqrt{R^2 \cdot \sigma_D^2 + \sigma_N^2}}{D}$$

where $R = N/D$ is a given population ratio, N is the numerator and D the denominator of the ratio. The errors σ_N and σ_D for any population have been assumed to follow a Poisson statistics. In addition, in the error budget we also include the uncertainty due to the positioning of the box edges: note that a slightly different ($\pm 1\sigma$) assumption in the definition of the box edge has little impact (typically 7-8%) on the star counts. This uncertainty has been quadratically added to the Poissonian error.

On the basis of the boxes shown in Fig. 5.7 we defined four population ratios [7], as listed in Tab. 5.2: (**i**) N_{RGB}/N_{SGB}; (**ii**) N_{RGB}/N_{He-Cl}; (**iii**) N_{SGB}/N_{He-Cl}; (**iv**) $N_{MS}/N_{(SGB+RGB)}$. For each selected model, corresponding theoretical population ratios have been estimated by convolving the isochrone set shown in Fig. 5.6 with an Initial Mass Function (IMF), according with the prescriptions of Straniero & Chieffi (1991). In order to check the sensitivity of the population ratios to the adopted IMF, we have used three different values for the IMF slope α: 2.35 (Salpeter, 1955), 2.30 (Kroupa, 2001) and 3.5 (Scalo, 1986) at M>$1M_\odot$. In the considered mass range (between 1 and 2 $M_\odot$), the theoretical population ratios are poorly dependent on

---

[7]Note that the bluest portion of the SGB can be affected by blending. To check this effect, we also defined a second box sampling the SGB population (SGB_s), by excluding the bluest region at (F555W-F814W)<0.7. The population ratios obtained by using this selection box (and reported in Tab. 5.2) are fully consistent with the results by using the standard SGB box, suggesting that blending effects (if any) in the SGB population have a negligible impact on the results.

the assumed IMF, with a 16% maximum variation (between Scalo and Kroupa IMFs) for the $N_{MS}/N_{(SGB+RGB)}$ ratios. Hence in the following the population ratios are computed by using a Salpeter IMF.

| Population | BaSTI | BaSTI | PEL | PEL | PEL | PADUA | Observed |
Ratio	Λ_{os}=0	Λ_{os}=0.2	Λ_{os}=0	Λ_{os}=0.1	Λ_{os}=0.25	Λ_{os}=0.25	
MS/(RGB+SGB)	2.40	6.05	2.10	3.27	7.06	6.92	4.00±0.40
SGB/He-Cl	4.16	1.63	4.90	2.01	1.62	1.05	2.03±0.22
RGB/He-Cl	1.95	1.07	2.41	1.64	1.03	0.78	1.45±0.19
RGB/SGB	0.58	0.65	0.49	0.81	0.64	0.75	0.71±0.10
SGB_s/He-Cl	1.39	0.64	1.43	0.85	0.61	0.36	1.12±0.12
MS/(RGB+SGB_s)	4.14	9.61	4.00	4.75	11.43	11.29	5.43±0.42

Table 5.2: Theoretical population ratios from BaSTI, PEL and Padua best-fit isochrones and corresponding observed ratios for NGC 1978.

We found that BaSTI and PEL canonical models predict a lower (by <40%) of the $N_{MS}/N_{(SGB+RGB)}$ and higher N_{RGB}/N_{He-Cl} and N_{SGB}/N_{He-Cl} (by <35% and <100%, respectively) population ratios with respect to the observed ones. Isochrones with high overshooting (Λ_{os}= 0.2-0.25) show an opposite trend, with higher (by <50%) $N_{MS}/N_{(SGB+RGB)}$ and lower (by <30%) N_{RGB}/N_{He-Cl} and N_{SGB}/N_{He-Cl} ratios. The isochrone with Λ_{os}= 0.1 from PEL dataset reasonably reproduces all the population ratios. Only the $N_{MS}/N_{(SGB+RGB)}$ ratio turns out to be $\sim$ 15% lower than the observed one.

We conclude that the best agreement with observations (both in terms of evolutionary sequence morphology and star counts) has been obtained by using PEL models computed with a mild overshooting (Λ_{os}= 0.1) and τ= 1.9 Gyr. Also, the required values of distance modulus and reddening are fully consistent with those generally adopted for NGC 1978. In order to estimate the overall age uncertainty, we took into account the major error source, namely the distance modulus. Hence, we have repeated the best-fitting procedure by using the PEL isochrones with mild-overshooting, and varying the distance modulus by $\pm$ 0.05 and $\pm$ 0.1 mag with respect to the reference value of 18.5. A variation of $\pm$ 0.05 mag still allows a good fit of the CMD features with isochrones within $\mp$ 0.1 Gyr from the reference value of 1.9 Gyr. A variation of $\pm$ 0.1 mag in the distance modulus, does not allows to simultaneously fit the He-Clump magnitude level and the extension of SGB, whatever age is selected. Hence, we can assign a formal error of $\pm$ 0.1 Gyr to our age estimate.

5.3 NGC 1783

5.3.1 The Color-Magnitude Diagram

Fig. 5.8 shows the observed CMD of NGC 1783 using only the ACS chip sampling the cluster core. The useful magnitude range is $17.6 \leq$ F555W ≤ 26. Indeed, we note that the brightest stars at F555W<17.6, could be in the non-linear regime of the CCD or saturated in their central pixels, making the corresponding magnitudes and colors somewhat uncertain.

The main features of the observed CMD can be summarized as follows:

(1) The MS extends over more than 6 magnitudes in the F555W band and the TO point is located at F555W∼21.2 (the identification of the TO magnitude was done by means of a parabolic fit of this region). The TO region shows a mild spread in color;

(2) the slope change of the MS is at F555W∼22.2 and flags the transition between radiative and convective core stellar structures;

(3) the SGB is a poorly populated sequence, with a typical magnitude of F555W∼20.5. We note that the blue edge of this sequence is not well-defined;

(4) the RGB is well populated and it extends over ∼5 magnitudes;

(5) the Helium-Clump is located at F555W∼19.25 and (F555W-F814W)∼1.15;

(6) the AGB Clump (corresponding to the base of the AGB sequence) is visible at F555W∼18.4.

Fig. 5.9 shows the radial CMDs by using the entire sample of stars detected in the ACS FoV. The bulk of the cluster population lies in the central 2 arcmin (by radius); at r>130" the SGB, RGB and He-Clump are barely detectable, while the brightest portion of the cluster MS is still visible. The mild color broadening of the TO region deserves a brief discussion. Recently, Bertelli et al. (2003) found a color dispersion in the brightest portion of the MS of NGC 2173, while Mackey & Broby Nielsen (2007) found a bifurcation of the bright MS region of NGC 1846, and interpreted it as a double TO. These two observational evidences suggest the possible existence of an age-dispersion in these stellar clusters. In order to check whether the broadening of the TO region in NGC 1783 can be ascribed to a possible age-dispersion as well, we calculated the color distribution of the MS stars in the 20.5<F555W<21.1 magnitude range. The color distribution turns out to be roughly Gaussian with $\sigma_{F555W-F814W} \approx 0.05$, which is fully consistent with the observational errors ($\sigma_{F555W} \sim \sigma_{F814W} \approx 0.03$, implying a color uncertainty $\sigma_{F555W-F814W} \approx 0.04$). Similar results are obtained by computing the color distribution in the radial CMDs of Fig. 5.9. Thus, we can conclude that the spread in color of the TO region in NGC 1783 can be explained in terms of photometric errors and there is not any evidence of an age-dispersion.
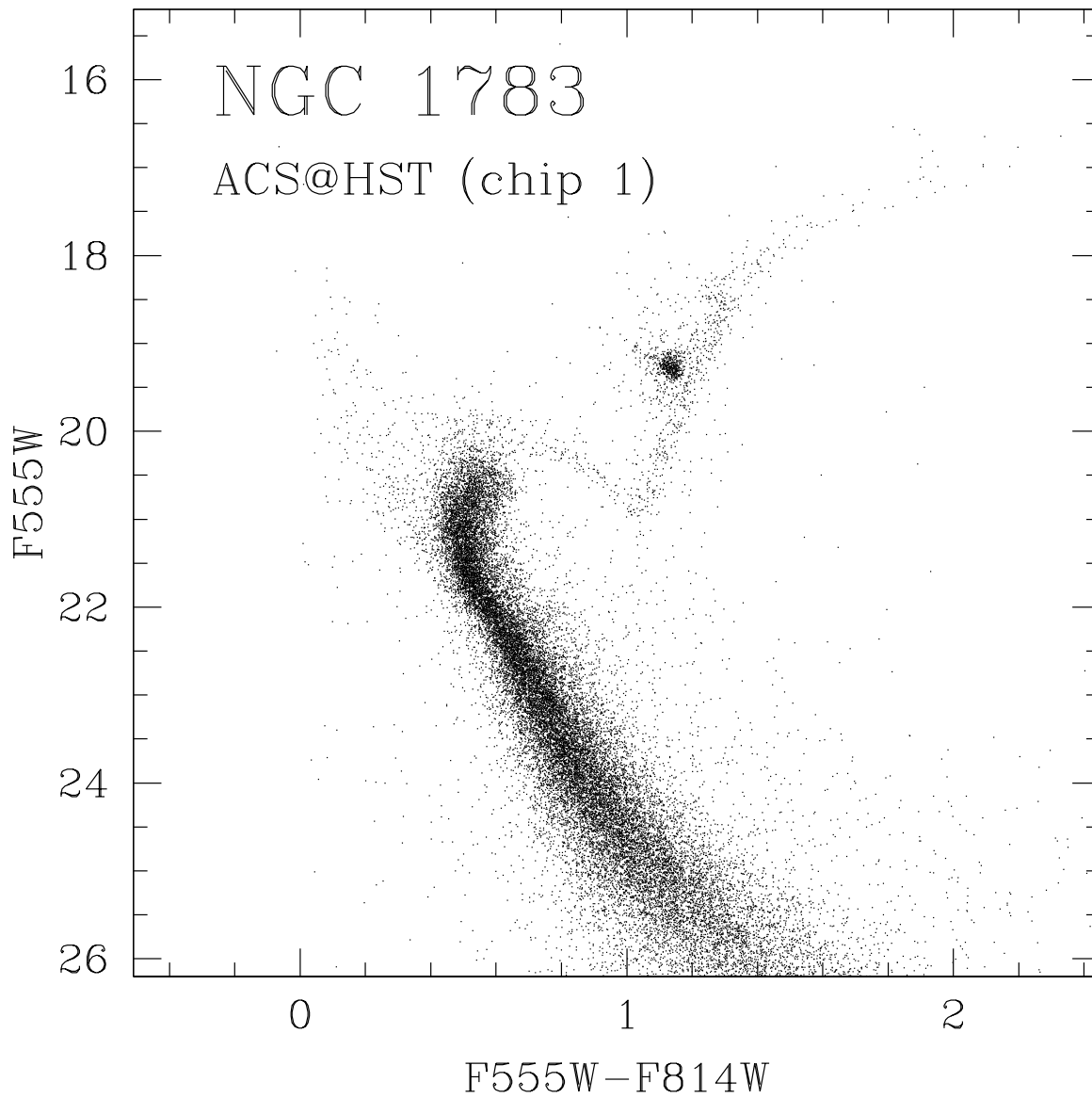
126

Figure 5.8: (F555W, F555W-F814W) CMD of the LMC cluster NGC 1783, obtained with ACS@HST (only stars lying into the chip containing the cluster core have been plotted).
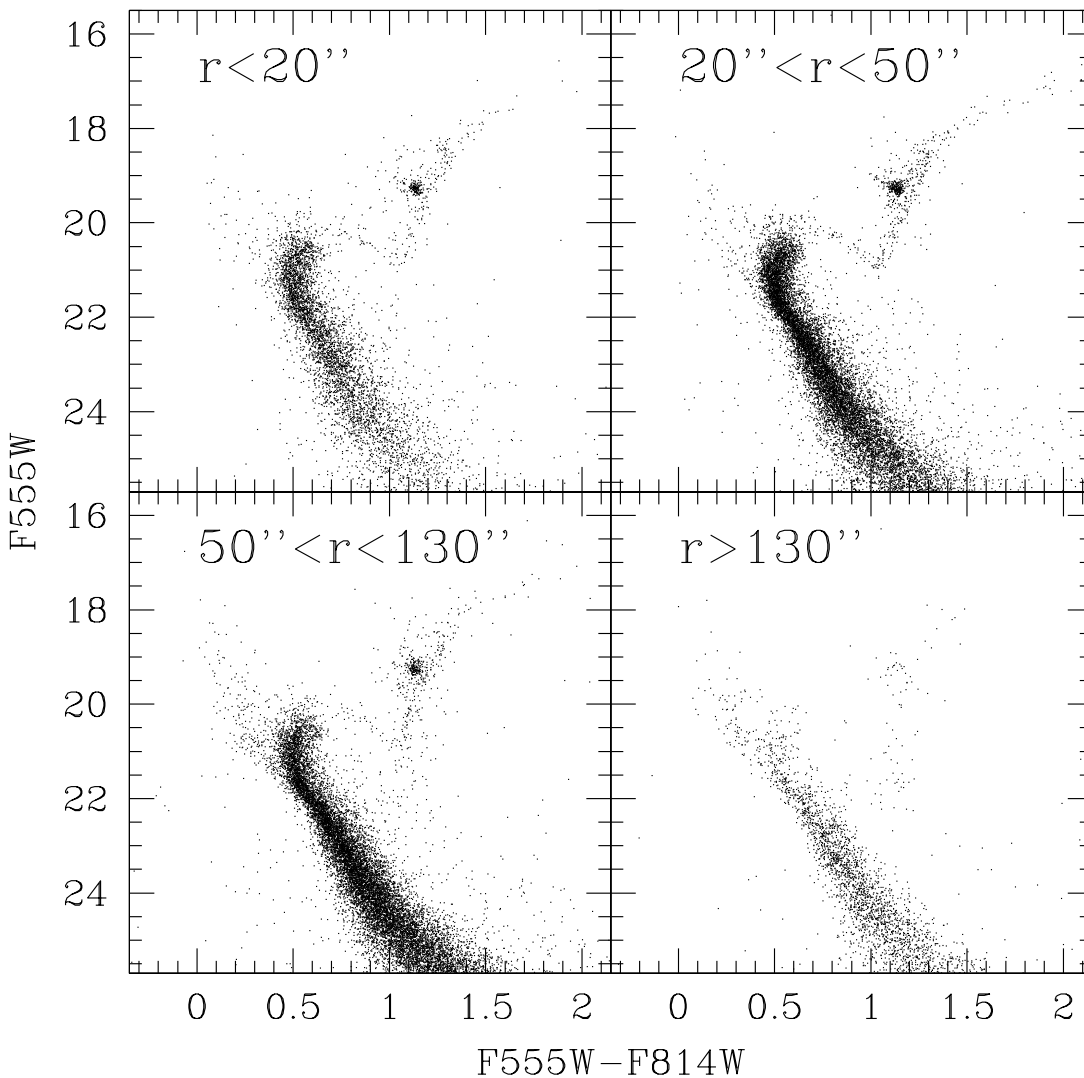
Figure 5.9: Radial (F555W ,F555W-F814W) CMD of NGC 1783 at increasing distances from the cluster center.

5.3.2   Completeness

In order to quantify the degree of completeness of the final photometric catalog, we used the artificial star technique (Mateo, 1988), by adopting the same procedure described in Sect. 5.2.2 for the cluster NGC 1978. We simulated a population of stars in the same magnitude range covered by the observed CMD (excluding stars brighter than F555W=17.6, corresponding to the

saturation level) and with a (F555W-F814W)$\sim$0.8 mean color. The number of artificial stars simulated in each run ($\sim$ 2,000) is always a small percentage ($\sim$5%) of the detected stars, A total of $\sim$250 runs were performed and more than 500,000 stars have been simulated. We have excluded from our analysis the very inner region of the cluster (r<20"), where the crowding conditions are prohibitive. Fig. 5.10 shows the completeness factor $\phi = \frac{N_{rec}}{N_{sim}}$, defined as the fraction of recovered stars over the total simulated ones, as a function of the F555W magnitude in two different radial regions, namely between 20" and 50" and at r>50" from the cluster center, respectively. In the inner region the sample is > 90% complete down to F555W$\approx$ 22.5, while in the outer region is > 90% complete down to F555W$\approx$ 24.
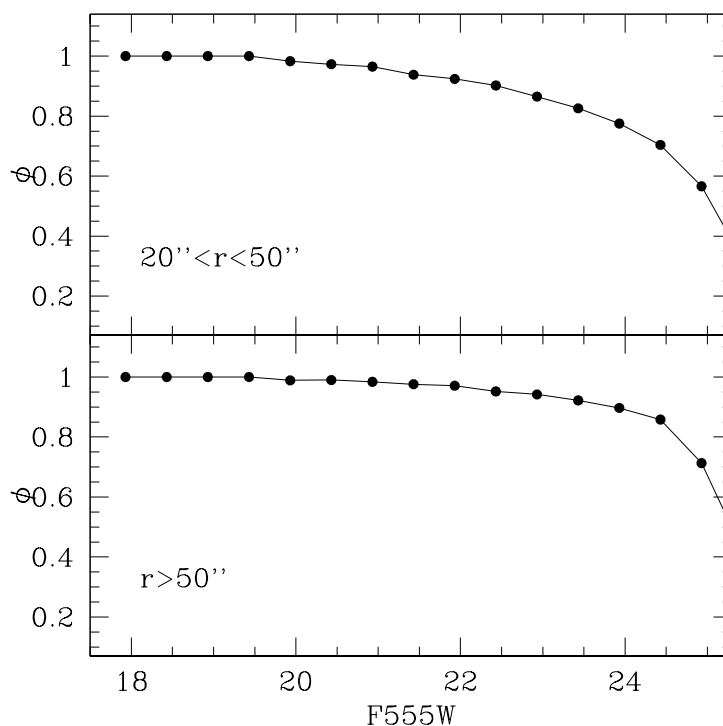
Figure 5.10: Completeness curves computed in two radial sub-regions of NGC 1783. The black points indicate the value of the $\phi = \frac{N_{rec}}{N_{sim}}$ parameter calculated for each 0.5 magnitude bin.

5.3.3 The cluster ellipticity and structural parameters

The knowledge of the position of each star over the entire extension of the cluster (and in particular in the innermost region) allows to compute the center of gravity (C_{grav}) with high precision. In doing this, we applied the procedure described in Montegriffo et al. (1995), averaging the α and δ coordinates of the detected stars with F555W< 22, in order to minimize the effects of incompleteness. The C_{grav} of the cluster turns out to be located at $\alpha= 4^h\ 59^m\ 09^s.78$ and $\delta=-65°$ 59' 17".82. This finding is in good agreement with our previous determination based on near-IR photometry (see Chapter 3).

We also used the ACS photometry of NGC 1783 to derive new estimates for the cluster ellipticity and structural parameters. The isodensity curves are computed with an adaptive kernel technique, accordingly to the prescription of Fukunaga (1972). We used all the stars in the first chip with F555W<22 in order to minimize incompleteness effects and we fit the isodensity curves with ellipses. Fig. 5.11 shows the cluster map with the isodensity contours (upper panel), the corresponding best fit ellipses (central panel) and their ellipticity as a function of the semi-major axis in arcsec (lower panel). The ellipticity ϵ (defined as $\epsilon=1-(b/a)$, where a and b are the major and minor axis of the ellipse, respectively) turns out to be 0.14± 0.03. This value results slightly lower than the previous determinations of Geisler & Hodge (1980) that found an average ellipticity of $\epsilon= 0.19$.

By following the procedure already described in previous papers (see Ferraro et al., 2004b), we also compute the projected density profile of the cluster. The area sampled by the first ACS chip has been divided in 18 concentric annuli, each one centered on C_{grav} and split in four sub-sectors. The number of stars lying in each sub-sector was counted and the mean star density was obtained. The standard deviation was estimated from the variance among the sub-sectors. The radial density profile is plotted in Fig. 5.12.

We used the Sigurdsson & Phinney (1995) code in order to compute the family of isotropic single-mass King models. These models are defined by three main parameters, the central potential W_0, core radius r_c and the concentration c= $\log{(r_t)}/(r_c)$, where r_t is the tidal radius. Fig. 5.12 also shows the single-mass King model that best fit the derived density profile. The best-fit model has been selected by using a χ^2 minimization (shown in the lower panel of Fig. 5.12).

We find $W_0= 5.5$, $r_c= 24.5$" and c= 1.16 , corresponding to a tidal radius $r_t= 5.9$' [8]. Our estimate of r_c is consistent with the one by Elson (1992) who found $r_c= 20$". The resulting r_t lies

---

[8]We underline that the structure of the profile and the corresponding derived parameters does not change if different magnitude limits are adopted.
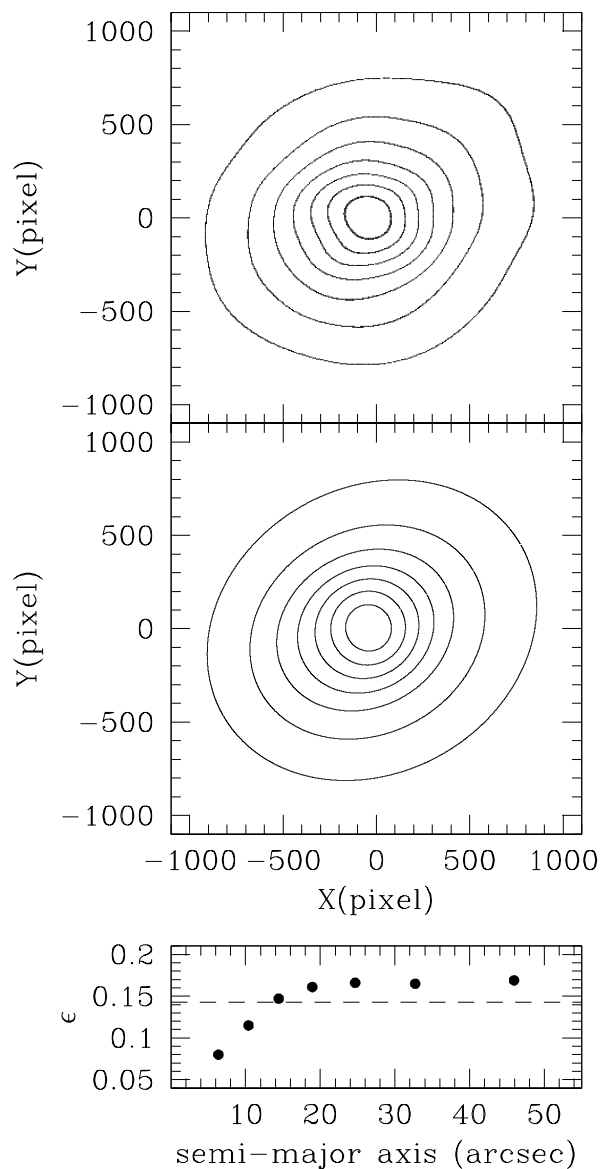
Figure 5.11: *Upper panel*: the map of NGC 1783 with the isodensity contours; *central panel*: the best fit ellipses to the isodensity contours; *lower panel*: ellipticity of the best fit ellipses as a function of the semi-major axis in arcsec. The horizontal dashed line indicates the mean value.

out of the field of view of ACS. In order to properly fit the most external points of the radial profile, the best-fit King model has been combined with a constant background level (corresponding to a density of 350 stars/$arcmin^2$), and shown as a horizontal dashed line in Fig. 5.12.

131
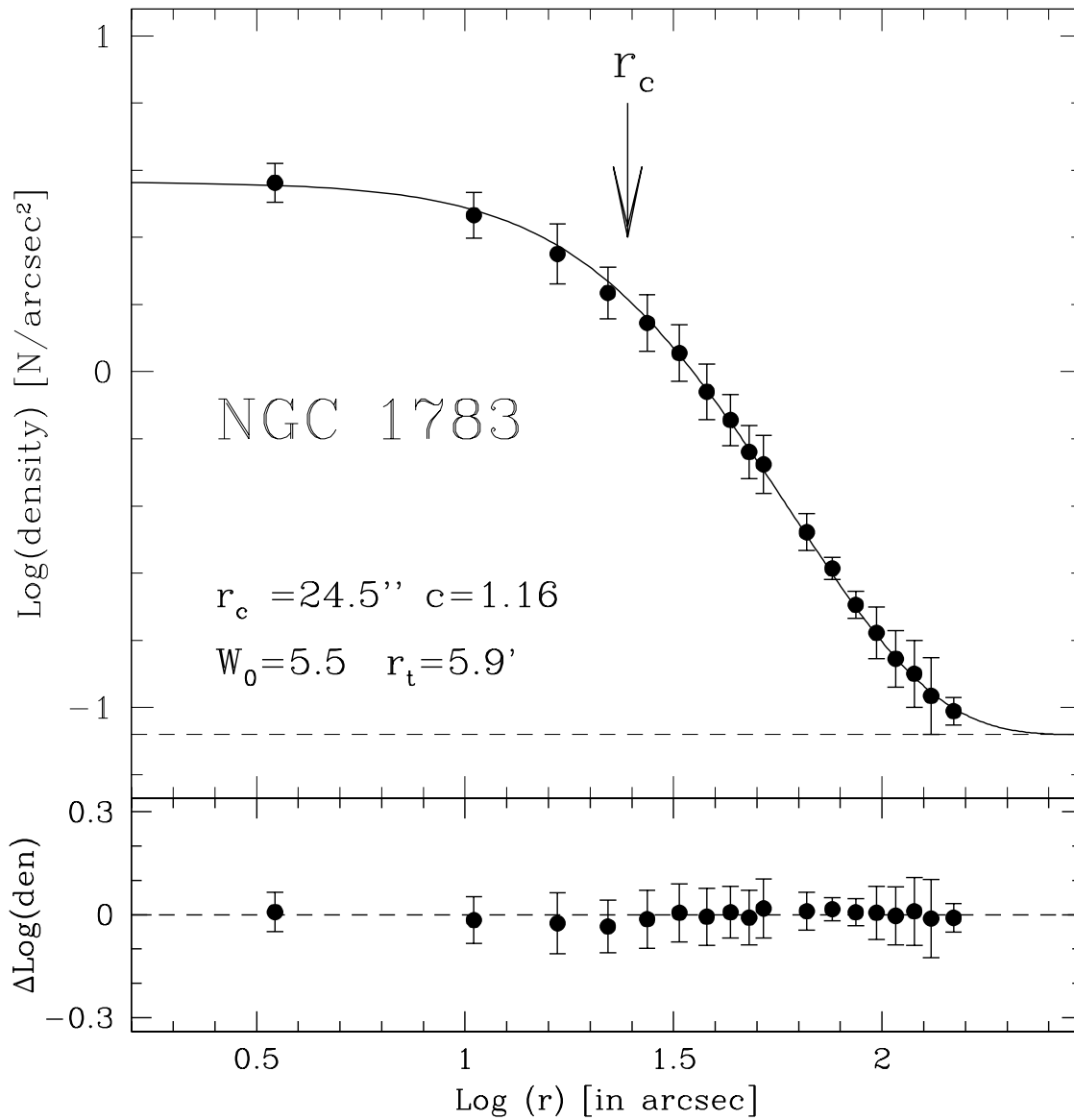
Figure 5.12: *Upper panel*: observed radial density profile for the cluster NGC 1783. The solid line is the best fit King model, with r_c=24.5" and c=1.16. The *horizontal dashed line* indicate the background level. *Lower panel*: the χ^2 test for the observed radial density profile and best-fit King model (solid line).

5.3.4 The cluster age

In the previous section we performed a detailed comparison of the observed morphology and star counts of NGC 1978 with different set of theoretical models and *overshooting* efficiencies. The best agreement between observations and theoretical predictions was reached with the Pisa Evolutionary Library (PEL).

Hence, we have used the PEL isochrones also to determine the age of NGC 1783. We select isochrones with Z= 0.008 (corresponding to [M/H]= -0.40 dex, as estimated in Chapter 4 from high-resolution spectroscopy), and with three different amount of *overshooting* efficiency, namely Λ_{os}= 0.0 for the canonical isochrones, and Λ_{os}= 0.10 and 0.25, representative of mild and strong *overshooting* regimes, respectively.

These theoretical isochrones have been transformed into the observational plane, by means of suitable conversions computed with the code described by Origlia & Leitherer (2000), and convolving the model atmospheres by Bessell, Castelli & Plez (1998) with the ACS filter responses. Guess values of $(m - M)_0$= 18.50 (Alves, 2004) for the distance modulus and E(B-V)= 0.10 (Persson et al., 1983) for reddening have been adopted. However, in order to obtain the best fit of the observed sequences we allowed these parameters to vary by $\leq |10|\%$ and $\leq |40|\%$ factors, respectively.

Fig. 5.13 shows the best-fit solutions for the different values of Λ_{os}, as obtained by matching the following features:

(1) the magnitude of the He-Clump;

(2) the magnitude difference between the He-Clump and the flat region of the SGB;

(3) the difference in color between the TO and the base of the RGB.

As can be seen, the canonical model with Λ_{os}= 0.0 fit the observational features (1) and (2) reasonably well with $(m - M)_0$= 18.57, E(B-V)= 0.13 and τ= 0.9 Gyr, but fails to reproduce feature (3).

Fig. 5.14 (panel (a)) shows a portion of the CMD, as zoomed onto the TO region, with the best-fit (τ= 0.9 Gyr) and 0.3 Gyr older (τ= 1.2 Gyr) isochrones. The older isochrones better fits feature (3) but predicts a too bright (by $\approx$0.3 magnitudes) He-clump. Moreover, it requires a $(m - M)_0$= 18.16 distance modulus, which is definitely too short for the LMC (Alves, 2004). Fig. 5.14 (panels (b) and (c)) shows a similar comparison for the overshooting models. For the Λ_{os}= 0.10 model (panel (b)), the best-fit (τ= 1.2 Gyr) and 0.2 Gyr older (τ= 1.4 Gyr) isochrones are plotted. As for the canonical model, the older isochrones somewhat better fits feature (3) but
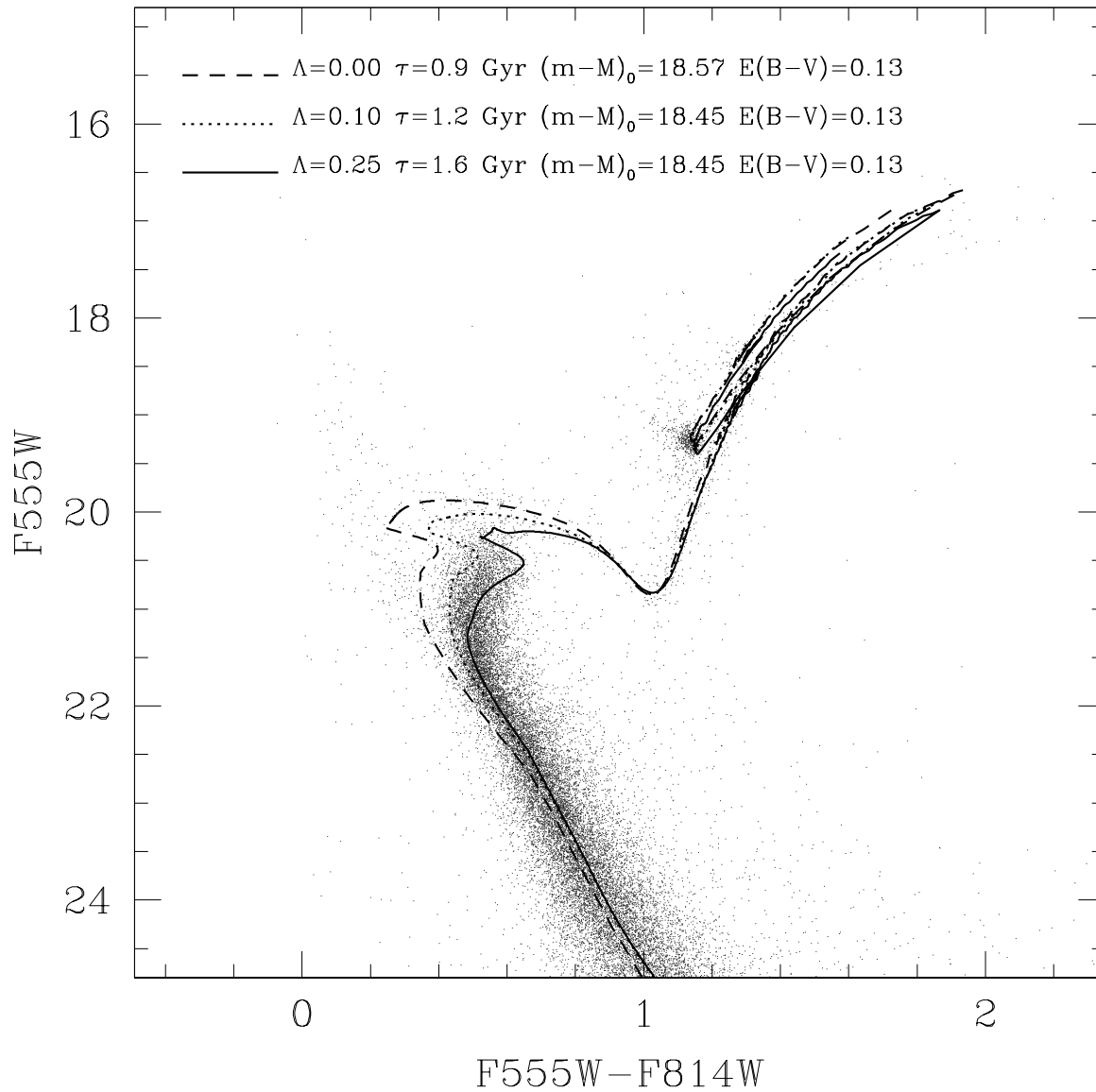
Figure 5.13: Best-fit theoretical PEL isochrones overplotted on the observed CMD of NGC 1783. Models with different assumptions of the overshooting efficiency (Λ_{os}) are used: the best fit age, distance modulus and reddening (see text) for each choice of Λ_{os} are also marked.

predicts a too bright (by $\approx$ 0.25 magnitudes) He-clump and a too short $(m-M)_0$= 18.25 distance modulus.

For the Λ_{os}=0.25 model (panel (c)), the best-fit (τ= 1.6 Gyr) and 0.2 Gyr younger (τ= 1.4 Gyr) isochrones are shown. The younger isochrone slightly better fits the SGB region but predicts a too blue MS. Also it predicts a slightly too faint (by $\approx$0.2 magnitudes) He-clump and too long $(m-M)_0$= 18.66 distance modulus.

In summary, we can conclude that canonical models, regardless the adopted isochrone age, do not provide an acceptable fit to the observed CMD, while models with Λ_{os}= 0.10 and 0.25 *overshooting*, E(B-V)= 0.13, $(m-M)_0$= 18.45 and ages between τ= 1.2 andτ= 1.6 Gyr, respectively, reasonably well reproduce all the three diagnostics features.

A quantitative check to discriminate between the different *overshooting scenarios* is to perform a comparison between the observed and theoretical LFs of the MS stars normalized to the number of the He-clump stars, defined as

$$\Phi_{norm} = \lg \frac{\sum_i N_{MS}}{N_{He-Cl}}.$$

Such a normalized LF is a powerful indicator of the relative timescales of the H and He burning phases. The observed Φ_{norm} is obtained by counting the number of MS stars (N_{MS}) in each 0.5 magnitude bin, after the correction for incompleteness and field contamination, and normalized to the total number of He-Clump stars. The innermost region of the cluster ($r < 20''$, see Fig. 5.9) has been excluded from this analysis because of its prohibitive crowding. Formal errors for the observed Φ_{norm} in each magnitude bin are computed under the assumption that star counts follow the Poisson statistics, by using the following formula:

$$\sigma_{\Phi_{norm}} = \frac{\sqrt{\Phi_{norm}^2 \cdot \sigma_{N_{He-Cl}}^2 + \sigma_{N_{MS}}^2}}{N_{He-Cl}}.$$

Since the ACS field of view is not large enough to properly sample the field population around NGC 1783, we used the most external region ($r > 150''$) of the decontamination field for NGC 1978. Indeed, these two clusters are close enough for the purpose of decontamination and their field RGB sequences are well-overlapped.

Fig. 5.15 shows the histogram of the number of MS stars per $arcmin^2$ at r> 150" from the center of NGC 1978. The number of MS and He-Clump stars in this field has been subtracted from the NGC 1783 cluster stellar counts, after the normalization for the sampled area.

Hence, the total number of stars in each magnitude bin is given by:
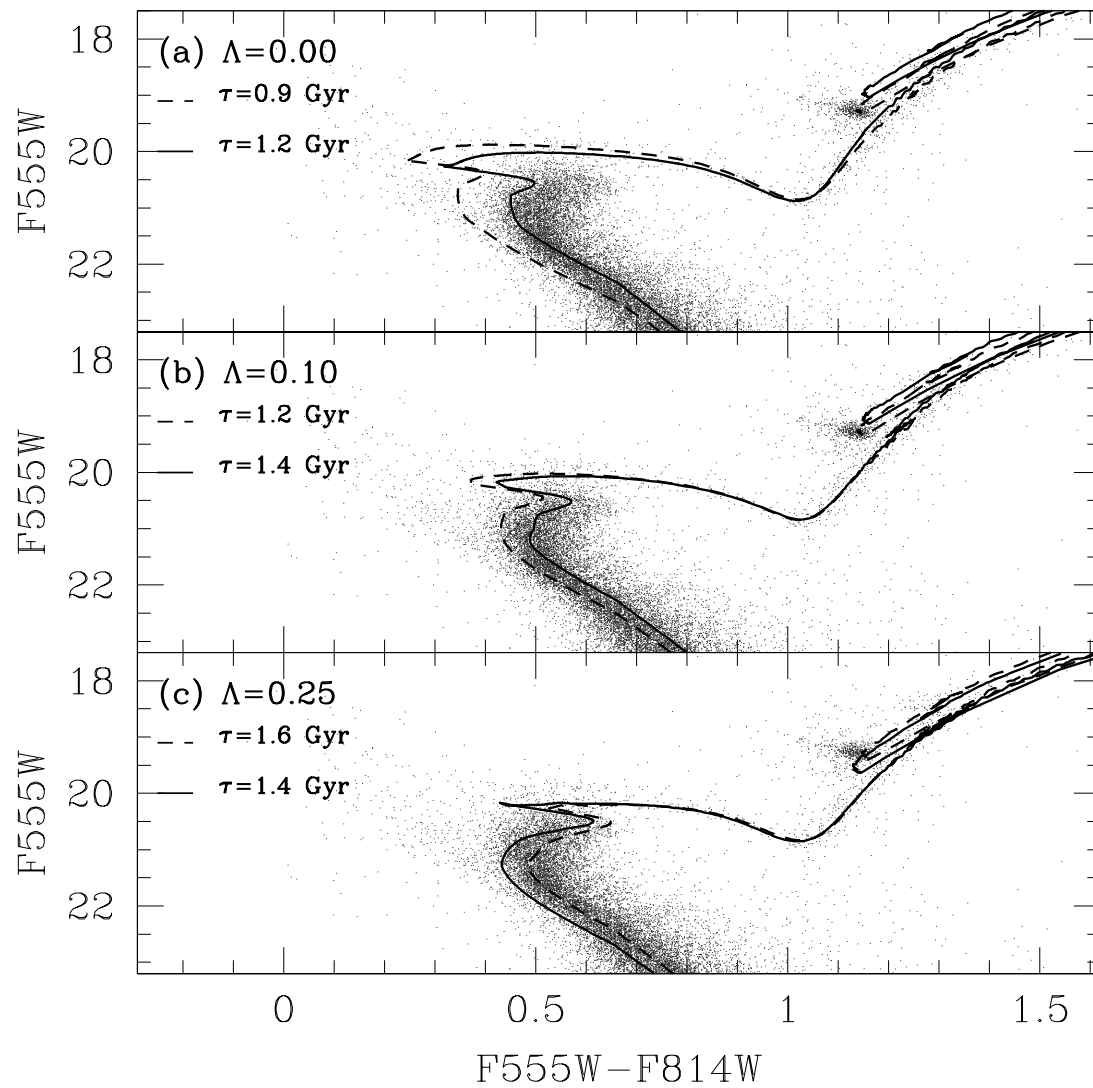
$$N_{corr} = \frac{N_{obs}}{\phi} - N_{field}.$$

Figure 5.14: Best-fit theoretical PEL isochrones overplotted on the observed CMD of NGC 1783. Models with different assumptions of the overshooting efficiency (Λ_{os}) are used: the best fit age, distance modulus and reddening (see text) for each choice of Λ_{os} are also marked.
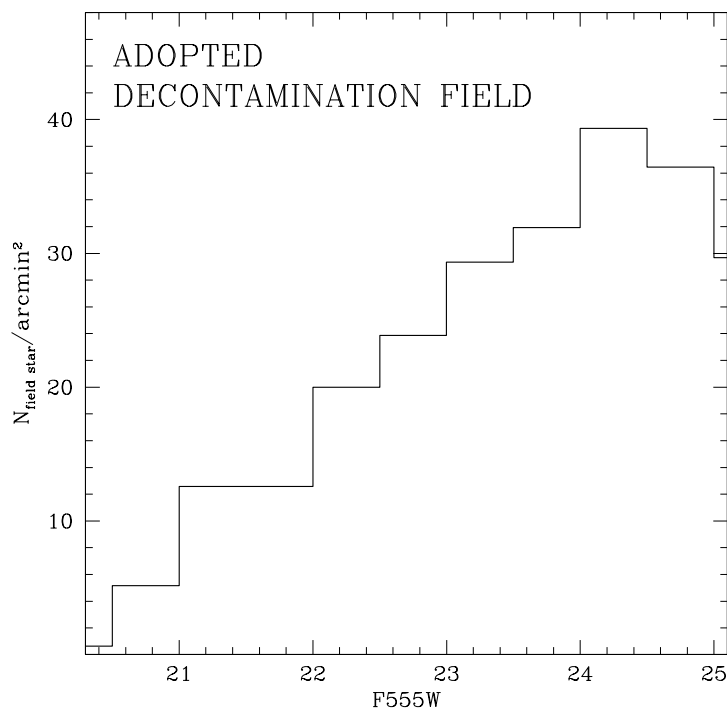
Figure 5.15: Histogram of the number of MS stars per $arcmin^2$ at r>150" from the center of NGC 1978.

In order to compute the theoretical Φ_{norm} predicted by the PEL models, we have adopted the well-know technique of synthetic diagrams. By using the best-fit models described above, we randomly distributed the stars along the isochrone according to a Salpeter IMF. An artificial dispersion has been added in order to simulate the photometric errors. For each model, 200 synthetic diagrams are computed by using Montecarlo simulations, and the corresponding Φ_{norm} are extracted and averaged together.

Fig. 5.16 (panel *(a)*) shows the observed LF (black points) compared with the theoretical expectations, computed by using the three different *overshooting* models. Clearly, the Λ_{os}=0.0 model predicts a Φ_{norm} value $\sim$ 10-15% lower than the observed one; the Λ_{os}= 0.10 and 0.25 models marginally (<5%) underestimate the observed value of Φ_{norm}. This small offset can be easily accounted for by adding a binary population in the synthetic LF. To do this, we assumed that a given fraction f_b of the simulated stars be the primary star of a binary system. The mass of the primary is randomly extracted, while the mass of the secondary star is assigned by adopting the mass ratio *q*, between the secondary and primary star. The magnitude of the binary system is given

137

by $M_{F555W}^{Binary} = -2.5 \cdot \log\left(10^{-2.5 \cdot (M_{F555W}^{prim} + M_{F555W}^{sec})}\right)$, where M_{F555W}^{Binary}, M_{F555W}^{prim} M_{F555W}^{sec} are the magnitudes of the binary, the primary and the secondary star, respectively. The latter has been obtained from the isochrone mass/luminosity relation. Panel *(b)* in Fig. 5.16 shows the comparison between the observed and theoretical Φ_{norm} with a binary population. The inclusion of $\approx$10% binaries with a flat distribution of mass ratios (*q*= 0.80) provide a good match between theoretical and observed Φ_{norm} for the models with overshooting. A residual discrepancy of $\approx$ 10% is still present between the observed and the theoretical Φ_{norm} as predicted by the Λ_{os}=0.00 model. The adopted binary fraction is somewhat smaller than previous estimates ($\leq$ 30%) in other LMC and SMC clusters (Testa et al., 1995; Barmina, Girardi & Chiosi, 2002; Chiosi & Vallenari, 2007).

5.4 Comparison between NGC 1783 and NGC 1978

We have investigated the main properties (in terms of morphology, structural parameters and age) of two massive, intermediate-age LMC clusters, namely NGC 1783 and NGC 1978, by using high-resolution ACS@HST photometry. Briefly, the main results obtained are summarized as follows:

(1) the firm detection of the RGB bump along the RGB of NGC 1978, located at F555W= 19.10$\pm$0.10; this features results to be not detectable in NGC 1783, due to its poorly populated RGB;

(2) the ellipticity of these two clusters turn out to be ϵ=0.14$\pm$ 0.03 and 0.30$\pm$ 0.02 for NGC 1783 and NGC 1978. The high-ellipticity of these two objects poses two major questions: *i)* why the LMC clusters in general, and NGC 1978 in particular, are, in average, more elliptical than those in the Milky Way? *ii)* why NGC 1978 is more elliptical than the other LMC clusters? Goodwin (1997) suggests that the relatively small LMC tidal field can preserve the pristine triaxial structure of the clusters, while the strong tidal field of our Galaxy tend to destroy it, thus removing at least part of the ellipticity. In order to explain the especially high ellipticity of NGC 1978 three main hypothesis have been proposed in the past: a merging episode, a rotation effect and an anisotropic velocity dispersion tensor (Fischer, Welch & Mateo, 1992). The merging scenario has been proposed because the broad RGB from ground-based BVRI photometry (Alcaino et al., 1999) and because the preliminary evidence of a metallicity dispersion from high-resolution spectroscopy of two RGB stars (Hill et al., 2000) (δ[Fe/H]$\sim$ 0.2-0.3 dex). However, the narrow RGB sequence presented in this work as well as the recent iron abundance estimate from high-
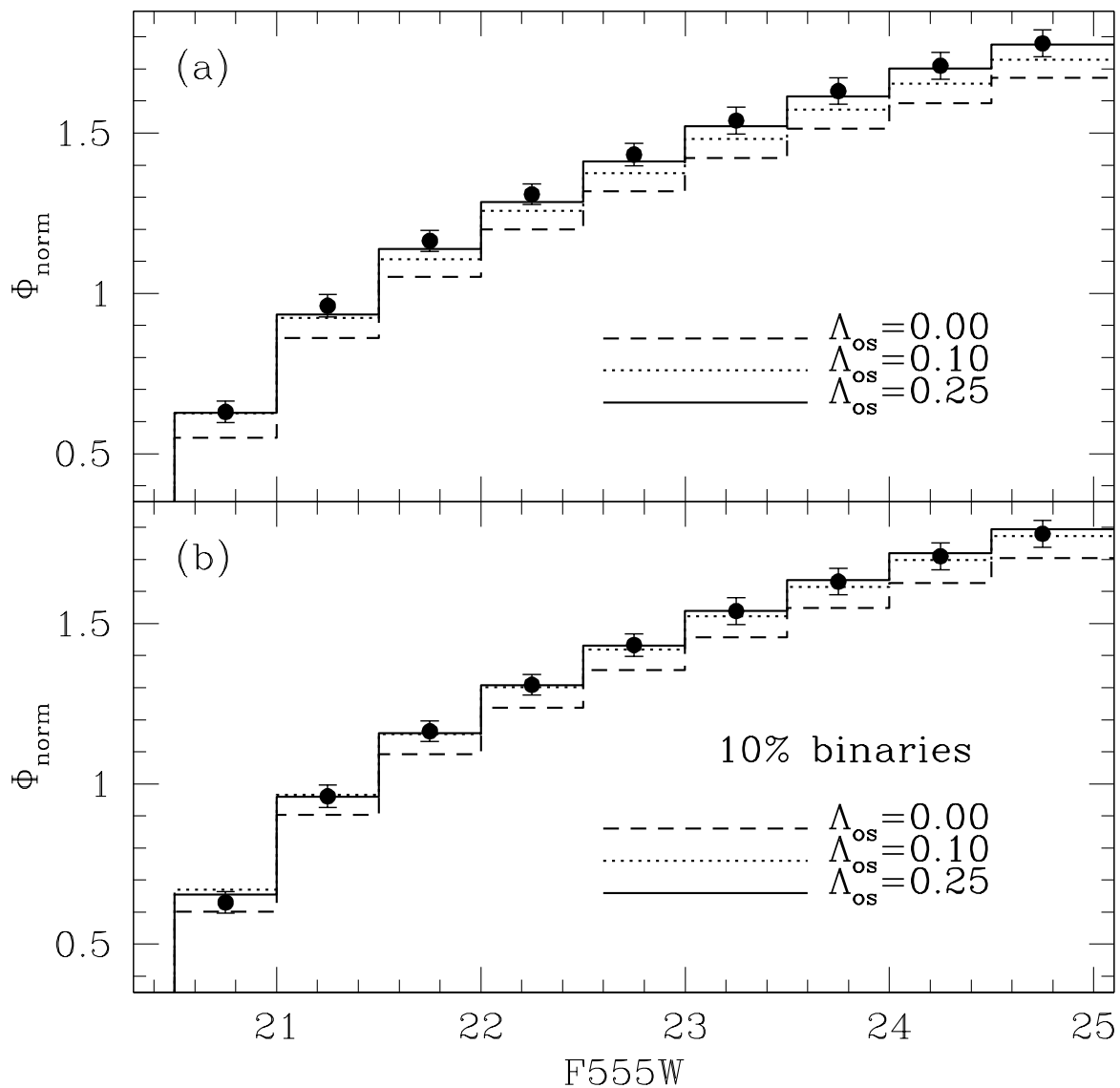
Figure 5.16: Panel *(a)*: integrated LF of the MS stars normalized to the number of He-Clump stars: *black points* indicate the observed LF and the error-bars correspond to their uncertainties. The three line are the theoretical LFs computed by adopting Λ_{os}=0.0 (dashed), 0.10 (dotted) and 0.25 (continuous). Panel *(b)*: same as panel *(a)*, but adding a 10% binary fraction in the computation of the theoretical LFs.

resolution spectra of eleven RGB stars presented by Ferraro et al. (2006) and discussed in Chapter 4 definitely excluded any significant metallicity spread within the cluster.

(3) We derived the structural parameters (r_c, r_t and c) for the cluster NGC 1783. These structural parameters and the age of the cluster inferred from this study, allow us to constrain the dynamical state of this cluster. The resulting core radius of r_c= 24.5" (corresponding to ∼ 5.9 pc adopting the distance modulus of $(m - M)_0$= 18.45, obtained from the best-fit with the *overshooting* models, see Sect. 5.3.4) is consistent with the age-core radius relationship discussed by Mackey & Gilmore (2003) and based on the surface brightness radial profiles of 53 LMC rich clusters. The youngest (ages <∼200 Myr) clusters of their sample exhibit core radii < 3 pc, while the older (both intermediate and old-age) stellar clusters show a more scattered distribution, with r_c between ∼1 and ∼8 pc, a major peak at r_c ∼2.5 pc and the presence of several objects with r_c >∼5 pc. The inferred concentration parameter, c= 1.16, is consistent with a not core-collapse cluster (Meylan & Heggie, 1997), as expected given the relatively young age of NGC 1783.

(4) We have studied the evolutive sequences in the observed CMDs of these two clusters, both in terms of morphologies and number counts, in comparison with different theoretical libraries. We have shown that the best fit solutions to the observed CMD features are obtained by selecting Λ_{OS}= 0.1-0.25 and τ= 1.2-1.6 Gyr for NGC 1783 (see Sect. 5.3.4) and Λ_{OS}= 0.1 and τ= 1.9 Gyr for NGC 1978.

The overall CMD characteristics of NGC 1783 are quite similar to those of NGC 1978, although there is evidence of an age difference. Further insight on the relative age of the two clusters can be obtained from the direct cluster-to-cluster comparison of the overall CMD properties. To this aim we can define the δV_{SGB}^{He-Cl} parameter as the magnitude difference between the luminosity distribution peak of the He-Clump and the flat region of the SGB. This *differential* parameter can provide an independent estimate of the age, and it is formally the analogous of the so-called *vertical method*, based on the magnitude difference between the TO and the Horizontal Branch magnitude level, and used to infer the age for the old globulars (see e.g. Buonanno, Corsi & Fusi Pecci, 1989). Fig. 5.17 shows the two observed CMDs with marked the δV_{SGB}^{He-Cl} parameter: we find δV_{SGB}^{He-Cl}= 0.90 and 1.56 for NGC 1783 and NGC 1978, respectively. This difference is an independent, clearcut indication that NGC 1783 is younger than NGC 1978.
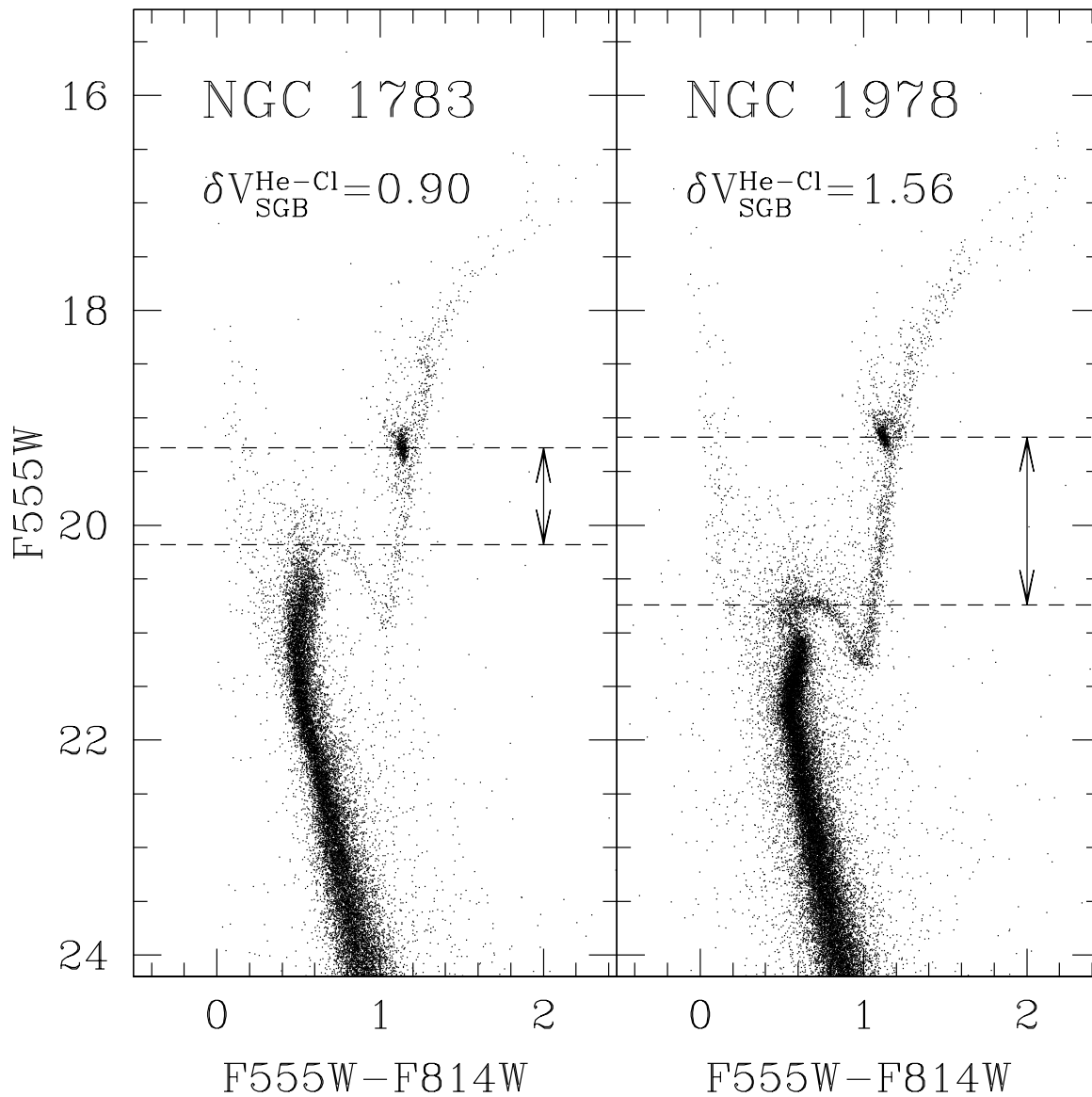
Figure 5.17: ACS@HST (F555W, F555W-F814W) CMDs for the LMC cluster NGC 1783 (left panel) and NGC 1978 (right panel). The arrows indicate the magnitude difference δV_{SGB}^{He-Cl} between the He-Clump and the flat portion of the SGB.

Fig. 5.18 shows the theoretical relations between the δV_{SGB}^{He-Cl} observable and the age, as derived from the PEL models with different amounts of *overshooting*. The grey area marked the region of the $(\tau, \delta V_{SGB}^{He-Cl})$ plane for a mild/strong overshooting efficiency appropriate for NGC 1783. Hence, by entering the measured δV_{SGB}^{He-Cl} in the above relations, an independent estimate of the age based on this differential parameter can be obtained. By using the measured value of $\delta V_{SGB}^{He-Cl} = 0.90$, we find τ= 1.4±0.2±0.1 Gyr for NGC 1783, where the first errorbar refers to the uncertainty in *overshooting* efficiency and the second to the uncertainties in the adopted reddening and distance modulus. This age is still consistent with the one inferred by Geisler et al. (1997) (τ= 1.3 Gyr), while it is significantly older than the age derived from the s–parameter ($\tau \sim$0.9 Gyr) and by Mould et al. (1989) (τ= 0.7-1.1 Gyr). In Chapter 3 we noted that the $N_{Bright-RGB}/N_{He-Cl}$ population ratio computed for NGC 1783 is too high for the clusters undergoing the RGB Phase-Transition, as suggested by the s–parameter age. Our new determination of an older age for NGC 1783, better reconcile the $N_{Bright-RGB}/N_{He-Cl}$ population ratio with the observed well-populated RGB.

Finally, we stress the importance of these new age estimates coupled with the new iron abundance determinations discussed in Chapter 4. This is especially important, since the correct shape of the AMR in the LMC is still matter of debate: in particular the origin of the observed bimodality in the LMC cluster age distribution has been interpreted as the evidence for two major episodes of star formation. Pagel & Tautvaisiene (1998) computed two different AMR semi-empirical models for the LMC, with a continuous star formation and with two burst episodes occurred ∼14 and 3 Gyr ago, respectively. Fig. 5.19 shows the results of these theoretical predictions with the position of these 2 clusters in the age-metallicity plane using the new coordinates obtained for these objects. Similar accurate ([Fe/H], τ) coordinates for a significant number of LMC clusters with different ages and metallicities are urgently needed to disentangle different formation scenarios. This is the aim of our ongoing global project. The grey boxes in Fig. 5.19 show the position of the clusters actually in preparation (see Chapter 4). By combining detailed chemical abundance (from high-resolution spectra) and ages (from high quality photometry) to a number of pillar LMC clusters, we plan to calibrate a suitable age and metallicity scale for the entire LMC globular cluster system, with the ultimate goal of providing a robust AMR.
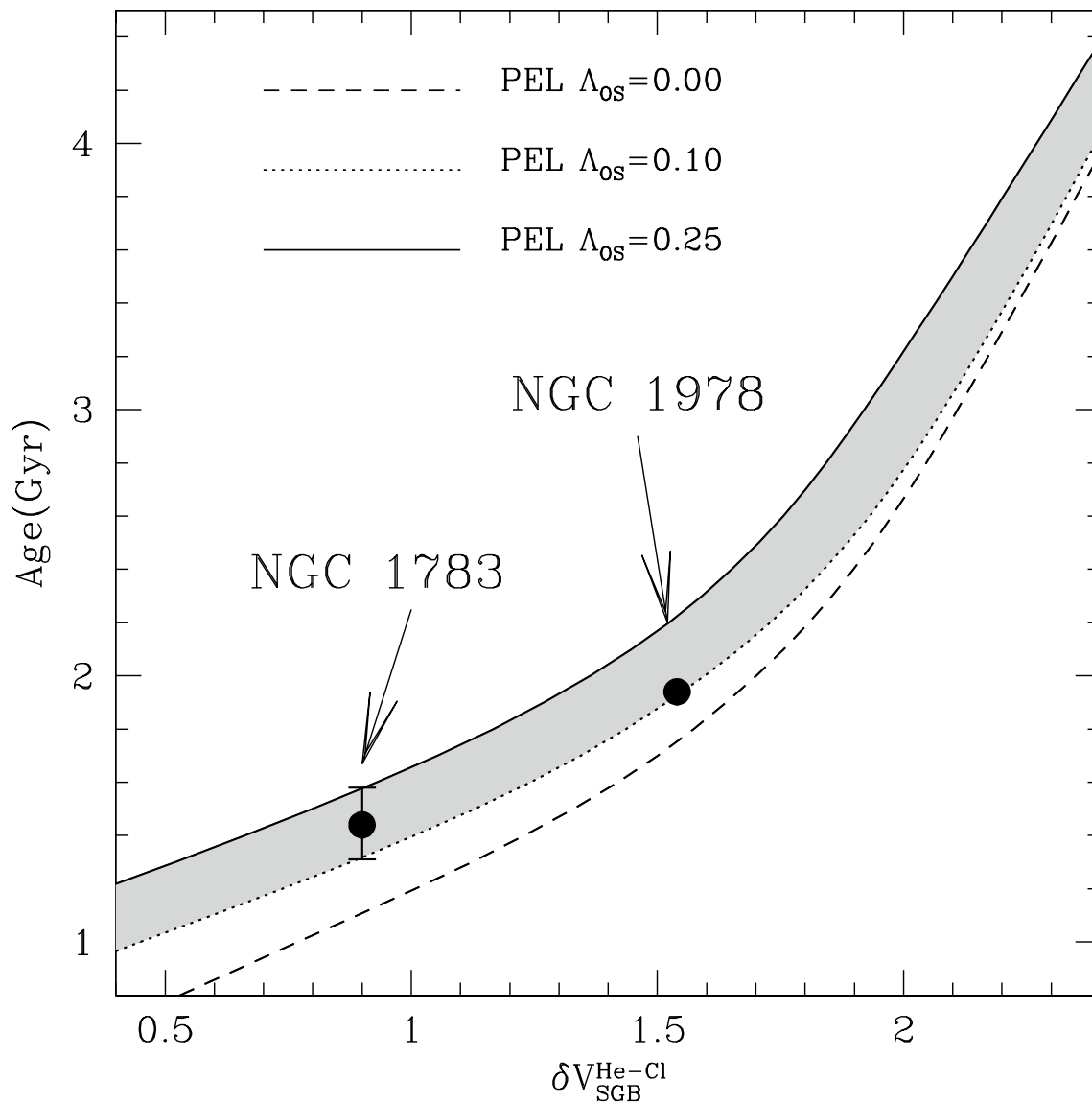
Figure 5.18: Theoretical predictions for the magnitude difference between the He-Clump and the flat portion of the SGB as a function of the age for three different *overshooting* assumptions: Λ_{OS}=0.0 (dashed line), Λ_{OS}=0.10 (dotted line) and Λ_{OS}=0.25 (solid line). The observed values for δV_{SGB}^{He-Cl} and the inferred ages for NGC 1783 and NGC 1978 are plotted as black points.
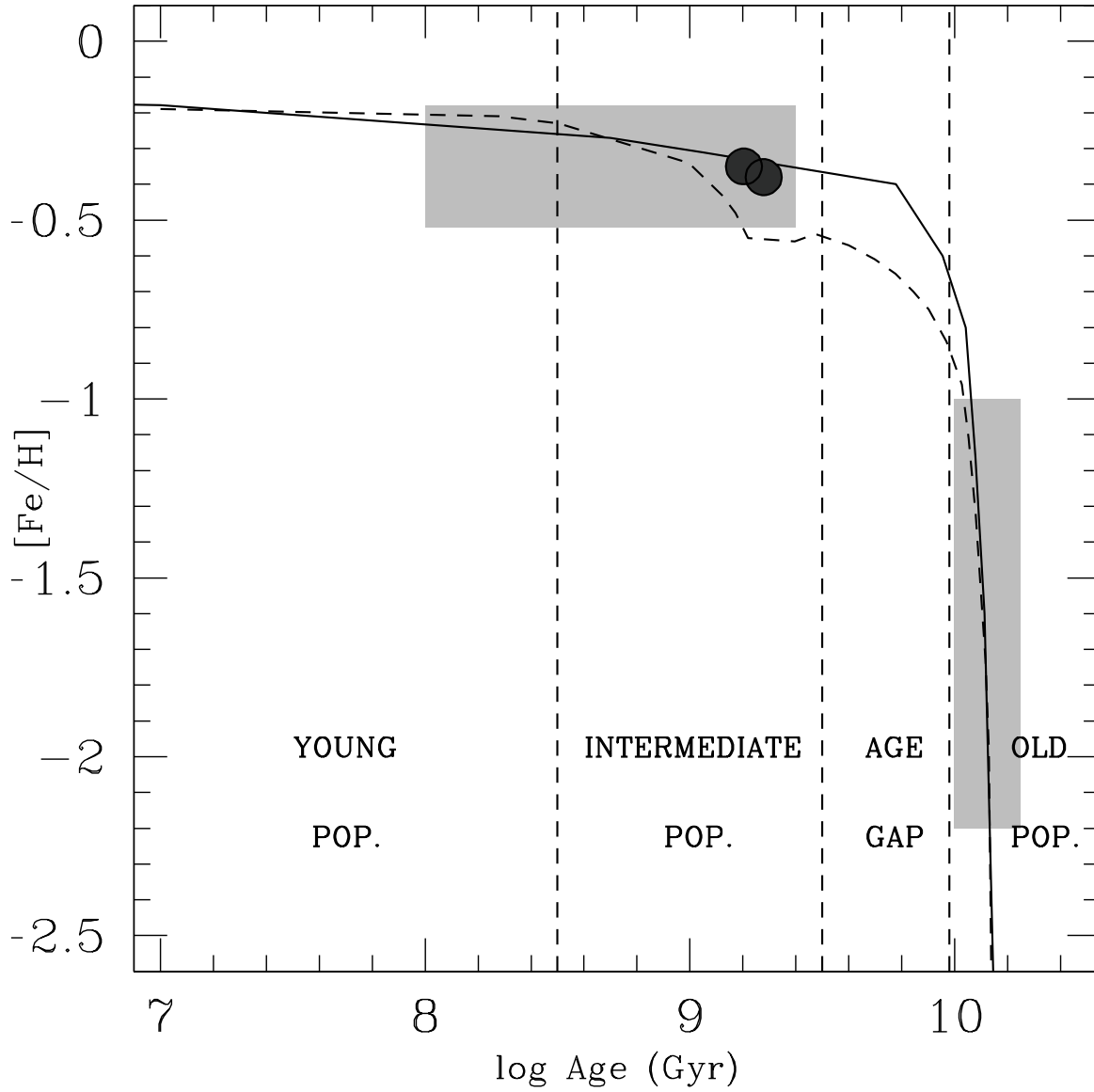
Figure 5.19: Theoretical predictions for the LMC AMR computed by Pagel & Tautvaisiene (1998). The solid line refers to an AMR obtained assuming continuos star formation, and the dashed line corresponds to a bursting model. The black points indicate the position of NGC 1783 and NGC 1978 using the metallicities and the ages derived in this study. The grey boxes represent the age/metallicity area covered by the sample of clusters which we are currently analyzing.

Chapter 6

Conclusions and future perspectives

Near-Infrared survey of the Magellanic Clouds

We obtained high-resolution J, H and K photometry for 33 Magellanic clusters (27 belonging to the LMC and 6 in the SMC), spanning the entire age range covered by this cluster system. We performed an accurate analysis of the AGB and RGB populations both in young and intermediate age clusters. In particular:

- By performing a detailed *census* of the AGB stars in the young and intermediate-age target clusters, we estimated that the AGB contribution to the total luminosity starts to be significant at ∼200 Myr and reaches its maximum at 500-600 Myr, with a following decrease. This maximum contribution derives mainly from the C-stars population. These stars account for ∼60-70% of the total luminosity in the 700-1000 Myr age range, according to the previous work by Frogel, Mould & Blanco (1990). For ages of ∼5-7 Gyr (an age range sampled by the SMC clusters of our database) the contribution of the AGB to the total cluster light is of ∼5%, with the total lack of C-stars.

- We computed population ratios, by using both star counts and luminosities, in order to estimate the contribution of the RGB stars (normalized to the He-Clump population and to the total cluster light). These observed RGB population ratios show a sharp enhancement at ∼700 Myr, suggesting that the RGB Ph-T occurs at this age, in a time-scale of ∼300 Myr. This represent the first empirical probe of the occurring of the so-called RGB Ph-T. The comparison with suitable theoretical models evidences as this behavior is in good agreement with the canonical models, while *overshooting* models predict a significantly larger age (∼1.3 Gyr) for the RGB Ph-T.

For ages greater than ∼1 Gyr the population ratios show a flattening, according to the predictions of theoretical canonical models.

The chemical composition of the LMC clusters

We performed a detailed abundance analysis of the most important chemical elements of 27 giant members of 4 LMC intermediate-age clusters. We compared the inferred abundance patterns with those of other intermediate age populations in different galactic environments, namely the LMC field, the Galactic thin disk and the Sgr dSph. Such an analysis allows us to obtain important information about the chemical properties of the intermediate-age population of the LMC:

- As unequivocally traced by both field and cluster stars, the intermediate-age population of the LMC is metal-rich, with an average iron content between 1/3 and half solar.

- The interstellar medium from which these stars formed had the time to be significantly enriched by SN Ia and AGB star ejecta, as traced by the $[\alpha/\text{Fe}]$ and [s-process/Fe] abundance patterns.

- An enhanced pollution of the gas (from which these clusters formed) by SN II and AGB stars with low metallicity could explain either the depletion of [Al/Fe] and [Na/Fe] and the enhancement of the [Ba/Y] abundance ratios with respect to the values measured in the Galactic thin disk stars.

- The lack of clear O-Na and Mg-Al anti-correlations seems to indicate that the studied LMC clusters did not undergo appreciable self-enrichment, as likely the old Galactic GCs did. However, this has to be proven on a better statistical ground.

- The enhanced [Eu/Fe] ratios appear to be in contradiction with the solar $[\alpha/\text{Fe}]$ ratio, despite the same nucleosinthetic site (massive stars). This decoupling between r- and α-elements seems to be a distinctive feature of several extragalactic environments (LMC, SMC, Sgr, dSphs).

- The chemical analysis of these clusters provides an overall picture of the metal-rich, intermediate-age component of the LMC cluster system, remarkably different with respect to the Galactic field populations of similar ages and metallicities. We found similar $[\alpha/\text{Fe}]$ and [iron-peak/Fe] ratios and discrepant light Z-odd and neutron-capture elements.

146

Moreover, the comparison with the Sgr dSph evidences some similarities ([Na/Fe], [Al/Fe] and the neutron capture elements pattern) but also several differences (as the average value of the [α/Fe] and [iron-peak/Fe] ratios). Our results point toward a scenario of chemical evolution dominated by previous generations of low-metallicity stars, able to produce the observed depletion of light Z-odd elements as well as the behaviour of the s-process elements. The extension of our study to additional younger and older LMC clusters will provide new insight towards the understanding of the LMC formation and chemical enrichment history.

The ages of the LMC clusters

We have began an extensive survey based on high-resolution photometry, in order to investigate the main morphological properties of a sample of massive LMC globular clusters and derive for these accurate ages. We have presented the results for two intermediate-age clusters, (namely NGC 1978 and NGC 1783), by using ACS@HST deep photometry and discussing different theoretical evolutionary libraries.

- We compared the morphologies and star counts along evolutionary stellar sequences in the observed CMDs and different evolutionary libraries, exploring different assumptions for the *overshooting* parameter, namely Λ_{OS}=0.0, 0.10 and 0.2/0.25. A very good match can be obtained only with the Pisa Evolutionary Library (PEL) assuming a non-zero Λ_{OS}. We obtained an age of 1.9 Gyr for NGC 1978 (adopting models with Λ_{OS}= 0.10) and of 1.4 Gyr for NGC 1783 (obtained by the average between the ages inferred by using models with Λ_{OS}= 0.10 and 0.25, because a clear discrimination between these two models results not trivial).

- We noted the necessity to include an amount of *overshooting* in order to well reproduce the observed population ratios. Of course, only two clusters not allow us to clearly disentangle clearly the amount of Λ_{OS}, but the results point toward the inclusion of a moderate amount of *overshooting*. The direct comparison between these two CMDs confirms the obtained age difference.

- The age estimate for these 2 clusters evidence a clear discrepancy with the ages inferred by adopting the s–parameter and the temporal calibration by Girardi et al. (1995). We found a difference $\Delta = Age_{TO} - Age_{s-par}$ of 0.5 Gyr and –1.5 Gyr for NGC 1783 and NGC 1978,

respectively. These first results confirm the urgency to define a new age scale for the LMC clusters based on direct measurement of the MS TO and by using this to define a new calibration for the s–parameter.

- We confirmed the high ellipticity of both the clusters, according to the previous determinations. We obtained $\epsilon = 0.30 \pm 0.02$ and 0.14 ± 0.03 for NGC 1978 and NGC 1783, respectively.

- We detected the RGB Bump along the RGB of NGC 1978 and located at F555W= 19.10 ± 0.10. This is the first detection of such an evolutive feature in a so young stellar population.

Future perspectives

The results discussed in this Thesis are only the first steps in order to derive new age and metallicity scales for the LMC clusters and in this way define a new robust AMR.
The works actually in progress and the future observational campaigns of this project are oriented to the following directions:

- The study of the main morphological features of the old LMC and SMC clusters in the near-infrared plane and the comparison with the near-infrared properties of the GGCs.

- To complete the chemical analysis of the other 5 LMC clusters (2 with ages less than $\sim$1 Gyr and 3 belonging to the old population) already observed with the optical high-resolution spectrograph FLAMES@VLT. Moreover, similar observations to study the chemical composition of SMC clusters are mandatory.

- The chemical analysis of 4 very young LMC and SMC clusters by using infrared high-resolution spectra obtained with CRIRES@VLT.

- The study of the optical CMDs of all the clusters for which we have derived accurate metallicities (similarly to the study of NGC 1783 and NGC 1978).

- A detailed study of the impact of the *overshooting* effects by using this extensive optical photometric database, in order to well calibrate the correct amount of *overshooting* to include, if any, in the evolutionary models to reproduce the observed stellar populations.

148

Bibliography

Alcaino, G., Liller, W., Alvarado, F., Kravtsov, V., Ipatov, A., Samus, N., & Smirnov, O., 1999, A&AS, 135, 103

Alonso, A., Arribas, S., & Martinez-Roger, C., 1999, A&AS, 140, 261

Alonso, A., Arribas, S., & Martinez-Roger, C., 2001, A&A, 376, 1039

Alves, D. R., Rejkuba, M., Minniti, D., & Cook, K. H., 2002, ApJ, 573, L51

Alves, D. R., 2004, New Astronomy Review, 48, 659

Andersen, J, 1999, Transactions of the IAU, Vol. XXIVA, p.36, 24, A36

Aoki, W., Ryan, S. G., Norris, J. E., Beers, T. C., Ando, H., Iwamoto N., Kajino, T., Mathews, G. J., & Fujimoto, M. Y., 2001, ApJ 561, 346

Arlandini, C., Kappeler, F., Wisshak, K., Gallino, R., Lugaro, M., Busso, M., & Straniero, O., 1999, ApJ, 525, 886

Barmina, R., Girardi, L., & Chiosi, C., 2002, A&A, 385, 847

Barklem, P. S., Piskunov, N., & O'Mara, B. J., 2000, A&AS, 142, 467

Baumueller, D. & Gehren, T., 1996, A&A, 307, 961

Becker, S., & Mathews, J., 1983, AJ, 270, 155

Bedin, L. R., Cassisi, S., Castelli, F., Piotto, G., Anderson, J., Salaris, M., Momany, Y. & Pietrinferni, A., 2005, MNRAS, 357, 1048

Bekki, K.,Couch, W. J.,Beasley, M. A., Forbes, D. A., Chiba, M., & Da Costa, G. S., 2004, ApJ, 610, L93

Bekki, K., & Chiba, M., 2005, MNRAS, 356, 680

Bellazzini, M., Ferraro, F. R., & Pancino, E., 2001, MNRAS, 327, L15

Bellazzini, M., Ferraro, R. R., Origlia, L., Cacciari, C., Pancino, E., Monaco, L., & Oliva, E., 2002, AJ, 124, 3222

Bertelli, G., Nasi, E., Girardi, L., Chiosi, C., Zoccali, M., & Gllart, C., 2003, AJ, 125, 770

Bessell, M. S. & Brett, J. M., 1988, PASP, 100, 1134

Bessell, M. S., Brett, J. M., Wood, P. R., & Scholz, M., 1989, A&AS, 77, 1

Bessel, M. S., Castelli, F., & Plez, B., 1998, A&A, 333, 231

Bhatia, R. K., Read, M. A., Hatzidimitriou, D., & Tritton, S.,1991, A&A, 87, 335

Bhatia, R. K., 1992, MmSAI, 63, 141

Bica, E., Geisler, D., Dottori, H., Clariá, J. J., Piatti, A. E., & Santos, J. F.C., Jr, 1998, AJ, 116, 723

Blanco, V. M., Blanco, B. M. & McCarthy, M. F., 1980, ApJ, 242, 938

Bloecker, T. & Schoenberner, D., 1991, A&A, 244L, 43

Bomans, D. J., Vallenari, A., & de Boer, K. S., 1995, A&A, 298, 427

Bonifacio, P., Hill, V., Molaro, P., Pasquini, L., Di Marcantonio, P., & Santin, P., 2000, A&A, 359, 663

Bono, G., Caputo, F., Cassisi, S., Castellani, V., & Marconi, M., 1997, ApJ, 479, 279

Bono, G., Castellani, V., & Marconi, M., 2002, ApJ, 565, L83

Bohm-Vitense, E., 1958, ZA, 46, 108

Bragaglia, A., Carretta, E., Gratton, R. G., Tosi, M., Bonanno, G., Bruno, P., Calí, A., Claudi, R., Cosentino, R., Desidera, S., Farisato, G., Rebeschini, M., & Scuderi, S., 2001, AJ, 121, 327

Brocato, E., Castellani, V., Ferraro, F. R.,Piersimoni, A. M.,& Testa, V.,1996, MNRAS, 282, 614

Brocato, E., Di Carlo, E., & Menna, G., 2001, ApJ, 560, 142

Brocato, E., Castellani, V., Di Carlo, E., Raimondo, G., & Walker, A. R., 2003, AJ, 125, 3111

Buonanno, R., Corsi, C. E., & Fusi Pecci, F. 1989, A&A, 216, 80

Burris, D. L., Pilachowski, C. A., Armandroff, T. E., Sneden, C., Cowan, J. J., & Roe, H., 2000, ApJ, 544, 302

Busso, M., Gallino, R., & Wasserburg, G. J., 1999, ARA&A, 37, 239

Buzzoni, A., 1989, ApJS, 71, 817

Buzzoni, A., 2002, AJ, 123, 1188

Cayrel, R., 1988, in IAU Symp. 132, "The Impact of Very High S/N Spectroscopy on Stellar Physics", ed. G. Cayrel de Strobel & M. Spite, Dordrecht, Kluwer, 345

Calzetti, D., de Marchi, G., Paresce, F., & Shara, M., 1993, ApJ, 402, 1

Cariulo, P., Degl'Innocenti, S., & Castellani, V., 2004, A&A, 421, 1121

Carrera, R., Gallart, C., Hardy, E., Aparicio, A., & Zinn, R., 2007, astro-ph/0710.3076

Carretta, E., Gratton, R. G., Bragaglia, A., Bonifacio, P., & Pasquini, L., 2004. A&A, 416, 925

Carretta, E., Bragaglia, A., Gratton, R. G., Momany, Y., Recio-Blanco, A., Cassisi, S., Francois, P., James, G., Lucatello, S., & Moehler, S., 2007, A&A, 464, 953

Cassisi, S. & Salaris, M., 1997, MNRAS, 285, 593

Castellani, V.,Degl'Innocenti, S., Marconi, M., Prada Moroni, P.G., Sestito, P., 2003, A&A, 404, 645

Clementini, G., Gratton, R., Bragaglia, A., Carretta, E., Di Fabrizio, L., & Maio, M., 2003, AJ, 125, 1309

Charlot, S., & Bruzual, G., 1991, ApJ, 367, 126

Chiosi, E., & Vallenari, A., 2007, A&A, astro-ph/070228

Cioni, M. R. L., van der Marel, R. P., Loup, C., & Habing, H. J., 2000, A&A, 359, 601

Cioni, M.-R., L., Girardi, L., Marigo, P., & Habing, H., J., 2005, astro-ph/0509881

Cole, A. A., Smecker-Hane, T. A., & Gallagher, J. S., 2000, AJ,120, 1829

Cole, A. A., Tolstoy, E., Gallagher III, J. S., & Smecker-Hane, T. A., 2005, AJ, 129, 1465

Cole, A. A., Gallagher III, J. S., Freedman, W., & Phelps, R., 1997, AJ, 113, 1700

Cowan, J. J., & Sneden, C., 2004, Carnegie Observatories Astrophysics Series, Vol. 4, ed. A. McWilliam and M. Rauch, Cambridge Univ. Press

Dall'Ora, M., Storm, J., Bono, G., Ripepi, V., Monelli, M., Testa, V., Andreuzzi, G., Buonanno, R., Caputo, F., Castellani, V., Corsi, C. E., Marconi, G., Marconi, M., Pulone, L., & Stetson, P. B., 2004, ApJ, 610, 269

de Freitas Pacheco,J. A., Barbuy, B. & Idiart, T., 1998, A&A, 332, 19

Den Hartog, E. A., Lawler, J. E., Sneden, C., & Cowan, J. J., 2003, ApJS, 148, 543

Dieball, A., Muller, H., & Grebel, E. K., 2002, A&A, 391, 547

Dirsh, B., Richtler, T., Gieren, W. P., & Hilker, M., 2000, A&A, 360, 133

Dolphin, A. E., Walker, A. R., Hodge, P. W., Mateo, M., Olszewski, E. W., Schommer, R. A., & Suntzeff, N. B., 2001, ApJ, 562, 303

Dopita, M. A., Vassiliadis, E., Wood, P. R., Meatheringhan, J. S., Harrington, J. P., Bohlin, R. C., Ford, H. C., Stecher, T. P., & Maran, S. P., 1997, ApJ, 474, 188

Elson, R. A., & Fall, S. M. 1985, ApJ, 299, 211

Elson, R. A., & Fall, S. M. 1988, AJ, 96, 1383

Elson, R. A., 1992, MNRAS, 256, 515

Ferraro, F. R., Fusi Pecci, F., Testa, V., Greggio, L., Corsi, C. E., Buonanno, R., Terndrup, D. M. & Zinnecker, H., 1995, MNRAS, 272, 391

Ferraro, F. R., Messineo, M., Fusi Pecci, F., de Palo, M. A., Straniero, O., Chieffi, A., & Limongi, M., 1999, AJ, 118, 1738

Ferraro, F. R., Sills, A., Rood, R. T., Paltrinieri, B., & Buonanno, R., 2003, ApJ, 588, 464

Ferraro, F. R., Origlia, L., Testa, V. & Maraston, C., 2004, ApJ, 608, 772

Ferraro, F. R., Sollima, A., Pancino, E., Bellazzini, M., Straniero, O., Origlia, L., Cool, A. M. 2004b, ApJ, 603, L81

Ferraro, F. R., Beccari, G., Rood, R. T., Bellazzini, M., Sills, A., & Sabbi, E., 2004, ApJ, 603, 127

Ferraro, F. R.,Mucciarelli, A., Carretta, E., & Origlia, L., 2006, ApJ, 645, L33

Fischer P., Welch, D. L., & Mateo, M., 1992, AJ, 104, 3

Freytag, B., Ludwig, H.-G., & Steffen, M., 1996, A&A, 313, 497

Fukunaga, K., 1972, "Introduction to statististical pattern recognition", Academic Press, New York

Frogel J. A., Persson, S. E., Aaronson, M., & Matthews, K., 1978, ApJ, 220, 75

Frogel, J. A., Mould, J. R. & Blanco, V. M., 1990, ApJ, 352, 96

Fulbright, J. P., 2000, AJ, 120,1841

Fusi Pecci, F., Ferraro, F. R., Crocker, D. A., Rood, R. T., & Buonanno, R., 1990, A&A, 238, 95

Gallart, C., Zoccali, M., Bertelli, G., Chiosi, C., Demarque, P., Girardi, L., Nasi, E., Woo, J.-H., & Yi, S., 2003, AJ, 125, 742

Geisler D., & Hodge, P., 1980, ApJ, 242, 73

Geisler, D., Bica, E., Dottori, H., Claria, J. J., Piatti, A. E., & Santos, J. F. C. Jr., 1997, AJ, 114, 1920

Geisler, D., Wallerstein, G., Smith, V. V., & Casetti-Dinescu, D. I., 2007, PASP, 119, 939

Girardi, L., Chiosi, C., Bertelli, G., & Bressan, A. 1995, A&A, 298, 87

Girardi, L., Bressan, A., Bertelli, G. & Chiosi, C., 2000, A&AS, 141, 371

Girardi, L., & Marigo, P., 2007, A&A, 462, 237

Glatt, K., Gallagher, J. S., Grebel, E. K., Nota, A., Sabbi, E., Sirianni, M., Clementini, G., Tosi, M., Harbeck, D., Koch, A., & Cracraft, M., 2008, AJ, 135, 1106

Gonzalez, G., & Wallerstein, G., 1999, AJ, 117, 2286

Goodwin, S., 1997, MNRAS, 186L, 39

Gratton, R. G., 1988, Rome Obs. Preprint, 29

Gratton, R. G., Carretta, E., Eriksson, K., & Gustafsson, B., 1999, A&A, 350, 955

Gratton, R. G., Carretta, E., Claudi, R., Lucatello, S., & Barbieri, M., 2003, A&A, 404, 187

Gratton, R. G., Sneden, C., & Carretta, E., 2004, ARA&A, 42, 385

Gratton, R. G., Lucatello, S., Bragaglia, A., Carretta, E., Momany, Y., Pancino, E., & Valenti, E., 2006, A&A, 455, 271

Gray, D. F., 1992, The Observation and Analysis of Stellar Photospheres, Cambridge, UK, Cambridge University Press.

Grebel, E. K., 1999, IAU Symposium 192, "The stejjar content of the Local Group", Eds, Whitelock & Cannon, ASP, Conf. Ser.

Grebel, E. K., 2004, in Origin and Evolution of the Elements, ed A. McWilliam & M. Rauch (Cambridge, Cambridge Univ. Press), 234

Greggio, L., 2005a, A&A, 441, 1055

Grocholski, A. J., Cole, A. A., Sarajedini, A., Geisler, D., & Smith, V. V., 2006, AJ, 132, 1630

Grocholski, A. J., Sarajedini, A., Olsen, K. A. G., Tiede, G. P., & Mancone, C. L., 2007, AJ, 134, 680

Harris, W. E., 1996, AJ, 112, 1487

Harris, J., & Zaritsky, D., 2004, A&A, 127, 1531

Hill, V., Andrievsky, S., & Spite, M., 1995, A&A, 293, 347

Hill, V., 1997, A&A, 324, 435

Hill, V., 1999, A&A, 345, 430

Hill, V., Francois, P., Spite, M., Primas, F., & Spite, F., 2000, A&AS, 364, 19

Hilker, M., Richtler, T., & Stein, D., 1995, A&A, 299, 37

Hughes, S. M., G., Wood, P. R., & Reid, N., 1991, AJ, 101, 1304

Hunter, D. A.,1999, IAUS, 190, 217

Hunter, D. A., Elmegreen, B. G., Dupuy, T. J., & Mortonson, M., 2003, AJ, 126, 1836

Iben, I., Jr., 1968, Nature, 220, 143

Iben, I. Jr. & Renzini, A., 1983, ARA&A, 21, 271

Iben, I. Jr, & Tutukov, A. V., 1984, ApJS, 54, 335

Iwamoto, K., Brachwitz, F., Nomoto, K., Kishmoto, N., Umeda, H., Hix, W. R., & Thielemann, F.-K., 1999, ApJS, 125, 439

Kerber, L. O., Santiago, B. X., Castro, R., & Valls-Gabaud, D., 2002, A&A, 390, 121

Kerber, L., Santiago, B., & Brocato, E.,2007, A&A, 462, 139

King, C. R., Da Costa, G., & Demarque, P., 1984, ApJ, 299, 674

Korn, A. J., Becker, S. R., Gummersbach, C. A., & Wolf, B., 2000, A&A, 353, 655

Korn, A. J., Keller, S. C., Kaufer, A., Langer, N., Przybilla, N., Stahl, O., & Wolf, B., 2002, A&A, 385, 143

Kurucz, R. L., 1993, CD-ROM 13, Smithsonian Astrophysical Observatory, Cambridge

Kurucz, R. L., 1994, CD-ROM 19

Johnson, R. A., Beaulieu, S. F., Gilmore, G., G. F., Hurley, J., Santiago, B. X., Tanvir, N. R., & Elson, R. A. W., 2002, MNRAS, 324, 367

Johnson, J. A., Ivans, I. I.& Stetson, P. B., 2006, ApJ, 640, 801

Kroupa, P., 2001, MNRAS, 322, 231

Lawler, J. E., Wickliffe, M. E., den Hartog, E. A., & Sneden, C., 2001, ApJ, 563, 1075

Lejeune, Th., Cuisinier, F., & Buser, R., 1997, A&AS, 125, 229

Letarte, B Hill, V., Jablonka, P., Tolstoy, E., Francois, P., & Meylan, G., 2006, A&A, 453, 547L

Luck, R. E., Moffett, T. J., Barnes III, T. G., & Gieren, W. P., 1998, AJ, 115, 605

Mackey, A. D. & Gilmore, G. F., 2004, MNRAS, 338, 85

Mackey, A. D., Payne, M. J., & Gilmore, G. F., 2006, MNRAS, 369, 921

Mackey, A. D., & Broby Nielsen, P., 2007, astro-ph/0704336

Magain, P. 1984, A&A, 134, 189

Mateo, M., Hodge, P., & Schommer, R. A., 1986, ApJ, 311, 113

Mateo, M., 1988, ApJ, 331, 261

Meylan, G., & Heggie, D. C., 1997, ARA&A, 8, 1

Maraston, C., 1998, MNRAS, 300, 872

Maraston, C., Kissler-Patig, M., Brodie, J. P., Barmby, P., & Huchra, J. P., 2001, A&A, 370, 176

Maraston, C., 2005, MNRAS, 362, 799

Matteucci, F.,& Chiosi, C., 1983, A&A, 123, 121

Matteucci, F., " The Chemical Evolution of the Galaxy", 2003, Astrophysic and Space Science
    Library, VOl. 253, Kluwer Academic Publishers, Dordrecht

McWilliam, A., & Williams, R. E., 1991, IAUS, 148, 391

Mc William, A., Preston, G. W., Sneden, C., & Searle, L., 1995, AJ, 109,2757

Merritt, D., Meylan, G., Mayor M., 1997, AJ, 114, 1074

Meurer, G. R., Cacciari, C, & Freeman, K. C., 1990, AJ, 99, 4

Meylan, G., Sarajedini, A., Jablonka, P., Djorgovski, S. G., Bridges, T., Rich, R. M. 2001, AJ,
    122, 830

Mighell, K. J., Sarajedini, A., & French, R. S., 1998, ApJ, 116, 2395

Minniti, D., Borissova, J., Rejkuba, M., Alves, D. R., Cook, K. H., & Freeman, K. C., 2003,
    Science, 301, 5639

Mishenina, T. V., Bienaymé, O., Gorbaneva, T. I., Charbonnel, C., Soubiran, C., Korotin, S. A., &
    Kovtyukh, V. V., 2006, A&A, 456, 1109

Monaco, L., Ferraro, F. R., Bellazzini, M., & Pancino, E., 2002, ApJ, 578. L50

Monaco, L., Bellazzini, M., Bonifacio, P., Ferraro, F. R., Marconi, G., Pancino, E., Sbordone, L., & Zaggia, S., 2005, A&A, 441, 141

Monaco, L., Bellazzini, M., Bonifacio, Buzzoni, A., Ferraro, F. R., Marconi, G., Sbordone, L., & Zaggia, S., 2007, A&A, 464, 201

Montegriffo, P., Ferraro, F. R., Fusi Pecci, F., & Origlia, L., 1995, MNRAS, 276, 739

Montegriffo, P., Ferraro, F. R., Origlia, L. , & Fusi Pecci, F, 1998, MNRAS, 297, 872

Moorwood, A. F. M., Cuby, G. J., & Lidman, C. 1998, The ESO Messenger, 91, 9

Mould, J., Jerome, K., Nemec, J., Jensen, J., & Aaronson, M., 1989, ApJ, 339, 84

Mucciarelli, A., Origlia, L., Ferraro, F. R., Maraston, C., & Testa, V., 2006, ApJ, 646, 939

Mucciarelli, A., Ferraro, F. R., Origlia, L., & Fusi Pecci, F., 2007, AJ, 133, 2053

Mucciarelli, A., Origlia, L., & Ferraro, F. R., 2007, AJ, 134, 1813

Mulas, G., Modigliani, A., Porceddu, I., & Damiani, F., 2002, Spie, 4844, 310

Norris, J. E., Ryan, S. G., & Beers, T. C., 1997a, ApJ, 488, 350

Oliva, E., & Origlia, L. 1998, A&A, 332, 46

Olsen, K. A. G., Hodge, P. W., Mateo, M., Olszewski, E. W., Schommer, R. A., Suntzeff, N. B., & Walker, A. R., MNRAS, 300, 665

Olszewski, E. W., Schommer, R. A., Suntzeff, N. B. & Harris, H. C., 1991, AJ, 101, 515

Origlia, L., & Leitherer, C., 2000, AJ, 119, 2018

Pagel, B., E., J., "Nucleosynthesis and chemical evolution of galaxies", 1997, Cambridge University Press

Pagel, B. E. J., & Tautvaisiene, G., 1998, MNRAS, 299, 535

Panagia, N., 1999, IAUS, 190, 549

Pancino, E.,Seleznev, A., Ferraro, F. R., Bellazzini, M. & Piotto, G., 2003, MNRAS, 345, 690

Pasquini, L. et al., Messenger, 110, 1

Persson, S. E., Aaronson, M., Cohen, J. G., Frogel, J. A., & Matthews, K.,1983

Pietrinferni, A., Cassisi, S., Salaris, M., & Castelli, F., 2004, ApJ, 612, 168

Pietrzynski, G., & Udalski, A., 2000, Acta Astronomica, 50, 355

Pompeia, L., Hill, V., Spite, M., Cole, A., Primas, F., Romaniello, M., Pasquini, L., Cioni, M-R.,
   & Smecker Hane, T., 2006, arXiv:astro-ph/0604009v2

Portegies Zwart, S. F., & Rusli, S. P., 2007, MNRAS, 374, 931

Prochaska, J. X., Naumov, S. O., Carney, B. W., McWilliam, A., & Wolfe, A., 2000, AJ, 120, 2513

Rafelski, M., & Zaritsky, D., 2005, AJ, 129, 2701

Reddy, B. E., Tomkin, J., Lambert, D. L., & Allende Prieto, C., 2003, MNRAS, 340, 304

Reddy, B. E., Lambert, D. L., & Allende Prieto, C., 2006, MNRAS, 367, 1329

Renzini, A., & Buzzoni, A. 1986, in Spectral Evolution of Galaxies, ed C. Chiosi & A. Renzini
   (Dordrechet Reidel)

Renzini, A. & Voli, M., 1981, A&A, 94, 175

Rich, M. R., Shara, M. M., & Zurek, D., 2001, AJ, 122, 842

Richtler, T., Spite, M., & SPite, F., 1989, A&A, 225, 351

Rieke, G. H., & Lebofsky, M. J. 1985, ApJ, 288, 618

Russell, S. C., & Bessell, M. S., 1989, ApJS, 70, 865

Sagar, R., & Pandey, A. K., 1989, A&AS, 79, 407

Salaris, M. & Cassisi, S., 1996, A&A, 305, 858

Salaris, M., Chieffi, A., & Straniero, O., 1993, ApJ, 414, 580

Salaris, M. & Cassisi, S., "Evolution of stars and Stellar Populations", Wiley, 2006

Salpeter, E. E., 1955, ApJ, 121, 161

Sarajedini, A., Grocholski, A. J., Levine, J., & Lada, E., 2002, AJ, 124, 2625

Sbordone, L., Bonifacio, P., Buonanno, R., Marconi, G., Monaco, L., & Zaggia, S., 2007, A&A, 465, 815

Scalo, J. M., 1986, Fundam. Cosmic. Phys., 11, 1

Schlegel, D. J., Finkbeiner, D. P., & Davis, M. 1998, ApJ, 500, 525

Schommer, R. A., Suntzeff, N. B., Olszewski, E. W., & Harris, H. C., 1992, AJ, 103, 447

Searle, L., & Zinn, R., 1978, ApJ, 225, 357

Searle, L., Wilkinson, A., & Bagnuolo, W. G. 1980, ApJ, 239, 803

Shara, M. M., Fall, S. M., Rich, R. M., & Zurek, D., 1998, ApJ, 508, 570

Shetrone, M., Venn, K. A., Tolstoy, E., Primas, F., Hill, V., & Kaufer, A., 2003, AJ, 125, 684

Sigurdsson, S., & Phinney, E. S., 1995, ApJS, 99, 609

Sirianni, M, Nota, A., De Marchi, G., Leitherer, C., & Clampin, M., 2002, ApJ, 579, 275

Sollima, A., Pancino, E., Ferraro, F. R., Bellazzini, M., Straniero, O., Pasquini, L. 2005, ApJ, 634, 332

Smecker-Hane, T. A., Cole, A. A., Gallagher III, J. S., & Stetson, P. B., 2002, ApJ, 566, 239

Smith, V. V., Hinkle, K. H., Cuhna, K., Plez, B., Lambert, D. L., Pilachowski, C. A., Barbuy, B., Melendez, J., Balachandran, S., Bessell, M. S., Geilser, D. P., Hesser, J. E., & Winge, C., 2002, AJ, 124, 3241

Spergel, D. N., Verde, L., Peiris, H. V., Komatsu, E., Nolta,M. R., Bennett, C. L., Halpern, M., Hinshaw, G., Jarosik, N., Kogut, A., Limon, M., Meyer, S. S., Page, L., Tucker, G. S., Weiland, J. L., Wollack, W., & Wright, E. L., 2003, ApJS, 148, 175

Staveley-Smith, L., Kim, S., Calabretta, M. R., Haynes, R. F., & Kesteven, M. J., 2003, MNRAS, 339,87

Stetson, P. B., 1987, PASP, 99, 191

Straniero, O. & Chieffi, A., 1991, ApJS, 76, 525

Sweigart, A. V., Greggio, L., & Renzini, A., 1989, ApJS, 69, 911

Sweigart, A. V., Greggio, L., & Renzini, A., 1990, ApJ, 364, 527

Testa, V., Ferraro, F. R., Brocato, V., & Castellani, V., 1995, MNRAS, 275, 454.

Testa, V., Ferraro, F.R., Fusi Pecci, F., Chieffi, A., Straniero, O., & Limongi, M., 1999, AJ, 118, 2839

Tinsley, B. M., 1979, ApJ, 229, 1046

Travaglio, C., Gallino, R., Arnone, E., Cowan, J., Jordan, F., & Sneden, C., 2004, ApJ, 601, 864

van den Bergh, S., 1981, A&AS, 46, 79

van den Bergh, S., & Morbey, C. L., 1984, ApJ, 283, 598

van den Bergh, S., 1998,PASP, 110, 1377

Venn, K. A., Irwin, M. Shetrone, M. D., Tout, C. A., Hill, V., & Tolstoy, E., 2004, AJ, 128, 1177

Zaritsky, D., 2004, ApJ, 614, L37

Zinn, R., 1980, ApJS, 42, 19

Zoccali, M., Cassisi, S., Piotto, G., Bono, G., & Salaris, M., 1999, ApJ, 518, L49

Westerlund, B. E. 1997, The Magellanic Clouds, Cambridge Astrophysics Series, 29, 72

White, R.E., & Shawl, S. J., 1987, ApJ, 317, 246